Titre: Title:	Modélisation de l'interaction entre une impulsion laser ultrabrève et une nanostructure plasmonique en milieu aqueux
Auteur: Author:	Etienne Boulais
Date:	2013
Type:	Mémoire ou thèse / Dissertation or Thesis
Référence: Citation:	Boulais, E. (2013). Modélisation de l'interaction entre une impulsion laser ultrabrève et une nanostructure plasmonique en milieu aqueux [Thèse de doctorat, École Polytechnique de Montréal]. PolyPublie. https://publications.polymtl.ca/1071/

URL de PolyPublie: PolyPublie URL:	https://publications.polymtl.ca/1071/
Directeurs de recherche: Advisors:	Michel Meunier
Programme: Program:	Génie physique

UNIVERSITÉ DE MONTRÉAL

MODÉLISATION DE L'INTERACTION ENTRE UNE IMPULSION LASER ULTRABRÈVE ET UNE NANOSTRUCTURE PLASMONIQUE EN MILIEU AQUEUX

ETIENNE BOULAIS
DÉPARTEMENT DE GÉNIE PHYSIQUE
ÉCOLE POLYTECHNIQUE DE MONTRÉAL

THÈSE PRÉSENTÉE EN VUE DE L'OBTENTION
DU DIPLÔME DE PHILOSOPHIÆ DOCTOR
(GÉNIE PHYSIQUE)
FÉVRIER 2013

UNIVERSITÉ DE MONTRÉAL

ÉCOLE POLYTECHNIQUE DE MONTRÉAL

Cette thèse intitulée :

MODÉLISATION DE L'INTERACTION ENTRE UNE IMPULSION LASER ULTRABRÈVE ET UNE NANOSTRUCTURE PLASMONIQUE EN MILIEU AQUEUX

présentée par : BOULAIS Etienne
en vue de l'obtention du diplôme de : Philosophiæ Doctor
a été dûment acceptée par le jury d'examen constitué de :

M. SKOROBOGATIY Maksim A., Ph.D., président
M. MEUNIER Michel, Ph.D., membre et directeur de recherche
M. LEWIS Laurent, Ph.D., membre
M. KIEFFER Jean-Claude, Ph.D., membre

REMERCIEMENTS

Je tiens premièrement à remercier mon directeur de recherche, Michel Meunier, qui m'a guidé pour la réalisation de ce projet et sans qui rien de tout cela n'eût été possible. Merci de la confiance que tu m'as accordée et de de m'avoir fait profité de ta longue, très longue expérience qui aura été à l'origine de bien des taquineries. Un grand merci également aux membres du jury qui ont accepté de siéger sur ce comité d'évaluation.

Un merci particulier à Rémi Lachaine qui a grandement contribué au succès du projet en travaillant sur les méthodes de détection des bulles et en relisant sans relâche mes interminables manuscrits. Merci à mon cousin François Bissonnette pour la conception graphiques de certains éléments. Merci aussi à Judith Baumgart, David Rioux, Andréanne Bolduc, Bastien St-Louis-Lalonde, Ali Hatef, Weiming Ding, Alexandre Robitaille, Mathieu Maisonneuve, Arnaud Maillard, Caroline-Miville Godin, Patrick Lavoie, Laure Humbert, Sébastien Besner, Julie Fantoni, Nancy Tawil, Guillaume Poulin et Étienne Bourbeau, qui m'ont accompagné au cours des années et avec qui j'ai eu plusieurs discussions enrichissantes, et d'autres, un peu moins. Merci à Yves Drolet et à Konstantinos Piyakis pour leur support technique.

Je tiens à remercier également le Conseil de Recherches en Sciences Naturelles et en Génie du Canada (CRSNG) ainsi que le Fond Québécois de Recherche en Sciences Naturelles et en Technologies (FQRNT) pour leur appui financier au projet. Je tiens aussi à souligner la contribution du Réseau Québécois de Calcul de Haute Performance (RQCHP) pour l'utilisation des ressources informatiques nécessaires à la bonne réalisation du projet.

Merci à Albert Huynh, Julia Wünsche, Tamara-Stéphanie Boulay et Marilou Morin pour les heures agréables passées au gymnase et les deux pieds dans le sable. Merci à Louis Lazure qui est là depuis le début, à Bruno et Martin Legris pour les heures à se percer les tympans, à Geneviève et Amélie Thibert qui m'ont aidé à passer à travers des étapes plus difficiles et aux autres que je ne peux tous nommer ici. Votre support a été essentiel à ma réussite. Merci également à Marie-Josée Laventure et Thang Hoang pour m'avoir fait découvrir la science.

Je ne peux évidemment pas passer sous silence ma famille. Merci à mon père et à ma mère pour leur soutien indéfectible, leur patience infinie et leur constante abnégation. J'espère pouvoir être à la hauteur lorsque mon tour viendra. Merci à ma soeur Annie, son conjoint Richard et à mon cousin Éric pour ces moments de détente si appréciés. Un merci spécial à ma filleule Camille, mon neveu Rémy ainsi qu'à Angélie et Guillaume pour rendre ma vie si agréable. Finalement, un remerciement spécial à Valéry Truchon qui a su continuer à m'endurer quand moi-même je ne m'endurais plus. Merci d'avoir été là pour moi. Une grande partie du succès de ce travail te revient de droit.

RÉSUMÉ

Ces dernières années ont été marquées par une rapide évolution du domaine des nanotechnologies biomédicales. Plus particulièrement, l'utilisation de laser à impulsions ultrabrèves pour affecter localement et avec précision certaines structures cellulaires et sub-cellulaires présente un intérêt grandissant. Ce type d'impulsion, grâce à leur temps d'impulsion très court ($\sim$ 100 fs), permet en effet l'ablation efficace de matériau organique transparent tout en réduisant les dommages collatéraux provoqués aux structures environnantes. Cette technologie est néanmoins limitée par certaines contraintes physiques et technologiques, telle que la limite de diffraction, qui restreint ses performances et son application. L'utilisation de structures métalliques aux dimensions nanométriques permet de pallier à ce problème. Ces nanostructures ont en effet l'étonnante capacité d'absorber et de concentrer l'énergie du champ laser dans des volumes nanométriques, bien inférieurs à la limite de diffraction. Cette propriété est causée par l'excitation d'une oscillation collective des électrons de conduction du métal induite par le champ électromagnétique incident, appelée plasmon, qui absorbe et amplifie localement le champ électrique. L'excitation de ce plasmon est de nature résonante à une longueur d'onde incidente qui dépend fortement de la géométrie, des dimensions, du matériau et de l'environnement de la nanostructure.

Le degré de localisation de l'énergie lumineuse atteint à l'aide de ces nanostructures plasmoniques est sans équivalent dans le monde macroscopique. Leur utilisation de concert avec des impulsions ultrabrèves permet par conséquent de concentrer l'énergie lumineuse et de réaliser l'ablation de structures avec une résolution bien supérieure à la limite de diffraction, et ce sans nécessiter un système optique de visualisation et de focalisation particulier. Au niveau cellulaire, cette technique permet de réaliser l'ablation ou la modification ciblée de structures cellulaires et sub-cellulaires avec une précision et une efficacité inégalée.

Bien que plusieurs études aient démontré le potentiel de cette technologie, la compréhension des mécanismes physiques fondamentaux et phénomènes induits par l'irradiation demeure limitée. En particulier, aucun modèle décrivant l'ensemble des sources potentielles de dommages aux structures cellulaires (hausse de température, génération de plasma, émission d'ondes de pression, formation de bulles de cavitation) possiblement induites par l'irradiation de nanostructure plasmonique par des impulsions ultrabrèves n'est actuellement disponible dans la littérature.

Cette thèse présente une modélisation complète de l'interaction d'une impulsion laser ultrabrève et d'une nanostructure plasmonique en milieu aqueux. Les propriétés optiques, mécaniques, thermiques de l'eau sont en effet suffisamment près de celles du milieu biologique

pour permettre l'obtention de tendances et résultats qui se transposent au milieu cellulaire tout en simplifiant considérablement le modèle.

Ce modèle, basé sur une représentation de type milieu continu et sur la résolution d'un système d'équation différentielles couplées dans un domaine tridimensionnel, simule la réponse optique et décrit l'élévation transitoire de température dans la nanostructure à l'aide d'un modèle à deux températures. Il inclut aussi la description de la production et du chauffage d'un plasma dans le milieu aqueux par le biais des mécanismes de photoionisation et d'ionisation par collision dans le champ proche de la nanostructure, ainsi que par l'émission photothermique d'électrons provenant directement de la nanostructure. Le modèle considère par ailleurs la modification locale l'indice de réfraction entraînée par ce plasma, ce qui altère la réponse optique transitoire de la nanostructure plasmonique. La relaxation énergétique du plasma couplée à une conduction thermique à l'interface métal/eau transfère l'énergie du laser aux molécules d'eau, dont l'évolution dynamique et thermodynamique est décrite à partir des équations de base de l'hydrodynamique. L'ensemble des équations du modèle est résolue de manière auto-cohérente par la méthode des éléments finis.

Le modèle est utilisé pour analyser l'interaction d'un laser femtoseconde infrarouge (45 fs, 800 nm, 200 mJ/cm^2) avec deux systèmes distincts : une nanoparticule d'or de 100 nm et un nanobâton d'or de 10×41 nm^2. La nanoparticule d'or présente une résonance plasmonique à un longueur d'onde incidente de $\sim$ 550 nm, et est donc hors-résonance à la longueur d'onde de 800 nm utilisée dans le cadre du travail. De son côté, le nanobâton possède une résonance plasmonique directement à la la longueur d'onde incidente, et est qualifié de système en-résonance.

Les résultats montrent la génération de bulles de cavitation autour des nanostructures. Des expériences de spectroscopie confirment les prédictions du modèle concernant la taille maximale des bulles créées ainsi que leur temps caractéristique de croissance pour les deux systèmes, ce qui valide le modèle proposé. Les résultats révèlent de plus la formation d'un plasma important dans le champ proche des nanostructures. Les simulations montrent un transfert énergétique rapide de ce plasma vers les molécules d'eau générant de fortes ondes de pression qui sont émises dans le milieu. Elles démontrent de plus l'importance capitale de ce plasma pour le mécanisme de cavitation. En effet, autant pour la nanoparticule que pour le nanobâton, la majorité de l'énergie du laser est déposée dans le plasma généré dans le champ proche de la particule, directement dans le milieu, et n'est pas absorbée directement par la nanostructure. Dans le cas de la nanoparticule de 100 nm, les résultats démontrent en fait que la présence de plasma est nécessaire pour expliquer la présence des bulles de vapeur qui sont observées expérimentalement à une fluence de 200 mJ/cm^2. L'énergie absorbée dans la nanoparticule n'est en effet pas suffisante pour entraîner un changement de phase dans l'eau

environnante. Cela représente un résultat majeur de la thèse, car aucune preuve tangible de ce phénomène de cavitation induit par le plasma n'était disponible dans la littérature antérieure. L'existence de ce mécanisme qui ne repose pas sur le chauffage de la nanoparticule pour induire la cavitation a de plus des conséquences importantes pour les applications en nanochirurgie.

En effet, dans le cas du système hors-résonance (nanoparticules de 100 nm), l'énergie absorbée par la nanostructure est assez faible pour que celle-ci ne soit pas endommagée lors de l'interaction, tel que confirmé par des expériences de spectroscopie. Cela confère un avantage considérable aux procédés de nanochirurgie par laser utilisant des nanoparticules hors-résonance. En effet, la fragmentation des nanoparticules peut entraîner la formation de très petites particules qui peuvent s'intercaler dans l'ADN des cellules et sont par conséquent toxiques. La faible énergie absorbée par les nanoparticules en les laissant intactes suite au traitement réduit donc ce risque et améliore la sécurité du procédé.

Au contraire, dans le cas du système en résonance (nanobâtons de 10×41 nm^2), les résultats montrent que l'énergie absorbée dans le nanobâton est suffisante pour l'endommager significativement aux fluences requises pour entraîner la cavitation dans le milieu. Irradier la structure avec une fluence sous le seuil de dommage ne résulte en effet qu'en une hausse de température ainsi qu'à la formation d'un plasma de faible densité par émission photothermique qui n'engendrent pas la production d'une bulle de vapeur dans le milieu. Ce résultat, corroboré par des expériences spectroscopiques, réduit considérablement l'intérêt des nanobâtons d'or dans le cadre d'une application en transfection cellulaire. De plus, les simulations montrent que les bulles de cavitation produites à haute fluence restent plus petites que les bulles produites autour des nanoparticules hors-résonance. Des expériences spectroscopiques confirment ce résultat contre-intuitif. Le modèle permet de démontrer que ce phénomène est issu de l'écrantage de l'excitation plasmonique résultant de la modification locale de l'indice de réfraction autour de la nanostructure causé par le plasma produit dans le milieu lors de l'irradiation.

Finalement, le modèle est utilisé pour développer une méthode permettant d'évaluer le potentiel de performance de nanostructures particulières soumises à une irradiation spécifique pour la nanochirurgie cellulaire. Cette méthode est basée sur l'introduction d'un facteur de mérite qui s'appuie sur la minimisation de la densité d'énergie absorbée dans la nanostructure pour éviter leur fragmentation, ainsi que sur la maximisation de l'énergie déposée dans le milieu afin de favoriser la formation d'une bulle de vapeur. Cette méthode prévoit que les nanoparticules d'or hors-résonance d'un diamètre de 175 nm sont les mieux adaptées à la nanochirurgie par laser utilisant des impulsions de 45 fs à une longueur d'onde de 800 nm. Elle confirme aussi le peu d'intérêt lié à l'utilisation de nanobâtons en-résonance pour ce type

de procédé.

En somme, cette thèse donne une vue globale des processus d'interaction entre un laser à impulsions ultrabrèves et une nanostructure plasmonique en milieu aqueux. Elle permet en outre d'approfondir notre compréhension des technologies de nanochirurgie cellulaire utilisant ce type d'interaction et offre des pistes intéressantes en vue de leur optimisation.

ABSTRACT

The past few years have seen the unfolding and rapid evolution of biomedical nanotechnologies. In particular, ultrafast laser pulses have been used to locally destroy or modify cellular and sub-cellular structures with exceptional precision. Those very short pulses ($\sim$ 100 fs) indeed allow the efficient ablation of organic transparent material, while limiting the collateral damages to the surrounding structures. In spite of its great efficiency and versatility, the technique is still limited by some physical constraints, such as the diffraction limit, which limit its performance and applicability. The introduction of nanoscale metallic structures can overcome this problem.Those nanostructures presents an astonishing capability to absorb an locally enhance incident laser energy into nanoscale volumes much smaller than the diffraction limit. This property arises from the laser field induced excitation of a collective oscillation of the metal's conduction electrons called plasmon. This plasmon absorbs and enhance the laser field in the vicinity of the structures. It has a resonant nature at a specific wavelength that depends strongly on the geometry, material, size and environment of the nanostructure. The degree of laser energy localization that can be possibly reached with those structures has no counterparts in the macroscopic world. Using plasmonic nanostructures with ultrafast laser pulses thus bring an unique capability to ablate or alter targeted cellular and sub-cellular structures with an astonishing precision, well beyond the diffraction limit, without even the need for a complex visualization and focussing apparatus.

While the great potential of this technology is now widely accepted, there is still a limited understanding of the basic mechanisms and processes triggered by the laser irradiation and leading to the damaging of the surrounding structures. In particular, there exists for the moment no complete modelling of the process that includes all potential sources of cellular damage, including temperature rise, plasma generation, pressure wave emission and vapor bubble formation.

This thesis presents such a modelling, with the cell environment emulated by a much simpler aqueous medium. Water is used as its optical, mechanical and thermal characteristic are similar enough to the cell environment to enable the transposition of the results and tendencies observed in water to this medium.

Modelling consists in a continuous medium based approach that uses coupled partial differential equations to simulate the nanostructure-water system's response to an ultrafast laser pulse. The the time-dependant field distribution in the system is simulated using classical electromagnetic theory, while the temperature in the nanostructure is calculated using a two-temperature model. Generation and heating of a plasma in the nanostructure's vicinity

from photoionization and impact ionization in the near-field, as well as from photothermal emission from the nanostructure at the metal interface are also included. This plasma locally modifies the refractive index, which alters the simulated optical response of the system. Energy relaxation from this plasma as well as heat conduction from the nanostructure's lattice transfer energy to the water, which dynamics and thermodynamics evolutions are simulated from hydrodynamic and energy conservation equations.

Modelling is used for analyzing the interaction of a near-infrared ultrafast laser pulse (45 fs, 800 nm, 200 mJ/cm^2) with two distinct systems : a 100nm gold nanoparticle and a 10×41 nm^2 gold nanorod. The gold nanoparticle shows a plasmon resonance at a ∼550 nm wavelength, and is thus slightly off-resonance at the 800 nm irradiation wavelength. In opposition, the gold nanorod shows a plasmon resonance directly at 800 nm and is thus in-resonance at the irradiation wavelength. The system of tightly coupled time-dependant non-linear partial differential equations is solved in 3D using a finite-element method.

The modelling shows the generation of vapor bubble around both systems, which maximal diameter and growth time are validated from spectroscopic measurements. Results show an important production of plasma in the nanostructure's near field, which fast relaxation heats rapidly the surrounding water, leading to the emission of strong pressure wave and to the formation of a vapor bubble. Simulations further demonstrate the crucial importance of the plasma in the cavitation mechanism. For both the nanoparticle and the nanorod, results show that most of the laser energy is indeed absorbed in the plasma surrounding the nanostructure rather than in the nanostructure itself. In particular, the energy absorbed in the nanoparticle is shown to be insufficient to induce the formation of a vapor bubble at 200 mJ/cm^2, whereas such a bubble is experimentally observed. This is a major result of the thesis, as such a plasma-mediated plasmonic enhanced cavitation mechanism has never been reported in the literature. The existence of this plasma-mediated mechanism that does not rely on the particle extreme heating to initiate cavitation has important consequences on cell nanosurgery applications.

For the off-resonance system (100nm nanoparticle), the energy absorption within the nanostructure is too weak to induce any significant damage to the particle, as confirmed by time-resolved spectroscopy experiments. This is a strong asset of off-resonance plasmonic enhanced laser cell nanosurgery technology, as fragmented nanostructures may create small DNA intercalating cytotoxic nanoparticles. The off-resonance process, by leaving the nanoparticles intact, thus reduces the risk for fragmentation and increases the overall security of the treatment.

In opposition, for the in-resonance system (10×41 nm^2 nanorod), results show that the energy absorption within the nanostructure is sufficient to induce significant damage at fluences

inducing cavitation. Sub damage threshold irradiation is shown to only result in a slight temperature increase and in the formation of a low-density plasma from photothermal emission that are insufficient to produce a vapor bubble around the structure. This result, confirmed by time-resolved spectroscopic experiments, considerably reduces the interest of gold nanorod for cell nanosurgery. In addition, simulations show that even vapor bubbles produced at high fluence stay smaller than the one produced around off-resonance nanoparticles. This counter-intuitive result is confirmed by spectroscopic experiments. The extensive modelling works allow to demonstrate that this reduction is due to the screening of the plasmon excitation resulting from the perturbation of the local refractive index around the nanostructure that arises from the plasma produced during the laser irradiation.

Finally, based on the same modelling, we develop a simple and efficient method to evaluate the potential of specific nanostructures and irradiation parameters for cell nanosurgery. We introduce a performance factor based on minimizing the energy density deposited in the nanostructure to avoid fragmentation, while maximizing the overall energy deposited in the system, to enhance the production of vapor bubbles. Results predict off-resonance 175 nm gold nanoparticles to be best suited for near-infrared ultrafast laser cell nanosurgery using 45 fs pulses at a wavelength of 800 nm. They also confirm the low interest of in-resonance gold nanorods for this type of process.

In summary, the thesis gives a complete view of the ultrafast laser interaction with plasmonic nanostructures in water and provides valuable insight for the understanding and optimization of plasmonic enhanced ultrafast laser cell nanosurgery.

TABLE DES MATIÈRES

LISTE DES TABLEAUX

LISTE DES FIGURES

LISTE DES ANNEXES

LISTE DES SIGLES ET ABRÉVIATIONS

NIR	Near infrared (Proche infrarouge)
SP	Surface plasmon (Plasmon de surface)
TP	Transverse plasmon band (Bande de plasmons transversaux)
LP	Longitudinal plasmon band (Bande de plasmons longitudinaux)
NP	Nanoparticle (Nanoparticule)
NS	Nanoshell (Nanocoquille)
NR	Nanorod (Nanobâton)
FDTD	Finite difference in the time-domain (Différences finies en domaine temporel)
DDA	Discrete dipole approximation (Approximation des dipôles discrets)
FEM	Finite-element method (Méthode des éléments-finis)
DNA	Deoxyribonucleic acid (Acide désoxyribonucléique)
RNA	Ribonucleic acid (Acide ribonucléique)
SAXS	Small angle x-ray scattering (Diffusion des rayons x à angle rasant)
PINEM	Photon-induced near-field electron spectroscopy (Spectroscopie électronique photo-induite en champ proche)
SEM	Scanning electron microscopy (Microscopie électronique à balayage)
TEM	Transmission electron microscopy (Microscopie électronique en transmission)
TTM	Two-temperature model (Modèle deux-températures)
PTTM	Parabolic two-temperature model (Modèle deux-température de type parabolique)
HTTM	Hyperbolic two-temperature model (Modèle deux-température de type hyperbolique)
EGFR	Epidermal growth factor receptor (Recepteur de factor de croissant épidermique)
YFP	Yellow fluorescence protein (Protéine fluorescente jaune)
DOX	Doxorubicin (Doxorubicine)

LISTE DES VARIABLES ET SYMBOLES

Constantes universelles

e	Charge de l'électron
c	Vitesse de la lumière
k_b	Constante de Boltzmann
$\hbar$	Constante réduite de Planck

Expressions relatives à l'irradiation laser

$\mathbf{E}$	Champ électrique
$\mathbf{H}$	Champ magnétique
k_0	Vecteur d'onde
ϵ_r	Permittivité relative
ϵ_0	Permittivité du vide
τ_p	Temps d'impulsion
ω	Fréquence angulaire du laser
I	Intensité de l'onde plane correspondant au champ électrique
S_{EM}	Taux de travail électromagnétique
σ_{ext}	Section efficace d'extinction
σ_{abs}	Section efficace d'absorption
σ_{sca}	Section efficace de diffusion
Q_{ext}	Efficacité d'extinction
Q_{abs}	Efficacité d'absorption
Q_{sca}	Efficacité de diffusion

Expressions relatives à la nanostructure d'or

G	Couplage électrons-phonons
τ_{e-ph}	Temps caractéristique de couplage électrons-phonons
T_e	Température électronique
T_l	Température du réseau
$\mathbf{q}_e$	Densité de courant de chaleur électronique
$\mathbf{q}_l$	Densité de courant de chaleur du réseau
C_e	Capacité thermique des électrons

C_l	Capacité thermique du réseau
τ_e	Temps de diffusion des électrons dans l'or
τ_l	Temps de diffusion des phonons dans l'or
κ_e	Conductivité thermique électronique
κ_l	Conductivité thermique du réseau
$f(\epsilon)$	Distribution de Fermi-Dirac
$g(\epsilon)$	Densité d'états
L_{ij}	Coefficients d'Onsager
v_l	Vitesse du son dans l'or
E	Module de Young dans l'or
ρ^{Au}	Densité de l'or
G_0	Couplage électrons-phonons dans l'or à $T_l = 300K$
$\mathbf{J}_0$	Densité de courant d'émission thermionique
A	Constante de Richardson
Φ	Travail de sortie de l'or dans l'eau
$\mathbf{J}^{th}$	Courant d'émission photothermique
$\mathbf{J}_0^{th}$	Courant d'émission thermionique
$\mathbf{J}_n^{th}$	Courant d'émission photothermique à n photons
$F(x)$	Fonction de Fowler
c_{Au}	Section efficace d'ionisation à 3 photons
J_{cond}^q	Densité de courant thermique à l'interface
q_0	Conductance à l'interface
T_l^f	Température de fusion de l'or
L	Chaleur latente de fusion de l'or
V	Volume de la nanostructure
σ_s	Surface de la nanostructure
S^{Au}	Entropie de l'or

Expressions relatives au plasma

u	Énergie cinétique du plasma
T_e	Température du plasma
n_e	Densité électronique du plasma
$\mathbf{J}^n$	Densité de courant électronique
$\mathbf{J}^q$	Densité de courant thermique
Q_{ei}	Couplage électrons-ions dans le plasma
τ_{ei}	Temps caractéristique de couplage électrons-ions

Q_{rad}	Perte énergétique du plasma par radiation
S_{photo}	Taux de photoionisation
S_{coll}	Taux d'ionisation par collision
S_{rec}	Taux de recombinaison des électrons dans l'eau
$\tilde{\Delta}$	Potentiel d'ionisation effectif dans l'eau
γ	Paramètre de Keldysh
F_j	Intégrale de Fermi d'ordre j
$K(x)$	Intégrale elliptique du second type
$E(x)$	Intégrale elliptique du premier type
μ	Potentiel chimique
Λ	Coulomb logarithm
b_{max}	Paramètre d'impact maximal
b_{min}	Paramètre d'impact minimal
T_F	Température de Fermi
m_e	Masse électronique
v_e	Vitesse des électrons
ω_p	Fréquence plasmon
ν_{en}	Fréquence de collision électrons-atomes neutres
ν_{ei}	Fréquence de collision électrons-ions
γ_c	Fréquence de collisions efficace des électrons
ν_{ci}	Fréquence d'ionisation par collision
n_a	Densité de molécules d'eau neutres
ρ_0	Densité nominale d'électrons disponibles
σ_a	Section efficace de collisions élastiques
σ_0	Section efficace d'ionisation par collision
σ	Conductivité du plasma
σ_{dc}	Conductivité du plasma à fréquence nulle
m	Masse réduite de l'exciton.

Expressions relatives à l'eau

ρ	Densité de l'eau
p	Pression
$\mathbf{v}$	Vitesse des molécules d'eau
T_m	Température de l'eau
S	Entropie de l'eau
κ	Conductivité thermique de l'eau

η	Coefficient de viscosité de l'eau
σ_s	Tension de surface de l'eau
κ_s	Courbure de la bulle
δ_s	Distribution de Dirac ayant comme support l'interface de la bulle
$\mathbf{n}$	Vecteur unitaire normal à la surface de la bulle
f	Énergie libre d'Helmohltz
m_{ion}	Masse d'une molécule d'eau
Π_s	Fonction échelon valant 1 dans la bulle et 0 à l'extérieure

CHAPITRE 1

INTRODUCTION

Ces deux dernières décennies ont vu l'avènement et le développement rapide du domaine de la plasmonique et, plus particulièrement, de celui de la nanoplasmonique. En effet, lorsque réduits à des dimensions de l'ordre de la centaine de nanomètres, les matériaux métalliques acquièrent des propriétés optiques particulières qui leur permettent d'absorber, de diffuser et de concentrer le champ lumineux avec une efficacité sans précédents [1, 2]. Ces propriétés spectaculaires résultent de l'excitation d'une oscillation collective des électrons de conduction de la nanostructures, appelé plasmon. Ce plasmon est induit par le champ électrique incident capable de pénétrer significativement la particule métallique lorsque ses dimensions sont réduites à des valeurs de l'ordre de la profondeur de peau ($\sim$ 25 nm aux fréquences optiques). L'excitation du plasmon est résonante à une longueur d'onde incidente qui dépend fortement de la géométrie, du matériau, des dimensions et de l'environnement de la nanostructure concernée, menant au phénomène de résonance plasmonique. Plusieurs matériaux sont en mesure de mener à une résonance plasmonique, la seule condition nécessaire étant de posséder une permittivité réelle négative, propriété partagée par l'ensemble des métaux, en particulier les métaux nobles (Au, Ag, Cu) et les métaux alcalins [3]. La résonance plasmonique entraine une forte absorption du champ incident ainsi que son amplification significative dans le champ proche à proximité de la nanostructure. Les nanostructures plasmoniques sont par conséquent de formidables concentrateurs d'énergie qui permettent de produire et contrôler des champs électriques à des dimensions nanométriques bien en deçà de la limite classique de diffraction, avec une efficacité sans équivalent.

L'exploitation des propriété optiques des nanostructures plasmoniques a permis le développement de technologies nouvelles qui trouvent applications dans divers domaines. Par exemple, les nanostructures plasmoniques entrent dans la conception d'antennes photocollectrices de nouvelles génération qui permettent d'améliorer l'efficacité des cellules solaires et photodétecteurs existants [4, 5]. Elles sont aussi au centre de récentes recherches visant à améliorer la capacité en mémoire des disques durs utilisés en informatiques [6, 7]. Elles sont de plus utilisées pour manipuler des objets nanométriques [8], ou encore pour réaliser des mesures optiques bénéficiant d'une résolution supérieure à la limite de diffraction [9].

Diverses stratégies sont activement développées pour auto-assembler des nanostructures plasmoniques individuelles afin d'en former des molécules plasmoniques et autres structures tridimensionnelles complexes [10, 11]. Ces assemblages ouvrent la voie au développement de

composants optiques [12], de sources cohérentes de champs optiques localisés (aussi appelées spaser) [13, 14] et à la construction de sources lasers nanoscopiques [15–17].
Les nanostructures plasmoniques sont en outre exploitées pour le développement de détecteurs biochimiques de précision qui peuvent offrir des résolutions pouvant aller jusqu'à la détection de molécules individuelles [18, 19].
L'introduction de nanostructures plasmoniques dans la recherche médicale moderne est aussi à la source du développement de nouvelles approches thérapeutiques, particulièrement en oncologie. L'utilisation de lasers continus avec des nanosphères, [20–23] nanobâtons, [24–27] ou structures coeur-couronnes [23, 28–31] fonctionnalisées permet de chauffer localement les cellules cancéreuses en vue de les détruire [32–34]. Cette technique est pleinement compatible avec les traitements de chimiothérapie conventionnels et peut même être utilisée en synergie avec celle-ci [35–39].
Parallèlement à ces innovations, l'introduction des lasers pulsés, et plus particulièrement des lasers à impulsions ultrabrèves, a permis le développement de nouvelles technologies dans le cadre de la microfabrication des métaux [40, 41], semiconducteurs [42], matériaux transparents [43, 44] ainsi que pour l'ablation de tissus biologiques [45]. Les lasers ultrarapides permettent de réaliser une ablation très précise des matériaux en raison du transfert d'énergie très rapide qu'ils impliquent, ce qui réduit l'étendue de la zone endommagée autour des régions ciblées [46]. L'ablation peut en effet être vue comme une transition directe de l'état solide à l'état de vapeur ou de plasma se produisant en quelques picosecondes, soit beaucoup plus rapidement que le temps requis à la conduction thermique dans le milieu. La région environnante n'a donc pas le temps d'être chauffée pendant l'ablation, ce qui réduit les dommages collatéraux.
De plus, les fortes intensités impliquées permettent d'atteindre des régimes d'ablation où l'absorption d'énergie se fait principalement par des processus non-linéaires d'ionisation [46, 47]. Cela permet l'ablation de structures avec une résolution supérieure à la limite de diffraction pour des fluences près du seuil d'ablation. Aussi, cette caractéristiques permet l'ablation de matériaux habituellement transparents à la longueur d'onde utilisée, tels que les verres et les matériaux biologiques. Par exemple, les lasers ultrarapides sont couramment utilisés pour graver des guides d'onde dans du verre [43, 48]. Au niveau médical, ils sont entre autre utilisés dans le cadre des chirurgies oculaires [49, 50].
Au niveau biologique, l'utilisation d'impulsions femtosecondes permet d'affecter localement, avec une résolution bien supérieure à la limite de diffraction, des structures telles que des chromosomes [51] et des organites cellulaires [43, 52, 53]. Cette classe d'applications se nomme la nanochirurgie cellulaire. Un exemple particulièrement intéressant, la transfection cellulaire par laser ultrarapide, consiste à focaliser un laser à impulsions ultrabrèves sur des membranes

cellulaires afin de les perforer et les rendre perméables à certaines molécules, telles que de l'ADN, de l'ARN ou des molécules de médicaments [54, 55]. Celles-ci peuvent alors pénétrer la cellule dont la membrane se referme sans affecter sa viabilité. Ce type de procédé a de nombreuses applications, allant de la thérapie génique à la recherche fondamentale en biologie cellulaire.

De récentes recherches visent maintenant à exploiter l'utilisation de lasers ultrarapides de concert avec la nanoplasmonique afin d'améliorer les applications de nanochirurgie cellulaire. La capacité unique des nanostructures plasmoniques à être fonctionnalisées permet de cibler certaines cellules ou structures cellulaires spécifiques [56]. Les propriétés d'amplification locale et d'absorption du champ lumineux permettent alors d'interagir localement, de façon réversible ou permanente, avec des structures cellulaires, sub-cellulaires ou moléculaires, et ce sans qu'un système complexe de focalisation et de visualisation ne soit requis.

Baumgart et al. utilisent par exemple l'interaction d'impulsions femtosecondes avec des nanoparticules d'or situées près des membranes cellulaires afin de les perforer de manière réversible et d'incorporer aux cellules de l'ADN exogène dans le cadre de thérapies géniques [57]. D'autres travaux utilisent cette interaction pour simplement provoquer la mort des cellules ciblées [58, 59]. Finalement, Csaki et al. utilisent un principe similaire pour endommager sélectivement certaines séquences d'ADN situées sur un chromosome, ouvrant la voie à une véritable chirurgie moléculaire [60].

Comme on peut le constater, les applications possibles de cette technologie sont virtuellement sans limite et ouvrent la voie à la manipulation et la destruction ciblées de structures aux dimensions extrêmement réduites, atteignant presque le niveau des molécules individuelles. Les perspectives en matière de développement de nouvelles approches thérapeutiques et de sciences biologiques fondamentales sont particulièrement intéressantes. Il est par conséquent important d'étudier les mécanismes physiques à la base de l'interaction entre une impulsion laser ultrabrève et une nanostructure plasmonique en milieu cellulaire afin de mieux comprendre et d'optimiser ces procédés.

1.1 Problématique

L'auteur s'intéresse aux mécanismes fondamentaux de l'interaction entre une impulsion laser ultrabrève (c'est-à-dire une impulsion de l'ordre de ≈100 fs) et une nanostructure plasmonique dans un milieu biologique. La description détaillée des phénomènes résultants de cette interaction est en effet nécessaire à la compréhension et l'optimisation des procédés de nanochirurgie cellulaire. Comme nous le verrons dans la suite de cette thèse, l'irradiation laser

induit de nombreux mécanismes d'absorption, de transfert et de dissipation d'énergie, tant dans la nanostructure que dans son environnement, qui s'échelonnent sur plusieurs échelles au niveau tant spatial que temporel. Plusieurs phénomènes, incluant la hausse rapide de température du milieu, l'apparition d'un plasma à proximité de la nanostructure, l'émission de fortes ondes de pression et la génération de bulles de vapeurs autour des nanoparticules sont susceptibles de causer des dommages aux structures biologiques environnantes. Une compréhension tant qualitative que quantitative de l'influence des paramètres géométriques de la nanostructure ainsi que des paramètres de l'irradiation laser sur l'intensité et l'étendue de ces phénomènes est requise afin de développer une compréhension globale de la nanochirurgie cellulaire par laser et de l'optimiser. Il n'existe cependant pour l'instant aucun modèle dans la littérature permettant de simuler de façon satisfaisante l'interaction d'un laser ultrarapide avec une nanostructure plasmonique en milieu biologique. La présente thèse vise à développer et à étudier un tel modèle.

1.2 Objectifs et plan de la thèse

Les objectifs de la thèse sont au nombre de trois :

1. Développer un modèle mathématique capable de simuler adéquatement le dépôt d'énergie, l'élévation de température, l'émission d'ondes de pression et le phénomène de cavitation résultant de l'interaction d'une impulsion laser ultrabrève avec une nanostructure plasmonique en milieu biologique.
2. Utiliser ce modèle afin de dégager les éléments dominants de l'interaction laser et la chaîne principale des événements menant à la cavitation dans le milieu.
3. Développer un cadre d'évaluation du potentiel de nanostructures plasmoniques particulières pour application en nanochirurgie cellulaire.

Afin de réaliser ces objectifs, la thèse est divisée comme suit :

Le chapitre 2 présente tout d'abord l'état de la connaissance sur les mécanismes d'interaction entre un laser pulsé et une nanostructure plasmonique. Celui-ci est une retranscription d'un article de revue récemment soumis à *Journal of Photochemistry and Photobiology C : Photochemistry Reviews*. Ce chapitre offre de plus une revue succincte des applications de cette technologie en nanochirurgie cellulaire afin de justifier l'importance et la pertinence de l'étude de ces mécanismes fondamentaux.
En se basant sur les mécanismes vus au chapitre 2, le chapitre 3 présente, détaille et

justifie le modèle mathématique qui est utilisé dans le corps de la thèse. On y propose un modèle basé sur une description de type milieu-continu composée de plusieurs équations différentielles aux dérivées partielles qui doivent être résolues de manière auto-consistante dans un espace tridimensionnel. L'eau est utilisée pour émuler le milieu biologique. Ce modèle offre une description complète des différents phénomènes mentionnés à la section Problématique et représente par conséquent une avancée considérable par rapport à ce que l'on retrouve actuellement dans la littérature.

Le chapitre 4 est une transcription d'un article paru récemment dans *Nano Letters*, (2012). Il utilise le modèle présenté au chapitre 3 et l'applique au cas spécifique de l'irradiation *hors-résonance* d'une nanoparticule d'or de 100 nm avec une impulsion femtoseconde dans le proche infrarouge, où la longueur d'onde du laser ne correspond pas à l'énergie du plasmon. On y présente des résultats expérimentaux qui valident le modèle, en plus de mettre en lumière l'importance du plasma créé en champ proche autour de la particule pour le phénomène de cavitation.

Le chapitre 5 est une transcription d'un article récemment soumis à *Journal of Physical Chemistry C*. Il concerne quant à lui le cas spécifique de l'irradiation *en-résonance* d'un nanobâton d'or de 10×41 nm^2 avec une impulsion femtoseconde dans le proche infrarouge, mais où cette fois la longueur d'onde du laser correspond à l'énergie du plasmon. On y découvre la présence de deux régimes d'irradiation en fonction de la fluence utilisée. En particulier, l'importance du plasma dans les mécanismes de cavitation y est confirmée et une modification importante des propriétés optiques des nanobâtons d'or due à la présence du plasma est observée. Ce chapitre démontre de plus que, aux fluences requises pour engendrer la cavitation dans le milieu, le nanobâton est irréversiblement endommagé par l'interaction laser.

Finalement, le chapitre 6 discute des implications de l'importance du rôle du plasma dans les mécanismes de cavitation dans le cadre de la nanochirurgie cellulaire. Basé sur les résultats présentés aux chapitres 4 et 5, un modèle simplifié est proposé. Un facteur de mérite relatif au potentiel d'une nanostructure particulière pour la nanochirurgie cellulaire est introduit. Le modèle simplifié permet de calculer ce facteur de mérite pour des nanoparticules hors-résonance et des nanobâtons en-résonance de différentes tailles. Basé sur ce facteur de mérite, des recommandations sont formulées quant aux structures à utiliser dans le cadre de la nanochirurgie cellulaire.

CHAPITRE 2

Plasmonics for pulsed-laser cell nanosurgery : fundamentals and applications

Ce chapitre retranscrit un article de revue soumis à Journal of Photochemistry and Photobiology C : Photochemistry Reviews, en 2012 [1]. Cet article décrit les aspects fondamentaux de l'interaction de lasers pulsés avec des nanostructures plasmoniques et présente son application à la nanochirurgie par laser, incluant les thérapies photothermiques, la transfection cellulaire, la chirurgie moléculaire et la livraison de médicament. Il présente plus particulièrement l'état des connaissances concernant les mécanismes d'interaction laser-nanostructures plasmoniques en milieu aqueux et les mécanismes de génération de bulles pour des impulsions femtosecondes et nanosecondes. Ce chapitre fait office de revue de littérature et présente les bases théoriques qui permettront le développement du modèle mathématique présenté au chapitre suivant. Il est à noter que cet article de revue a été écrit ultérieurement à l'article présenté au chapitre 4 du corps de la thèse. Ainsi, ses méthodes et conclusions générales sont rapidement résumées dans ce chapitre. Celles-ci seront explicitées de façon plus détaillée aux chapitres subséquents.

2.1 Authors

Etienne Boulais, Rémi Lachaine, Ali Hatef & Michel Meunier

Laser Processing Laboratory,
Department of Engineering Physics, École Polytechnique de Montréal,
CP6079, Succ. Centre-ville, Montréal, QC, Canada, H3C 3A7.

2.2 Abstract

This review describes the fundamental aspects of pulsed laser interaction with plasmonic nanostructures, and its applications to cell nanosurgery, including the destruction, modification or manipulation of molecular, sub-cellular and cellular structures. The review assumes no prior knowledge of the field of plasmonics and begins with a short review of the basic theory of plasmon excitation and optical properties of nanoscale metallic structures. Fundamentals

1. E. Boulais, A. Hatef, R. Lachaine et M. Meunier. Plasmonics for pulsed-laser cell nanosurgery : fundamentals and application. *Journal of Photochemistry and Photobiology C : Photochemistry Reviews*, Manuscript ID : JPR-D-12-00038, 2012

of short and ultrashort laser pulse interaction with plasmonic nanostructures in a water environment are then discussed. Special emphasis is put on the consequences of the irradiation on the surrounding environment of the nanostructure, including heating, low-density plasma generation, pressure wave release and formation of vapor bubbles. The paper is concluded with a review of different applications of pulsed-laser interaction with plasmonic nanostructures for cell nanosurgery, including photothermal therapy, plasmonic enhanced cell transfection, molecular surgery and drug delivery.

2.3 Introduction

The past few years have seen the unfolding and rapid evolution of the field of plasmonics and in particular of the field of nanoplasmonics. The ability to produce and control electric fields on nanoscale dimensions below the light diffraction limit [1, 2] allow the development of novel science and technology that find applications in a wide variety of domains. Plasmonic nanostructures are for instance being involved in the design of light-harvesting components to enhance the efficiency of solar cells [4] and photodetectors [5]. They also enter in the development of new techniques aiming to improve current data storage capability [6, 7] and are used as nanometric optical tweezers to trap and manipulate nanoscale objects [8]. Near-field optical spectroscopy enables optical measurement at dimensions below the diffraction limits [9]. DNA-based strategies are currently being developed to self-assemble them into plasmon molecules and tridimensional complex structures [10, 11]. They can be assembled to construct optical components [12], new sources of coherent highly localized optical fields known as spaser [13, 14], or even nanoscale laser sources [15–17]. Very precise biochemical sensors [18] can also be realized, with resolution down to the single molecule [19], by exploiting either the plasmon resonance of nanoparticles arrays [19, 61, 62], the so-called Fano resonance of more complex systems [63, 64] or the localized enhancement of the Raman signal (Surface Enhanced Raman Spectroscopy, also known as SERS) [65, 66]. Nanoplasmonics also offers new therapeutic possibilities, in particular concerning cancer treatment. Continuous wave laser interaction with functionalized nanospheres [20–23], nanorods [24–27] and nanoshells [23, 28–31] is used to generate heat [32–34] and destroy cancer cells. Hybrid structures coupling plasmonic enhanced cell laser heating to conventional chemotherapy further increase the efficiency of the hyperthermia treatment [35–39].

This review covers the interaction of short and ultrashort laser pulses with plasmonic nanostructures. The high intensity optical fields produced can be exploited to interact very precisely with the environment. When nanostructures are deposited on solid surfaces, irradiation may produce sub-wavelength ablated features that could provide alternative to cur-

rent nanolithographic processes. When nanostructures are in the vicinity of cells, pulsed laser irradiation yields to nanoscale vapor bubbles that can be used for diagnostic and therapeutic purposes. Sub-cellular and molecular structures can be affected with unrivalled precision. Cell membranes may be disrupted, enabling the transfer of drugs, DNA, or RNA molecules into the cytoplasm without inducing any permanent damage. More drastically, selective lysis of the cell may also be induced. Nanoplasmonics hence offers new therapeutic avenues for cancer and other diseases.

This review is divided in three major parts. It begins with an overview of the basic theory of plasmon excitation and optical properties of nanoscale metallic structures. The fundamentals of short and ultrashort laser pulse interaction with a plasmonic nanostructure in a water environment is then discussed, with a special emphasis on the consequences of the irradiation for the surrounding environment of the nanostructure, including rapid heating, low-density plasma generation, pressure wave release and formation of vapor bubbles. The paper is then concluded with a review of different applications of pulsed-laser interaction with plasmonic nanostructure for cell nanosurgery, including photothermal therapy, plasmonic enhanced cell transfection, molecular surgery and drug delivery.

2.4 Optical Properties of Plasmonic Nanostructures

Nanoplasmonics is a field at the edge of the optical and condensed matter sciences that concerns the interaction of electromagnetic fields with particles having dimensions of the order of the wavelength [3].This section covers the basic theory and fundamentals of nanoplasmonics. The origin of plasmons and of the plasmon resonance is first presented. It is followed by a discussion on the influence of the dimensions and the shape of the nanostructures on the plasmon properties.

2.4.1 Plasmons and plasmon resonance

The first comprehensive complete mathematical study of plasmon resonance sets back to 1908, with the seminal work from Gustav Mie that presents an analytical treatment of the absorption and scattering of light by a sphere [67]. Prior to that milestone, the human civilization had already taken advantage of the peculiar optical properties that are characteristic of nanoscale particles of noble metals. The most cited example is beyond any doubt the Lycurgus glass cup (from 4th century A.D.) [68] that shows a red color when seen in transmission but a green color when seen in reflection (see figure 2.1a). This behavior is due to the presence of small gold and silver nanoparticles (NPs) embedded in the glass, as shown in figure 2.1b. As seen from figure 2.1c, the absorption and scattering spectra of Au is stri-

kingly modified when transformed from bulk to nanospheres. The figure shows the example of 25 nm radius AuNPs with a scattering and absorption maximum near 530 nm, in the green region of the spectrum, explaining the origins of the Lycurgus glass cup's colors. Silver particles presents the same behaviour, with a plasmon peak around 400 nm.
This strong modification of the absorption and scattering spectra for NPs arises from the concentration of the optical energy at the nanoscale, which has no counterparts in the macroscopic world. This represents the major interest in the use of NPs for a vast range of applications, including cell nanosurgery.

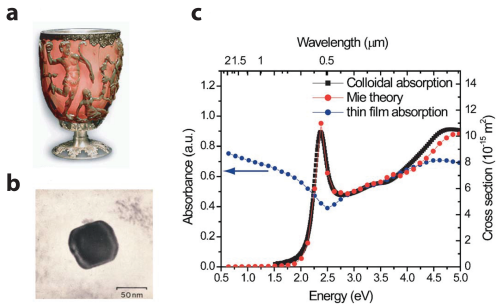

Figure 2.1 a. The Lycurgus glass cup, demonstrating the bright red color of gold nanocrystals in transmitted light. b. Scanning electron microscopy (SEM) image of a typical nanocrystal embedded in the glass (courtesy of the British museum). c. Calculated absorption spectrum of a thin gold film (blue dots) and of 30-nm AuNPs in water (red dots) using classical electromagnetic theory. A measured absorption spectrum of an aqueous solution of 30-nm Au colloids (black dots) shows good agreement with the theory. Taken from [68]

Plasmon resonance arises in metallic nanostructures which dimensions are reduced to sizes around the skin depth (l_s) [3]. For noble metals, l_s is $\sim$25 nm for optical frequencies. Electric field is thus able to penetrate the material and interacts with the electrons of metallic particles with a radius $R \sim l_s$. The field drives the electrons into an oscillatory movement restrained by a restoration force between the displaced electrons and the uncompensated lattice ions left behind (see figure 2.2a). The situation is the electromechanical analog to the classical problem of the damped forced oscillator, resulting in the onset of the resonance phenomenon characteristic to this class of problem [69]. The oscillator created is called a localized surface plasmon (LSP), with a characteristic frequency ω_{sp} called plasmon frequency. Excitation of the NP with an incident wave having a frequency near ω_{sp} leads to the so-called "plasmon resonance" responsible for the extraordinary optical properties of the NPs. The plasmon frequency ω_{sp} depends on the composition, the size, the shape and the environment

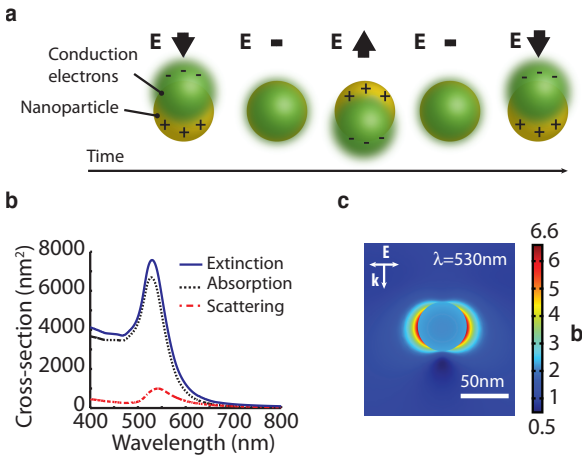

Figure 2.2 a. Principle of the plasmon resonance. The electric field (black arrow) drives the displacement of the conduction electrons (green sphere) of the NP (yellow sphere). Displaced electrons leave uncompensated lattice ions behind, resulting in the building of a restoration force. This electromechanical oscillator is the localized surface plasmon. b. Scattering (red line), absorption (black line) and extinction (blue line) cross-sections for a R=25 nm gold nanosphere in water showing a plasmon resonance around 550 nm. c. Cross-section of the electric field enhancement around a R=25 nm gold nanosphere near resonance (λ=530 nm). Light polarization is horizontal and propagation is from top to bottom. A maximum field enhancement of 6.6 along with energy absorption is apparent from the figure.

of the nanostructure. Many materials can support the excitation of SPs, the only restriction being that the real part of their permittivity is negative [3]. This condition is a characteristic of metals, especially the noble (Au, Ag, Cu) and the alkaline metals.

Plasmon resonance confers extraordinary optical properties to metallic nanostructures. Figure 2.2b shows the scattering and absorption cross-section of a R=25 nm AuNP in water and Figure 2.2c shows the electric field distribution around the particle at the resonance wavelength ($\lambda \approx 530$ nm). Strong energy absorption at resonance is visible from both figures, as well as significant near-field enhancement in the polar regions. The existence of this near-field motivates the use of plasmonic nanostructures for many applications requiring high intensity fields for non-linear interaction with material, including SERS [65, 66] and ultrafast laser cell nanosurgery [57, 70].

Yurtsever et al. [71] recently developed a technique combining an ultrafast laser pump with ultrafast electron microscopy for the space-time visualization of the near-field. In this technique, called photon-induced near-field electron spectroscopy (PINEM), the laser pump pulse excites the near-field around the particle as a simultaneous ultrashort electron pulse image the field by utilizing the inelastic scattering with the field's component parallel to the electron

propagation vector. Figure 2.3 shows the enhanced near-field around laser-excited AgNPs, which general aspect is consistent with the calculations shown in Figure 2.2c for AuNPs.

2.4.2 Size and geometry dependence of plasmon resonance

Nanoparticles

Plasmon resonance and resulting optical properties of NPs are highly dependant on their size and their environment. As this work concerns cell nanosurgery, we will be particularly interested in the optical properties of AuNPs in aqueous environment. AuNPs are indeed mainly used in a biomedical context because of their relative non-toxicity [21]. Aqueous environment also presents optical characteristics similar to biological medium and is commonly used in the context of laser interaction with cellular environment [72].

Figure 2.4 presents the optical properties of AuNPs in a water environment as obtained from the Mie theory using the bulk permittivity [73]. Indeed, the permittivity of metallic nanostructures is similar to the bulk permittivity for D>10 nm, limit below which it begins to be affected by surface scattering and quantum confinement effects [74]. As seen from Figure 2.4a and 2.4b, for small NPs (diameters 10-30 nm), the plasmonic resonance occurs at a wavelength around 520 nm, independent on the NPs size. Also, the energy is mainly absorbed by the NP, light scattering being negligible in this regime (see Figure 2.4a) . Figure 2.4c however shows a significant enhanced near-field near the poles of the particle. This near-field however does not couple to the far field for small particles and stays confined to its close vicinity. In addition, the symmetry of the field distribution indicates that the response of the material to the incident field is mostly dipolar.

As the NPs dimension increases, Figure 2.4b and Figure 2.4d shows the plasmon resonance shifting slightly to the red portion of the spectrum, mostly due to contribution of multipole and retardation effects to the resonance process [75]. Also, scattering contribution is shown to become much more important for larger NPs. Figure 2.4e confirms that, whereas it was almost inexistent for NPs smaller than 30 nm, the importance of scattering significantly increases with the size of the NP, and even dominates absorption for particles with diameters D>40 nm. Inset of Figure 2.4e further reveals that this contribution grows as $\sim R^3$, consistent with the calculation of the radiation rate from an oscillating dipole [3]. Figure 2.4f shows the field distribution around a $150nm$ AuNP in water, irradiated at resonance (λ=640 nm). Field enhancement is clearly visible from the figure, with an asymmetric shape characteristic of multipolar contributions. As we will see in the next sections, the near-field has a tremendous importance for many applications.

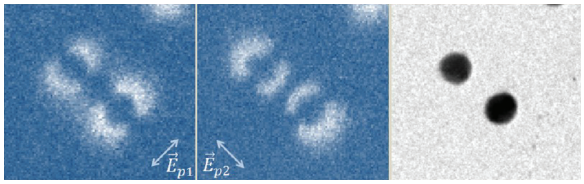

Figure 2.3 PINEM images of two close-by silver particles for two polarizations. The particles are separated by 70 nm (edge-to-edge). Taken from [71]

Nanoshells

Nanoshells (NSs) composed of a hollow, dielectric, semiconducting, or magnetic core covered with a thin metallic shell as been introduced some years ago [76–81]. One of the greatest asset of those structures consist in the fact that the ratio of the shell thickness on the core radius can be modulated to shift the absorption resonance to the near-infrared (NIR) portion of the spectrum. Biological tissue transmissivity being the highest in the NIR [82], this represents a valuable asset for many applications such as cell nanosurgery and cell imaging [28–30, 83–87].

TEM imaging of Au NS is presented in Figure 2.5a. While the standard Mie theory can only be used with homogeneous spheres, a generalized version of the Mie theory has been developed to calculate the optical properties of such coated spheres structures [88]. Figure 2.5b shows the scattering, absorption and extinction efficiencies for a SiO_2-Au core shell with a constant outer radius of 75 nm and an inner radius of 45 nm, 55 nm and 65 nm, in water. Results show a strongly red-shifting plasmon resonance as the inner radius on outer radius ratio increases, as well as an increasing efficiency comparable with the one observed for AuNPs (see Figure 2.4d). Figure 2.5b shows the field enhancement distribution around a 75 nm outer radius/65 nm inner radius SiO_2-Au core shell irradiated at resonance (λ=863 nm). Results show a field enhancement factor of 9.1, almost twice as large as the one obtained for a AuNP with the same dimension (see figure 2.4f). Low absorption in the gold layer at resonance is also apparent from figure 2.5b.

Nanorods

Nanorods (NRs) also provides spectrum tunability to the near-infrared and are composed of metal only [19, 25, 89–92]. Their shapes look like a solid cylinder capped with two hemispheres (See figure 2.5d). Optical properties of those structures cannot be calculated from Mie theory because of the broken spherical symmetry. Numerical methods such as the discrete dipole approximation (DDA) [93], the finite difference in the time domain (FDTD) [94] or FEM

[95] must be used. Special care must be taken to ensure that the contribution from NRs of all possible orientations is considered to simulate the optical response of a randomly-oriented sample. Another approach consists in using ellipsoids as an approximation for the NRs. Optical properties of ellipsoids can be evaluated analytically from the Lorenz-Mie theory [96]. Expressions valid in the quasi-static regimes are also available [97]. Figure 2.5e presents numerical results for the scattering, extinction and absorption efficiency of a $10\times41\text{nm}^2$ AuNR in water irradiated along its long axis using a finite-elements method. Note the plasmon peaks in the near-infrared corresponding to the excitation of the longitudinal plasmon ((LP) band. Experimental optical absorption measurements also show a smaller plasmon peak near 510 nm associated to the transverse plasmon (TP) band of misoriented NRs [89, 92]. Figure 2.5e shows optical efficiencies much larger for AuNRs ($\approx$17) than the one calculated for AuNPs and SiO_2/Au NSs($<$10) and is dominated by absorption. Note that the calculated efficiency becomes much less if a randomly oriented NRs distribution is considered. The position of the LP band is easily tuned by adjusting the length over diameter ratio of Au NRs, as shown by Yu et al. [89]. Another interesting feature of Au NRs is the high enhancement of the near-field that it provides. Figure 2.5f shows a field enhancement of $\approx$ 77 near the tips of the particle, an order of magnitude higher than the field enhancement obtained with AuNPs and SiO_2/Au NSs . This high enhancement is attributed to the lightning rod effect that greatly intensify the local electric field due to the confinement at the NR tip [98–101]. This large field enhancement is highly valuable for non-linear applications depending on high field intensity.

Other types of nanostructures

The variety of nanostructures that are being synthesized is growing at a fast pace. Those include (but are not limited to) nanocages [102–106], nanocubes [107–109], nanoprisms [110–112], nanostars [113–116], nanorice [117–120], nanobars [118], nano rings, [121–123] and nano crescent [124, 125]. All of those structures present interesting optical properties, but have not yet been used extensively with pulsed laser for cell nanosurgery purposes. The extensive discussion on their specific properties is thus beyond the scope of this review, and the interested reader is referred to the literature cited above for further details.

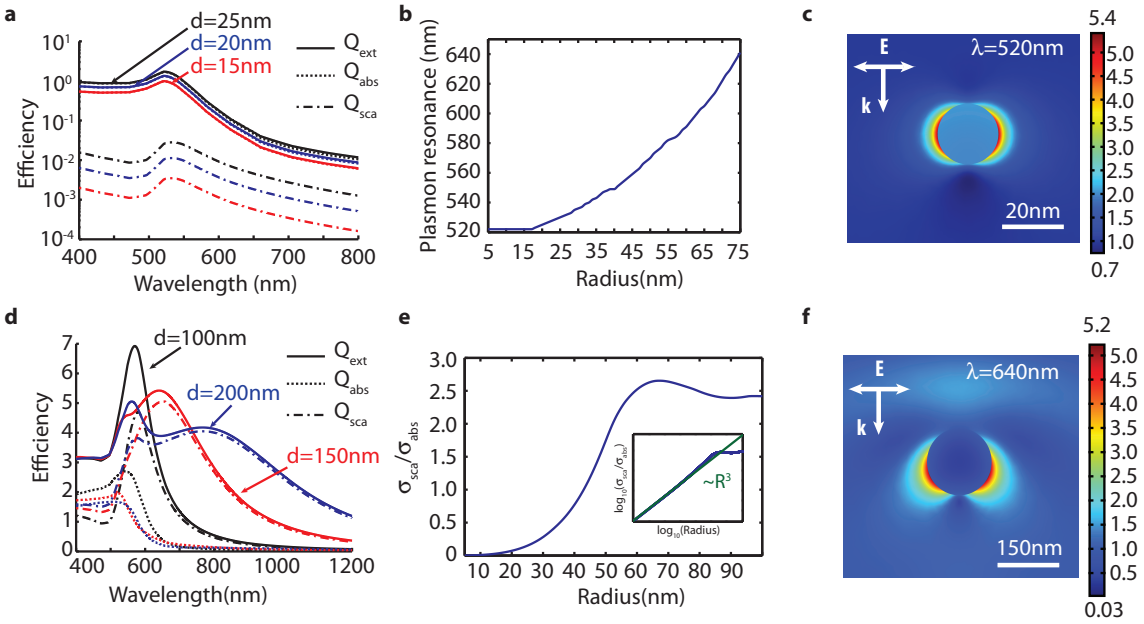

Figure 2.4 Plasmon resonance of AuNPs a. Extinction, scattering and absorption efficiencies as a function of the incident wavelength for AuNPs with diameters D=15 nm, 20 nm and 25 nm . Calculations are made with the full Mie theory. Efficiencies are defined as $Q_x = \sigma_x/(\pi R^2)$, with R being the NP radius and σ_x being the cross-section. b. Position of the plasmon resonance peak as a function of the NP radius. c. Electric field enhancement distribution around a D=20 nm AuNP irradiated at plasmon resonance (λ=520nm). Electric field polarization **E** and propagation vector **k** are indicated on the figure. d. Extinction, scattering and absorption efficiencies as a function of the incident wavelength for AuNPs with diameters D=100 nm, 150 nm and 200 nm in the multipolar regime. e. Ratio of the scattering cross-section over the absorption cross-section as a function of the particle radius at the plasmon resonance. Logarithmic graph demonstrating a R^3 dependence is shown in inset. f. Electric field enhancement distribution around a D=150 nm AuNP irradiated at plasmon resonance (λ=641nm). Electric field polarization **E** and propagation vector **k** are indicated on the figure.

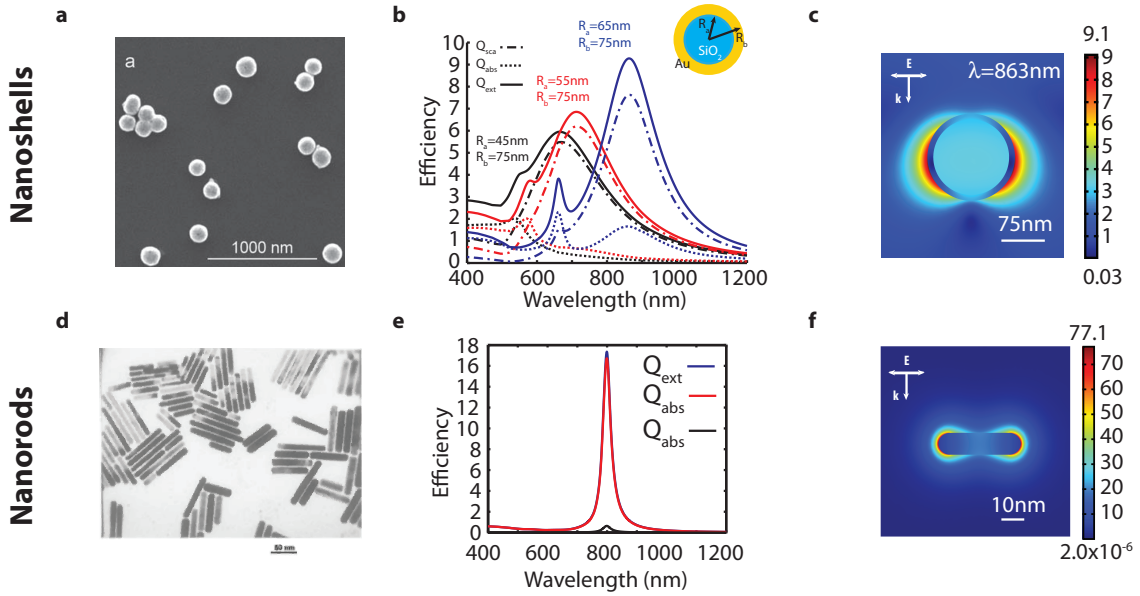

Figure 2.5 a. SEM image of SiO_2/Au NSs taken from [85] b. Scattering, absorption and extinction efficiencies for a SiO_2/Au NSs with a constant outer radius of 75 nm and an inner radius of 45 nm, 55 nm and 65 nm, in water. Efficiencies are defined as the ration between the optical cross-section and the geometric cross-section. c. Field enhancement distribution around a 75 nm outer radius/65 nm inner radius SiO_2/Au NSs in water, irradiated at resonance (λ=863 nm) d. TEM imaging of Au nanorods with a 7.6 aspect ratio. Taken from [89] e. Scattering, exctinction and absorption efficiencies of a 10×41 nm^2 AuNRs in water, irradiated along its long axis. Efficiencies are defined as the ratio between the optical cross-section and the geometric cross-section. f. Field enhancement around a 10×41 nm^2 AuNR in water, irradiated along its long axis.

2.5 Fundamentals of pulsed laser interaction with plasmonic nanostructures in water

Absorption of a laser pulse by a nanostructure triggers a series of energy transfer events occuring in various time scale. Figure 2.6 summarizes the energy pathway following the laser irradiation. This section details this pathway.

2.5.1 Plasmon excitation and decay

When a laser beam interacts with a plasmonic nanostructure, photons are absorbed by the electrons oscillation and excite the plasmon oscillation. This plasmon oscillation induces an enhanced electric field in the near-field that can interact non-linearly with the medium if the laser intensity is sufficient. The near-field has also been shown to induce local ablation of a NP in the pole region following a femtosecond irradiation [126]. The plasmon oscillation dephases in 1-10 fs [75, 127–129].

Figure 2.7 details the different relaxation channels for the plasmon. The plasmon can decay by exciting electrons from the s-p band (intra-band process) or from the d-band (inter-band process) to levels above the Fermi level ϵ_F. This damping is non-radiative and the energy of the plasmon is ultimately transferred to a population of nonthermal electron-hole pairs (Landau damping) in the nanostructure. Non-radiative processes are determined by the nanostructure's band structure and are therefore size-independent. However, an inter-band process requires a sufficient plasmon energy to excite d-band electrons beyond the Fermi level. Plasmons thus non-radiatively decay much slowly in structures resonant in the NIR (such as NRs and NS) than in NPs [130].

Alternatively, the plasmon can decay by emitting photons in a radiative process. This process is negligible for small particles but becomes important as their dimension increases, being linked to the scattering cross-section of the NPs. Plasmon may also decay from non-linear interaction with the environment in the enhanced near-field. Real systems may also suffer from additional size-dependent dephasing processes [131, 132] including chemical interface damping caused by charge transfer with adsorbate or surface states [133, 134], surface scattering[75, 134–136], direct emission of electrons, occurring under strong excitation conditions [137], and increased Landau damping caused by a surface and confinement induced broadening of the discrete eigenstates of the holes and electrons [75, 138, 139].

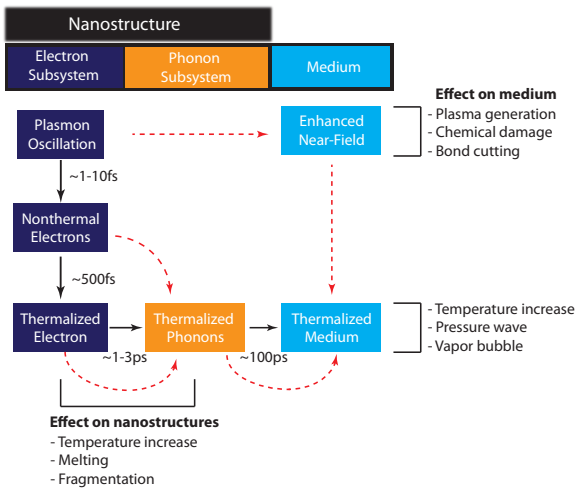

Figure 2.6 Basic mechanisms of energy absorption and dissipation in laser-excited plasmonic nanostructures. The photons create a plasmon oscillation within the material. This plasmon creates an enhanced near-field in the medium around the nanostructure. The plasmon decays in ∼1-10 fs into a nonthermal electron distribution that internally thermalizes in ∼500 fs. Electrons transfer their energy and thermalize with phonons in $1 - 3ps$. Figure shows that energy transfer from both nonthermal and thermal electrons contributes to the phonon thermalization. Phonons give their energy to the surrounding medium within a time scale of ∼100 ps. Non-linear interaction in the near-field also contributes to the energy transfer to the medium. Potential consequences of the energy transfer on the nanostructure and on the surrounding medium are also indicated.

2.5.2 Thermalization of the electron subsystem

Through electron-electron scattering processes, the nonthermal electrons created by the plasmon decay thermalize to a Fermi-Dirac distribution in ∼500 fs [75, 127, 129, 140] although Sun et al. [129] reported much longer energy-local thermalization times of ∼2.5 ps for electrons lying near the Fermi surface in reason of the k-space filling. Much faster thermalization times (<100 fs) has however been shown by Link et al. [140] to result from the excitation of d-band electrons. They also show that thermalization time is considerably reduced in the case of high excitation since a greater k-space is available for energetic electrons, which increase the scattering rate in accordance with the Fermi liquid theory.

2.5.3 Thermalization of the electron subsystem with the phonon subsystem in the nanostructure

The electron subsystem thermalizes with the phonon subsystem in ∼1-3 ps [127, 129, 141, 142]. This electron-phonon coupling is however dependent on the laser power as it is a function

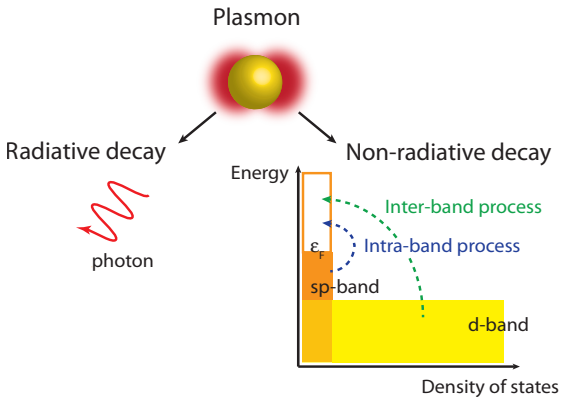

Figure 2.7 Non-radiative and radiative decay paths for the surface plasmons. A Plasmon can either decay radiatively by the emission of photons, or non-radiatively. Non-radiative processes involve the excitation of an electron from the conduction band to an unoccupied energy level over the Fermi level (ϵ_F) creating electron-hole pairs in the conduction band (also called a Landau damping). Intra-band processes relate to electrons that originate from the sp-band, and inter-band processes involve electrons originating from the lower energy d-band.

of the electronic heat capacity that depends on the electronic temperature [127]. The electron-phonon coupling time has however been demonstrated to be independent of both particle shape and size, though Arbouet et al. [143] reported a strongly increased electron-phonon coupling for small (D<10 nm) particles. Because of the relatively long electron thermalization time (∼500 fs) the independent picture of thermalized electron interacting with phonons to thermalize them is somewhat misleading. Energy transfer from nonthermal electrons to phonons also contributes to the phonon thermalization, which complicates considerably the analysis of the energy transfer within the NP.

Potential consequences of the energy transfer to the nanostructure's electron and phonon subsystem include temperature increase, melting and fragmentation. Those are detailed in much details in the following sections.

2.5.4 Energy transfer to the environment

Following the thermalization of the phonons, the energy is released to the surrounding medium through phonon-phonon scattering in ≈100 ps [127]. This timescale is however also highly dependent on the particular system and laser power.

The energy transfer to the environment can be used to locally damage, destroy or modify cellular and sub-cellular structures. This technology evolves from the field of surface nanoablation where laser interaction with plasmonic NPs [144–151],nanoprisms [152, 153] or NRs

[154, 155] deposited on a surface are used to create ablated features with resolution below the diffraction limit. Extensive review of this technology is available elsewhere [156].
In a cellular environment, the same technique can be used to either induce a highly localized heating of cells or sub cellular components, to emit high intensity pressure wave, or to generate nanoscale bubbles in the medium. Those plasmonic nanobubbles are used to induce cell death or to break the cell membrane barrier to allow introducing drugs or RNA/DNA molecules for gene therapy. For high intensity laser, the enhanced near-field around the nanostructure may in addition create a nanoscale plasma that can induce highly localized chemical damage to biomolecules and break chemical bonds. We will show that those tools are becoming increasingly important in the intensive research for cancer therapy. Beyond cancer treatment, the highly localized interaction has also been applied to the inactivation of proteins, the knockout of certain genes in DNA molecules, the perturbation of chromatin assembly and the destruction of bacteria.
In the following sections, we first study the fundamentals of pulsed laser interaction with plasmonic nanostructures in water. This medium has indeed proven to be adequate for the modeling of laser processes occurring in cell medium [45, 72, 157]. The first section is concerned with nanosecond (ns) and picosecond (ps) pulsed laser that are regrouped under the term "short pulses". This regime is characterized by pulse durations τ_p much longer than the electron-phonon coupling time τ_{e-ph} $\sim$1-3 ps. Those longer pulses involve thermodynamic equilibrium between the electron and phonon subsystem along with the reduced importance of non-linear processes taking place in the near-field due to the lower laser intensity. The following section is concerned with ultrashort pulses with pulse duration τ_p much shorter than the electron-phonon coupling time. This regime is characterized by the non-equilibrium heating of the phonon and electron subsystems and by the increasing importance of the near-field. This regime typically involve femtosecond (fs) pulses.

2.6 Fundamentals of short-pulsed laser interaction with plasmonic nanostructures in water

Figure 2.8 schematizes the different phenomena induced by a short pulsed-laser interaction with a resonant plasmonic NP surrounded by water. The onset of each phenomenon depends on the deposited energy, i.e. the laser fluence, as indicated on the figure.

2.6.1 Heating of nanoparticle and water

The most trivial phenomenon occurring following the laser irradiation is the heating of the NP and the subsequent heat transfer to the water by a simple conduction process at the

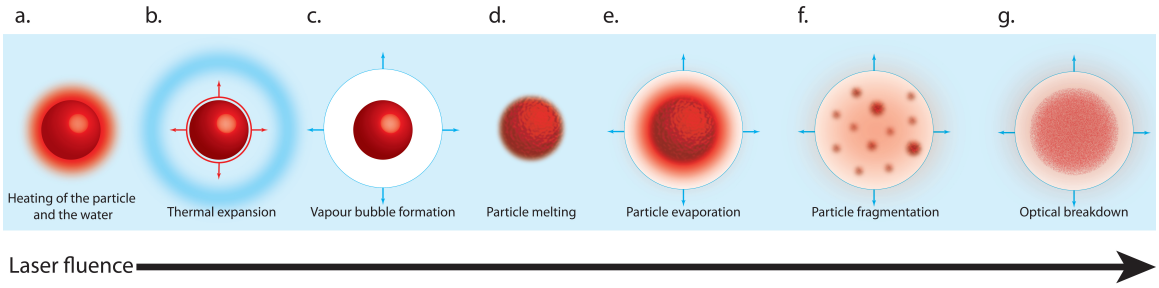

Figure 2.8 Phenomena resulting from the interaction of a short-pulsed laser with a resonant plasmonic NP surrounded by water as a function of laser fluence. a. Laser heats the particle and the surrounding water. b. Temperature rise in the NP induces thermal expansion of the lattice, leading to the emission of a pressure wave in the medium. c. Temperature rise in the water induces the formation of a vapor bubble in the water by explosive boiling. d. The particle is melted. e. Evaporation from the melted particle surface and formation of a vapor blanket around the particle. f. Fragmentation of the NP in pieces of various sizes. g. Optical breakdown of the particle

surface (figure 2.8a). As the pulse length is much larger than the electron-phonon equilibrium time τ_{e-ph} ≈1-3 ps, the energy transfer from a ps or ns laser to a plasmonic NP embedded in water heats both the electron and phonon subsystems in thermodynamic equilibrium with one another. Both the NP and the surrounding water are heated simultaneously. τ_T is a time characterizing the energy transfer by conduction from the NP to the water and is defined by [158]

$$\tau_T = \frac{\rho C r_0^2}{3k_w} \tag{2.1}$$

where ρ is the particle density, C, its heat capacity, r_0, its radius, and k_w is the thermal conductivity of the surrounding water. For a AuNP in water, τ_T ≈30 ps-30 ns for diameters varying form 10 nm-200 nm. For short pulses, $\tau_p \approx \tau_T$ and heat conduction to the surrounding water hence occurs in a timescale comparable to the heat deposition time.

2.6.2 Lattice expansion

Heating of the NP induces its expansion. This has been experimentally confirmed by x-ray scattering measurement of the lattice parameter as a function of laser fluence by Plech et al. [159]. The rapid NP expansion pushes the water at the interface and leads to the formation of a stress which relaxes through the emission of a pressure wave. Pustovalov et al. [158]

introduced the characteristic relaxation time of thermomechanical stress τ_c as

$$\tau_c \approx r_0/c_s \tag{2.2}$$

where c_s =1500 m/s is the speed of sound in water and r_0 is the particle radius. τ_c is about ∼3 ps-67 ps. Pustovalov et al. argued that important stress confinement and pressure wave emission are generated if $\tau_p \leq \tau_c$. Pressure wave emission in the short pulse regime is in consequence presumed to be of limited effect.

2.6.3 Vapor bubble nucleation in water

Heat transfer from the particle's surface to the water may cause phase change and bubble formation in the surrounding liquid. Normal boiling is associated to the presence of heterogeneities within the liquid. Nucleation occurring at those sites then must be fast enough to dissipate the energy at the rate at which it is deposited in the system so that the surface condition is fixed to the saturation pressure and temperature [45, 162, 163]. This process is however too slow to occur significantly in the case of short pulse laser heating.
Bubbles in liquid in contact with a short laser pulse heated surface is hence usually associated to the phenomenon of phase explosion which is a combination of spinodal decomposition and homogeneous nucleation [45]. Characteristic time of liquid-vapor equilibrium τ_{LV} has been evaluated by Skripov to vary between 1-10 ns for a liquid far from the critical point. [160, 164]. Rapidly heated water cannot build up pressure at a sufficient rate, and its pressure hence drop below the saturated pressure as it enters the metastable region (see sketched trajectory I. in the phase diagram in figure 2.9a). Liquid water in this region seeks to relax to the equilibrium value and homogeneous nucleation of gas bubbles takes place on a time scale that depends strongly on the temperature and on the extent of the incursion in the metastable region. Classical nucleation theory can be used to evaluate the kinetic of this free energy barrier limited process [165–169] :

$$J = n_l \sqrt{\frac{3\sigma}{\pi m}} exp\left(-\frac{16\pi\sigma^3}{3k_bT(\eta p_s - p_0)^2}\right) e^{-\tau_{lag}/t} \tag{2.3}$$

with

$$\eta = e^{\frac{p_0 - p_s}{n_l k_b T}} \tag{2.4}$$

and

$$\tau_{lag} = \frac{2\pi M}{RT} \frac{4\pi\sigma p_s}{(p_s - p_0)^2} \tag{2.5}$$

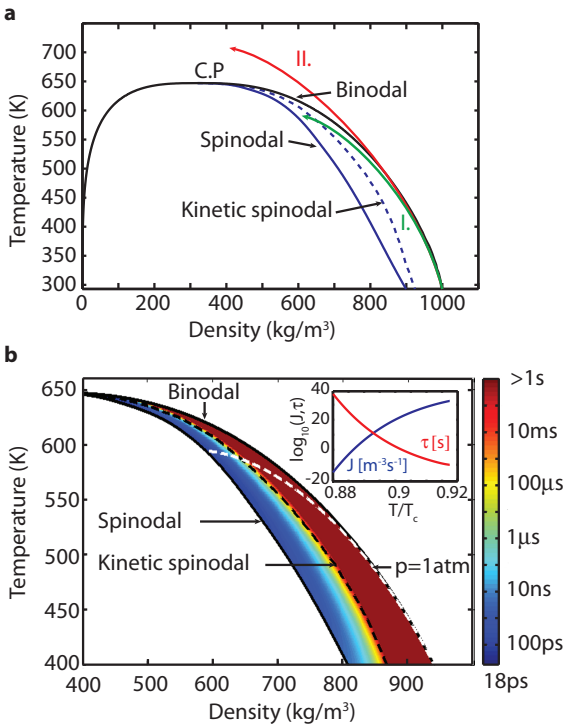

Figure 2.9 a. $\rho - T$ phase diagram for water. The spinodal (solid blue line), kinetic spinodal (dashed blue line) and binodal (black line) are indicated. Note that only the liquid-vapor portion of the spinodal is shown. C.P is the critical point. The solid green line labelled I. sketches a trajectory leading to phase explosion. The solid red line labelled II. sketches a trajectory leading to trivial fragmentation as proposed by Lorazo et al. [160] et Perez et al. [161]. See text for details. b. Zoom on the metastable portion of the $\rho - T$ phase diagram of water. Color scale presents the metastable lifetime τ_{ms}, considering a heated volume consisting in a 5 nm thick layer around a 30 nm radius particle. Spinodal, kinetic spinodal and binodal are shown on the graph. The dashed white line shows the 1 atm isobar. Permanent regime nucleation rate (in $\mathrm{m}^{-3}\mathrm{s}^{-1}$) and values of τ_{ms} (in s) are shown as a function of the reduced temperature along the 1 atm isobar.

were J represents the density rate of nucleation of sustainable bubbles provided and τ_{lag} is the lag introduced by the finite time needed to grow the nucleated bubbles to a sustainable critical radius [168]. In equations 2.3, 2.4 and 2.5, σ is the surface tension, m is the molecular mass, p_0 is the liquid pressure, p_s is the saturation pressure, n_l is the water number density, M is the molar mass, and R is the gas constant. Note that plasmonic nanostructures can be viewed as heterogeneities that could potentially reduce locally the free energy barrier for the liquid-vapor phase transition. The homogeneous mechanism presented in this section must thus be interpreted as a limiting case, and the real nucleation rate J might be larger than the one presented in equation 2.3.

Figure 2.9b shows the lifetime of the metastable state τ_{ms} as a function of the $\rho - T$ position in the metastable state by assuming a $5nm$ thick heated layer around a 60 nm NP and using the values from the IAPWS equation of states [170]. It shows that this lifetime gets as low as 18 ps as the water approaches the spinodal, in agreement with molecular dynamics studies [171]. This lifetime is much shorter than the value calculated by Martynyuk et al. and reported by Kelly et al. [163] giving τ_{lag} ∼1-100 ns. Kelly et al. however discounted the calculations from Martynuk based on experiments demonstrating that phase explosion occurs on time scale ranging from 15-300 ps, in agreement with the time scale presented in figure 2.9b. The inset in figure 2.9b shows the rate of nucleation J (in the permanent regime) and the lifetime of the metastable state τ_{ms} as a function of the reduced temperature T/T_c as the spinodal is approached along the p=1 atm isobar. This figure shows that the lifetime drastically decreases as the temperature gets around $0.9T_c$ which is usually taken as the temperature limit for important homogeneous bubble nucleation and phase explosion [45, 158, 160, 162–164, 169, 171–173].

The spinodal curve is defined as the locus of states of infinite compressibility and is considered as the boundary of metastability. If the thermodynamic state reaches the spinodal, the water goes from a metastable region to an unstable region. In this locus, there is no energy barrier between the two phases and the phase transition is thus not an activated process [45]. Small fluctuations extending over large spatial scale lead to the rapid relaxation of the water to the saturation curve into an equilibrium state of mixed phase composed of liquid and saturated vapor. This relaxation from the low pressure unstable state to the equilibrium state also involves a significant pressure increase, hence the name phase explosion. Note that the classical nucleation theory does not account for the spinodal decomposition mechanism. Indeed, even on the spinodal line, the classical nucleation theory predicts a non-zero activation barrier, which is in opposition with the definition of the spinodal [174]. The lifetime of the unstable state once the spinodal is reached might as a consequence be much shorter than what is shown on figure 2.9b. This problem calls for a nonclassical nucleation theory [174–176]. In

particular, a simple theory from Oxtoby et al. [175] predicts a relaxation rate at the spinodal equivalent to the pre-exponential factor of the classical theory (equation 2.3), which is $\approx 10^{39}$ $m^3 s^{-1}$ for water. The paper shows also more advanced theories that bring corrections to this value while keeping approximately the same order of magnitude. This relaxation rate implies a $< 1fs$ lifetime for the volume considered in figure 2.9b at the spinodal, calling for an almost instantaneous spinodal decomposition.

The spinodal is thus the ultimate limit of the stability for a thermodynamic system [45]. Physically, however, density fluctuation induce a rapid relaxation to the saturation curve way before a thermodynamic state reaches the spinodal, so that a specific system may never reach the spinodal [171]. Defining τ_M the lifetime of the metastable state (i.e. the time for the state to relax to equilibrium through homogeneous nucleation), and τ_R, the lifetime of the metastable state due to statistical fluctuation, one can see that a metastable state where $\tau_R << \tau_M$ challenges the very concept of metastability [72, 177, 178]. Hence, the physical boundary of the metastable states is rather defined as the locus where $\tau_R = \tau_M$ and is called the kinetic spinodal. This concept has proven very useful in the study of short pulse laser ablation and where the crossing of the kinetic spinodal is often used as the onset of phase explosion [70, 72].

In addition to the above-mentioned phase explosion mechanism, Lorazo et al. [160] and Perez et al. [161] reported the formation of vapor bubbles in a laser-heated liquid from a "trivial fragmentation mechanism" for pulses in the ps and ns regimes. This mechanism arises from liquid being heated along the binodal curves and getting into the supercritical states without entering the metastable region. Once in the supercritical state, the water adopts the heterogeneous structure characteristic of the supercritical fluid at moderately low density and expands. Although those results concern silicon [160] and molecular solids [161] (from a Lennard-Jones potential), it is plausible that such a mechanism also exists in water, depending on the fluence and the pulse length. It has however not been reported and further molecular dynamics study of laser-induced water cavitation is necessary to clarify this point.

2.6.4 Bubble dynamics

Once created, the bubble grows and collapses in a $\sim$100 ps to $\sim 1\mu$s, depending on the laser pulse width and energy. Onset of the bubble shields the surrounding water from heat conduction from the particle due to the low thermal conductivity of the water vapor compared to the liquid vapor. Since the bubbles are formed within $\approx$100 ps, bubbles can also interact with the incident laser for long enough pulses. Vapor bubbles indeed create a modified refractive index region around the particle that modifies its interaction with the electromagnetic field. In particular, a particle at first resonant at a particular irradiation wavelength when

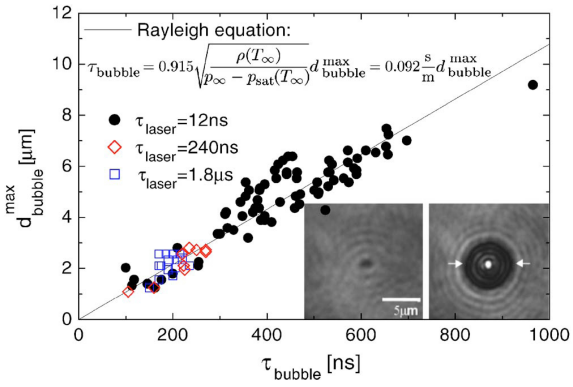

Figure 2.10 Plot of the Rayleigh equation with ambient pressure $p_\infty = 101$ kPa, saturated vapor pressure $p_{sat}(20^\circ C) = 2.33$ kPa, water density $\rho(20^\circ C)$ =998 kg/m^3 and plot of the measured maximum bubble diameters around melanosomes at $(0.5\pm0.1)\tau_{bubble}$. Photographs of a melanosome before irradiation (left) with a 12 ns pulse at 369 mJ/cm^2 and the corresponding bubble (τ_{bubble} =533 ns) around the same melanosome (right) at 255 ns after nucleation are shown. Taken from [179]

surrounded by water, is no more resonant when surrounded by a low refractive index vapor layer. The bubble in addition scatters a significant proportion of the incoming electromagnetic energy. For instance, while a 60 nm AuNP is resonant at 530 nm, its resonance is shifted to 520 nm when surrounded by a 500 nm vapor bubble. Its absorption cross-section at a wavelength of 530 nm is reduced from 1.12×10^4nm^2 to 2.12×10^3nm^2 when surrounded by a 200 nm vapor bubble, while its scattering cross-section incereases from 2.72×10^3 nm^2 to 1.96×10^5 nm^2. A process designed to optimize the energy deposition into the NP hence benefits from shorter pulses so that the majority of the pulse energy is absorbed before the bubble nucleation onsets.

After nucleation, the bubble's dynamic is driven by the vapor pressure that initially is at high temperature and pressure condition. As the bubble expands, the pressure decreases and the energy is lost due to heat conduction with the surrounding medium and friction. Both pressure from the liquid surrounding the bubble and the surface tension limit the bubble growth, which eventually reaches a maximum, and collapses. The duration of the collapse stage is roughly the same as that of the growth stage. Upon collapsing, the pressure increases again, initiating a new growth and collapse phase, known as bubble oscillation [157, 179–183]. Generation of shock waves, plasma formation and sonoluminescence are also associated with the collapse of cavitation bubbles [184–187].

The bubble dynamics can in theory be perfectly described by the theory of compressible fluid dynamics (see for example the classic from Laudau et Lifshitz [188]). However, the presence

of the dynamic phase change, of sharp pressure gradients and the multiple time and dimension scales make this problem a difficult one to tackle, even with modern computational fluid dynamics (CFD) techniques. In particular, Furlani et al. [189] proposed an interesting scheme using incompressible fluid mechanics in the liquid, and approximations based on the equation of state of an ideal gas to simulate the nucleation and growth of vapor bubbles around ns laser heated plasmonic nanostructures. However, this approach remains computationally intensive, and simpler approaches are sometimes needed for quick estimation and evaluation of experimental data. Neglecting heat conduction from the bubble to the surrounding liquid and mass transport across the bubble boundary (from evaporation or condensation), and assuming incompressibility of the liquid and polytropic dependence of the vapor pressure in the bubble, one writes the Rayleigh-Plesset equation [185, 190]

$$\rho_L \left(R\ddot{R} + \frac{3}{2}\dot{R} \right) = p_0 \left(\frac{R_0}{R} \right)^{3\kappa} - p_{ext} - \frac{2\sigma}{R} - 4\mu\frac{\dot{R}}{R} \tag{2.6}$$

where R is the bubble radius, R_0 is the initial radius, ρ_L is the (incompressible) liquid density, p_0 is the initial pressure, p_{ext} is the pressure of the surrounding liquid, σ is the surface tension and μ is the viscosity. κ is an exponent characterizing the expansion/compression. Isothermal expansion/compression yield κ =1 and adiabatic expansion/compression, (κ ≤1.66) [191]. Equation 2.6 is solved by providing initial radius and velocity. R_0, p_0 and κ are usually varied to fit experimental data. Using the Rayleig-Plesset equation, it is possible to derive a relation that links a bubble lifetime (τ_{bubble})to its diameter d_{bubble}^{max} [190].

$$\tau_{bubble} \approx 0.915 \sqrt{\frac{\rho_L}{p_{ext} - p_{sat}(T_{ext})}} d_{bubble}^{max} \tag{2.7}$$

where T_{ext} is the temperature of the surrounding water and p_{sat} is the saturation pressure. Considering T_{ext} =293 K, ρ_L =998 kgm^{-3} and p_{sat} =2.3 kPa,

$$\tau_{bubble} \approx 0.092 d_{bubble}^{max} \tag{2.8}$$

Neumann et al. [179] showed a nice agreement between this theory and observation using fast flash photography technique for bubbles of diameters between 1-10 μm generated around melanosomes by 12 ns, 240 ns and 1.8 μs pulsed laser. Results are reproduced in figure 2.10. In opposition with this result, Vogel et al. [157] reported the inaccuracy of the Rayleigh equation for τ_{bubble} <1 μs, arguing that it neglects the surface tension effect that becomes important for small bubbles. Including that effect, they showed that the Rayleigh equation underestimates the actual bubble radius by a factor up to ≈2 for very small bubbles. Theoretical study by Brujan et al. [192] confirmed this effect. The maximal radius of a bubble may also be

estimated from the energy absorbed in the system [158].

$$R_{max} \approx \left(\frac{3}{4\pi} \frac{E}{p_{ext}} \right)^{\frac{1}{3}} \tag{2.9}$$

However, theoretical work from Brujan et al. [192] showed rather a squared root scaling in fluence for bubbles with radius below 1 mm. Experimental measurements from Plech et al. [193] gave an exponant ≈0.45 rather than 1/3, which they attributed to the larger amount of energy dissipated in the medium for smaller bubbles that provide better heat conduction with the surrounding water at the beginning of the bubble formation.

2.6.5 Bubble detection techniques

Two different basic methods have been developed to detect and characterize vapor bubbles generated around plasmonic NPs. The first technique is based on the analysis of x-ray scattering from a laser-synchronized synchrotron irradiation [159, 191, 193]. The second one is an all-optical method exploiting the light scattering properties of the vapor bubble [70, 180, 184, 194–197]. Other bubble-detection techniques involving acoustic methods [183] may also be used but provides poor space and time resolution for nano-sized object when compared to the optical and x-ray techniques [196]. We will now briefly describe bubble detection techniques and summarize the experimental results concerning the nucleation and dynamics of bubbles.

x-ray scattering is a very precise way to probe the laser-NP interaction and the formation of bubbles. Small angle x-ray scattering (SAXS) and signal from the liquid scattering can be used to determine the bubble size and kinetics [193]. The principal drawback of this technique is the requirement for a synchrotron emission synchronized with a pulsed laser, which is not widely available. Plech et al. [193] used the European Synchrotron Radiation Facility at the time-resolved beam line ID09b which produce 100 ps x-ray pulses. A scheme of the setup is shown in figure 2.11a. For their experiments, the synchrotron pulse was synchronized with a fs laser pulse with a delay adjustable with a 5 ps step, allowing the time-resolved measurement of the bubble kinetic. In addition, it is possible to relate this measurement to x-ray powder scattering to evaluate the NP temperature and melting from the lattice expansion data [198]. Note that it is in principle not necessary to use fs pulses and that the same technique could also be used to study the dynamics of a ns laser induced bubble. No example of such measurement is however found in the literature.

Optical techniques are based on the detection and evaluation of extra scattering introduced by the presence of a vapor bubble, or other nanoscale events such as emission of pressure

waves, around the NPs. Two variants of this methods has been introduced to characterize nanoscale bubbles : the scattering imaging and the thermal lens method.

Scattering imaging is a well-known methods that have been successfully applied to the visualization of bubbles due to laser irradiation in both water [199] and cellular medium [200]. Lapotko et al. [180, 196] adapted this technique to the visualization of nanoscale bubbles generated around plasmonic NPs. A scheme of their experimental setup is shown in figure 2.11b. They use two pulsed-laser. A first laser (either a 10 ns or 0.5 ns at 532 nm) , called the pump laser, is tuned to the AuNP plasmon band and is focused into a gold colloidal sample to generate the nanobubbles around the particles. A second laser (0.5 ns at 690 nm), the probe, is used to side-illuminate the sample at specific delay times. The scattered field from the NP-vapor bubble system is collected to produce time-resolved imaging of the vapor bubble. A typical result is shown in figure 2.11c.

While allowing visualizing the bubble generation, this technique cannot be used to reliably characterize the bubble dynamics. Lapotko et al. [180, 196] used another method based on the thermal lens method to monitor the kinetic of the bubble evolution. In their setup (2.11d), a second continuous laser, the probe laser, is focused into the sample. Scattering events (such as bubble and pressure wave) deviate the beam. The power of the axial part of the beam is then measured by a photodetector. In their experiments, Lapotko et al. ensured that only one NP is present in the focal volume (case i. in figure 2.11d). The presence of a bubble around a particle thus results in a slight dip in the probe beam power measured at the photodiode. A typical result is shown in figure 2.11e. This allows measuring the precise lifetime of the bubble, which can be related to its diameter by the Rayleigh formula. The probe beam may also be focused into a spatial filter prior to the photodiode, so that the perturbed part is removed and only the unperturbed part is measured, enhancing the sensitivity [197].

Plech et al. [193] and Boulais et al. [70] used a similar setup to characterize nano bubbles generated around plasmonic NPs. However, while Lapotko et al. could detect signal issued from individual bubbles, their method rather uses an ensemble measurement as multiple NPs are present in the focal volume and contribute to the scattering signal (case ii. in figure 2.11d). A typical signal is shown in figure 2.11f. Note the slight asymmetrical shape in the response signal attributed to the presence of temporal dephasing in the bubble ensemble. They also used a different method, based on the Mie theory, to evaluate the bubble diameter, that does not rely on the measurement of the bubble lifetime. From the known value of the laser parameters and the concentration of the colloidal solution, they evaluated the scattering cross-section of an average NP-bubble system. Knowing the theoretical extinction cross-section for a NP-bubble system of a given diameter, they then deduced the diameter of the average bubble in the system. While this technique gives a good method to obtain

order-of-magnitude estimation of the bubble dimension, it is not very reliable as large errors are introduced by the fluence, size and orientation (for asymmetrical particles) distribution within the sample.

2.6.6 Short-pulsed plasmonic enhanced laser induced bubble characterization

Thorough characterization of bubbles allows a better understanding of the generation, growth and collapse mechanisms. Using optical techniques, Lukianova-Hleb et al. [180] determined the threshold fluence for the production of bubbles around gold nanostructures and studied the influence of different parameters on both the threshold fluence and the lifetime of the bubble generated at the threshold.

Geometry dependence of the bubble formation threshold

Performing thorough measurements on spheres with diameters 10-250 nm and shells (hollow gold spheres) of 60 nm and 250 nm irradiated with 0.5 ns, 532 nm pulses, they have found no bubble signal up to a certain threshold fluence where a bubble with a 9±1 ns lifetime becomes visible. Threshold fluence is around 100 mJ/cm^2 for 250 nm and 90 nm AuNPs, and is reduced to around 42 mJ/cm^2 for 250 nm silica-gold shell and further down to 20 mJ/cm^2 for clusters of 250 nm AuNPs. They associated the efficiency of the shell to its reduced heat capacity, and the efficiency of the cluster to the merging of the individual vapor layer from the tightly coupled NPs into one joint nucleus that can expand with the starting size of the cluster. Another paper from Lapotko et al. [196] also showed the reduction of the bubble formation threshold for NRs, coreshells, and coreshell clusters, which is surprising as the 532 nm irradiation wavelength does not match their plasmon band position. Note that another paper from Lukianova-Hleb et al. [201] reported much higher values of bubble formation threshold using the exact same laser, with 360 mJ/cm^2 and 180 mJ/cm^2 for 90 nm and 250 nm AuNPs respectively.

Pulse width dependence of the bubble formation threshold

Lukianova-Hleb et al. [180] studied the influence of the pulse duration on the bubble generation around gold NPs. Unsurprisingly, increasing the pulse length from 0.5 ns to 10 ns increased the vapor bubble threshold 13-fold and 24-fold for 30 nm and 100 nm AuNPs respectively due to the reduced thermal confinement. Similar results are reported by Lapotko et al. [196].

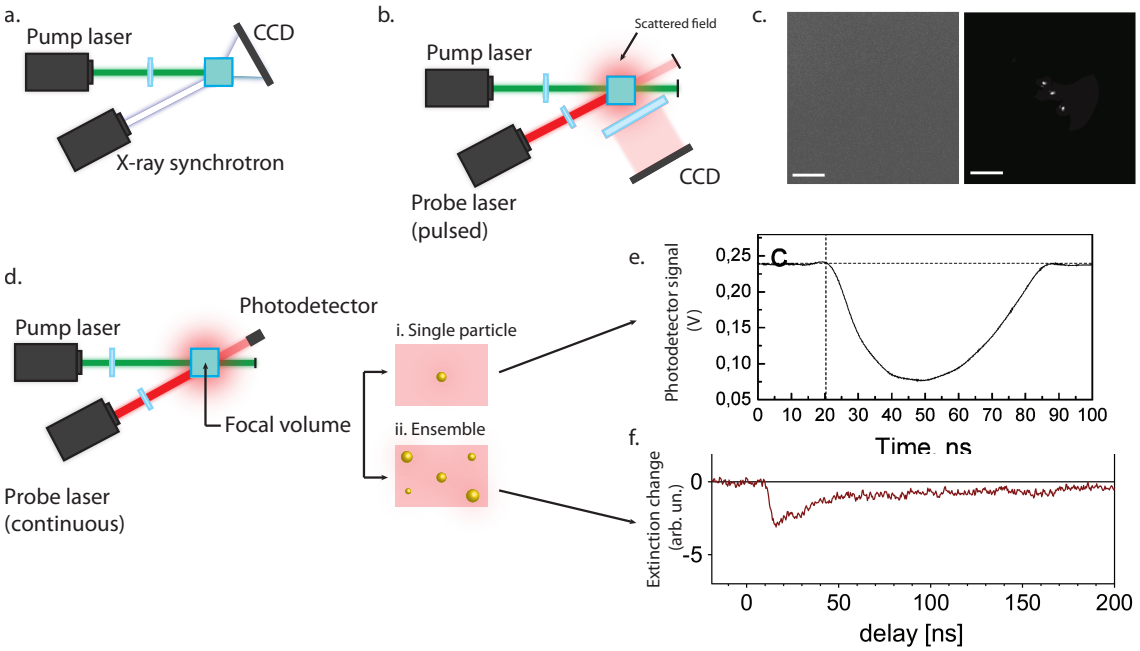

Figure 2.11 Detection and characterization of vapor nanobubbles around plasmonic NPs. a. Scheme of experimental setup for the x-ray scattering based detection method. b. Scheme of experimental setup for the time-resolved optical scattering imaging method. c. Time-resolved optical scattering images obtained for : (left) a suspension of 30 nm AuNPs (no pulse), (right) 30 nm AuNP exposed to a single pump laser pulse (532 nm, 0.5 ns, 0.9 J/cm^2). Scale bar is 6 μm. Taken from [196]. d. Scheme of experimental setup for the optical scattering time-resolved spectroscopy method. Focal volume is shown in the case of an individual AuNP and an ensemble of AuNPs. e. Typical time response for a single 80 nm AuNP obtained with a single pump laser pulse (vertical dashed line) near the photothermal bubble generation threshold fluence. Taken from [180]. f. Transient extinction change of a NP suspension of 80 nm diameter by a 660 nm probe beams excited with a single 10 ns laser pulse at 532 nm at a fluence of 30 mJ/cm^2. Taken from [193]

Impact of the vapor bubble on the NPs environment

For fluence lower than the bubble formation threshold, Lukianova-Hleb et al. [180] found that the impact of the NP irradiation on their environment was purely thermal, whereas higher fluence produced a signal characteristic of a bubble and the gradual disappearance of the heating response, up to bubbles with lifetime of 12-13 ns. They thus concluded that the impact of nanobubbles on its surrounding medium is purely mechanical, with the exception of the smallest bubbles (τ_{bubble} =[9-12 ns]) that do not provide thermal insulation of the medium. Plech et al. also explained the modified dependence on energy of the observed experimentally (i.e. 0.45 instead of the theoretically predicted 1/3 exponent) using the argument of weak

thermal insulation from small nanobubbles [193]. In another paper, Lapotko et al. [184] reported the failure to observe any sonoluminescence, or pressure wave signal related to the collapse of the bubble and attributed this feature to the presence of the nanostructure that prevents the bubble from extreme heating.

Comparison with theoretical results

Lukianova-Hleb et al. [180] pointed out that the lifetime of the vapor bubble does not gradually decrease to zero as the fluence is reduced. Small bubbles are hence not allowed to be generated around the NPs. They argue that this behavior does not match the classical theory of bubble formation at a heated surface, which does not predict a minimum bubble diameter around NPs.
From a thermal model based on the hydrodynamic equation and the stiffened equation of state, they also showed that the fluence theoretically required to bring water to its critical point (647 K) is much lower than the experimental threshold fluence. The authors therefore concluded that additional energy must be provided to the vapor layer to make it grow and become a bubble. The bubble must indeed overcome the pressure of the outer layer to grow, which on the nanoscale is significantly increased by the surface tension pressure since it is inversely proportional to the curvature radius. To prove their point, they studied the variation of the threshold fluence as a function of the particle diameter, which should thus increase. The threshold fluence is shown to increase 18-fold as the diameter is reduced from 80 nm to 10 nm. At the same time, their simulation showed that the theoretical fluence needed to bring water to its critical point do not follow a similar trend, with a 6-fold increase only, supporting their hypothesis.
This conclusion strongly disagrees with another study made by Plech et al. [193] using similar techniques. The authors indeed reported bubble formation threshold that corresponds well with the calculated fluence needed to bring the surrounding water at the critical point, except for the smallest particles (18 nm). Further studies are thus required to clarify this point.

2.6.7 Melting, evaporation, fragmentation and plasma formation in the nanostructure

If the laser fluence is increased beyond the bubble nucleation threshold, the absorbed energy is, at some point, sufficient to cause the onset of morphological and phase transformation within the nanostructure itself.
Melting occurs under achievement of the melting temperature T_M inside the particle. Once melted, the nanostructures will reshape into spheres due to the surface tension of the melted

metal [158]. This reshaping has been observed by Takami et al. [202] for 5-50 nm AuNPs when irradiated with 16 mJ/cm^2, 7 ns pulses at 532 nm. For AuNRs, using 800 nm, 7 ns pulses, Link et al. [203, 204] determined a much higher reshaping fluence threshold ≈250 mJ/cm^2. Reshaping of core-shell structures has also been observed. Aguirre et al. [205] observed that low-energy ns irradiation of silica-gold core-shells leads to the formation of colloidal AuNPs in solution.

It is of interest to note that the temperature for homogeneous melting of small nanostructures is reduced from the bulk value. For NPs with diameters below 10 nm, a 1/R dependence has been observed for both tin and gold NPs [206, 207]. NPs with larger diameter are shown to have homogeneous temperature near the bulk melting point. Similar reduction of the latent heat of melting has also been observed [206]. Phase transition of NPs however starts with the formation of a thin liquid layer at the surface, a process known as surface melting, occurring for temperature well below the homogeneous melting point [208–212]. Surface melting has been associated to the very low temperature of reshaping observed by Petrova et al. [210] for AuNRs continuously heated at 523 K for 1 h. Insawa et al. [212] also observed the surface melting of ≈38×29 nm^2 ellipsoidal AuNPs around 120 K below the bulk melting point. Ercolessi et al. [213] studied theoretically the problem using molecular dynamics simulations and observed surface melting for gold clusters with more than 350 atoms.

Heating beyond melt leads to the evaporation of the NP. Pustovalov et al. [158] studied theoretically the evaporation process from the surface of laser-heated NPs and concluded that the evaporation of AuNP can form a metal vapor blanket around it, which expansion could form pressure wave in the surrounding medium. Further increase of the laser fluence may result in the particle fragmentation. From theoretical consideration Zharov et al. [214] estimated the fragmentation fluence threshold to ≈40 mJ/cm^2 for a 70 nm AuNP irradiated with a 10 ns, 532 nm pulse. Takami et al. [202] observed the size reduction of 5-50 nm AuNPs when irradiated with at 30 mJ/cm^2, in good agreement with the theoretical value from Zharov et al. [214]. In opposition, Link et al. irradiated AuNRs with 800 nm, 7 ns pulses, and determined a much higher reshaping fluence threshold ≈250 mJ/cm^2 and fragmentation threshold ≈1 J/cm^2 [203, 204]. Fragmentation of silica-gold core-shell structures by high energy ns laser into small colloidal AuNPs has also been observed [205].

Laser fragmentation mechanisms are usually associated to a photo thermal process resulting from the heating of the liquid melt, or to a Coulomb explosion mechanism resulting from a massive ejection of electrons from the NP that triggers fission due to electrostatic repulsion [215]. In particular, Yamada et al. [216] observed a high density of solvated electrons resulting from the irradiation of ≈8 nm gold NPs in a solution of sodium dodecyl sulcate with 10 ns, 355 nm, 1 J/cm^2 pulses, which supports the Coulomb explosion mechanism for small metallic

NPs.
Increasing even further the laser fluence will result in optical breakdown within the particle and to the formation of a plasma cavity, associated with the generation and propagation of intense pressure wave in the medium. Pustovalov et al. [158] estimated the temperature threshold for optical breakdown over 10 000K along with a simple analytic approximate model to evaluate the resulting velocity and pressure distribution in the liquid .

2.7 Fundamentals of ultrashort pulsed-laser interaction with plasmonic nanostructures in water

In many aspects, the interaction of ultrashort laser pulses (τ_p ≈10-500 fs) with plasmonic nanostructures in water is similar to the case of short laser pulses (τ_p ≈500 ps-10 ns). The different phenomena pictured in figure 2.8 still occurs, but the fluence range and the mechanisms implied are significantly different.

2.7.1 Ultrafast laser heating of plasmonic nanostructures

As the pulse length is much shorter than the electron-phonon equilibrium time (τ_{e-ph} ≈1-3 ps) [127, 129, 141, 142], energy transfer from a fs laser to a plasmonic NP embedded in water heats the electrons out of equilibrium with the phonon subsystem. As indicated in figure 2.6, the laser pulse excites a plasmon oscillation that decays into a nonthermal electron distribution that thermalizes to a Fermi-Dirac distribution in ≈ 500 fs [75, 127, 129, 140] with a temperature T_e that is different from T_l, the temperature of the phonon subsystem. Heat transfer in this case can be described using a hyperbolic two-temperature model (HTTM) based on the quantum and statistical mechanics [70, 217, 218]

$$C_e(T_e)\frac{\partial T_e}{\partial t} = -\nabla \cdot \mathbf{q_e} - G(T_e - T_l) + S_{EM}(\mathbf{r}, t) \tag{2.10}$$

$$\tau_e \frac{\partial \mathbf{q_e}}{\partial t} + \mathbf{q_e} = -\kappa_e \nabla T_e \tag{2.11}$$

$$C_l(T_l)\frac{\partial T_l}{\partial t} = -\nabla \cdot \mathbf{q_l} + G(T_e - T_l) \tag{2.12}$$

$$\tau_l \frac{\partial \mathbf{q_l}}{\partial t} + \mathbf{q_e} = -\kappa_l \nabla T_l \tag{2.13}$$

where C is the heat capacity, T is the temperature, S_{EM} is the laser energy input, $\mathbf{q}$ is the heat flux and κ is the thermal conductivity. The subscripts "e" and "l" refer to the electrons and lattice respectively. The electron-phonon coupling constant G has a value of 2.5×10^{16} $\mathrm{Wm^{-3}K^{-1}}$ for gold at room temperature [219]. A model giving the temperature dependence

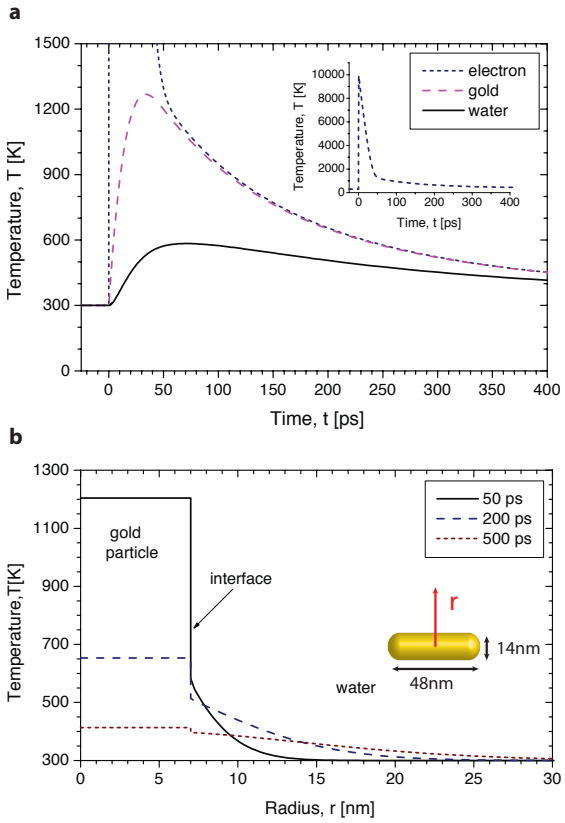

Figure 2.12 a. Temporal evolution of temperature profiles of 48×14 nm^2 AuNR and its surrounding water at the surface following irradiation with a laser pulse of fluence, $F_{pulse} = 4.70$ Jm^{-2}. In the inset, the electron temperature as a function of time is shown. b. Temperature profiles at different times after laser exposure ($F_{pulse} = 4.70$ J m^{-2}) as a function of radial distance at the mid-length of the 48×14 nm^2 AuNR at the z = 0 plane. Taken from [172]. The NR shown in inset has been added for clarity.

of G can be found in [220]. Note also that for particle larger than ≈10 nm, the electron-phonon coupling is very similar to the bulk value [221–223]. Numerical values and expression for C and K for gold can be found in the Supporting Informations of a recent work from Boulais et al. [70].

The HTTM model reduces to the usual parabolic two-temperature model (PTTM) introduced by Anisimov [224] and applied by many authors for fs heating of nanostructures [127, 149, 172, 219, 223, 225, 226].

$$C_e(T_e)\frac{\partial T_e}{\partial t} = -\nabla\left(\kappa_e \nabla T_e\right) - G(T_e - T_l) + S_{EM} \tag{2.14}$$

$$C_l(T_e)\frac{\partial T_l}{\partial t} = -\nabla\left(\kappa_l \nabla T_l\right) + G(T_e - T_l) \tag{2.15}$$

In contrast to the PTTM, the HTTM model considers the finite propagation speed of heat in space whereas the PTTM model assume infinite heat propagation speed, which could lead to inaccuracy depending on the specific system geometry and irradiation time. In addition, a certain caution is indicated in the use of both the HTTM and PTTM model to describe the ultrafast heating of metallic NPs. Those models indeed imply a complete time-separation between the thermalization of the electron subsystem to a Fermi-Dirac distribution and the thermalization with the phonon subsystem. This picture is in general not adequate as the thermalization time for electrons (≈500 fs) is *not* significantly shorter than the electron-phonon thermalization time (≈ 1-3 ps). Hence, a significant proportion of the energy transfer from electrons to phonons does not occur between thermalized electrons and phonons, but between *non-thermal* electrons and phonons. Groeneveld et al. [227] showed that this results in reducing the relaxation rate between electrons and phonons. However, the effect becomes less important as the temperature of the electron gas increases. Groeneveld et al. indeed calculated that the non-thermal distribution related effect becomes significant for electronic temperature below 600 K.

As the thermal capacity of electrons C_e is much lower than the one associated to the phonon C_l, very high electronic temperatures can be reached in the structure. Ekici et al. [172] used a PTTM model to evaluate the electronic and lattice temperature of a 14×48 nm^2 AuNR in water after a 250 fs, 470μ J/cm^2, 800 nm single laser pulse. Their result is reproduced in figure 2.12a. The electronic temperature is shown to reach near 10 000 K as the lattice temperature stays below 1300 K. The phonon and electron subsystems in gold are seen to be completely thermalized after ≈50 ps.

Energy transfer to the water by conduction from the heated lattice is also affected by the ultrafast nature of the laser interaction. The finite thermal conductance at the water/particle

[172, 198, 228, 229] indeed becomes important in the ps time-scale and will strongly affect the temperature distribution within the sample for rapidly heated particle. Specifically, a discontinuity will appear at the water/particle interface. This discontinuity is clearly visible from figure 2.12a and 2.12b. The temperature difference between water and gold at the interface is shown to disappear within ≈500 ps. This calculation uses the value of (105±15) MW $m^{-1}K^{-1}$ for the conductance at the gold/water interface estimated by Plech et al. [198].

2.7.2 Lattice expansion and structural oscillation

The rapid heat transfer to the gold lattice induced by the interaction with an ultrafast pulse induces a rise in temperature much faster than the expansion time of the nanostructure. It triggers the formation of a large stress state within the structures, followed by a fast increase in size, and by an oscillation around the new equilibrium position corresponding to the new temperature. This process is similar to a spring mass system which equilibrium position is displaced more quickly than its oscillation period [225].

The oscillations are readily observable in a pump-probe time-resolved spectroscopy experiment. The setup is presented in figure 2.13a. It consists in splitting a fs pulse into two pulses of different fluences. The large fluence pulse, called the pump pulse, is focused into the sample consisting of a colloidal suspension of nanostructures. The second low fluence pulse, called the probe pulse, first passes through a delay line before being focused in the sample, and thus arrive some time after the pump pulse. The transmission of the probe is then measured with a photodiode, accounting for the state of the nanostructures at this particular time. Varying the delay between the pump and the probe pulses allow to study the nanostructures' response to the fs excitation as a function of time, with a resolution of some hundreds fs, ultimately limited by the time-width of the fs pulses. Oscillations that modify the extinction cross-section of the nanostructures are thus observable. A typical signal for 46.9×11 nm^2 AuNRs pumped and probed with a wavelength of 800 nm is shown in figure 2.13b . The early response (≈ 0-10 ps) is linked to the electron system excitation and subsequent energy transfer to the phonon system. Clear oscillations with a period of ≈63 ns can be seen from the figure. The damping of the oscillation is a combination of an homogeneous damping due to energy dissipation and of an inhomogeneous damping due to the dispersion in NRs size within the sample [230].

For spherical NPs, the symmetric breathing mode is excited, with almost all of the excitation in the fundamental mode. The breathing mode consists in the periodic increase and decrease of the radius, hence modifying the particle's volume. The period of the n^{th} breathing mode is given by [223]

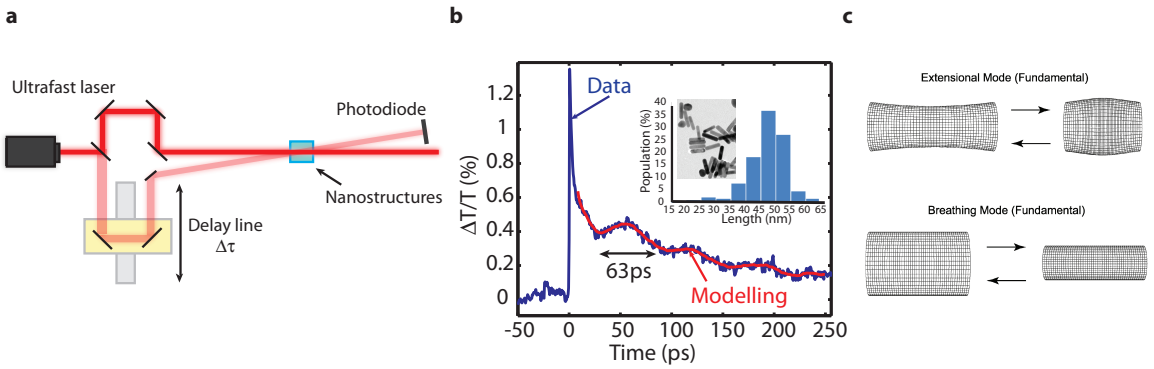

Figure 2.13 a. Pump-probe optical setup used to probe the oscillation. The ultrafast laser beam is split in two. The pump beam is directed at the sample while the much lower intensity probe beam passes first through a delay line. Probe intensity is recorded using a photodiode. b. NR oscillations following a 100 μJ/cm^2, 45 fs irradiation. Figure shows the experimental (blue line) and simulated (red line) variation in the sample extinction as a function of time. The time origin is fixed at the pump irradiation time. c. Scheme of the vibrational modes in NRs. Taken from [223]

$$T_{bm-NP}^{(n)} = \frac{2\pi R}{\xi^{(n)} c_l} \tag{2.16}$$

with R, the radius, c_l, the longitudinal speed of sound, c_t, the transverse speed of sound, and ξ_n, an eigenvalue obtained from

$$\xi cot\xi = 1 - \left(\frac{\xi c_l}{c_t}\right)^2 \tag{2.17}$$

Using values from bulk gold, $\xi^{(0)}$ =2.95 [223]. Using pump-probe spectroscopy, Hodak et al. measured the oscillation frequency of AuNPs as a function of diameter and show a nice agreement with the theoretical value [231]. They confirmed the fundamental breathing mode as the principal oscillation mode excited and showed that the speed of sound in NPs are similar to their bulk value.

In the case of AuNRs, two different modes could be excited : the breathing mode and the extension mode. Both are schematically represented in figure 2.13c. The period of the nth breathing mode is given by [223]

$$T_{bm-NR}^{(n)} = \frac{2\pi a}{\phi^{(n)} c_l} \tag{2.18}$$

where ϕ is an eigenvalue obtained from

$$\phi J_0(\phi) = \frac{1-2\nu}{1-\nu} J_1(\phi) \tag{2.19}$$

a is the radius of the NR, c_l is the longitudinal speed of sound, J_n is the n^{th} Bessel function and ν is the Poisson ratio. The period of the extension mode is given by

$$T^{(n)}_{ext-NR} = \frac{2L}{(2n+1)\sqrt{E/\rho}} \tag{2.20}$$

with E, the Young modulus, L, the NR's length and ρ, its density. As the extension mode modifies the aspect ratio of the rod, it can be observed by probing the sample at a wavelength near the longitudinal plasmon band. Figure 2.13b shows the oscillation of 46.9×11 nm^2 NRs pumped and probed with a wavelength of 800 nm. The red line correspond to an oscillation with a period given by equation 2.20 and including the homogeneous and heterogeneous damping found in the paper from Pelton et al. [230]. This confirms that the observed oscillation comes from the excited extension mode of the NRs.

The breathing mode does not modify the aspect ratio but rather varies the volume of the particle. It is much more difficult to observe due to its lower period and to its higher sensitivity to inhomogeneous damping [232]. Hu et al. [233] however successfully observed this mode using a probe laser tuned to the transverse plasmon band, with a measured period in good agreement with the theoretical prediction.

Analysis of those oscillations can be used to evaluate the temperature inside the nanostructure and their size distribution, as well as measure their properties under extreme temperature and pressure conditions. In particular, Hu et al. [234] evaluated the temperature corresponding to the onset of cavitation for 20nm diameter AuNPs in water, yielding a temperature of 550±50 K, in good agreement with the explosive boiling mechanism .

Finally, it is of interest to evaluate the impact of the rapid lattice expansion on the pressure distribution in the surrounding water. Volkov et al. [235] studied this effect using a numerical model of the laser interaction with a AuNP, including a PTTM model to calculate the temperature within the particle, and the Navier-Stokes equations to account for the water dynamics and thermodynamics, considering the effect of the lattice expansion on the pressure distribution. Their results showed an increased influence of the lattice expansion on the pressure distribution in water during the first picoseconds following the irradiation (t<20 ps). Note that their results do not include the subsequent oscillations of the NP, which effect, however, should be negligible compared to the rapid initial expansion.

2.7.3 Heat-mediated vapor bubble formation

Bubbles can be generated around plasmonic nanostructures with ultrafast laser pulses by two general mechanisms. First, similar to the case of short pulses, heat transfer from the particle lattice can rise the water temperature near $0.9T_c$ and induce the formation of a vapor bubble through explosive boiling. Such bubbles have been observed by Kotaidis et al. [191] following the irradiation of NPs of 9 nm of diameter. Using small angle x-ray scattering, they showed the formation of nanoscale vapor bubble after the interaction with 400 nm, 100 fs ultrashort pulse, with a threshold fluence of 29 mJ/cm^2. Figure 2.14a shows the size evolution of the bubble as a function of time for a fluence near the threshold. Results show a good agreement with the dynamic calculated from the Rayleigh-Plesset equation. In another paper, Siems et al. [193] measured the bubble threshold as a function of the particle diameter. Their results, presented in figure 2.14c, show a bubble fluence threshold in agreement with the calculated fluence at which the water temperature reaches the explosive boiling temperature ($0.85T_c$). Note that due to the finite interface conductance, the temperature inside the particle is much higher than the temperature in the water. Koitadis et al. [159] in particular showed that NPs with diameters < 30 nm, melts for fluences lower than the bubble threshold (see figure 2.14c).

Volkov et al. [235] modelled the generation of vapor bubbles due to the conduction heat transfer from ultrashort laser pulse heated NPs. Results show the emission of a ≈60 MPa pressure wave and a temperature rise in the water reaching the critical temperature for an absorbed fluence of 7.2 mJ/cm^2 by a 100 nm diameter particle. This corresponds to an incident fluence of 3.8 mJ/cm^2, considering the absorption a AuNP at a wavelength of 400 nm. This simulation however did not consider the finite conductance at the water/particle interface, which may explain the lower threshold obtained. However, Ekici et al. [172] included this effect and studied the interaction of a 48×14 nm^2 AuNR with a 250 fs, 800 nm ultrafast laser [172]. Their results show a bubble formation threshold fluence of ≈450 μJ/cm^2, slightly over the calculated melting fluence threshold (≈400 μJ/cm^2).

Cavitation mediated by the heat transfer from the particle's lattice is very similar to short pulse cavitation. Indeed, even if the energy is transferred from the laser to the NP's lattice in a very short time (≈1-3 ps), energy is transferred to the water in a much longer time corresponding to the phonon-phonon scattering time (≈ 100 ps). The thermodynamics pathway should thus be very similar to what has been presented in the section concerning short pulses (see curves I. and II. in figure 2.9).

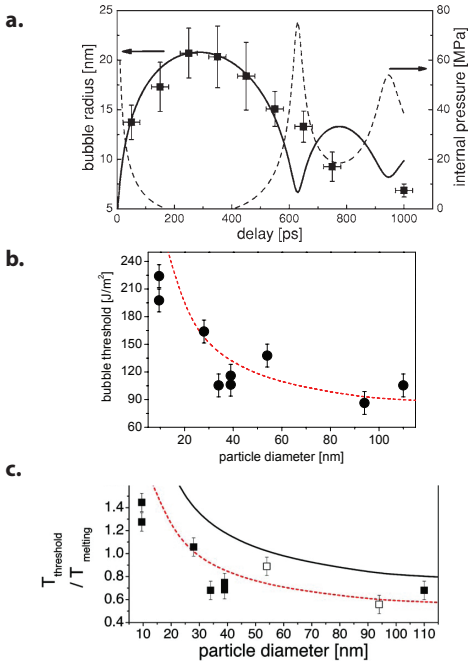

Figure 2.14 Vapor bubbles generated around AuNPs by a 400 nm, 100 fs ultrashort laser pulse. a. Bubble radius and pressure transients of the water vapor inside the bubbles generated at a fluence near 29 mJ/cm^2 as calculated from the Rayleigh-Plesset equation together with the measured radii. The first maximum in pressure at 650 ps marks the collapse of the bubbles, the following modulations are only expected for oscillatory bubble motion. Taken from [191] b. Bubble formation threshold as a function of NP diameter for fs laser excitation and x-ray probing. The dashed line stands for a threshold estimation at 85% of the critical temperature of water. Taken from [193]. c. Temperature of the NP at the vapor nucleation relative to the melting temperature of gold. The open and full symbols are deduced from different measurement techniques. The whole and dashed lines stand for a threshold estimation at T_c and $0.85T_c$ respectively. Taken from [236].

2.7.4 Plasma-mediated vapor bubble generation

Using ultrashort pulses, it is possible to generate cavitation bubbles around plasmonic NPs in a completely different way. The high intensity of the electric field implied by the fs pulse in conjunction with the near-field enhancement around the particle may be used to induce non-linear absorption *directly* in the water and generate a plasma. This plasma diffuses and by collision and recombination transfers its energy to the water molecules, producing a rapid temperature and pressure increase that may lead to the generation of a bubble.
The production of plasma in water by fs laser pulses and the following mechanical, thermomechanical and chemical effects have been extensively studied by Vogel et al. [72, 237]. These authors described the formation of plasma in water as the generation of quasi-free

electrons that have sufficient energy to be able to move without being captured by local potentials. Following a work by Sacchi [238], the authors represented water as an amorphous semiconductor-like structure with a ∼6.5 eV band gap separating the highest occupied molecular orbital to the quasi-free excited state [239–242]. Note that the process of photoexcitation of electrons within water is a very complex subject (see for example the work by Coe et al. [243] and by Couto et al. [244]), but that this simplified picture seems sufficient to give accurate results in our case.

Two main mechanisms are responsible for the photoexcitation of electrons and the formation of plasma in water : photoionization and collision (avalanche) ionization. Photoionization is the direct transition of an electron from the ground state to the excited quasi-free state induced by the absorption of photons. It is described by the Keldysh theory [245]. Once quasi-free electrons are created, they absorb the laser energy through an inverse Bremmstrahlung process. Once they reach ∼1.5 times the bandgap, they have enough energy to collide with neutral atoms and knock out an extra electron across the band gap [72]. A third process that can occur in the case of plasmon-enhanced plasma generation in water is photo-assisted thermal injection of electrons from the heated electrons of the nanostructure. Figure 2.15 schematizes those processes. We will now describe them into more details.

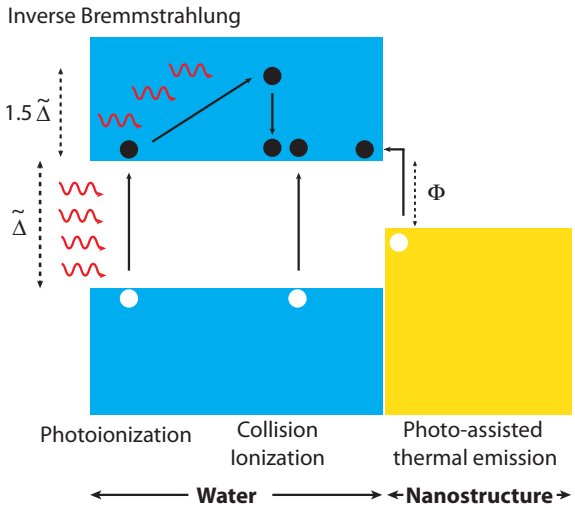

Figure 2.15 Schematic description of the different processes that can generate plasma into water in the case of plasmonic enhanced plasma generation in water

Photoionization

Keldysh introduced the Keldysh parameter for the photoionization of solids γ [47, 72, 245–248]

$$\gamma = \frac{\omega}{e|\mathbf{E}|}\sqrt{m\Delta} \tag{2.21}$$

where e is the charge of the electron, m is the exciton reduced mass defined as $\mathrm{m}^{-1}=\mathrm{m}_e^{-1}+\mathrm{m}_h^{-1}$, Δ is the ionization potential and $\mathbf{E}$ is the electric field. Note that following the work from Keldysh [245], the parameter γ for solids is $\sqrt{2}/2$ the one for individual atoms and gases, which bring some confusion in the literature [44, 249, 250]. It is important to note that the Keldysh parameter is fundamentally defined as a function of the field intensity $|\mathbf{E}|$ in V/m and *not* as a function of the laser field irradiance I in W/m^2. As many authors define the Keldysh parameter as a function of the irradiance, one could be tempted to use the time-averaged power flow given by the Poynting's vector to calculate it. However, this will yield the correct result only in the case of plane waves since, in this case, $I =< S >= \frac{1}{2}n\epsilon_0 c_0|\mathbf{E}|^2$. For general electromagnetic field, using the value $I =< S >$ will not yield the correct value for γ.

For short pulses, the ionization potential must be corrected to account for the oscillation energy of the electron due to the laser field. This effective potential $\tilde{\Delta}$ is defined from the Keldysh parameter γ [245]

$$\tilde{\Delta} = \frac{2}{\pi}\Delta\frac{\sqrt{1+\gamma^2}}{\gamma}E\left(\frac{1}{\sqrt{1+\gamma^2}}\right) \tag{2.22}$$

with $E(x)$ the complete elliptic integral of the second kind. Defining $\gamma_1 = \gamma/\sqrt{1+\gamma^2}$ and $\gamma_2 = 1/\sqrt{1+\gamma^2}$, Keldysh then writes the photoionization rate as :

$$\eta_{PI} = \frac{2\omega}{9\pi}\left(\frac{m\omega}{\tilde{\gamma}\hbar}\right)^{3/2} Q(\gamma, \frac{\tilde{\Delta}}{\hbar\omega})e^{-\pi\langle\frac{\tilde{\Delta}}{\hbar\omega}+1\rangle\frac{K(\gamma_1)-E(\gamma_1)}{E(\gamma_2)}} \tag{2.23}$$

with K and E, the complete elliptic integrals of the first and second kind and $\langle x\rangle$ is the integer part of x. Q is defined as

$$Q = A\sum_{n=0}^{\infty}\Phi\left(\sqrt{\frac{\pi^2\left(2\langle x+1\rangle - 2x + n\right)}{2K\left(\gamma_2\right)E\left(\gamma_2\right)}}\right)e^{\beta} \tag{2.24}$$

The function $\Phi(z)$ is defined as

$$\Phi(z) = \int_0^z e^{y^2 - z^2} dy \tag{2.25}$$

The prefactor A is defined as

$$A = \sqrt{\frac{\pi}{2K\left(\gamma_2\right)}} \tag{2.26}$$

and the exponent is defined as

$$\beta = -\pi n \frac{K\left(\gamma_1\right) - E\left(\gamma_1\right)}{E(\gamma_2)} \tag{2.27}$$

Those equations yield the photoionization rate as a function of the Keldysh parameter γ, represented in figure 2.16a. The Keldysh parameter defines the photoionization mechanism that is dominant for specific laser parameters and material. For $\gamma \gg 1$, i.e. for large frequency and band gap, but low laser intensity, the largest contribution comes from the multiphoton ionization process, where the electron absorbs simultaneously many photons to come over the potential barrier. Under this condition, $\eta_{PI} \approx \left(|\mathbf{E}|^2\right)^k$ where k is the number of photons needed to go over the potential barrier. For $\gamma \ll 1$, i.e. for large laser intensity, electrons can directly go through the potential barrier by a tunnelling process, and the k exponent is reduced. Figure 2.16b schematically represents the tunnelling and multiphoton ionization processes at a wavelength of 780 nm. Curves in figure 2.16a show the photoionization rate calculated using approximate theory considering either tunnelling or mulitphoton ionization only processes. In the case of fs ionization of water, Vogel et al. demonstrated that $\gamma \approx 1$, so that only the complete Keldysh theory is accurate.

Collision ionization

Once in a quasi-free state, electrons can absorb the laser energy through inverse Bremmstrahlung absorption [72] and increase their kinetic energy. Once they get enough energy, they can collide with neutral water molecules to knock out additional electrons to the quasi-free states. Vogel et al. estimated this energy to $1.5\tilde{\Delta}$ and calculated the rate of ionization by collision as :

$$\eta_{coll} = \frac{1}{\omega^2\tau^2 + 1}\left(\frac{e^2\tau|\mathbf{E}|^2}{m_e\left(1.5\tilde{\Delta}\right)} - \frac{m_e\omega^2\tau}{M}\right) \tag{2.28}$$

where m_e is the electron mass, M is the mass of the water molecule and τ is the electron scattering lifetime (taken constant as ≈1.7 fs).

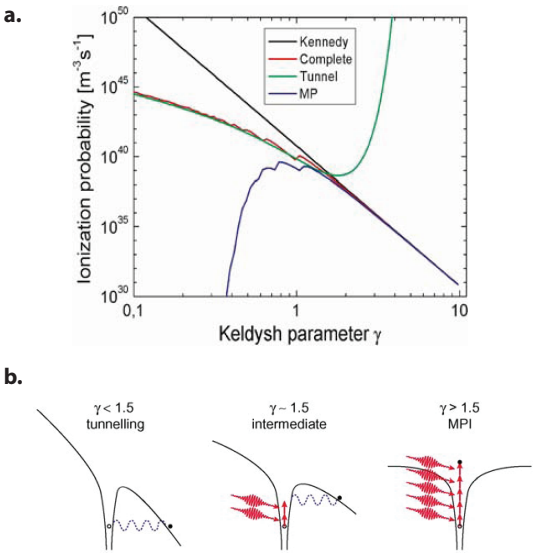

Figure 2.16 a. Ionization probability as a function of the Keldysh parameter at λ =780 nm. The red line is calculated from the complete Keldysh theory. The blue and green line are approximation of the Keldysh theory valid in the multiphoton and tunnelling limit respectively. The black line is calculated from the approximate theory due to Kennedy et al. [246]. Taken from [72]. b. Schematic representation of the multiphoton and tunnelling ionization processes. Taken from [44].

Boulais et al. [70] used a more complex model where the energy and density of the plasma are calculated in parallel without fixing an a priori energy to initiate the collision ionization. The plasma conductivity is calculated from the plasma collision frequency with neutral water molecules ($\sigma_a \approx 2\times10^{-19}\mathrm{m}^2$) [251] and the plasma collision frequency with the ionized water molecules, calculated from the dense plasma theory [252]. This conductivity determines the rate of absorption of the laser energy ($\sigma|\mathbf{E}|^2$). Using the same method as Hallo et al. [253] in their study of plasma formation in dielectric material, they determined the collision ionization frequency from the calculated plasma temperature and density. The interested reader is referred to the above-cited literature for details.

Photothermal emission

Following the laser irradiation, the electrons of the nanostructure may be heated to very high temperatures, above 10 000 K. A those temperatures, electrons may be injected over the metal/water energy barrier into the quasi-free states of the water, and thus participate to the plasma generation. In addition, photons non-linearly absorbed in the nanostructure can also participate to the process, yielding to a photo-assisted thermal process. The energy barrier at

the water/gold interface Φ has been determined experimentally as $\Phi \sim 3.72$ eV by Zolotovitskii et al. [254]. Boulais et al. [70] proposed an expression to evaluate this contribution to the plasma, based on the Fowler-Dubridge theory [255]. However, Boulais et al. did not consider any correction to this current due to the polarization of the NP, which should limit the injected current [220].

Plasma diffusion and bubble formation

Once created, the plasma diffuses and recombines. Boulais et al. [70] used a formalism similar to the semiclassical Boltzman transport equation to evaluate the diffusion. Collisions with neutral and ionized molecules, along with carrier recombination, transfer the energy from the electrons to the water molecules, yielding water temperature rise, pressure wave generation and, possibly, vapor bubble formation.

Important energy transfer from the plasma occurs when the plasma reaches a density $\approx 10^{20}$-$10^{21} \mathrm{cm}^{-3}$. [72]. In particular, Vogel et al. determined that for λ =800 nm, a density $\approx 0.236 \times 10^{21} \mathrm{cm}^{-3}$ defined the cavitation threshold, in pure water without NPs. Figure 2.17 presents the laser fluence necessary to generate a density of 10^{21} cm^{-3} electrons in pure water. This simple calculation can serve as an interesting approach to evaluate the importance of the plasma in the cavitation process in a given situation. While this curve has been calculated for pure water, one can evaluate the influence of the presence of the plasmonic nanostructure by simply dividing the fluence required in the case of pure water by the square of the maximum electric field enhancement factor, as calculated from the Mie theory.

In the case of in-resonance irradiation of AuNPs, plasma generation plays only a minor role in the cavitation mechanism. For instance, in the situations considered in figure 2.14 (100 fs, 400 nm), the threshold fluence for the generation of vapor bubble is way lower than the fluence that would be required to generate a plasma density near 10^{21} cm^{-3}. In particular, the fluence required for important plasma contribution when irradiating a 100 nm AuNP is $\approx$ 65 mJ/cm^2-80 mJ/cm^2, considering the $\sim$2.5 field enhancement factor, while the observed bubble formation threshold is rather around 9 mJ/cm^2 [193]. In the case of in-resonance interaction, plasma generation is thus very weak near the bubble formation threshold and becomes an important factor only for much higher fluences. In this regard, Bisker et al. [256] demonstrated that the 10^{21} cm^{-3} was not reached around Au and Ag NPs, or AuNRs, for fluence below the melting threshold when the nanostructures were irradiated with a wavelength tuned to their plasmon resonance.

It is however possible to use a slightly detuned laser irradiation to generate an important plasma in the water without over-heating the particle. Boulais et al. used a 800 nm, 45 fs laser to interact with a off-resonance100 nm AuNP in water. They theoretically showed that

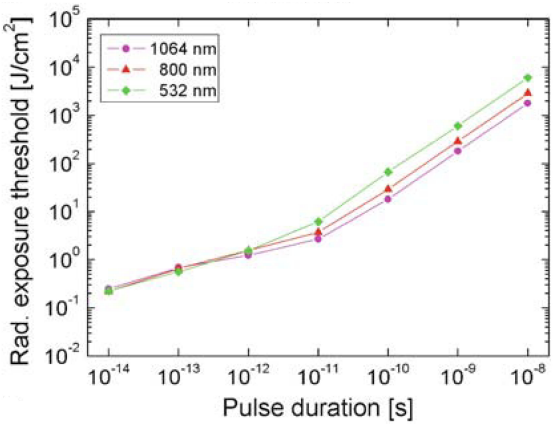

Figure 2.17 Fluence required to generate a 10^{21} cm^{-3} plasma as a function of the pulse time width, for three different wavelengths. Taken from [72]

for a 200 mJ/cm^2 irradiation, only 10% of the total energy absorption took place in the particle, while the remaining 90% formed a heated plasma around the particle. Figure 2.18a, b and c show the calculated plasma density around the particle. The calculated produced vapor bubble has dimensions D$\sim$1.2 μm, as shown in figure 2.19a and b, in agreement with spectroscopic studies. The plasma is shown to be responsible for the initiation of a cavitation process, the energy absorbed in the particle being much too low to increase the water temperature beyond the $0.9T_c$ limit, as shown on figure 2.19b and c. In another study, the particle is further shown experimentally to remain intact following the laser treatment, in agreement with the theory [57]. Similar results have been obtained by Warshavski et al. [257].

Plasma-mediated bubble nucleation is slightly different from heat-mediated bubble nucleation as the energy transfer is much faster, in the order of τ_{ei} $\approx$1-3 ps. The heat transfer is so fast that water undergoes a quasi-isochoric transition, as observed by Boulais et al. [70], yielding high pressure that results in the propagation of intense pressure wave in the medium, as shown in figure 2.18d, e and f. Note the order of magnitude of the calculated pressure, which is much higher than the one calculated by Volkov et al. [235] in the case of heat-mediated bubble formation. Boulais et al. observed the initial formation of the vapor bubble occuring in the supercritical conditions, without penetrating the phase coexistence region (see figure 2.19c).

In analogy with the theory of laser ablation of solid targets [160, 173, 258–260], this is much similar to the trivial fragmentation mechanism discussed in section 2.6.3. However, the strain rate associated to the ultrafast processes being very large, it is also possible that the nucleation occurs in non-equilibrium states, as observed by Lorazo et al. [160] in the case of liquid silicon. Depending on the laser fluence and pulse width, initial bubble formation may alternatively

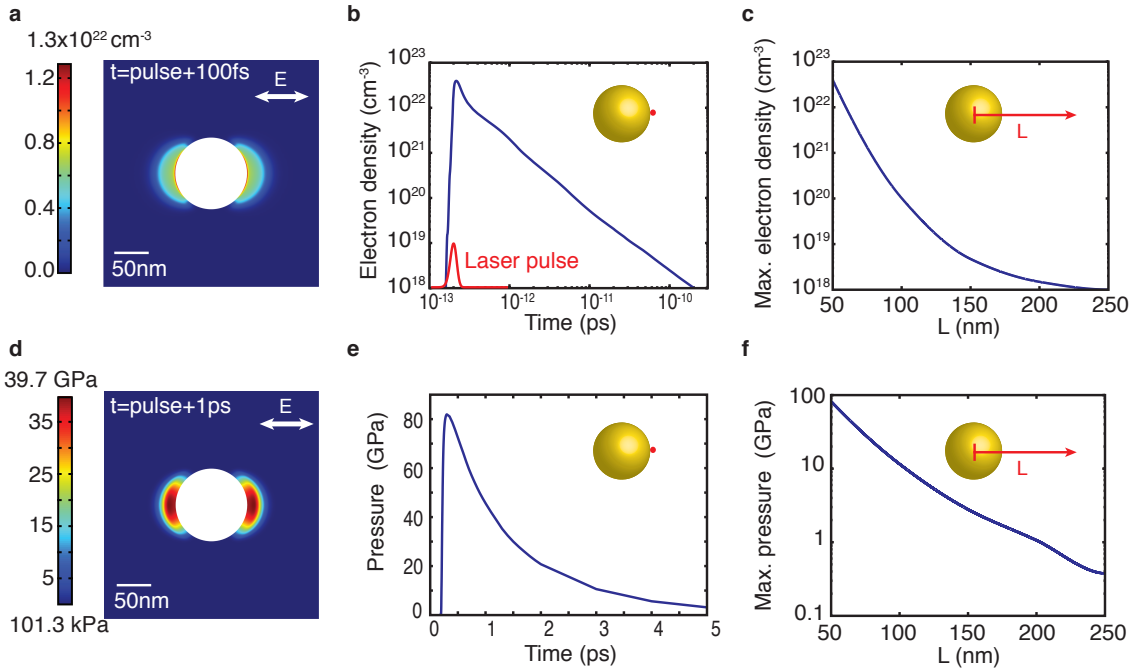

Figure 2.18 Characterization of the plasma density and pressure distribution around a 100 nm NP after a 200 mJ/cm^2, 45 fs, 800 nm laser irradiation. Polarization of the laser is horizontal and the propagation vector is perpendicular to the plane of the figure. The pulse is a gaussian centred at time=200 fs. a. Cross-section of the plasma distribution 100 fs after the pulse maximum. Incident field is perpendicular to the plane of the figure. b. Time evolution of the plasma density at the pole of the NP corresponding to the highest point of the plasma density. Red line shows the laser pulse. c. Reached maximum plasma density as a function of distance from the nanosphere. d. Cross-section of the pressure distribution 1 ps after the pulse maximum. Incident field is perpendicular to the plane of the figure. e. Time evolution of the pressure distribution at the pole of the NP corresponding to the pressure highest point. f. Reached maximum pressure as a function of distance from the nanosphere. Taken from [70].

occur through explosive boiling in the metastable region. The exact mechanism leading to the ultrafast laser plasma-mediated bubble formation remains unclear in the literature.

2.7.5 Melting and fragmentation of the nanostructure

As in the case of short pulse interaction, melting and fragmentation of the NPs may occur for irradiation with sufficient fluences. The ultrashort nature of the laser pulse however introduces some particularity, and the apparition of new mechanisms.

For example, Link et al. observed much lower melting threshold (in the order of 100X) for AuNRs using fs pulses than ns pulses [203, 204, 261]. They also showed that the range of fluence where only melting of the NRs occurred without fragmentation was much larger for fs

pulses than for ns pulses. This behavior is attributed to the short electron-phonon coupling time. Plech et al. [211] also determined a very low surface melting temperature of $104°C$ under fs excitation. Link et al. [262] showed that the melting process of a AuNR occurred in 30-35 ps, independently of the power used or the aspect ratio of the NRs.

Non-thermal channels of material modification, such as the Coulomb explosion, are expected to become more important in the fs regime. Werner et al. [263] indeed presented fs transient absorption experiments that provided direct spectroscopic observation of fragmentation at time scale within 100 ps, due this mechanism. The observed threshold fluences for 60 nm AuNPs and 150 fs pulses were 7.3 mJ/cm^2 and 3.6 mJ/cm^2 for 400 nm and 532 nm irradiation respectively. Note that this is well below the bubble formation threshold reported by Plech et al., shown in figure 2.14, for similar experimental conditions (400 nm, 100 fs). Werner et al. attributed the onset of the Coulomb explosion to the ejection of electrons from thermionic emission due to the very high temperature reached by the electrons in the fs irradiation regime. Fragmentation then occurs because of the Rayleigh instability [264]. They suggested $T_e \approx$ 7260-7640 K as the electronic temperature threshold required for the Coulomb explosion to occur for 60 nm AuNPs.

Plech et al. [126] also observed mass removal from the poles of a 38 nm AuNP irradiated with 100 fs, 400 nm ultrashort laser pulses for fluences well below the melting threshold and temperatures an order of magnitude below the explosive boiling threshold. They associated the result to non-thermal material ejection due to the near-field enhancement at the pole of the NP.

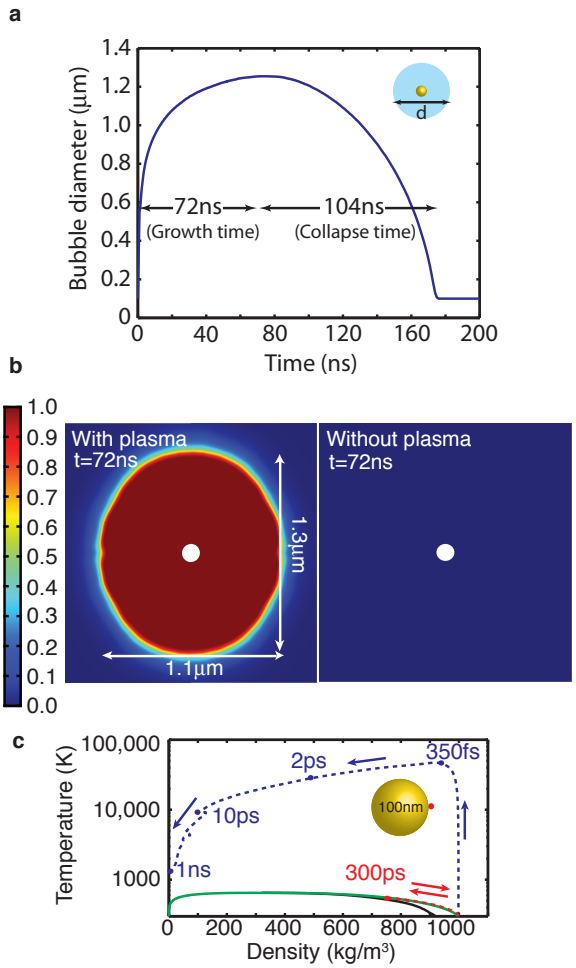

Figure 2.19 Generation of a vapor nanobubble around a 100 nm NP after a 200 mJ/cm^2, 45 fs, 800 nm laser irradiation. a. Time evolution of the average diameter of the vapor bubble created around the NP after the irradiation. b. The left panel shows the vapor bubble around the NP 72 ns after the irradiation. The bubble is at its maximal extension. Dryness fraction is represented on the figure. The bubble boundary is fixed at a 10% dryness fraction. The right panel presents the bubble obtained when the contribution from the plasma is neglected. c. Phase space trajectory of water situated near the pole of the NP during the first ns following the irradiation. Green line is the binodal curve, black line is the kinetic spinodal, red line is the trajectory when no plasma is present and blue curve is the trajectory including the plasma contribution. The trajectory when no plasma is present is along the binodal curve and reaches its maximal temperature 300*ps* after the laser pulse. Taken from [70]

2.8 Plasmonic enhanced pulsed-laser cell nanosurgery

The last sections reviewed quite extensively the phenomena that occur following the pulsed-laser irradiation of plasmonic nanostructures in water. A cellular environment is considered as being similar enough to water to assume that the basic mechanisms, theoretical and experimental results obtained in a water environment will stay approximately the same.
Many physical processes described above can lead to molecular and cell damaging in a cellular environment. For instance, temperature increase around the particle may induce protein denaturation [158, 265] and prolonged exposition to moderately high temperature may induce cell death, a process known as hyperthermia [21, 22, 27]. Low-density electronic plasma generation in the medium is associated with chemical damage to molecules [72]. Finally, vapor bubbles, pressure wave and fragmentation of the nanostructure are also associated with important damaging effects [158].
One of the principal advantage of the use of AuNPs is the possibility for active targeting, involving the use of peripherally conjugated moieties that specifically bind to particular types of cells and increase their endocytosis during the incubation time that precedes the treatment. This internalization process has proven to be determinant in the efficiency of the laser interaction process. This allows for specific treatment limited to those cells only, hence decreasing the need for costly and complex laser focussing and visualization system required for direct laser targeting. NP targeting strategies is a vast subject beyond the scope of the present paper. The interested reader is referred to reviews by Byrne et al. [56] and Peer et al. [266] for further details.
In the next section we will discuss some of the most promising applications for pulsed laser interaction in cell nanosurgery. Note that this review is not exhaustive and only aims to give the reader a glimpse of the great potential of this technology for therapeutic applications.

2.8.1 Plasmonic photothermal therapy

The use of heat as a method for tumor therapy has a long history and goes back to 1700 B.C. when people was using the hot tip from a firedrill for breast cancer therapy [27]. In the modern days, other means to selectively heat tissues have been introduced, including radiofrequency [268, 269], microwaves [270], ultrasound waves [271] and laser irradiation [272, 273]. While those methods gain a certain success, their application is limited due to the important amount of collateral damage it brings to surrounding tissues. The development of targeted technologies with cellular precision is therefore required.
Plasmonic photothermal therapy uses targeted plasmonic nanostructures to act as localized source of heat to damage and destroy specific cancer cells. Over the years, many groups have

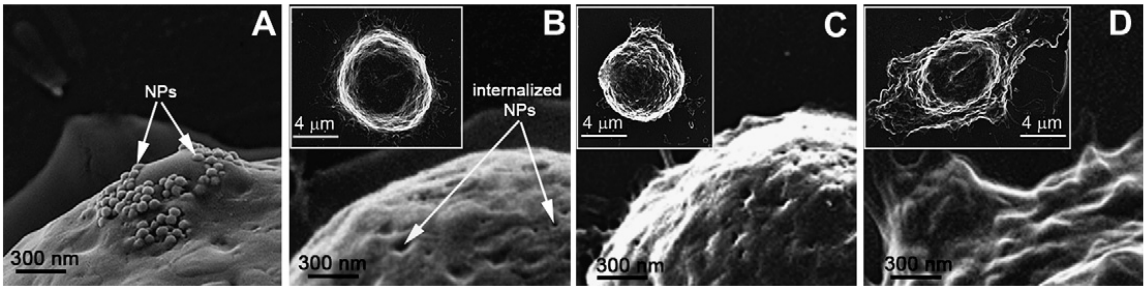

Figure 2.20 Scanning electron microscopy image of prostate cancer cells at different stages. After incubation with gold NPs showing a. membrane coupling and b. internalization c. After irradiation of a single laser pulse yielding c. a non-invasive vapor bubble with a lifetime of 25±5 ns and d. an ablative bubble with a lifetime of 300±42 ns. Images of the whole cell are shown in inset of b, c and d. Taken from [267].

demonstrated, both *in vivo* and *in vitro*, the destruction of cancer cells and the ablation of tumours using continuous wave laser with AuNPs [26], core-shell structures [28–30] and AuNRs [24]. The use of core-shell structures and AuNRs are particularly interesting has their plasmon band lies in the NIR where tissues are less absorbent [82], reducing collateral damages and enabling deeper tissue treatment (up to 10 cm for breast tissue). With continuous wave laser, cell death occurs due to purely thermal damages such as protein denaturation, coagulation and cell membrane destruction [27], following a several minutes irradiation. However, with pulsed irradiation, the formation of vapor bubbles around the nanostructures is thought to be the main source of damage to the cell [90, 274, 275], yielding the possibility for further localization and reducing the treatment time down to a single-pulse event. Representative examples of photothermal applications of plasmonic enhanced pulsed-laser cell nanosurgery are summarized in figure 2.21.

Pitsillides et al. [276] used immunotargeted gold nanospheres with 20 ns, 565 nm laser pulses to induce the death of lymphocytes. Using ∼100 pulses of 500 mJ/cm^2, they showed a lethality for target cell ranging from 54% to 95%. depending on the number of AuNPs per cell, whereas only 2%-8% of the untargeted cells were killed. Nedyalkov et al. [277] demonstrated the use of 40 nm, 100 nm and 200 nm AuNPs using 532 nm, 15 ns laser pulses at fluences in the range 50-100 mJ/cm^2 for photothermal therapy of HeLa cancer cells and showed the fragmentation of the AuNPs in this range of fluences.

Li et al. [278] used 25 nm-50 nm AuNPs conjugated with transferrin molecules for imaging, targeting and therapy of breast cancer cells. 5 min irradiation from a 10 Hz, 530 nm, ns pulsed-laser resulted in significant cellular damage for laser intensity over 7 W/cm^2, which they attributed to thermal energy. They showed a much higher damage threshold for untar-

Application	Laser & Target	Particles	Principle	Comments	Ref.
Photothermal therapy 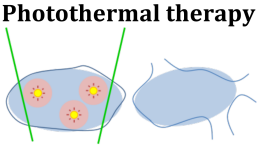	λ=565nm, τ_p=20ns, F=500 mJ/cm² E : ~100 pulses T : Lymphocytes	- 20 and 30nm - AuNPs - Conjugated	- Bubbles	- Lethality : 54%-95%	[275]
	λ=532nm, τ_p=15ns F=50-100mJ/cm² E : 5-40s@10Hz T : HeLa cervical cancer cells	-40,100,200nm - AuNPs - Unconjugated	- Bubbles - High energy fragments - Stress wave - Chemical effects	- NPs fragmentation	[276]
	λ=530nm, τ_p= ns F=700mJ/cm² E : 5min@10Hz T : Breast cancer cell	- 25-50nm - AuNPs - Conjugated	- Thermal energy	- Good efficiency of transferrin-conjugated AuNPs for cancer therapy	[277]
	λ=532nm, τ_p=12ns F=~200mJ/cm² E : 5min@10Hz T : Lymphoblasts	- 2-250nm - AuNPs - Conjugated	- Bubbles	- Greatest efficiency with 10-30nm AuNPs	[278]
	λ=420-570nm, τ_p=12ns F=0.1-5J/cm² E : 100 pulses T : Staph. aureus bacteria	- 10,20,40 nm - AuNPs - Conjugated	- Bubbles	- Killing of bacteria	[273]
	λ=532nm, τ_p=6-7ns F=40-60mJ/cm² E : Single pulse T : HSC-3 oral cancer cells	- 30nm - AuNPs - Conjugated	- Bubbles - Dissociation of DNA	- Nuclear targeted NPs more efficient than cytoplasm-targeted NPs	[280]
	λ=532nm, τ_p=0.5ns F=175mJ/cm² E : Single pulse T : Prostate cancer cell in zebrafish	- 60nm - AuNPs	- Bubbles -Conjugated	- Theranostic - In-vivo	[281]
	λ=765nm, τ_p=200fs F=~7.5mJ/cm² E : Scan@77MHz T : Malignant KB cells	- 12.6x46.5nm² - AuNRs - Conjugated	- Photothermal degradation of the actin network	- Higher efficiency of membrane-bound NRs	[91]
	λ=800nm, femtosecond F=~5mJ/cm² E : Scan@80MHz T : HeLa cervical cancer cells	- Size not given - AuNRs - Conjugated	- Photothermal	- Better efficiency for circular polarization	[58]
	λ=800nm, τ_p= 100fs F=0.1-1mJ/cm² E=2 min@1KHz T : HSC-3 oral cancer cells	- 30nm - AuNPs - Conjugated	- 2-photons absorption - 2nd harmonic generation	- NIR process	[57]

Figure 2.21 Representative examples of photothermal applications of plasmonic enhanced pulsed-laser cell nanosurgery. In the Laser & Target boxes, λ is the laser wavelength, τ_p is the pulse duration, F is the fluence of a single laser pulse, E is the pulse exposure and T is the targeted cell.

geted NPs (14 W/cm^2), with a cellular uptake of ∼25% the one of targeted NPs. The damage threshold when no NPs were present was around 1600 W/cm^2.

Zharov et al. [279] used 532 nm, 12 ns laser pulses with various size of AuNPs for the thermolysis of lymphoblasts. They found the greatest kill efficiency with 10-30 nm AuNPs for ≈200 mJ/cm^2 irradiation. This is consistent with theoretical results from Baffou et al. [280] that predicted an optimal 40 nm diameter to maximize the temperature increase for irradiated AuNPs.

Using optical *in situ* probing technique Zharov et al. then showed a significant correlation between bubble formation and cell damage induced by the particle. They also determined an optimal incubation time of ≈ 15 h. They used a similar system for demonstrating the killing of Staphylococcus aureus bacteria [274].

Huang et al. [281] also presented an interesting study showing that nuclear-targeted NPs were more effective than cytoplasm-targeted NPs for ns pulse laser phototherapy of HSC-3 oral cancer cells.

Finally, Wagner et al. [267] demonstrated the use of anti-EFGR targeted 60 nm AuNPs with 0.5 ns, 532 nm to ablate *in vivo* human prostate cancer cells transplanted into zebrafish. They also introduced the theranostic technique consisting in a two-pulse process that first generates a non-invasive vapor bubble to detect the cancer cells through optical scattering, followed by a second larger ablative bubble that aim to destroy the cell. The paper also presents SEM imaging of cancer cells targeted with AuNPs, showing their membrane coupling and internalization. SEM imaging of the consequence of the non-invasive and of the ablative bubble on the cell's morphology is also presented. Those pictures are reproduced in figure 2.20.

Although Wagner et al. [267] demonstrated the *in vivo* implementation of the technique in small living organisms, *in vivo* application of the work presented above is limited by the visible wavelength used that is heavily absorbed by the living tissues. NIR irradiation would be much preferable to allow deeper penetration into biological tissues. Tong et al. [91] thus used folate-conjugated AuNRs targeted toward the plasma membrane of malignant KB cells with fs-laser irradiation to induce cell death. Monitoring of the internalization process shows the KB cells heavily coated with targeted NRs after 6h incubation and a slow migration of the NRs toward the perinuclear region after 17 h. Their results showed an increased efficiency of the fs-laser photothermal process when compared to continuous laser, and attribute the cell membrane blebbing to the degradation of the intracellular actin network. They also demonstrated the higher efficiency of membrane-bound NRs compared to internalized NRs, in opposition to the result obtained by Huang et al. [281] for ns pulses. NIR fs-laser induced photothermal ablation of human cervical cancer cell (HeLa) with transferrin-conjugated

AuNRs is also presented by Li et al. [59] and shows a better efficiency for circularly polarized compared to linearly polarized light.
Finally, Huang et al. [58] showed the use of 0.1-1 mJ/cm^2, 800 nm fs-laser pulses at 1 KHz to irradiate off-resonance anti-EGFR conjugated AuNPs during 2 minutes (total fluence of 15-150 Jcm^2) to realize photothermal ablation of HSC-3 oral cancer cells. Since the absorption of AuNPs is very low at 800 nm, they attribute the effect to either a two-photon absorption within the particle, or to secondary absorption of photons issued from plasmonic enhanced second harmonic generation. This hypothesis is supported by the squared dependence of the number of dead cells on the incident laser power.

2.8.2 Molecular surgery

In addition to killing cells, plasmonic NPs also brings the possibility to selectively damage individual molecules. There are many source of possible damage at the molecular level. Heating of the surrounding of a NP may lead to the breakdown of the protein's structure, a process known as thermal denaturation [158, 265]. Vogel et al. [72] also reported the possible chemical breaking of biomolecules by the quasi-free electrons of the plasma that can be generated around laser-excited NPs. Capture of low-energy electrons may indeed induce damage to molecules and initiate their fragmentation [282–284]. Mechanisms of molecule breaking by free electrons are however beyond the scope of this review and the interested reader is referred to the above-cited literature for further details.
Reports on plasmon-enhanced damage to specific molecules are rather sparse. Representative examples of molecular surgery applications of plasmonic enhanced pulsed-laser cell nanosurgery are summarized in figure 2.23. Pitsillides et al. [276] reported the successful inactivation of the anti-fluorescein rabbit IgG protein by 20 nm AuNPs irradiated with 200 mJ/cm^2, 532 nm, 20 ns pulses. Their results showed that direct conjugation of the protein on the NP yields a complete inactivation of the protein, whereas significantly less inactivation ($\sim$10%) is obtained when the protein is prevented from associating directly with the NP. This demonstrates the very short range at which the inactivation is possible and the degree of localization of the process. Hüttmann et al. [285] also reported the inactivation of alkaline phosphatase protein conjugated to 15 nm gold NPs and irradiated with $\sim 10^4$ pulses (50 mJ/cm^2, 35 ps) from a 527 nm laser. They evaluated a damage range below 10 nm.
Csaki et al. [60] targeted certain DNA sequences along chromosomes with $\approx$60 nm gold-silver coreshell structures. Following a fs-laser irradiation, high-resolution imaging confirms that targeted regions of the DNA sequences were transformed into nanoscale cavities of sub wavelength dimensions, extending over several tens of nanometers, as shown on figure 2.22.
Single molecule manipulation is the last frontier of nanotechnology. Much work is required to

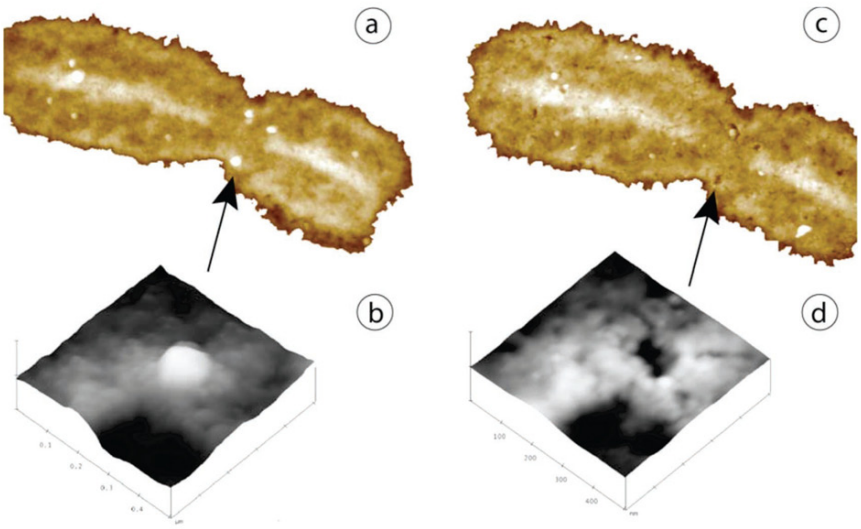

Figure 2.22 Highly localized energy conversion at sequence-specific bound NPs on metaphase chromosomes. AFM images : overviews (a,c) and 500nm×500 nm zooms (b,d) of the marked regions. Particles targeting certain DNA sequences on a chromosome before (a,b) and after (c,d) laser irradiation. The irradiation results in a disappearance of the particles in the AFM image and the formation of nanocavities at these locations (cf. d). Taken from [60].

develop this exciting field that brings interesting possibilites for both therapeutic applications and fundamental science.

2.8.3 Cell membrane optoporation and transfection

The concept behind cell membrane optoporation is very similar to photothermal therapy and is presented in figure 2.24. Laser irradiation of membrane-bound and internalized nanostructures are used to open transient pores in the membrane that allow molecular transport into the cytoplasm. The laser parameters must be adjusted to create pores that do not compromise the cell viability and from which the cell can recover. This method is used to make different molecules, such as DNA, RNA and drugs, cross the membrane barrier and is a promising tool for gene therapy and cancer treatment. Representative examples of cell membrane optoporation and transfection applications of plasmonic enhanced pulsed-laser cell nanosurgery are summarized in figure 2.23.
Laser cell transfection (without NPs) has been introduced by Tsukokachi et al. [286] in a paper presenting the transfection of normal rat kidney cells with 355 nm, 5 ns pulses from a Nd :YAG laser. This paper has been followed by many other authors that demonstrated the use of laser pulses to induce transfection of various cell types [54, 55, 72, 157, 287–293].

Application	Laser & Target	Particles	Principle	Comments	Ref.
Molecular nanosurgery 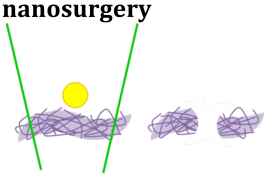	λ=532nm, τ_p=20ns F= 200mJ/cm² E : 1-100 pulses T : IgG proteins	- 20nm - AuNPs - Conjugated	- Thermal	- Short range	[275]
	λ=527nm, , τ_p=35ps, F=50mJ/cm² E : ~10^4 pulses T : alkaline phosphatase	- 15nm - AuNPs - Conjugated	- Thermal - Photochemical	- Damage range below 10nm	[285]
	λ=800nm, , τ_p=fs F=20-30μJ/cm² E : Unknown T : DNA sequences	- 60nm - AuAg coreshell - Conjugated	- 2-photons absorption	- ~10nm cavities	[59]
Cell membrane optoporation and transfection 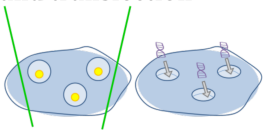	λ=532nm, τ_p=20ns, F= 500mJ/cm² E : ~100 pulses T : Lymphocytes	- 20nm - AuNPs - Conjugated	- Bubbles	- Membrane recovers in 2min - Uptake of 10-kDa FITC-D	[275]
	λ=532nm, τ_p=6ns, F= 500mJ/cm² E : 1-50 pulses T : Hodgkin's disease and lymphoma cells	- 15,30nm - AuNPs - Conjugated	- Bubbles	8-68% efficiency	[294]
	λ=532nm, τ_p=0.5ns, F=110-150mJ/cm² E : Single pulse T : Various	- Size not given - AuNPs clusters	- Bubbles	- Transfection of DNA plasmids - ~70% efficiency	[295]
	λ=760nm, femtosecond F=18mJ/cm² E : 10s@80MHz T : epithelial breast cancer cells	- 80nm - AuNPs - Conjugated	- Low-density plasma	- Uptake of 10-kDa FITC-D	[296]
	λ=800nm, , τ_p=45fs, F=100mJ/cm² E : 10s@80MHz T : melanoma cells	-100nm - AuNPs - Unconjugated	- Plasma-mediated bubbles	- ~70% optoporation efficiency - Transfection of YFP-SMAD2 plasmids - ~25% transfection efficiency	[56]
Drug delivery 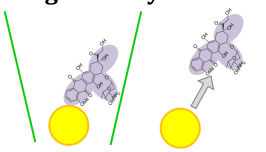	λ=532nm, τ_p=0.5ns, F= 0.01-1J/cm² E : Single pulse T : Liposome	- 80nm - AuNPs - Unconjugated	- Bubbles	- Disruption of liposomes to release cargo	[299]
	λ=820nm, τ_p=70ps, F= 15-25mJ/cm² E : Single pulse T : DOX	- 50nm - AuNSs clusters	- Bubbles	-Single pulse - Release DOX in HN31 carcinoma cancer cells breaking endosome - 31-fold increase of therapeutic efficacy	[300]
	λ=800-1100nm, τ_p=100fs, F= ~1.7mJ/cm² E : -60s@1KHz T : DNA	-11x44nm² and 17x89nm² - AuNRs	- Particle melting	- Selective melting - Release of DNA	[301]
	λ=527nm, τ_p=250ns, F= ~40-200mJ/cm² E : 2s-30s@1kHz T : DNA	- 41nm - AuNPs	- Particle melting	- Selective melting	[302]
	λ=800nm, τ_p=130fs, F= ~3.5-20.4mJ/cm² E : 2s@1KHz T : DNA	- 40nm - AuNS	- Hot electron and bond vibration	- Release siRNA and disrupt the endosome	[304]
	λ=730–820nm, τ_p=6.5ns, F= ~1-4mJ/cm² E : 2min@10Hz T : DNA	- 50nm - Au nanocages	- Temperature increase	- Hydrophopic/ hydrophilic transition	[106]

Figure 2.23 Representative examples of molecular surgery, cell membrane optoporation and transfection and drug delivery applications of plasmonic enhanced pulsed-laser cell nanosurgery. In the Laser & Target boxes, λ is the laser wavelength, τ_p is the pulse duration, F is the fluence of a single laser pulse and E is the pulse exposure. In the case of cell membrane optoporation and transfection, T is the targeted cell, while in the case of drug delivery and molecular surgery T is respectively the cargo and the targeted molecule.

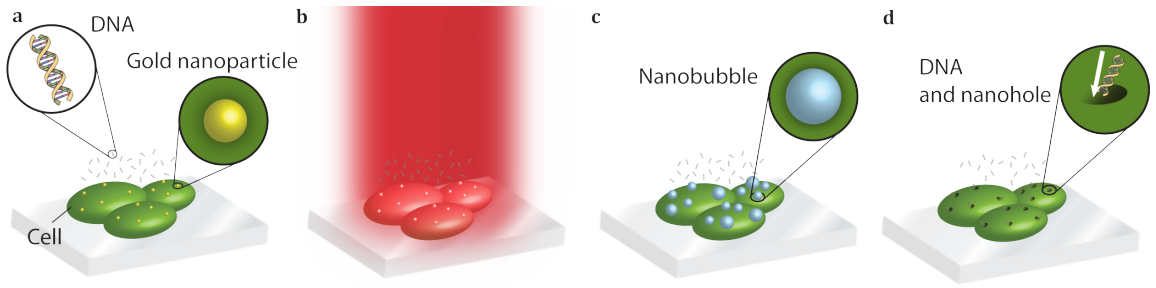

Figure 2.24 Principle of plasmonic cell transfection. a. Targeted plasmonic nanostructures are incubated with cells and are membrane-bound and internalized. Molecules (such as exogenous DNA, RNA and drugs) are added to the cell sample but are not incorporated due to the cell membrane barrier. b. The NPs are irradiated. c. A series of phenomena including heat transfer and bubble formation around the particles occur. d. This leads to the formation or transient nanoscale pores in the membrane, which allow the incorporation of exogenous DNA, RNA or drugs.

However, laser cell transfection implies a sequential treatment in which each cell must be treated separately by a tightly focused laser. That brings major issues concerning both the high-speed transfection of large population of cells *in vitro*, and more importantly, the *in vivo* application of the technique. The use of nano absorbers such as plasmonic NPs that can target specific cells and locally enhance the impact of the laser irradiation brings an elegant solution to the problematic.

Pitsillides et al. [276] achieved permeabilization of the cell membrane of lymphocytes cell by irradiating 20 nm AuNPs with 20 ns, 500 mJ/cm^2 pulses from a 532 nm laser. Their results showed the uptake of 10-kDa fluorescein-dextran conjugates (FITC-D), a membrane-impermeable probe, and suggested that the plasma membrane recovers within 2 min after irradiation. Yao et al. [294] presented a similar experiment, where 10-kDa FITC-D are transfected in Hodgkin's disease and lymphoma cells using 6 ns, 532 nm laser pulses with 15 nm and 30 nm AuNPs. They showed a 8%-68% transfection efficiency depending on the diameter of the AuNPs (15 nm or 30 nm), their conjugation, the laser parameters and the cell line. Both studies associated the permeabilization mechanism to the formation of cavitation bubbles due to the laser-NP interaction.

Recently Lukianova-Hleb et al. [295] reported the use of internalized clusters of AuNPs with a single 110-150 mJ/cm^2, 532 nm, 0.5 ns pulse for the transfection of DNA plasmids in various cell types with high efficacy (∼70% after 48 h), selectivity (∼100%) and cell viability (∼80%).

However, as it was the case for plasmonic photothermal therapy, application of the work

presented above is limited *in vivo* by the visible wavelength used that is heavily absorbed by the living tissues [82]. NIR irradiation would be much preferable to allow deeper penetration into biological tissues. Ben-Yakar et al. [296] shortly reported the use of 80 nm targeted AuNPs irradiated with 18 mJ/cm^2, 760 nm, fs pulses at 80 MHz to induce the uptake of 10-kDa FITC-D in epithelial breast cancer cells. The membrane disruption is attributed to the formation of a low-density plasma in the particle enhanced near-field. Following preliminary studies by Schomaker et al. [297, 298], Baumgart et al. [57] reported the transfection of cancer melanoma cells with YFP-SMAD2 cDNA plasmids using 100 mJ/cm^2, 800 nm, 45 fs, 1 KHz laser pulses. They reported a ∼70% perforation efficiency, an ∼80% cell viability and a 25% transfection efficiency, three times higher than what they obtained using a standard lipofectamine transfection technique on the same cell line (see figure 2.25). Baumgart et al. attributed the membrane disruption to the formation of an electronic plasma in the near-field of the NPs and to the cavitation bubble formation resulting from its relaxation. In a recent study, Boulais et al. presented a complete model and spectroscopic study of the fs laser-NP interaction in water that confirms this mechanism [70]. Spectroscopic studies demonstrated that the particles are not damaged by the treatment.

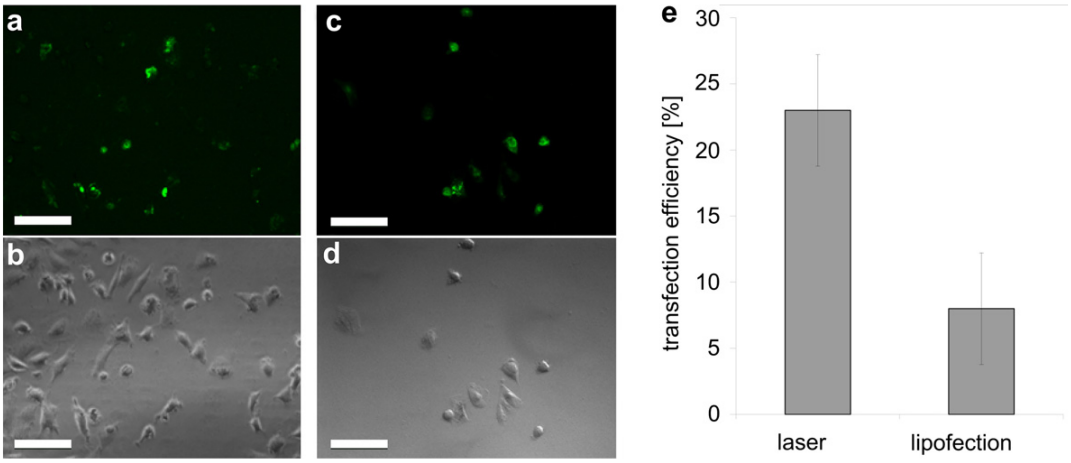

Figure 2.25 Comparison of transfected cells with YFP-SMAD2 cDNA plasmid : fs laser plasmonic enhanced transfection and lipofection. a. Fluorescence and b. phase contrast image of cells transfected by plasmonic enhanced fs laser pulses ; c. fluorescence and d. differential interference contrast (DIC) image of cells transfected by Lipofectamine. Scale bars : 100 mm. e.Transfection efficiency of the laser based transfection method and lipofection. Error bars represent standard deviation ; n≥3. Taken from [57].

2.8.4 Drug delivery

Plasmonic nanostructures can also be used as vectors allowing the controlled release of specific cargo molecules. Representative examples of drug delivery applications of plasmonic enhanced pulsed-laser cell nanosurgery are summarized in figure 2.23.

Anderson et al. [299] loaded liposomes with fluorescent proteins and plasmonic NPs. Irradiation of the liposome with ns laser pulses created bubbles around the NPs that broke the liposome and ejected its content. Lukianova-Hleb et al. used the same principle to release encapsulated doxorubicin (DOX), a well known drug used in cancer chemotherapy, into the cytoplasm of cancer cells [300]. The encapsulated drugs and AuNSs are targeted separately to the cancer cells and are internalized. In targeted cancer cells, endosomes containing both clustered AuNPs and encapsulated DOX will form. Irradiation of the clustered AuNPs with short laser pulses forms cavitation bubble that breaks both the DOX capsule and the endosome membrane, releasing the drug into the cell. The authors showed a 31-fold increase of the therapeutic efficacy, along with significant reduction of the drug dose, treatment time and non-specific toxicity when compared to standard treatment.

Other works focused on the release of cargo directly attached on the nanostructure. Wijaya et al. [301] showed the release of DNA oligonucleotides from AuNRs due to their selective melting using ultrafast irradiation. DNA molecules were loaded on two types of AuNRs with different aspect ratio using thiol conjugation. The laser wavelength could be tuned to the plasmon resonance of a certain type of NRs and thus release only specific cargo. A similar process has been recently published by Thibaudau et al. [302] using AuNPs instead, with 250 ns laser pulses. Jain et al. [303] studied the mechanisms of gold-sulfur bond resulting from fs laser heating . They concluded that the bond dissociation mechanism involved the coupling between the photoexcited hot electrons and the gold-sulfur bond vibrations rather than a conventional heating process.

Braun et al. [304] used a similar principle and used ≈40 nm hollow AuNSs thiol bounded with si-RNA conjugates to silence specific genes in cells. The NS is further coated with a Tat-lipid conjugate that facilitates the delivery of the assembly into the cell. A 800 nm fs laser is then used to release the si-RNA from the NS and to disrupt the endosome in which the nanostructure was placed following the initial uptake, yielding efficient gene silencing.

Finally, an interesting work from Yavuz et al. [106] used Au nanocages coated with polymers that go from a hydrophilic to a hydrophobic state when the temperature is increased beyond $32°C$. The nanocage itself is permeable to the cargo molecules and become impermeable only if the coating polymer is in its hydrophilic state. Heating of the assembly with a pulsed NIR laser thus allows controlling the permeability of the system and the controlled release of the cargo.

2.9 Conclusion

In summary, this paper reviewed the basic theory of nanoplasmonics, i.e. the interaction of nanoscale metallic structures with light. The excitation of collective oscillations of electrons in those particles, called plasmon, has been shown to have profound impacts on their optical properties. In particular, strong absorption and scattering occur at a particular irradiation wavelength corresponding to the plasmon resonance. Size and shape dependence of the optical properties of nanostructures have also been discussed.

We then reviewed the different relaxation channels of the plasmon oscillation and the basic theory of short and ultrashort laser pulses with plasmonic nanostructures in water. We showed that irradiating plasmonic nanostructures with high intensity lasers have important consequences on both the NP (heating, lattice expansion, melting, fragmentation,...) and its environment (heating, pressure wave release, vapor bubble formation,...). The importance and specific mechanisms leading to those different phenomena have been shown to strongly depend on the pulse time-width. In particular, we showed that important non-linear effects might arise in the near-field of plasmonic NPs following ultrashort pulses irradiation.

Finally, we reviewed a series of technologies that use the different phenomena triggered by pulsed laser irradiation of nanostructure to damage, destroy, or transiently modify the properties of cells, sub-cellular, molecular and even sub-molecular structures. Those technologies have been showed to find applications in a wide range of field, from cancer therapeutics to fundamental biology.

With the rapidly developing field of nanoplasmonics that introduces new nano systems with unsuspected optical properties at a fast pace, plasmonic nanostructures will beyond any doubt continue to offer new ways and means to control light for the diagnostic and therapy of diseases, and this for many years to come.

Acknowledgement

The authors would like to thank the National Science and Engineering Research Council (NSERC) as well as the Fond Québécois de Recherche en Nature et Technologie (FQRNT) for funding. Fruitful discussions with J. Baumgart, B. St-Louis-Lalonde, Eric Bergeron, Andréanne Bolduc and J.-J. Lebrun are also acknowledged.

CHAPITRE 3

Description du Modèle

3.1 Introduction

Tel que vu au chapitre précédent, l'irradiation laser d'une nanostructure plasmonique en milieu cellulaire est le point de départ d'une série de phénomènes susceptibles d'affecter les structures cellulaires et sub-cellulaires de la cellule. Les travaux de recherche menés en laboratoire concernent principalement l'utilisation de ces dommages afin de d'induire la perméabilisation transitoire des membranes cellulaires pour incorporer du matériel génétique exogène (ADN, ARN) aux cellules dans le cadre de thérapies géniques. Cependant, de nombreuses autres applications sont possibles et ont été rapidement revues à la section 2.8.
La suite de la thèse s'intéressera uniquement à l'utilisation de lasers ultrarapides dont la durée d'impulsion est beaucoup plus courte que le temps de couplage electrons-ions τ_{ei} ≈1-3 ps [127, 129, 141, 142]. Les travaux de simulation concerneront plus spécifiquement aux impulsions lasers de 45 fs à une longueur d'onde de 800 nm qui se comparent aux impulsions obtenues avec le système laser disponible en laboratoire qui est utilisé pour la validation du modèle et les traitements cellulaires (Système laser Spitfire de Spectra-Physics, temps d'impulsion : 45 fs, énergie par impulsion : 6 mJ, longueur d'onde d'irradiation : 800 nm).
Bien que l'on cherche à modéliser des processus ayant lieu dans un milieu biologique à proximité d'une membrane cellulaire, nous modéliserons l'interaction d'un laser ultrarapide avec une nanostructure plasmonique en milieu aqueux. La principale motivation de cette simplification provient de la relativement bonne connaissance des caractéristiques physiques et thermodynamiques des milieux aqueux. De plus, des expériences ont démontré la similarité des milieux aqueux et des milieux biologiques dans le cadre de travaux portant sur l'interaction de milieux biologiques avec des faisceaux lasers ultrarapides [72]. Conséquemment, l'utilisation de l'eau comme environnement pour les nanostructures semble être un compromis acceptable.
Les principaux événements survenant suite à l'irradiation d'une nanostructure plasmonique en milieu aqueux avec une impulsion laser ultrabrève ainsi que les échelles de temps auxquels ils surviennent sont présentés à la figure 3.1. Comme indiqué sur cette figure, l'irradiation laser excite un plasmon, c'est-à-dire une oscillation collective des électrons qui amplifie localement le champ électrique, dans le champ proche près des pôles de la particule. Tel que discuté à la section 2.5.1, le plasmon se désexcite avec un temps caractéristique ≈1-10 fs

en émettant des photons (processus radiatif), en créant des paires électrons-trous nonthermiques dans la nanostructure (processus non-radiatif), et en ionisant les molécules situées dans le champ proche par une combinaison de photoionisation et d'ionisation par impact. Notez que la présence du plasma dans le milieu modifie localement sa fonction diélectrique, et conséquemment la distribution de champ et les propriétés d'absorption et de diffusion de la particule plasmonique.

Suite à la désexcitation du plasmon, on peut diviser les processus en deux selon le milieu dans lequel ils se produisent.

Dans la nanostructure, la population d'électrons nonthermiques atteint un équilibre thermique (i.e. est représentée par une distribution de Fermi-Dirac) dans un temps caractéristique ≈500 fs [75, 127, 129, 140]. Les électrons transfèrent par la suite leur énergie aux phonons (réseau atomique) avec un temps caractéristique ≈1-3 ps [127, 129, 141, 142]. Les électrons très énergétiques peuvent aussi être émis directement dans le milieu par un processus photothermique, participant à la génération du plasma. Bien que le transfert d'énergie aux phonons de la particule s'effectue assez rapidement, l'énergie accumulée dans la particule prendra plusieurs nanosecondes à se dissiper dans le milieu. Tel que vu à la section 2.7, la température élevée de la particule peut provoquer son expansion, sa fusion et même sa fragmentation. En particulier, nous avons montré à la section 2.7.2 qu'un chauffage rapide de la particule provoque l'excitation de modes d'oscillations rapides caractérisés par une période de l'ordre de 10 ps.

Dans le milieu environnant la nanoparticule, le plasma électronique excité dans le champ proche diffuse, collisionne avec les molécules d'eau et se désexcite, transférant son énergie aux molécules d'eau dans un temps caractéristique qui dépend fortement de sa densité (≈ 500 fs pour une densité de 10^{21}cm^{-3} [70]). Les molécules d'eau sont conséquemment chauffées extrêmement rapidement et atteignent un état caractérisé par de très hautes températures et de fortes pressions. En relaxant, cet état génère une importante onde de pression et possiblement entraîne une transition de phase vers un état gazeux et forme une bulle de vapeur nanométrique autour de la NP, un phénomène appelé nanocavitation. Les différents processus de nucléation de bulles dans le cadre de processus ultrarapides ont été discutés en détails à la section 2.7.3. De plus, il est à considérer qu'une partie de l'énergie transférée à l'eau l'est aussi par un processus de conduction au niveau de l'interface nanostructure/eau.

Veuillez noter que dans le domaine de la mécanique des fluides, le terme cavitation est habituellement réservé à la formation de bulle suite à des processus n'impliquant pas de chauffage, mais simplement un changement brusque de pression. C'est par exemple le cas lors de la formation de bulles autour d'une hélice de bateau en mouvement. En comparaison, les processus en jeu lors d'une interaction laser impliquent plutôt à la fois des phénomènes mécaniques et

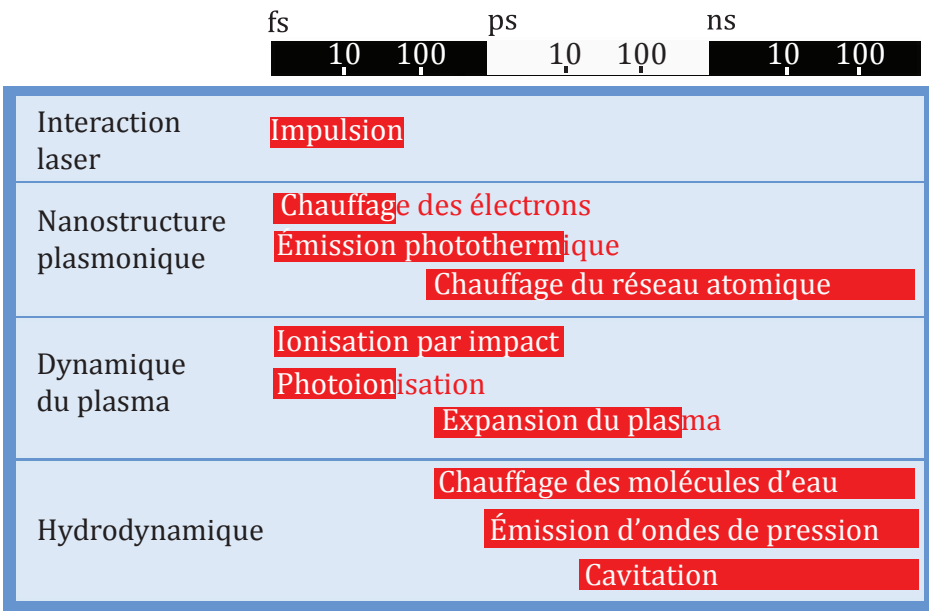

Figure 3.1 Illustration schématique des différents événements découlant de l'interaction d'un laser ultrarapide avec une nanostructure plasmonique en milieu aqueux

thermiques. Le terme cavitation sera tout de même utilisé par souci de simplicité.
Dans le cadre de la nanochirurgie cellulaire, la hausse de température, le choc mécanique provoqué par l'onde de pression, la présence d'électrons énergétiques dans le milieu, ainsi que la présence d'une bulle de cavitation sont autant de causes susceptibles d'endommager de façon importantes les structures biologiques environnantes. Il est donc primordial que le modèle développé puisse décrire correctement la dynamique de ces quatre phénomènes.

3.2 Modèles existants

Les modèles permettant de simuler la réponse complète, incluant les phénomènes de cavitation, de l'interaction d'une nanoparticule plasmonique et d'une impulsion laser ultrabrève sont pour le moment inexistants dans la littérature.
Plusieurs techniques existent pour modéliser la réponse exclusivement optique des nanoparticules. Des méthodes analytiques, basées essentiellement sur la théorie de Mie ou une de ses généralisations, permettent de calculer les distributions de champs autour de nanosphères [67], de structures coeur-couronnes [88], ou d'ellipsoïdes de révolution [96]. Pour ce qui est d'une géométrie d'arbitraire, plusieurs méthodes numériques ont été développées. Parmi les plus populaires citons l'approximation des dipôles discrets (DDA) [93], la méthode des différences finies en domaine temporel (FDTD) [94], et la méthode des éléments finis [95]. Une

revue des différentes techniques est présentée par Kahnert et al. [305].

Plusieurs modèles sont disponibles pour traiter l'évolution thermique d'un matériau suite à une irradiation laser ultrarapide. Des méthodes très complètes basées sur des approches de type dynamique moléculaire (MD) ont été développées [160, 173, 259]. Bien que la plupart des travaux utilisant cette méthode étudie l'ablation de surfaces dans le vide, certains travaux utilisant cette méthode étudient aussi l'ablation de surfaces recouvertes d'une mince couche d'eau [306]. Bien que donnant des bons résultats, ces méthodes sont lourdes et demandent des ressources computationnelles considérables, si bien que seules des structures relativement petites ($\sim 10^5$ atomes) peuvent être simulées. Il est par conséquent impensable d'espérer simuler la cavitation autour des particules de diamètre $\sim$100 nm utilisées pour les expériences ($\sim 10^7$-10^8 atomes, sans compter les molécules d'eau formant la bulle).

Certaines simulations basées sur le modèle deux-températures, introduit à la section 2.7.1, ont été effectuées sur des nanostructures plasmoniques en milieu aqueux. Ekici et al. utilisent un modèle deux-températures pour simuler la réponse thermique d'un nanobâton de 14×48 nm^2 soumis à une impulsion laser de 200 fs à une longueur d'onde de 760 nm [172]. La température du milieu environnant est calculée à l'aide d'une équation de diffusion de la chaleur. Ce modèle décrit bien la température de la nanostructure jusqu'à la cavitation du milieu. L'auteur stipule que la cavitation a lieu lorsque la température du milieu aqueux atteint $0.9T_c$, où T_c est la température critique de l'eau. Par contre, la formation et la dynamique des bulles de cavitation n'est pas décrite par ce modèle. Volokov et al. proposent un modèle semblable, mais en ajoutant une description de l'aspect thermodynamique et dynamique de l'eau qui est modélisé par une équation de diffusion de la chaleur couplée aux équation de Navier-Stokes compressibles ainsi qu'à une équation d'état appropriée [235]. Cependant, aucun de ces travaux ne considère la présence d'absorption non-linéaire et la formation de plasma dans l'eau et traite essentiellement la particule comme un nanoabsorbeur d'énergie.

Des modèles décrivant la formation de plasma par un laser ultrarapide dans des matériaux transparents ont été développés. Vogel et al. ont étudié le phénomène de cavitation subséquent à l'irradiation de l'eau par un laser ultrarapide menant à la formation de plasma dans le cadre d'applications en nanorchirurgie cellulaire [72]. Hallo et al. utilisent une approche semblable pour étudier la formation de cavités dans des matériaux diélectriques [253]. Par contre, aucun de ces modèles n'inclue la présence de nanostructures plasmoniques permettant d'amplifier localement le champ électrique.

Finalement, Bisker et al. proposent un modèle de formation de plasma dans le champ proche de particules nanoplasmoniques suite à une impulsion laser ultrabrève [256]. Cependant, aucune description de l'évolution thermique ou dynamique de l'eau n'est proposée, et la modélisation du chauffage des nanoparticules est grandement simplifiée.

On constate qu'il n'existe pas dans la littérature de modèle satisfaisant intégrant tous les phénomènes engendrés par l'interaction d'un laser ultrarapide avec une nanostructure plasmonique dans un milieu aqueux. Une modélisation mathématique complète du procédé, en permettant la compréhension de ces phénomènes ainsi que la prédiction quantitative de leurs impacts, est nécessaire à un meilleur contrôle et à une optimisation des techniques de nanochirurgie par laser amplifié par nanostructures plasmoniques.

3.3 Description du modèle proposé

Les figures 3.2 et 3.3 illustrent la structure du modèle mathématique proposé. Le modèle complet est divisé en quatre sous-modèles en interaction les uns avec les autres.
Un premier sous-modèle (intitulé "Interaction Électromagnétique" dans la figure 3.2 et correspondant à l'équation 3.2 à la figure 3.3) modélise l'interaction électromagnétique avec le système nanostructure-eau. Ce modèle calcule la distribution du champ électromagnétique $\mathbf{E}$ qui détermine la source d'énergie étant absorbée linéairement et non-linéairement dans la nanostructure et l'eau environnante. La permittivité ϵ_r dépend des propriétés du plasma autour de la nanostructures.
Dans la nanostructure, un sous-modèle modélise à la fois la température électronique T_e et l'évolution en température du réseau T_l (équations 3.3 à 3.6 à la figure 3.3). La chaleur est fournie aux électrons de la nanostructure à partir du terme S_{EM}, lui même calculé à partir de la distribution de champ $\mathbf{E}$. Les températures électroniques et de réseau sont couplées par l'entremise des collisions électron-phonon G.
Dans l'eau, un premier sous-modèle ("Dynamique du plasma") modélise la température et la densité du plasma (équations 3.7 et 3.8 à la figure 3.3). La densité du plasma est généré par les termes de photoionisation (S_{photo}) et ionisation par collision (S_{coll}) qui dépendent tous les deux de $\mathbf{E}$ et sont donc couplés au modèle électromagnétique. Un terme de recombinaison S_{ref} gère la recombinaison du plasma. Le plasma est chauffé par l'impulsion laser (terme S_{EM}), et l'équation de conservation de l'énergie considère le couplage énergétique électrons-molécules (Q_{ei}), les pertes radiatives (Q_{rad}), l'utilisation de l'énergie cinétique pour l'ionisation par collision $\tilde{\Delta}S_{coll}$ ainsi que les pertes dues à la recombinaison des porteurs ($S_{ref}(u/n_e)$). Noter que la présence de plasma modifie l'indice de réfraction locale, ce qui entraîne un couplage bidirectionnel entre le modèle "Dynamique du plasma" et le modèle "Interaction Électromagnétique". Aussi, la génération de plasma due à l'émission photothermique à partir de la nanostructure est introduit au travers des conditions frontières et entraîne un couplage entre le modèle "Dynamique du plasma" et le modèle "2-Température".
Finalement, un dernier sous-modèle calcule la température, la densité ainsi que la vitesse des

molécules d'eau (équation 3.9-3.11 à la figure 3.3). L'équation 3.9 est une équation de conservation de la masse. L'équation de conservation d'énergie (équation 3.10) montre les termes qui fournissent la chaleur aux molécules d'eau : le terme dû au couplage énergétique électron-molécule Q_{ei}, ainsi que le terme dû à la recombinaison du plasma. Il y a par conséquent un couplage évident entre le modèle de dynamique du plasma et le modèle hydrodynamique. Un terme de chauffage par l'entremise de la conduction thermique à partir du réseau de la nanostructure est aussi appliqué sous la forme d'une condition frontière, entraînant un couplage entre le modèle "2-Températures" et le modèle "Hydrodynamique". Les autres termes de l'équation 3.10 décrivent le chauffage par frottement visqueux et la conduction thermique. L'évaluation de la phase et de la pression de l'eau est aussi gérée par ce sous-modèle. L'équation 3.11 est une équation de conservation du moment qui inclue un terme dû à la pression, un terme dû à la tension de surface de la bulle, ainsi qu'un terme dû à la viscosité. La suite de cette section détaille la mise en équation du modèle général et explicite l'ensemble des termes en détaillant chacun des sous-modèles.

3.3.1 Interaction électromagnétique

Plusieurs méthodes existent pour calculer l'interaction électromagnétique. L'une des principales méthodes utilisées dans la littérature est l'approximation des dipôles discrets [93]. Cependant, comme nous avons besoin de calculer le champ proche et non seulement le champ à l'intérieur de la particule, cette méthode perd son intérêt principal. Nous utilisons pour notre part une méthode par éléments finis qui possède l'avantage de donner directement le résultat du champ proche et de bien s'adapter à la simulation de la réponse optique de particules de formes arbitraires. Les calculs sont réalisés à l'aide du code commercial Comsol (www.comsol.com). Une approche de type harmonique est utilisée. Cette approche néglige la transitoire du champ électrique au cours duquel celui-ci n'est pas sinusoïdal. Elle consiste à poser

$$\mathbf{E}\left(\mathbf{x},t\right)=\mathbf{E}\left(\mathbf{x}\right)e^{-i\omega t} \tag{3.1}$$

Les équations de Maxwell pour le champ électromagnétique peuvent alors se réécrire sous la forme de l'équation d'Helmholtz, tel que présenté à l'équation 3.2 à la figure 3.3. Cette équation peut alors être résolue à l'aide de la méthode des éléments finis et on peut reconstruire le champ électromagnétique dépendant du temps en se servant de (3.1). Des conditions frontières parfaitement absorbante (perfectly matched layers ou PML) sont utilisées à la frontière du domaine pour émuler un domaine infini.
La réponse électromagnétique de l'or est modélisée par sa permittivité électrique et sa perméabilité magnétique. Comme les effets magnétiques dans l'or sont très faibles, ceux-ci sont

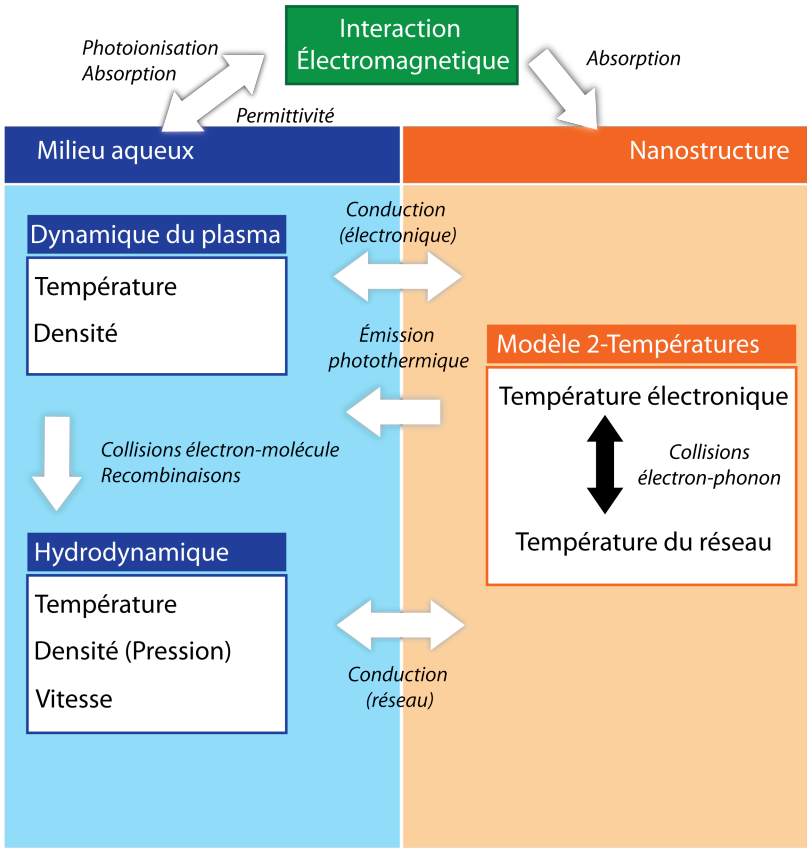

Figure 3.2 Structure du modèle

négligés de sorte que $\mu = \mu_0$. La constante diélectrique de l'or en fonction de la longueur d'onde incidente est tirée de [73]. Cette constante diélectrique ne comprend cependant pas les effets non-linéaires tel l'absorption 2-photons. L'impact de cette absorption n'est habituellement pas considéré dans les modèles d'ablation des métaux. Nous faisons de plus l'hypothèse dans le calcul que l'indice de réfraction n'est pas modifié par la géométrie. Tel que vu à la section 2.4.2, des effets importants de la géométrie sur la réponse optique des matériaux apparait pour des nanoparticules de diamètres inférieurs à 10 nm. Nous nous limiterons à des diamètres supérieurs à cette valeur dans le cadre de cette étude.

Il est à noter que l'équation de Helmholtz est une équation stationnaire et non dépendante du temps. Pour chacun des pas de temps, la distribution du champ électrique dans le système est calculée à partir de l'intensité instantanée de l'onde plane incidente qui est temporellement Gaussienne. La présence du plasma modifie la permittivité locale, et celle-ci est réutilisée à chacun des pas de temps pour calculer une nouvelle distribution de de champ électrique.

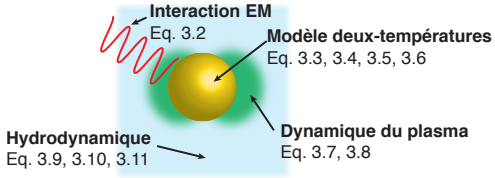

Équation	Variables
Interaction Électromagnétique	
(3.2) $\nabla^2\mathbf{E}+k_0^2\varepsilon_r\mathbf{E}=0$	$\mathbf{E}$: Champ électrique k_0 : Vecteur d'onde ε_r : Permittivité relative complexe
Modèle 2-Températures	
(3.3) $C_e\frac{\partial T_e}{\partial t}+\nabla\cdot\mathbf{q}_e-G(T_e-T_l)+S_{EM}$	G : Couplage électrons-phonons S_{EM} : Taux de travail électromagnétique T_e : Température électronique T_l : Température du réseau $\mathbf{q}_e$: Densité de courant de chaleur él. $\mathbf{q}_l$: Densité de courant de chaleur rés. C_e : Capacité thermique des électrons C_l : Capacité thermique du réseau τ^{Au}_e : Temps de diffusion des électrons τ^{Au}_l : Temps de diffusion des phonons κ_e : Conductivité thermique él. κ_l : Conductivité thermique rés.
(3.4) $\tau_e^{Au}\frac{\partial\mathbf{q}_e}{\partial t}+\mathbf{q}_e=-\kappa_e\nabla T_e$	
(3.5) $C_l\frac{\partial T_l}{\partial t}+\nabla\cdot\mathbf{q}_l=G(T_e-T_l)$	
(3.6) $\tau_l^{Au}\frac{\partial\mathbf{q}_l}{\partial t}+\mathbf{q}_l=-\kappa_l\nabla T_l$	
Dynamique du plasma	
(3.7) $\frac{\partial u}{\partial t}+\nabla\cdot\mathbf{J}^q=S_{EM}-Q_{ei}-Q_{rad}$ $-\tilde{\Delta}S_{coll}-S_{rec}(u/n_e)$	u : Énergie cinétique du plasma n_e : Densité du plasma $\mathbf{J}^n$: Densité de courant électronique $\mathbf{J}^q$: Densité de courant thermique Q_{ei} : Couplage électrons-ions Q_{rad} : Perte énergétique par radiation S_{photo} : Taux de photoionization S_{coll} : Taux d'ionisation par collision S_{rec} : Taux de recombinaison $\tilde{\Delta}$: Potentiel d'ionisation effectif
(3.8) $\frac{\partial n_e}{\partial t}+\nabla\cdot\mathbf{J}^n=S_{photo}+S_{coll}-S_{rec}$	
Hydrodynamique	
(3.9) $\frac{\partial\rho}{\partial t}+\nabla\cdot(\rho\mathbf{v})=0$	ρ : Densité de l'eau $\mathbf{v}$: Vitesse des molécules d'eau T_m : Température de l'eau S : Entropie de l'eau κ : Conductivité thermique de l'eau η : Coefficient de viscosité σ_s : Tension de surface κ_s : Courbure de la bulle δ_s : Distribution de Dirac ayant comme support l'interface de la bulle $\mathbf{n}$: Vecteur unitaire normal à la surface de la bulle. p : Pression
(3.10) $\rho T_m\left(\frac{\partial S}{\partial t}+\mathbf{v}\cdot\nabla S\right)=\nabla\cdot(\kappa\nabla T_m)$ $+\frac{1}{2}\eta\left(\frac{\partial v_i}{\partial x_k}+\frac{\partial v_k}{\partial x_i}-\frac{2}{3}\delta_{ik}\frac{\partial v_l}{\partial x_l}\right)^2$ $+Q_{ei}+S_{rec}(u/n_e)$	
(3.11) $\rho\left(\frac{\partial v_i}{\partial t}+v_k\frac{\partial v_i}{\partial x_k}\right)=-\frac{\partial p}{\partial x_i}+\sigma_s\kappa_s\delta_s\mathbf{n}$ $+\frac{\partial}{\partial x_k}\left[\eta\left(\frac{\partial v_i}{\partial x_k}+\frac{\partial v_k}{\partial x_i}-\frac{2}{3}\delta_{ik}\frac{\partial v_l}{\partial x_l}\right)\right]$	

Figure 3.3 Sommaire de la mise en équation du modèle

L'utilisation de l'équation d'Helmholtz stationnaire fait implicitement l'hypothèse que l'amplification de champ atteint son régime stationnaire beaucoup plus rapidement que le temps d'impulsion. Le temps requis pour atteindre le régime stationnaire est lié au temps de désexcitation du plasmon qui est de l'ordre de 1-10 fs [3]. En particulier, Sönnichsen et al. a mesuré un temps de désexcitation de l'ordre de 1-2 fs pour des particules d'or de 100 nm de diamètre [130]. Ce temps de désexcitation devrait de plus tendre à diminuer pour des impulsions très énergétiques. Il est donc justifié d'utiliser cette approche pour modéliser l'interaction d'impulsions laser ultrabrèves avec des nanostructures plasmoniques.

3.3.2 Description des phénomènes se produisant dans la nanoparticule

Chauffage des électrons et du réseau : le modèle deux températures

Comme mentionné précédemment, un modèle de type deux-températures est utilisé pour calculer l'évolution en température des systèmes de phonons et d'électrons dans la nanostructure. Le modèle général utilisé est un modèle couplé hyperbolique basé sur les équations de transport de Boltzmann. Les équations de base composant ce modèle sont présentées à la figure 3.3 (équations 3.3-3.5). Veuillez noter qu'un tableau résumant les différents paramètres et expressions concernant la modélisation de nanostructures d'or, présentés dans les prochains paragraphes, est disponible à l'annexe A.

Propriétés de transport électronique

Dans l'or, nous utilisons une densité d'état théorique incluant les électrons de la bande $5d^{10}6s^1$. Comme l'étendue des énergies à laquelle cette densité est disponible est limitée, nous avons étendu celle-ci aux plus hautes énergies avec une densité d'état de type électrons libres. La densité d'état de l'or est présentée à la figure 3.4. Une fois cette densité d'état obtenue, il est aisé de calculer la capacité thermique à partir de [308] :

$$C_e = \frac{\partial}{\partial T_e}\left(\int \epsilon f(\epsilon) g(\epsilon) d\epsilon\right) \tag{3.12}$$

Pour ce qui est de la conductivité thermique, celle-ci est évaluée à partir des équations semiclassiques de transport de Boltzmann [308] :

$$\kappa_e = L_{22} - L_{21} L_{11}^{-1} L_{12} \tag{3.13}$$

où les L_{ij} sont les coefficients d'Onsager, qu'on peut trouver dans [308]. Le temps de diffusion

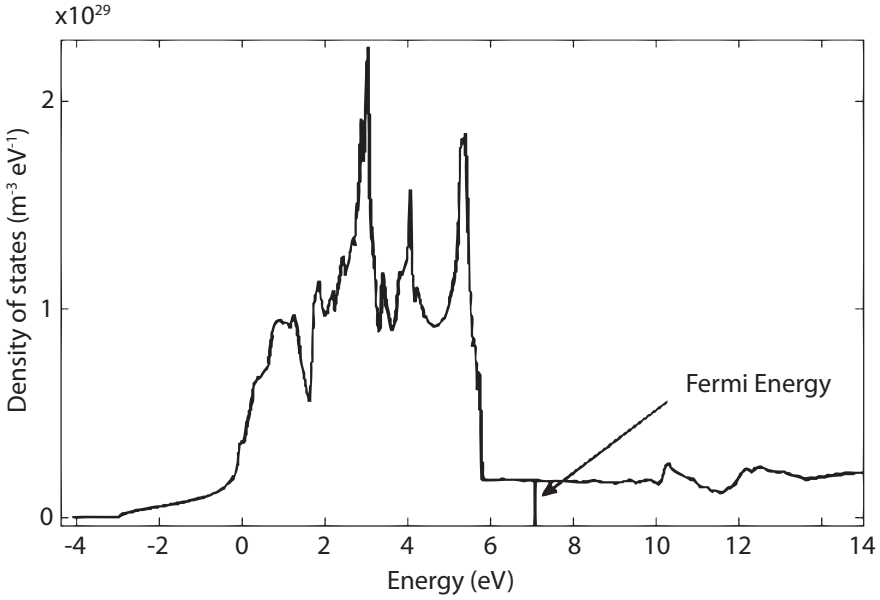

Figure 3.4 Densité d'état des électrons dans l'or massif [307].

des électrons $\tau_e$et des phonons τ_l sont donnés par les expressions suivantes [218, 309] :

$$\tau_e(T_e, T_l) = \frac{1}{1.2 \times 10^7 T_e^2 + 1.23 \times 10^{11} T_l} \tag{3.14a}$$

$$\tau_l = 0.8ps \tag{3.14b}$$

Propriétés de transport du réseau

La capacité thermique C_l du réseau (en J m^{-3}K^{-1}) est donnée par l'expression empirique suivante [172] (sous le seuil de fusion) :

$$C_l = \rho \left(109.579 T_l + 0.128 T_l - 3.4 \times 10^{-4} T_l^2 + 5.24 \times 10^{-7} T_l^3 - 3.93 \times 10^{-10} T_l^4\right) \tag{3.15}$$

Dans cette équation, ρ est la densité de l'or en kg/m^3, T_l est la température du réseau en K. Pour ce qui est de la conductivité thermique du réseau K_l, on utilise l'approximation classique [308] :

$$\kappa_l = \frac{1}{3} v_l^2 \tau_l C_l \tag{3.16}$$

La vitesse du son dans l'or est calculée à partir de la formule :

$$v_l = \sqrt{\frac{E}{\rho^{Au}}} \tag{3.17}$$

où E=42 GPa est le module de Young dans la direction [100], E=81GPa dans la direction [110] [210, 310] et ρ^{Au} =19.3 g/cm^3 est la densité de l'or [172]. On trouve des vitesse de 2050 m/s et 1475 m/s dans les directions [110] et [100] respectivement. On voit que la conductivité thermique du gaz de phonon est très faible, de l'ordre de 1-10 Wm^{-1}K^{-1}, comparativement à celle des électrons qui se situe autour de 300 Wm^{-1}K^{-1}. Pour cette raison, K_l est souvent négligée dans les calculs. Pour notre part, nous ne la négligeons pas, mais nous nous contentons d'une vitesse du son isotrope de 2000 m/s dans les calculs.

Couplage électrons-phonons

L'expression pour le couplage électron-phonon dans l'or est tirée de [220] où on la définit comme :

$$G = G_0 \frac{g_\epsilon}{g^2(\epsilon_f)} \tag{3.18}$$

avec

$$g_\epsilon = \int g^2(\epsilon) \left(-\frac{\partial f}{\partial \epsilon} d\epsilon \right) \tag{3.19}$$

et G_0 =2.5×10^{16} Wm^{-3}K^{-1} [219, 220]. Cette formulation permet de tenir compte de l'effet des bandes d sur le couplage électron-phonon à haute température électronique.

Émission thermoionique et émission photothermique

L'émission thermoïonique est traitée de façon très standard dans le modèle. On évalue premièrement la barrière de potentiel que les électrons de la nanostructure ont à surmonter pour atteindre le plasma situé dans le milieu aqueux. Cette barrière a été déterminée expérimentalement dans [254] comme étant $3.72eV$. La densité de courant d'émission thermoïonique s'écrit alors :

$$\mathbf{J}_0^{th} = AT^2 e^{-\frac{\Phi}{k_b T_e}} \tag{3.20}$$

où Φ est le travail de sortie de l'or dans l'eau et A est la constante de Richardson égale à 120 Acm^{-2}K^{-2}. Afin que ce traitement soit justifié, il faut s'assurer que la quantité d'électrons ayant quitté la nanostructure est négligeable par rapport à la quantité totale d'électrons présents dans celle-ci. Ceci est une des balises qui limite l'étendue de la validité du modèle.
En plus de l'émission thermoionique pure, l'émission photothermique est aussi susceptible

d'émettre des électrons du métal vers le liquide. Ce phénomène est particulièrement important dans le cadre d'une interaction avec un laser ultrarapide en raison de l'intensité des champs électriques impliqués. Le phénomène consiste à considérer l'absorption multiphotonique susceptible de fournir l'énergie nécessaire à un électron du métal pour qu'il soit éjecté de sa surface vers le milieu environnant. Ce mécanisme est décrit par la théorie de Fowler-DuBridge [311]. Noter qu'il faut distinguer ce type de processus d'éjection du processus dit de Fowler-Nordeim où le champ électrique est suffisamment intense pour déformer la barrière de potentiel et permettre aux électrons de la bande de conduction du métal de la traverser par effet tunnel. Le paramètre de Keldysh γ décrit l'importance du processus d'ionisation multiphotonique par rapport au processus d'émission par effet tunnel [312].

$$\gamma = \frac{\omega}{e|\mathbf{E}|}\sqrt{m\Phi} \tag{3.21}$$

Pour $\gamma \gg 1$, l'ionisation multiphotonique domine. Dans notre cas, avec une irradiation à 800 nm, on voit que la théorie de Fowler-DuBridge décrit correctement le processus d'éjection d'électrons pour des champs ne dépassant pas environ $1{\times}10^{10}$ V/m. Une telle valeur de champ est bien au-dessus de ce qui est utilisé dans le cadre de ce travail. La théorie de Fowler-DuBridge stipule que le courant des particules émises d'une surface par photoémission thermiquement assistée peut s'écrire comme [311, 312] :

$$\mathbf{J}^{th} = \sum \mathbf{J}_n^{th} \tag{3.22}$$

où les $\mathbf{J}_n^{th}$ correspondent à l'émission produite par l'absorption de n photons. Plus particulièrement, $\mathbf{J}_0^{th}$ correspond à l'émission purement thermoïonique. Les $\mathbf{J_n}$ s'écrivent :

$$\mathbf{J}_n = a_n \left(\frac{e}{h\nu}\right)^n A I^n T_e^2 F\left(\frac{nh\nu - \Phi}{k_b T_e}\right)\mathbf{n} \tag{3.23}$$

où a_n est une constante, A est la constante de Richardson et $F(x)$ est la fonction de Fowler tracée à la figure 3.5 et $\mathbf{n}$ est le vecteur unitaire normal à la surface.
De par la forme de la fonction de Fowler, on voit que, pour l'or irradié à 800 nm, tous les termes dont l'énergie additionnée des n photons ne dépasse pas la barrière de potentiel vers le milieu externe peuvent être négligés. De même, il est attendu que la section efficace d'ionisation diminue à mesure que le nombre de photons impliqués dans l'interaction augmente. Ainsi, on s'attend à ce que les a_n diminuent fortement à mesure que n augmente. Alors, les termes dominants de la sommation sont simplement $\mathbf{J}_0$ et $\mathbf{J}_3$ pour l'or en milieu aqueux. On peut

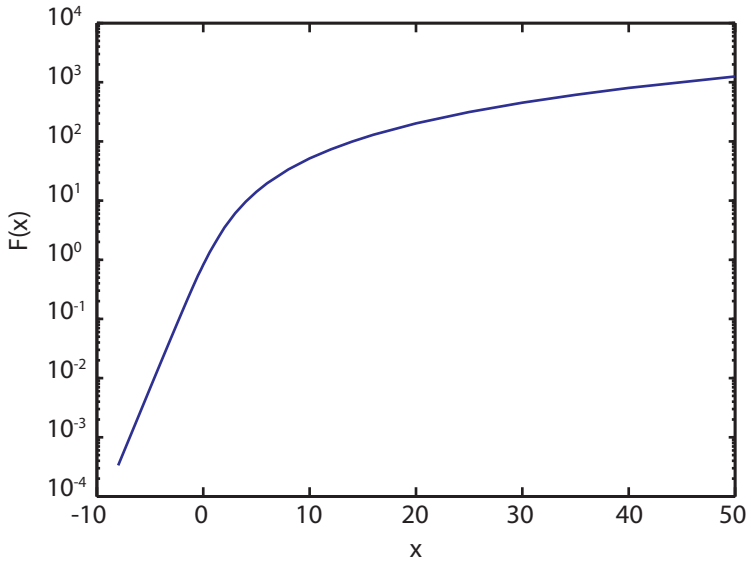

Figure 3.5 Fonction de Fowler

réécrire 3.23 comme [255]

$$\mathbf{J}^{th} = \mathbf{J}_0^{th} + c_{Au} \frac{2\left(k_b T_e\right)^2}{\left(3\hbar\omega - \Phi\right)^2} F\left(\frac{3\hbar\omega - \Phi}{k_b T_e}\right) I^3 \mathbf{n} \tag{3.24}$$

où c_{Au} est la section efficace d'ionisation à 3 photons déterminée expérimentalement dans [313] comme étant $1{\times}10^{-7}$ $\frac{A/cm^2}{(MW/cm^2)^3}$. Noter que le I dans 3.23 et 3.24 représente l'intensité *équivalente* de l'onde plane correspondant au champ électrique incident. En effet, toutes ces expressions ont été développées et mesurées dans le cas où l'onde incidente était plane. Dans ce cas, $I = \frac{1}{2} Re\left[|\mathbf{E} \times \mathbf{H}^*|\right]$ ou $I = \frac{1}{2}\epsilon c |\mathbf{E}|^2$ peuvent être utilisés indépendamment puisqu'ils sont équivalents. Cependant, ultimement, ce n'est pas I mais bien $|\mathbf{E}|^2$ qui couple avec la matière. Ainsi, si on est en présence d'ondes non-planes, il ne faut pas faire l'erreur d'utiliser $I = \frac{1}{2} Re\left[|\mathbf{E} \times \mathbf{H}*|\right]$ comme terme de couplage avec le matériau, mais bien $I = \frac{1}{2}\epsilon c |\mathbf{E}|^2$.
Noter que le traitement de l'émission photothermique est grandement simplifié dans notre modèle. En effet, aucune correction due à la polarisation de la nanostructure suite à l'émission n'est considérée. Celle-ci devrait cependant entraîner une certaine réduction du courant photothermique réellement émis suite à l'interaction laser [220]. Le courant idéalisé calculé dans le cadre du modèle devrait par conséquence surestimer le courant réel et devrait être interprété comme une borne supérieure à ce dernier. Comme nous le verrons dans les chapitres subséquents, les cas où l'influence de ce courant est significative se limitent principalement à l'irradiation de NRs en résonance à de basses fluences, bien en-deçà des fluences d'opération

requises pour la nanochirurgie cellulaires, en particulier pour la transfection cellulaire. Ainsi, bien qu'approximatif, ce modèle simple suffit amplement à nos besoins.

Conduction de chaleur à l'interface

La conduction de chaleur à l'interface or/eau est limitée par une conductance finie à l'interface. Ainsi, le courant de chaleur émis de la nanostructure vers son environnement s'écrit :

$$J_{cond} = q_0 \left(T_e - T_m\right) \tag{3.25}$$

avec q_0 =105×10^6 $\mathrm{Wm^{-2}K^{-1}}$ [172].

Fusion de la nanostructure

La fusion de la nanostructure est tenue en compte en utilisant un modèle de type enthalpique où une contribution due à la chaleur latente de fusion est introduite dans la capacité thermique utilisée pour le calcul de T_l. Ainsi,

$$\rho^{Au} C_l = \rho C_l^0 + \delta(T_l - T_l^f)\rho^{Au} L \tag{3.26}$$

où L est la chaleur latente de fusion et T^f est la température de fusion de l'or.
Dans le cas de nanostructures, ces deux paramètres dépendent des dimensions et peuvent diverger considérablement de leur valeur connue pour des matériaux macroscopiques. La méthode utilisée afin d'évaluer leur valeur est tirée de [314, 315]. On définit le paramètre α comme :

$$\alpha = \frac{\sigma_s}{4\pi \left(\frac{3V}{4\pi}\right)^{2/3}} \tag{3.27}$$

où V est le volume de la particule et σ_s, sa surface. La température de fusion modifiée peut alors s'écrire :

$$T_f = T_f^0 \left(1 - 6\alpha \frac{r}{\left(2\frac{3V}{4\pi}\right)^{1/3}}\right) \tag{3.28}$$

Dans notre cas, T_f^0 =1337 K et r =0.135 nm est la moitié du paramètre de maille du réseau pour l'or [315]. On définit ensuite la chaleur latente comme :

$$L = T_f \Delta S^{Au} \tag{3.29}$$

où ΔS^{Au} est le changement d'entropie au point de fusion et T_f est la température de fusion. On peut alors exprimer :

$$\Delta S^{Au} = \Delta S^{Au,0} + \frac{(3/2)k_b}{ln\left(1 - \frac{5r}{\alpha^{1/2}\left(\frac{3V}{4\pi}\right)^{1/3}}\right)} \tag{3.30}$$

Dans notre cas $\Delta S^{Au,0}$ =9.37 J kg^{-1}K^{-1}. La chaleur latente et la température de fusion des nanostructures d'or peuvent alors être connues en fonction de leur taille et être utilisées dans l'équation 3.26.

Commentaire sur les oscillations et la dynamique du réseau

Tel que vu à la section 2.7.2, l'irradiation de nanostructures plasmoniques avec une impulsion laser ultrabrève mène à la génération d'un champ de contrainte dans le matériau qui relaxe en entrainant une rapide expansion ainsi que l'oscillation du réseau atomique de la nanostructure. Dans son étude théorique, Volkov et al. ont déterminé l'impact de cette rapide expansion sur la pression de l'eau environnant la nanostructure [235]. Ses résultats démontrent que l'expansion du réseau a un impact considérable sur la pression durant les premières 20 ps suivant l'irradiation. La pression engendrée par ce phénomène est de l'ordre de ∼10 MPa. Par contre, son effet sur la température de l'eau est négligeable. Dans les chapitres suivants, nous verrons que les pressions engendrées suite à l'irradiation d'une nanostructure plasmonique à l'aide d'un laser ultrarapide sont de plusieurs ordres de grandeur supérieures à ∼10 MPa en raison de l'excitation d'un plasma dans le champ proche des particules. Nous allons donc négliger l'impact de l'expansion thermique et des oscillations thermiques sur la dynamique de l'eau autour de la nanostructure.

3.3.3 Propriétés et dynamique du plasma

Tel que décrit à la section 2.7.4, l'irradiation d'une nanostructure plasmonique à l'aide d'un laser ultrarapide, dans certaines conditions, est en mesure de générer un plasma dans l'eau dans le champ proche amplifié à proximité de la nanostructure. L'énergie contenue dans ce plasma ainsi que sa densité sont décrites par les équations 3.7-3.8 présentées à la figure 3.3. Les prochains paragraphes visent à détailler ces équations et les différentes contributions qui les composent. Un tableau résumant les expressions et paramètres relatifs à la dynamique du plasma est aussi présenté à l'annexe A.

Photoionisation

Le terme de photoionisation (S_{photo}) dans l'équation 3.8 de la figure 3.3 est calculé à partir de la théorie de Keldysh [245]. Cette théorie est décrite en détails à la section 2.7.4. Le lecteur est référé à cette section pour le détail des équations. Cette formulation est entièrement justifiée si la densité électronique du plasma reste relativement faible. Cependant, dans le cas d'un plasma fortement dégénéré, l'expression doit être modifiée. En effet, afin qu'un photon puisse transférer son énergie à un électron, l'état final de ce dernier se doit d'être accessible. Dans le cas d'un plasma fortement dégénéré occupant les niveaux excités des molécules d'eau, de tels états récepteurs ne sont plus disponibles pour des énergies en bordure du minimum de la bande excitée. Concrètement, plus d'énergie est nécessaire pour faire passer l'électron de son état fondamental à son état excité. En première approximation, on peut affirmer que les états associés aux énergies inférieures au potentiel chimique sont complètement remplis. Ainsi, le potentiel d'ionisation effectif des molécules d'eau doit être majoré par l'énergie de pénétration du potentiel chimique à l'intérieur de la bande excitée. Il est à noter qu'en principe cette condition est quelque peu relâchée à mesure que la température augmente, celle-ci ayant pour effet de libérer certains états situés en deçà du potentiel chimique. Ce relâchement est cependant négligé dans le modèle.

Cinétique du plasma

Le traitement de l'ionisation par impact (S_{coll}) est basé sur une approche du type plasma. Il se base sur celui utilisé par Hallo et al. dans [253]. Afin de déterminer le taux d'ionisation et le comportement du plasma formé, nous devons premièrement être en mesure de calculer les fréquences de collisions des différentes espèces en présence entre elles.

Collision électron-ion

La fréquence des collisions électron-ion est donnée par [316] :

$$\nu_{ei} = \frac{Ze^4 n_e \Lambda}{3\epsilon_0^2 m_e^{1/2} (2\pi k_b T_e)^{3/2} \left(1 + e^{(-\mu/k_b T_e)}\right) F_{1/2}} \tag{3.31}$$

où Z est la charge de l'ion (1 dans notre cas), n_e est la densité de porteurs dans le plasma, T_e est leur température et $F_{1/2}$ est l'intégrale de Fermi d'ordre 1/2 définie par :

$$F_j = \frac{1}{\Gamma(j+1)} \int_0^\infty \frac{t^j dt}{1 + e^{(t-\mu/k_b T_e)}} \tag{3.32}$$

Noter que :

$$\lim_{\mu/k_bT_e \to -\infty} \left(1 + e^{-\mu/k_bT_e}\right) F_{1/2} = 1 \tag{3.33}$$

On retrouve donc l'expression du temps de collisions d'un plasma classique tel que donné par le formalisme de Fokker-Planck dans la limite du gaz électronique non-dégénéré [317]. Le logarithme de Coulomb Λ est quant à lui donné par [316] :

$$\Lambda = max\left[2, \frac{1}{2} ln\left(1 + \left(\frac{b_{max}}{b_{min}}\right)^2\right)\right] \tag{3.34}$$

où les paramètres b_{max} et b_{min} représentent respectivement les paramètres d'impact minimaux et maximaux lors d'une collision de type Coulombienne. Le paramètre d'impact maximal correspond à la distance maximale de l'ion au delà de laquelle son effet se fait encore sentir, et est habituellement pris comme étant la longueur de Debye dans le matériau.

$$b_{max} = \left(\frac{n_e e^2}{\epsilon_0 k_b \sqrt{T_e^2 + T_F^2}} + \frac{n_e e^2}{\epsilon_0 k_b T_m}\right)^{-1/2} \tag{3.35}$$

Le paramètre d'impact minimal est habituellement pris comme le paramètre d'impact nécessaire pour obtenir un angle de collision supérieur à $\pi/2$ dans la théorie des collisions de Rutherford. Pour des énergies encore plus importantes, le paramètre d'impact minimal est défini par le principe d'incertitude d'Heisenberg, de sorte que, au final, :

$$b_{min} = max\left[\frac{Ze^2}{4\pi\ \epsilon_0 m_e v_e^2}, \frac{h}{2m_e v_e}\right] \tag{3.36}$$

où v_e est la vitesse moyenne des électrons. La fréquence de collision des électrons avec les ions ν_{ei} est de plus limitée par $\frac{\omega_p}{\sqrt{6}}$ dans le cas non-idéal de manière à ce que le libre parcours moyen d'un électron ne devienne pas inférieur à la distance entre deux ions [252].

Collision électron-neutre

La fréquence de collision des électrons avec les espèces neutres est donnée par l'équation [253] :

$$\nu_{en} = n_a \sigma_a v_e \tag{3.37}$$

où σ_a est la section efficace de collision élastique, n_a est la densité d'atomes neutres. ν_{en} est bornée par $v_e\left[\frac{1}{2}\left(n_a \frac{4\pi}{3}\right)^{1/3}\right]$ dans le cas non-idéal [252], considérant le fait que le libre parcours moyen des électrons ne peut pas être plus faible que la distance séparant deux espèces neutres.

Fréquence de collision totale et ionisation par impact

La fréquence de collision efficace des électrons est déterminée par :

$$\gamma_c = \nu_{en} + \nu_{ei} \tag{3.38}$$

Ionisation par impact

Le taux de création de porteur par collision (S_{coll}) est donné par :

$$S_{coll} = \nu_{ci} n_e \tag{3.39}$$

avec

$$\nu_{ci} = n_a \sigma_0 v_e \left((7.5\beta - 1)\sqrt{\frac{\beta}{\pi}} e^{-1/\beta} + (3.75\beta^2 - 3\beta + 1) erfc(1/\sqrt{\beta}) \right) \tag{3.40}$$

où n_a est la densité d'espèces neutres, σ_0 est la section efficace d'ionisation par collision et β est le rapport entre l'énergie des porteurs et le potentiel d'ionisation.

$$\beta = \frac{3 k_b T_e}{2\tilde{\Delta}} \tag{3.41}$$

Noter que dans le cas d'un gaz électronique fortement dégénéré, de façon similaire au cas de la photoionisation, le potentiel d'ionisation effectif doit être majoré par l'énergie du potentiel chimique si celui-ci est situé au-dessus du minimum de la bande du niveau excité.
La densité nominale d'électrons disponibles ρ_0, la section efficace de collision élastique σ_a, la section efficace d'ionisation par collision σ_0 et le potentiel d'ionisation Δ sont résumés au tableau 3.1

Tableau 3.1 Propriétés d'ionisation de l'eau

Paramètre	**Symbole**	**Valeur**
Section efficace de collision élastique	σ_a	2×10^{-19} m^2 [251]
Section efficace d'ionisation par collision	σ_0	8.97×10^{-22} m^2 [318]
Potentiel d'ionisation	Δ	6.5 eV [72]
Densité nominale d'électrons disponibles	ρ_0	6.68×10^{22} cm^{-3} [72]

Taux de recombinaison du plasma

Le taux de recombinaison (S_{rec})du plasma est établi empiriquement [72] :

$$S_{rec} = 2 \times 10^{-9} cm^3 s^{-1} n_e^2 \tag{3.42}$$

Absorption d'énergie par le plasma

L'absorption de l'énergie électromagnétique du laser par les électrons libres du plasma se fait par l'entremise d'un processus de type Bremmstrahlung inverse. Le taux de travail électromagnétique est donné par :

$$S_{EM} = (1/2) Re[\sigma *] |\mathbf{E}|^2 \tag{3.43}$$

où σ est la conductivité du plasma, dont l'expression est donnée par le modèle de Drude [72, 253].

$$\sigma = \frac{\sigma_{dc}}{1 - j\omega/\gamma_c} \tag{3.44}$$

avec, ω la fréquence angulaire du laser et σ_{dc}, la conductivité à fréquence nulle donnée par :

$$\sigma_{dc} = \frac{n_e e^2}{\gamma_c m} \tag{3.45}$$

Couplage énergétique électron-ion

Le couplage énergétique électron-ion est calculé à partir de la fréquence de collision efficace des électrons γ_c donnée à l'équation 3.38 [252, 319]

$$Q_{ei} = 3(m_e/m_{ion}) n_e \gamma_c k_b (T_e - T_m) \tag{3.46}$$

où m_e est la masse de l'électron (9.109×10^{-31} kg) et m_{ion} est la masse d'une molécule d'eau (3.02×10^{-26} kg).

Perte énergétique du plasma par radiation

La perte énergétique du plasma due à la radiation thermique de type Bremmstrahlung est donnée par [319]

$$Q_{rad} = \frac{1}{4\pi\epsilon_0} \frac{4e^2}{\sqrt{3}\hbar c} \frac{k_b^2 T_e^2}{m_e c^2} n_e \gamma_c \tag{3.47}$$

où c est la vitesse de la lumière.

Courants de chaleur et de particules dans le plasma

Le courant particulaire ($\mathbf{J}^n$) et le courant de chaleur ($\mathbf{J}^q$) dans le plasma sont calculés à partir de l'équation de transport semiclassique de Boltzmann, faisant intervenir les coefficients d'Onsager [308]. Ces courants comprennent un courant de diffusion (proportionnel au gradient du potentiel chimique) et un courant thermoélectrique (proportionnel au gradient de température).

$$\mathbf{J}^n = (-1/e)\left(L^{11}\left(\nabla\mu/e\right) + L^{12}\left(-\nabla T_e\right)\right) \tag{3.48}$$

et

$$\mathbf{J}^q = (-1/e)\left(L^{21}\left(\nabla\mu/e\right) + L^{22}\left(-\nabla T_e\right)\right) \tag{3.49}$$

où L_{11} et L_{12} sont définis en fonction de

$$\Lambda^{(\alpha)} = \frac{e^2}{\gamma_c}\int \frac{d\mathbf{k}}{4\pi^3}\left(-\frac{\partial f}{\partial \epsilon}\right) v(\mathbf{k})v(\mathbf{k})\left(\epsilon(\mathbf{k}) - \mu\right)^{\alpha} \tag{3.50}$$

et

$$L^{11} = \Lambda^{(0)} \tag{3.51}$$

$$L^{21} = T_e L^{12} = -\frac{1}{e}\Lambda^{(1)} \tag{3.52}$$

$$L^{22} = \frac{1}{e^2 T_e}\Lambda^{(2)} \tag{3.53}$$

Les différentes intégrales sont calculées à partir de l'approximation d'un gaz d'électrons libres pour le calcul des vitesses électroniques $v(\mathbf{k})$.

Modification locale de la permittivité

La modification de l'indice de réfraction réel de l'eau en fonction des paramètres thermodynamiques est donnée par la base de donnée de l'IAPWS [170]. Cependant une modification supplémentaire de l'indice de réfraction est provoquée par la création d'un plasma dans le milieu. La permittivité du milieu s'écrit :

$$\epsilon_r = \epsilon_\infty + \frac{i\sigma}{\epsilon_0\omega} \tag{3.54}$$

où ϵ_∞ est la permittivité relative de l'eau sans le plasma, ω est la fréquence du laser, γ_c est la fréquence efficace de collision des espèces du plasma donnée par l'équation 3.38 et la conductivité σ est donnée par l'équation 3.44.

3.3.4 Hydrodynamique et propriétés thermodynamiques de l'eau

Dans le milieu aqueux, les variables qui doivent être calculées sont la vitesse $\mathbf{v}$ des particules du fluide, sa densité locale ρ, sa température T_m, ainsi que sa pression p. L'évolution de ces variables est régie par un système d'équations composé de l'équation de continuité pour la conservation de la masse (figure 3.3, équation 3.9), d'une équation de conservation de l'énergie (figure 3.3, équation 3.10), des équations de Navier-Stokes pour la conservation de la quantité de mouvement (figure 3.3, équation 3.10), et d'une équation d'état. À la frontière de la particule, le transfert de chaleur est régi par l'équation 3.25, alors que la vitesse du fluide est nulle ainsi que la diffusion des molécules d'eau perpendiculaire à l'interface. Habituellement, dans le cas des fluides incompressibles, les équations sont posées de manière à résoudre pour $(T_m, \mathbf{v}, p)$ et l'équation d'état s'écrit $\rho = f(p, T_m)$. Cependant, dans notre cas, la hausse de température du milieu cause une forte variation de la densité du fluide. Les équations sont alors plutôt posées de manière à résoudre pour $(T_m, \mathbf{v}, \rho)$ avec une équation d'état $p = f(\rho, T_m)$.
Dans cette section, nous allons décrire les différentes équations régissant l'évolution des variables thermodynamiques du milieu avant de décrire avec plus de détail l'équation d'état utilisée.
Les hypothèses suivantes sont considérées :

1. L'état thermodynamique de l'eau peut-être représenté par une équation d'état à l'équilibre.
2. Le mélange vapeur-liquide est traité comme un fluide homogène en tout point.
3. La cavitation s'effectue suite à un phénomène d'explosion de phase. Le liquide métastable devient un mélange homogène liquide-vapeur à la pression de saturation de façon instantanée lorsque la spinodale cinétique est atteinte.

L'hypothèse 1 implique l'atteinte d'un équilibre thermique local dans l'eau, malgré la nature ultrarapide du procédé. Cette hypothèse décrit l'évolution thermodynamique de l'eau comme une succession d'états pouvant être décrits par son équation d'état à l'équilibre. L'atteinte de cet équilibre thermique a été vérifiée pour des temps de l'ordre de la picoseconde dans le cas de matériaux à l'état solide irradiés avec un laser femtoseconde à une fluence sous le seuil menant à la formation de plasma [160, 320, 321]. On peut faire l'hypothèse qu'une situation semblable prévaut dans l'eau. En effet, la présence du plasma électronique créé dans l'eau lors de l'irradiation laser peut sous certaines conditions modifier son équation d'états. Or, ce plasma recombine très rapidement, de sorte que sa densité devient très faible dans un temps caractéristique de l'ordre de $\sim$1 ps, soit beaucoup plus rapidement que le temps requis pour que l'eau subisse une expansion significative. L'évolution thermodynamique de l'eau se

produit donc à partir d'un état initial de haute température et de pression déterminé par l'énergie qui y est déposée lors de la relaxation du plasma. Comme une expansion significative ne débute qu'à une échelle de temps bien supérieure au temps caractéristique de relaxation du plasma, il est justifié de faire l'hypothèse que le plasma n'a que très peu d'influence sur l'équation d'état de l'eau lors de son évolution thermodynamique. Cette situation est en parfaite analogie avec les modèles de type deux-températures couramment utilisés dans le cadre d'études théoriques concernant l'ablation laser de différents matériaux.

L'hypothèse 2 implique que l'on représente le matériau comme un fluide homogène en tout point. Cependant, l'atteinte d'un équilibre thermique local dans l'eau discuté à l'hypothèse 1 n'implique pas nécessairement une homogénéité de phase, ni par ailleurs l'atteinte d'un état d'équilibre entre les phases. L'irradiation d'un matériau à l'aide d'un laser femtoseconde peut en effet créer des états transitoires hors-équilibre, tel que décrit par Lorazo et al. [160]. Le modèle, basé sur une représentation de type milieu-continu du fluide, néglige donc sa structure "microscopique" et ne considère que ses propriétés "macroscopiques". En particulier, à la saturation, le modèle considère l'eau comme un mélange parfaitement homogène de liquide et de vapeur dont les propriétés sont définies en fonction de la proportion de chacune des phases dans le mélange. Cette hypothèse évite l'introduction d'un modèle de type moléculaire qui alourdirait considérablement les calculs et rendrait très difficile, voire impossible, l'obtention de résultats pour la taille des systèmes impliqués en nanochirurgie par laser (bulles de l'ordre du μm). Par ailleurs, les bulles simulées étant relativement grosses, il est raisonnable de penser que la possible hétérogénéité de la structure microscopique du fluide n'a que peu d'influence sur la dynamique des bulles.

L'hypothèse 3 établit la manière dont les changements de phases sont abordés dans le modèle et sera discutée en détail plus loin. En résumé, cette hypothèse considère que l'eau reste liquide dans la région métastable, sous la courbe de saturation, jusqu'au croisement de la spinodale cinétique où il se transforme immédiatement en un mélange homogène d'eau et de vapeur (conformément à l'hypothèse 2) avec une pression correspondant à la pression de saturation.

En somme, ces trois hypothèses permettent de construire un modèle de génération et de dynamique de bulle reposant sur des bases théoriques raisonnables, tout en conservant la possibilité d'étudier des systèmes dont les dimensions demeurent d'intérêt pour les applications en nanochirurgie cellulaire ($\sim 1\mu m$). Au-delà des simples considérations théoriques, la confrontation des résultats obtenus par simulation avec des mesures expérimentales assurera la validité du modèle et de ses hypothèses. De telles vérifications expérimentales, montrant un très bon accord avec les simulations, sont présentées aux chapitres 4 et 5.

Équation d'état à basse température (T_m<1273 K) et à basse pression (p<1 GPa)

L'équation d'état utilisée pour l'eau est celle issue de l'IAPWS-95 [170], conçue pour des usages scientifiques et métrologiques. Il existe aussi l'IAPWS-97, mais il ne s'agit que d'une approximation de la version 95 développée pour les besoins de l'industrie. Cette formulation est basée sur le développement d'une équation semi-empirique pour l'énergie libre d'Helmholtz de l'eau donnée par :

$$f = f\left(\rho, T_m\right) \tag{3.55}$$

Il est alors possible à partir de cette énergie libre de déduire l'ensemble des propriétés thermodynamiques de l'eau. Nous utiliserons principalement l'entropie de la substance, S, et son équation d'état, respectivement donnés par les équations suivantes :

$$p = \rho^2 \left(\frac{\partial f}{\partial \rho}\right)_{T_m} \tag{3.56}$$

$$S = -\left(\frac{\partial f}{\partial T_m}\right)_{\rho} \tag{3.57}$$

L'IAPWS fournit aussi des formulations pour les propriétés non-thermodynamiques telles la viscosité et la conductivité thermique.
L'IAPWS95 a été testée et est conforme aux résultats expérimentaux dans sa région fluide stable jusqu'à des températures de 1273 K et des pressions de 1 GPa. Des tests mentionnés dans la documentation de l'IAPWS montrent que l'énergie d'Helmholtz se comporte correctement jusqu'à des pressions de ∼100 GPa et des températures jusqu'à 5000 K [170]. Ils montrent aussi que les propriétés thermodynamiques calculées à l'aide de l'équation d'états se comportent correctement lorsqu'elles sont extrapolées dans les régions métastables. Les propriétés non-thermodynamiques (viscosité, conductivité thermique) ont le même domaine de validité.

Équation d'état à haute température (T_m>1273 K) et à haute pression (p>1 GPa)

Pour les températures et pressions en dehors de la zone de validité de l'équation d'état fournie par l'IAPWS, nous utilisons l'équation d'état fournie par SESAME [322]. Cette équation d'état est tabulée pour des températures allant jusqu'à $\approx 2\times10^8$ K et des pressions allant jusqu'à $\approx 10^9$ GPa. Celle-ci est générée à partir d'une combinaison de modèles théoriques. La discrétisation est cependant très grossière (3520 points sur toute l'étendue du domaine couvert) et la validation de cette équation d'état est beaucoup moins systématique que celle de l'IAPWS.

Binodale, spinodale et spinodale cinétique

Dans le diagramme de phase de l'eau, la binodale représente la courbe d'équilibre de coexistence entre la phase vapeur et la phase liquide. Lorsque soumis à une contrainte, un liquide peut temporairement entrer dans une région du diagramme de phase appelée région métastable, qui se situe entre la binodale et la spinodale. La spinodale est la limite de stabilité d'une phase homogène du fluide. Dans la région instable, $\delta^2 f < 0$, menant entre autre à $C_p < 0$ et $\frac{\partial p}{\partial V} > 0$. La spinodale est alors définie comme l'ensemble des points (ρ, T_m, p) tel que $\delta^2 f = 0$. Un fluide dont l'état se situe entre la spinodale et la binodale du système est un liquide métastable dont on suppose le temps de vie assez long pour qu'il demeure liquide tout au cours de son passage dans cette zone du diagramme de phase. La spinodale est alors le point limite du diagramme de phase où le liquide subit un brusque changement de phase et se transforme en un mélange hétérogène liquide-vapeur. Cependant, le liquide devient instable avant d'atteindre la spinodale du système. On définit la spinodale cinétique comme la limite où le temps de vie τ_M du liquide métastable devient inférieure au temps τ_R de relaxation vers un équilibre local [177]. La zone où un liquide peut effectivement se trouver dans un état métastable est donc limitée à la région entre la binodale du système et la spinodale cinétique du système. La spinodale cinétique peut s'exprimer en fonction de la seule équation d'état et de de la tension de surface du fluide [177]. Une expression pour la spinodale cinétique se retrouve dans [177]. Dans le cadre du modèle proposé, celui-ci permet au liquide d'entrer dans la région métastable jusqu'à la spinodale cinétique, puis traite la décomposition spinodale en faisant l'hypothèse que le fluide reste un mélange homogène des phases liquides et gazeuses à l'équilibre dont les propriétés thermodynamiques sont les moyennes pondérées des deux phases en présence. Le lecteur est référé à la section 2.6.3 pour une discussion plus approfondie des mécanismes d'explosion de phase en lien avec le diagramme de phase de l'eau.

Effet de la tension de surface

Lors de la création d'un interface entre la vapeur d'eau et le liquide, la présence d'une énergie de surface se traduit par l'apparition d'une force à l'interface appelée tension de surface. Mathématiquement, celle-ci vient modifier l'équation de conservation du mouvement du fluide (équation 3.11 à la figure 3.3) par l'introduction d'un terme proportionnel à σ_s. Le point délicat dans nos simulation est de définir l'emplacement géométrique de cet interface. Nous fixons arbitrairement cet interface au lieu géométrique où le titre (pourcentage massique de vapeur) est de 10%. Nous définissons ensuite la fonction Π_s qui prend la valeur 1 à l'intérieur de la bulle et la valeur 0 à l'extérieur de la bulle. Le vecteur normal à la surface à

l'interface s'écrit alors :

$$\mathbf{n} = \frac{\nabla \Pi_s}{|\nabla \Pi_s|} \tag{3.58}$$

et la courbure locale est définie comme

$$\kappa_s = -\nabla \cdot \mathbf{n} \tag{3.59}$$

3.4 Résolution du système d'équations et validation numérique

3.4.1 Méthode numérique employée

Les équations 3.2 − 3.11 présentées à la figure 3.3 sont résolues à l'aide de la méthode des éléments finis. La figure 3.6 résume de plus les différentes conditions frontières appliquées aux différentes variables qui sont nécessaire à la résolution du système. Le logiciel commercial Comsol est utilisé (www.comsol.com) afin de résoudre le problème. Le domaine comprenant la nanostructure et son environnement est premièrement discrétisé en éléments. Le domaine est choisi suffisamment grand afin que les conditions frontières au bord n'influence pas la solution à proximité de la particule. La solution dépendante du temps du système est obtenue en utilisant l'algorithme appelé α-Généralisé [323, 324], implémenté dans Comsol, et qui transforme le système d'équations 3.2-3.11(10 équations différentielles à 10 inconnus) en un système d'équation algébrique non-linéaire. Ce système est résolu en appliquant une méthode de type Newton à chacun des pas de temps.
En principe, toutes les équations doivent être résolues en 3D. Cependant, pour des raisons d'économie de ressources, dans le cas de petites particules, il est possible de résoudre l'ensemble des équations en tenant compte de cette symétrie axiale. En effet, comme pour des petites particules la distribution de champ engendrée par l'équation 3.2 présente essentiellement une symétrie axiale (en raison d'une domination de la composante dipolaire de la réponse optique), il est possible de simplifier le problème et de traiter l'ensemble des équations 3.3-3.11 en 2D, en tenant compte de cette symétrie pour des temps ultérieurs au dépôt d'énergie.

3.4.2 Interaction électromagnétique

3.4.3 Maillage et convergence

Le maillage des géométries est réalisé à l'aide d'éléments tétraédriques en 3D et triangulaires en 2D. Un exemple de maillage type utilisé pour une particule de 100 nm de diamètre

Variable		Conditions aux frontières au bord de la particule		Conditions aux frontière au bord du domaine	
Champ électrique	**E**	N/A	N/A	"Perfectly matched layer"	
Température électronique	T_e	Continuité avec T_p	$T_e = T_p$	N/A	N/A
Température du réseau	T_l	Courant de chaleur à l'interface	$-\mathbf{n}\cdot\mathbf{q}_l = J_{cond}$	N/A	N/A
Densité du plasma	n_e	Émission photothermique	$\mathbf{n}\cdot\mathbf{J}^n = J^{th}$	Isolé	$\mathbf{n}\cdot\mathbf{J}^n = 0$
Température du plasma	T_p	Continuité avec T_e	$T_e = T_p$	Isolé	$\nabla T_p = 0$
Densité de l'eau	ρ	Isolation	$\rho\mathbf{v}\cdot\mathbf{n} = 0$	Valeur initiale	$\rho = \rho_0$
Température de l'eau	T_m	Isolation	$-\mathbf{n}\cdot(\kappa\nabla T_m) = J_{cond}$	Valeur initiale	$T_m = T_0$
Vitesse de l'eau	**v**	Vitesse nulle	$\mathbf{v} = 0$	Pression initiale	$p = p_0$

Figure 3.6 Sommaire des conditions aux frontières appliquées aux différentes variables du système d'équations différentielles.

est présenté à la figure 3.7.La figure 3.7a présente le maillage 3D utilisé pour l'étape du dépôt d'énergie. Il contient ≈87000 éléments. La figure 3.7b présente le maillage 2D utilisé pour l'étape de croissance de la bulle. Il contient ≈9000 éléments. Un agrandissement de la région centrale de ce maillage est présenté à la figure 3.7c. Noter qu'en plus de la symétrie axiale, on peut profiter de la quasi-symétrie de réflexion de la distribution de champ dans le cas de particules assez petites, ce qui est le cas pour des particules de 100 nm.

Un polynôme de degré 2 est utilisé comme fonction de base pour l'ensemble des variables, mis à part le champ de vitesse de l'eau dans l'équation de Navier-Stokes qui utilise une fonction de base de degré 3.

Il est impératif que le maillage utilisé soit suffisant pour assurer la convergence du système d'équations vers sa solution. Comme le modèle comporte plusieurs échelles de temps et de distance impliquées, plusieurs maillages différents sont utilisés, dépendamment du temps écoulé depuis l'impulsion laser.

La convergence du maillage a été effectuée avec un modèle test où une impulsion laser de fluence 200 mJ/cm^2, de durée 45 fs et de longueur d'onde 800 nm interagit avec une NP de 100nm de diamètre. Nous estimons qu'un niveau de maillage équivalent appliqué à d'autres

systèmes (NRs, NPs de tailles différentes) entraîne un niveau de convergence similaire.
Durant l'impulsion laser, le champ amplifié autour de la nanostructure et le plasma créé dans le champ proche entraînent la création de gradients importants autour de la particule. Par conséquent un maillage très fin est requis à la frontière de la particule. Nous utilisons un maillage constitué de ≈ 87000 éléments, avec des éléments d'au plus $4nm$ à la frontière pour les calculs. L'erreur de la section efficace de diffusion (linéaire) calculée comparée à la théorie de Mie est alors de moins de 5% à 800 nm. Utiliser 3× plus d'éléments, c'est-à-dire environ 295000 éléments, ne permet pas d'améliorer la précision de cette section efficace. De même l'énergie totale déposée sous forme de plasma dans le système suite à cette augmentation du maillage n'est modifiée que de 1.6%. Par conséquent, nous considérons que le maillage comprenant les 87000 éléments est suffisant pour assurer la convergence lors de l'étape du dépôt d'énergie.
Lors de l'étape de la création et croissance de la bulle, le maillage est quelque peu modifié pour accélérer les calculs. Cette étape est réalisée en symétrie axiale (2D). Le maillage utilisé est composé de ≈9000 éléments triangulaires. La taille maximale et le temps de croissance de la bulle engendrée suite à l'interaction d'un impulsion laser ne variant que de respectivement 5% et4% lorsqu'un maillage 3× plus fin est utilisé (≈25000 éléments), le maillage de ≈9000 éléments semble suffisant pour assurer la convergence lors de cette étape.

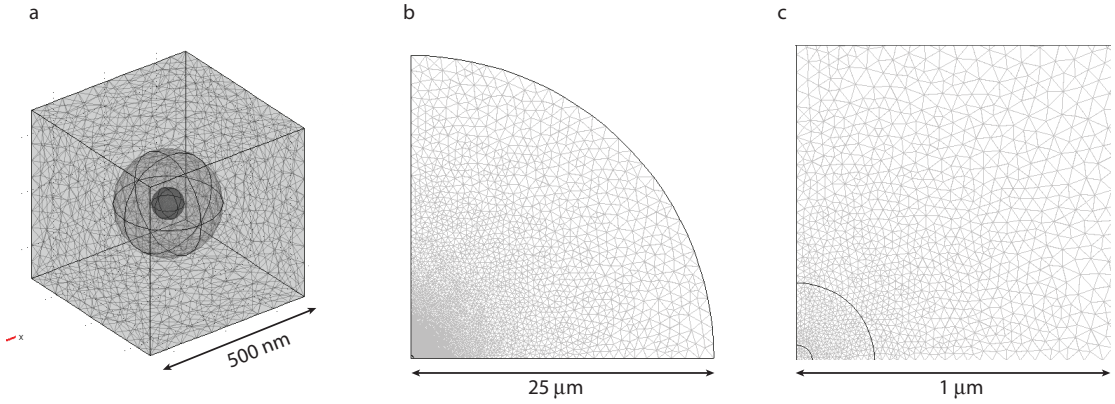

Figure 3.7 Maillages utilisés lors de la résolution du système d'équation différentielles. **a**. Maillage 3D utilisé lors du dépôt d'énergie. **b**. Maillage 2D utilisé ultérieurement au dépôt d'énergie. bf c. Agrandissement de la région centrale du maillage présenté en **b**.

3.4.4 Pas de temps et convergence

Le pas de temps utilisé lors de la résolution dépendante du temps est choisi automatiquement par Comsol afin que la solution reste en deçà d'une erreur globale estimée numériquement, multipliée par un certain seuil de tolérance. Nous utilisons un seuil de tolérance relatif de 0.01%, signifiant que l'erreur globale estimée pour le pas de temps choisi est inférieure à 0.01% de la norme du vecteur solution. Afin de s'assurer que ce seuil est suffisant, la simulation a été répétée avec un seuil de tolérance moins restrictif de 0.1%. La taille maximale de la bulle n'ayant varié que de 0.1% suite à ce changement, la tolérance de 0.01% employée assure la convergence de la solution.

CHAPITRE 4

Plasma mediated off-resonance plasmonic enhanced ultrafast laser induced nanocavitation

Ce chapitre retranscrit un article publié dans Nanoletters en 2012 [1]. Celui-ci décrit en détail les mécanismes physiques menant au phénomène de cavitation lors de l'irradiation d'une nanoparticule d'or de 100 nm par un laser femtoseconde produisant des impulsions de 45 fs, d'une fluence de 200 mJ/cm^2, à une longueur d'onde de 800 nm. L'article démontre que la cavitation résulte de la formation d'un plasma aux dimensions nanométriques excité dans le champ proche amplifié autour de la nanoparticule. L'énergie déposée par ce plasma est 11× supérieure à celle absorbée dans la nanostructure. Dans le contexte de la nanochirurgie cellulaire, cette nouvelle approche permet de créer des bulles en milieu liquide en irradiant des nanoparticules sans les endommager, tout en utilisant une longueur d'onde dans le proche infrarouge qui est peu absorbée par les tissus environnants, ce qui la rend particulièrement intéressante. Un document contenant certains détails complémentaires concernant la modélisation ainsi qu'un graphique supplémentaire montrant le comportement oscillatoire des bulles créées autour des nanoparticules à haute fluence est disponible en annexe A.

4.1 Authors

Etienne Boulais, Rémi Lachaine & Michel Meunier

Laser Processing Laboratory,
Department of Engineering Physics, École Polytechnique de Montréal,
CP6079, Succ. Centre-ville, Montréal, QC, Canada, H3C 3A7.

4.2 Abstract

The generation of nanobubbles around plasmonic nanostructures is an efficient approach for imaging and therapy, especially in the field of cancer research. We show a novel method using infrared femtosecond laser that generates ≈800 nm bubbles around off-resonance gold nanospheres using 200 mJ/cm^2, 45 fs pulses. We present experimental and theoretical work that demonstrate that the nanobubble formation results from the generation of a nanoscale

1. E. Boulais, R. Lachaine et M. Meunier, Plasma mediated off-resonance plasmonic enhanced ultrafast laser induced nanocavitation. *Nano Letters* **12**(9), 4763-4669, 2012.

plasma around the particle due to the amplified near-field rather than from the heating of the particle. Energy absorbed in the nanoplasma is indeed more than 11 times the energy absorbed in the particle. When compared to the usual approach that uses nanosecond laser to induce the extreme heating of in-resonance nanoparticles to initiate bubble formation, our off-resonance femtosecond technique is shown to bring many advantages, including avoiding the particles fragmentation, working in the optical window of biological material and using the deposited energy more efficiently.

4.3 Introduction

The use of plasmonic nanobubbles for imaging and therapy has emerged in the past few years as a valuable tool in cancer treatment [57, 184, 194, 214, 267, 295, 299, 300, 325]. Nanoscale bubbles can be generated following the interaction of a nanosecond [180, 196] or femtosecond [126, 159, 191] laser with resonant nanoparticles (NPs). High absorption cross-section then results in the extreme heating of the NPs, which in turn leads to cavitation, but also most likely to the destruction of the NPs at the fluence used for applications, which could result in toxicity issue [57, 326]. Also, wavelengths near the gold nanoparticle resonance lie outside the optical window of biological material [82] (600 nm-1100 nm) which may cause issues concerning collateral damage to tissues during treatment. Inspired by the technology of focussed ultrafast laser cell transfection in which laser-induced cavitation bubbles are used to permeabilize cell membrane [54, 55, 72, 157, 287–293], and driven by the need for a method that leaves the NPs intact and uses a wavelength in the optical window of biological material, a novel technique using *off-resonance* plasmonic gold NPs irradiated with a broadly focussed infrared femtosecond laser has been recently introduced [57, 297].

Physical mechanisms leading to cavitation remain however unclear in that case. Indeed, the low absorption cross-section of the off-resonance NPs should prevent any extreme heating at fluences used for transfection, as confirmed by earlier studies showing that the interaction leaves the NPs undamaged [57]. It is thus not obvious that the energy absorbed in the NP can be responsible for the formation of the nanobubble. In this paper, a combination of experimental measurements and modelling allows us to clearly demonstrate that, in the case of ultrafast off-resonance interaction, nanocavitation mechanism is rather dominated by the energy transfer from a plasma created by multiphotons ionization in the amplified near-field around the NPs. Damaging effect of amplified near-field has been reported in the case of surface ablation [149, 327] and non-thermal ablation of the NP itself in a water environment [126], but to our knowledge has never been cited has a way to initiate cavitation in a liquid medium. We therefore demonstrate the possibility to create a vapour nanobubble around

a NP using the scattered near-field instead of relying on the energy absorbed directly in the particle itself. Note that we will use the word cavitation throughout the text to simply mean vapour bubble generation. Indeed, since our mechanism rely on an initial non-thermal effect followed by a thermal effect, the boundary between generation of thermal bubbles and cavitation is quite thin.

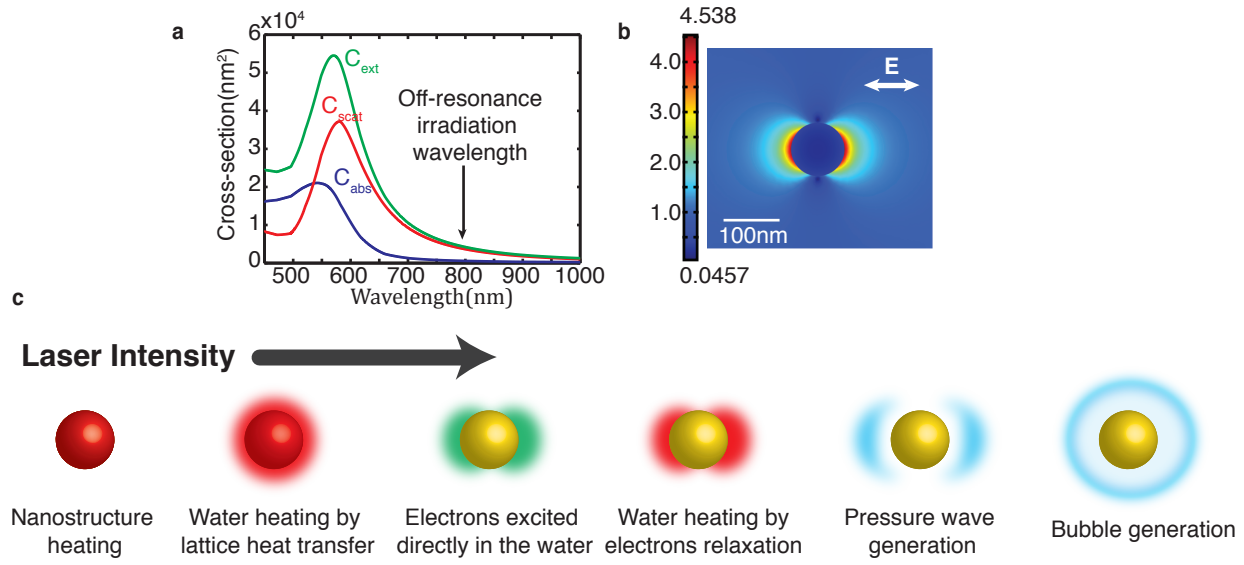

Figure 4.1 General picture of the interaction between a linearly polarized ultrafast laser and an off-resonance nanoparticle. **a**. Calculated absorption, scattering and extinction cross-sections for a 100nm NP in water as a function of the incident wavelength. **b**. Simulation results of the electric field enhancement in and around the nanoparticle showing both low field absorption in the particle and near-field enhancement. **c**. Schematics of the different phenomena that can occur following the irradiation classified in term of the laser intensity that characterize their onset.

4.4 A broad picture of ultrafast laser interaction with off-resonance nano particles

We study the interaction of a linearly polarized single infrared femtosecond pulse (800 nm, 45 fs) with off-resonance plasmonic NPs (gold, 100 nm diameter) in water, this medium modelling adequately a cellular environment under laser irradiation [45]. Figure 4.1a shows that at 800 nm, the NP has a very limited absorption (σ_{abs} ≈5.7×10^{-16}m^2), as well as some scattering (σ_{scat} ≈3.7×10^{-15}m^2). Although this scattering is much lower than in the case of

a resonant interaction (≈540 nm) , figure 4.1b shows that it still results in the formation of a small region about 50 nm wide around the particle that experiences an amplified near-field. Consequences of the energy absorption and scattering by the NP depend on the intensity of the incident laser, as schematized in figure 4.1c. For low laser intensity, absorption only occurs in the nanostructure, leading to the heating of first the electrons of the gold, and then, within a few picosecond, the lattice itself. As the laser intensity increases, the lattice is heated more and more, leading to a significant, but slow, heating of the surrounding water. When the intensity of the incident laser reaches a level where the amplified near-field gets over the optical breakdown threshold, non-linear absorption of the laser energy occurs in the vicinity of the particle, leading to the generation of an electronic plasma around the nanostructure, directly in the water. This process is quite similar to what happens in the case of ultrafast focussed laser cavitation (without plasmonic NPs) [72]. In our case, the plasma is however confined to the near-field instead of the whole focal volume, thus becoming a nanoplasma. Some contribution to this nanoplasma could also come from thermionic emission from the particle, but this will be shown to be negligible. Once created, the plasma still continues to absorb laser energy through an inverse Bremmstrahlung process, diffuses, and eventually cedes its energy to the water molecules in a few picoseconds. If the laser intensity is sufficient to create an important nanoplasma, significant heating of the water molecules could result from electron relaxation. Now, this energy transfer being very fast, important stress confinement will occur leading to the release of a more or less important pressure wave, depending on the laser intensity. Finally, following this pressure wave emission, if the laser intensity is important enough, nanocavitation will occur. Please note that many other phenomena, such as particle fragmentation, may happen at higher intensity but are not considered in this work.

4.5 Experimental evidence for off-resonance plasmonic enhanced ultrafast laser induced nanocavitation

While laser generated nanobubbles cannot be readily measured using optical microscopy because of the diffraction limit, it is still possible to detect and characterize them using an optical in-situ probing setup. This setup exploits the variation in the extinction cross-section of an irradiated NPs suspension sample when cavitation occurs [196]. A 5 mW, CW, 633 nm, He :Ne probe laser (5.5 μ m spot size measured at $1/e^2$, Rayleigh length of 399μ m) is colinearly aligned with the femtosecond pump laser and is spatially filtered after the sample (1 cm wide cuvette). All experiments are conducted in deionized water. Note that the probe laser power is too low to induce any noticeable heating of the particle. Creation of vapour bubbles around NPs perturbs momentarily the local permittivity, scatters the beam and increases the

portion blocked by the spatial filter. This results in a decrease of the optical power measured at the photodiode, as shown in figure 4.2a. Variation of the transmitted probe power is shown in figure 4.2b for a pump fluence of 200 mJ/cm^2 (5.5 μm spot size measured at $1/e^2$, Rayleigh length of 316 μm). This choice of fluence is not arbitrary as it has been reported to induce efficient cell membrane optoporation when coupled to 100 nm diameter NPs in actual transfection experiments [57]. NPs are in addition shown to remain fairly intact following the irradiation in this range of fluence [57]. Figure 4.2b shows no variation in the transmitted signal when the sample contains no NPs, even at much higher fluence (630 mJ/cm^2). However, when NPs are present (1.2×10^9 particles/mL), a decrease in the transmitted signal can be observed for a fluence of 200 mJ/cm^2. This variation can be associated to the growth and collapse of a nanoscale bubble. One could argue that this slight modification may originate from other sources than a cavitation bubble. However, as pump power is increased, the curve varies continuously to a fluence where an oscillatory behaviour appears, phenomenon usually linked to successive growth and collapse phases of vapour bubbles [157, 179–183] (see Figure 2 in Supplementary Information showing oscillatory behaviour at a slightly higher fluence of 450 mJ/cm^2). It is thus legitimate by extension to assume that the signal shown in figure 4.2b also comes from cavitation bubbles. The oscillatory behaviour is not observed at these lower fluences either because bubbles are too small to present a detectable oscillatory signal or because it is somehow quenched by the presence of NPs.

A very fast expansion in the order of 80 ns followed by a much longer ≈300 ns recovery phase can be seen from figure 4.2b. This asymmetric growth and collapse phase contrasts with the time-symmetric bubbles observed using nanosecond [180] laser with resonant particles. The very rapid growth is consistent with a bubble created directly in the medium, very rapidly, through direct action by the near-field, followed by a fast expansion. The asymmetric time-shape can be in part attributed to the ultrafast nature of the cavitation mechanism, as it will be shown later. However, the much longer recovery time of the bubble is also associated to the presence of many bubbles of different sizes, and thus different lifetimes, in the focal volume that contribute to the total signal. [193]

It is furthermore possible to deduce the maximal bubble diameter from the experimental signal of figure 4.2b. Using Mie-coated theory [328] for a gold nanosphere in water surrounded by a vapour layer, assuming that every nanosphere irradiated inside the focal volume contributes with an equivalent bubble and assuming that those bubble-nanoparticle systems scatter light independently, we can deduce an approximate maximal average diameter of 813 nm for the nanobubbles created with a 200 mJ/cm^2 irradiation. The bubble formation is undoubtedly due to the presence of the NPs as irradiating only water, even with a much higher fluence, produces no bubbles. Whether the energy transfer from the lattice or from

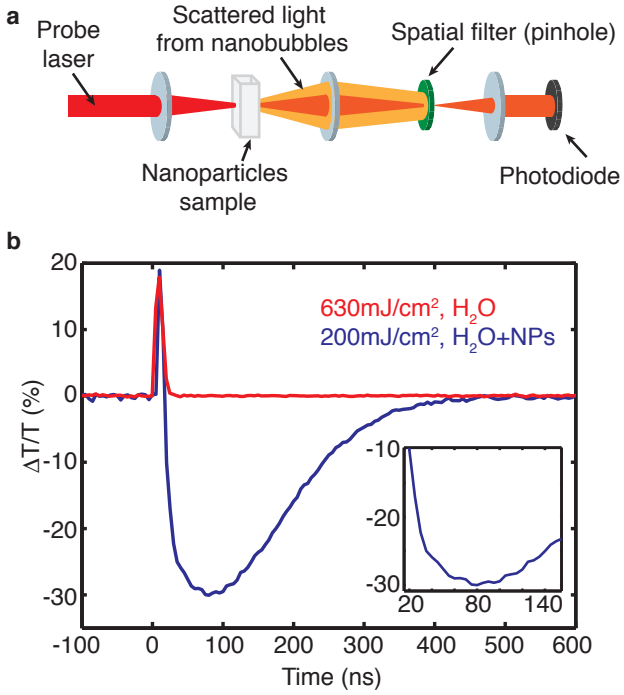

Figure 4.2 Experimental detection of vapour nanobubbles around 100 nm NPs. **a**. Principle of the plasmonic nanobubbles detection method. As nanobubbles are formed, scattered light does not go through the pinhole, resulting in a decrease in the transmission. **b**. Experimental variation of the transmitted power from a He :Ne CW probe following a 45 fs, 800 nm irradiation of a sample containing only water at 630 mJ/cm^2(red line), and a sample containing 1.2 $\times 10^9$ particles/mL of 100 nm diameter gold nanopshere at 200 mJ/cm^2 (blue line). Inset shows a zoom near the minimum.

the plasma dominates the cavitation dynamic is questionable. Previous models considering the lattice conduction mechanism only, and thus neglecting plasma production, have been previously proposed [172, 235]. However, to understand the origin of the cavitation and the dimension of the vapour bubble created, we must take a deeper look into the energy absorption mechanism and the different phenomena that are triggered by the laser irradiation.

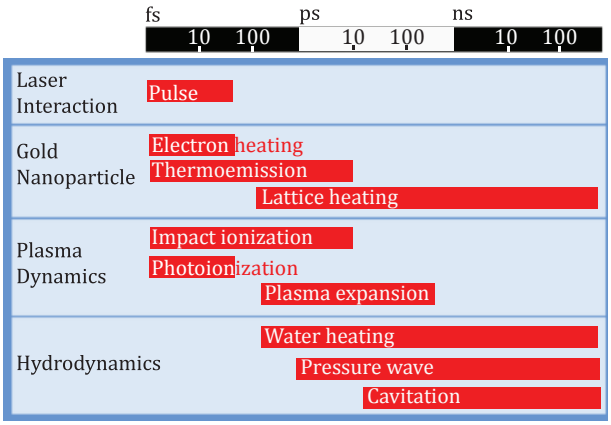

Figure 4.3 Timeline of events following the interaction of an ultrafast laser irradiation with an off-resonance plasmonic nanosphere in water

4.6 Modelling off-resonance plasmonic enhanced ultrafast laser induced nanocavitation

We developed a complete model that includes the different phenomena that occur following the the irradiation by an ultrafast laser of an off-resonance plasmonic nanostructure. Those phenomena are presented in figure 4.3 along with their characteristic time scale. As the laser energy is absorbed by the electrons of the structure, a strongly amplified near-field induces a non-linear absorption in the medium, which, along with electrons emitted from the metallic surface, produces a plasma in a confined volume around the nanostructure. This nanoplasma in turn contributes to an electromagnetic energy absorption, getting more and more important through collision ionization. This initial energy transfer, from the electromagnetic field to the electrons of both the metallic nanostructure and the water molecules, is the starting point of a series of phenomena that lead to cavitation. Energy transfer from the electrons of the NP to the lattice occurs in a time scale characterized by the electron-phonon coupling time ($\tau_{e-ph} \approx 1$ ps) [141]. Energy transfer from the electrons of the plasma to the water molecules ($\tau_{ei} \approx 500$ fs, as given in [72] with an electron density of 10^{21}cm^{-3}), along with energy transfer from the heated nanostructure lattice ($\tau_{lw} \approx$100 ps) [172], induces a

rapid rise of the water temperature leading to stress confinement. Relaxation of that stress generates a pressure wave travelling away from the nanostructure and induces the formation of a vapour bubble. Other characteristic times presented in figure 4.3 are estimated from the model.

A complete model enabling the adequate description of the off-resonance plasmonic enhanced ultrafast laser induced nanocavitation and the determination of the dominant cavitation mechanism have to include a correct description of all the above-mentionned phenomena. The complete mathematical model is conceptually divided into four parts, as illustrated in figure 4.3 by the four boxes. Those four sub-models are tightly coupled and the whole system has to be solved in a self-consistent way. Finite-element method has been used to perform the calculations. Note that we do not consider nanostructure ablation or fragmentation. Indeed, as experimental evidences suggest that no particle fragmentation occurs for 100 nm gold NP under a 45 fs, 800 nm laser pulse for fluences below 500 mJ/cm^2 [57], proper description of that particular process is not relevant for fluences used in cell transfection experiments (100-200 mJ/cm^2).

Electromagnetic interaction between the laser irradiation and the nanostructure-water system is calculated using Helmohltz equation. Energy transfer from the electromagnetic field is the energy source for NP heating and plasma production in the water surrounding the particle. The NP thermodynamic evolution is modelled using a hyperbolic two-temperature scheme based on the Boltzmann semiclassical transport equation [218]. Plasma in the surrounding water is generated by multiphoton ionization, described by Keldysh theory [72], impact ionization [253] and thermo-assisted photoemission from the particle, as described by the Fowler-Dubridge theory [255]. The laser-heated plasma density and temperature evolution is described using a diffusive process [253] as its kinetic properties are determined using the dense plasma theory [252, 316]. The presence of this plasma alters the local permittivity, which in turn modifies the near-field enhancement so that the model is self-consistent. Collisions between electrons from the plasma and water molecules, recombination of the electrons, as well as heat conduction from the particle lattice contribute to heat the water molecules. General heat transfer equation for a viscous fluid coupled to compressible Navier-Stokes equations, including surface tension effects, describes the water dynamic. A combination of the IAPWS95 [170] and SESAME [322] equation of state is used, ensuring a validity range well beyond the relevant pressure and temperature range. Under the saturation curve, liquid water enters a metastable state described by the above-mentioned equation of state until it crosses the kinetic spinodal that represents the limit of mechanical stability where phase explosion occurs [72, 177]. Beyond that limit, water pressure relaxes to the saturation pressure as all other parameters return to their phase equilibrium value. This has to be interpreted as liquid

water undergoing a phase transformation to a homogenous liquid-vapour mixture at equilibrium. Surface tension is enforced at the interface of the bubble, fixed at a vapour dryness fraction of 10%. This method has the disadvantage to induce the formation of a smooth water/vapour transition instead of a sharp interface. It has however been proven to adequately capture the pressure and density evolution in water [235]. The interested reader is referred to the Supplementary Information for further description of the mathematical model.

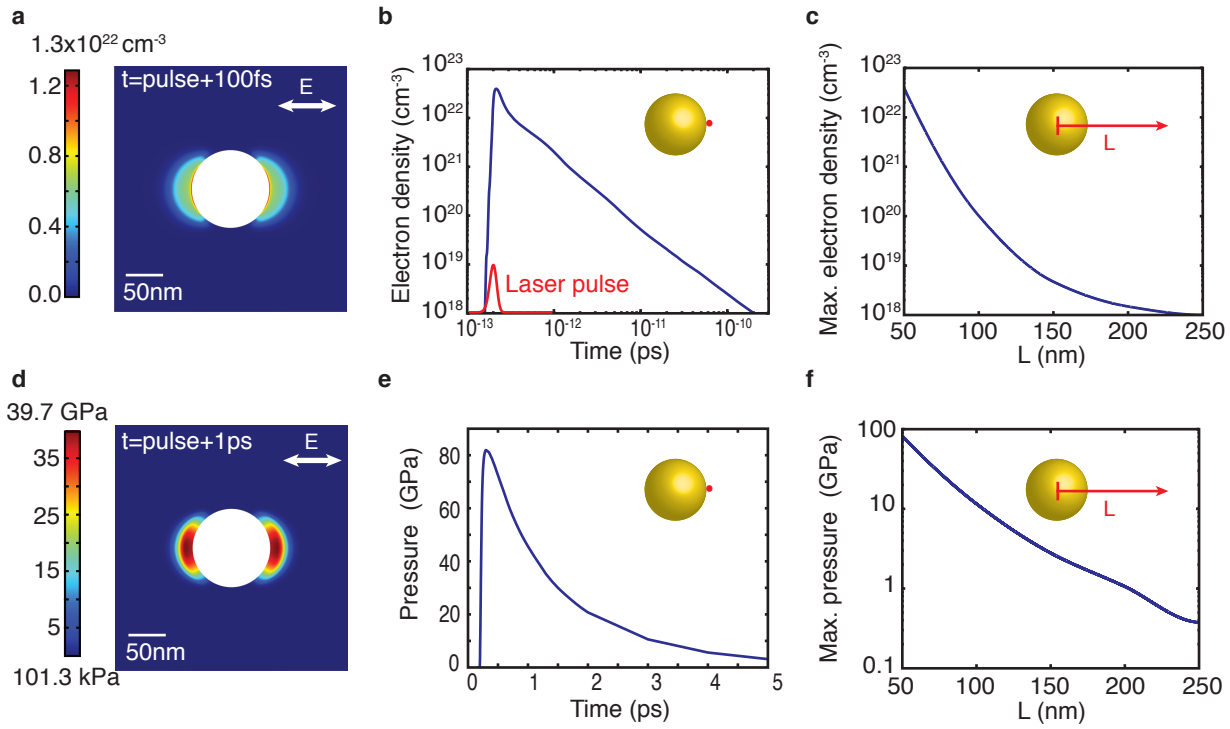

Figure 4.4 Characterization of the plasma density and pressure distribution around a 100 nm nanoparticle after a 200 mJ/cm^2, 45 fs, 800 nm laser irradiation. Polarization of the laser is horizontal and the propagation vector is perpendicular to the plane of the figure. The pulse is a gaussian centred at time=200 fs. **a**. Cross-section of the plasma distribution 100 fs after the pulse maximum. Incident field is perpendicular to the plane of the figure. **b**. Time evolution of the plasma density at the pole of the nanoparticle corresponding to the highest point of the plasma density. Red line shows the laser pulse. **c**. Reached maximum plasma density as a function of distance from the nanosphere. **d**. Cross-section of the pressure distribution 1 ps after the pulse maximum. Incident field is perpendicular to the plane of the figure. **e**. Time evolution of the pressure distribution at the pole of the nanoparticle corresponding to the pressure highest point. **f**. Reached maximum pressure as a function of distance from the nanosphere.

4.7 Results and discussion

Calculations confirm the generation of a nanoplasma by the amplified near-field of the nanostructure. Maximal electron density is hence reached near the poles where the near-field is the most intense, as shown in figure 4.4a. Plasma reaches its highest density of $4\times10^{22}\text{cm}^{-3}$ during the laser pulse and then diffuses and recombines, reducing its density below $1\times10^{21}\text{cm}^{-3}$ in less than 2 ps, as shown in figure 4.4b. Figure 4.4c shows that density over $1\times10^{21}\text{cm}^{-3}$, commonly taken as a characteristic density for the optical breakdown [72], is limited to a small volume about 30 nm thick around the particle, justifying the name nanoplasma. It is instructive to compare the amount of plasma produced through photothermal emission from the particle to the one generated directly in the water by the near-field through photoionization and impact ionization. Calculations show that the former accounts for only 11% of the total electrons, consistent with the dominance of scattering over absorption for this type of particle under a 800 nm irradiation, as shown in figure 4.1a. Indeed, the total energy deposited in the plasma is over 11 times superior to the one absorbed in the nanostructure itself. For a 200 mJ/cm^2, 45 fs pulse, the energy absorbed in the plasma is about 11 pJ whereas the energy absorbed in the particle is only 1 pJ, accounting for the observed absence of structural modification of the NPs following the irradiation [57].

Plasma relaxation and collision heats rapidly the water surrounding the particle, building up a strong pressure due to stress confinement. Figure 4.4d shows the pressure distribution 1 ps after the laser pulse. Note the geometric similarity with the plasma distribution of figure 4.4a, supporting a direct causality relation between the plasma relaxation and the stress generation. Figure 4.4e shows the time evolution of the maximal pressure, located at the particle pole. Shortly after the initial stress confinement, water mechanically relaxes through the emission of a strong pressure wave that propagates in the water. Pressure damps rapidly, as shown on figure 4.4f, where the maximum pressure drops below 1 GPa as near as 200 nm from the NP centre.

Following the emission of the pressure wave, a vapour bubble appears around the NP. Figure 4.5a shows the time evolution of the bubble average diameter. Results show a very rapid bubble expansion, which is consistent with the experiment, that culminates with the formation of a spheroidal bubble with a maximal average diameter around 1.2 μm, 72 ns after the laser irradiation. Both the maximal average diameter and the theoretical growth time compare well with the experimental values of respectively 813 nm and 80 ns. The left panel of figure 4.5b shows this bubble. The weak spatial asymmetry is a consequence of the near-field enhancement asymmetry. The right panel of figure 4.5b demonstrates that cavitation results mainly from the relaxation of the plasma generated around the particle following

the irradiation and not from the energy transfer from the heated lattice. Indeed, this figure shows that no vapour bubble is created if we perform the same simulation *without* considering the contribution of the plasma to the heat transfer. Heat transfer from the lattice alone is thus not able to generate a cavitation bubble under this irradiation condition, in opposition to the experimental results. Energy transfer from the plasma is thus identified as the main mechanism for off-resonance plasmonic ultrafast laser enhanced nanocavitation. Two reasons explain this domination. First, as mentioned before, calculations show that the total energy contained in the plasma is about 11 times the energy absorbed in the NP. Second, plasma relaxation and collisions with water molecules result in a much faster heat transfer than heat conduction from the lattice. This leads to a greater stress confinement resulting in a stronger pressure stress that promotes cavitation.

Phase space trajectory of the water near the pole of the NP is very useful to illustrate this concept. Figure 4.5c shows such a trajectory when the plasma contribution is considered (blue line) and when only heat transfer from the particle lattice is present (red line). In the case where heat transfer is dominated by plasma relaxation, the energy transfer characteristic time is very fast, of the order of τ_{ei} ≈500 fs, much shorter than the liquid-vapour equilibration time (τ_{LV} ≈[10-100] ps) [160]. Water hence experiences a fast quasi-isochoric heating, reaching 47 060K. The supercritical water then relaxes, decreasing its temperature and its density, eventually creating a cavitation bubble. The situation is very different when only heat transfer from the NP lattice is considered. In opposition to the fast heating from the plasma, the heat transfer in the case of lattice conduction is much slower, in the order of τ_{lw} ≈100 ps≈ τ_{LV}. Water would then experience a slow heating on the saturation curve (green line), leading to a much more modest pressure build-up of 19 MPa and a temperature of 546 K, slightly below the critical temperature. The water would then relax, still on the saturation curve, leading to no significant density decrease and hence no cavitation bubble generation. Heat transfer from the plasma is thus necessary to explain the formation of the vapour bubble that is detected experimentally.

As seen from figure 4.5a, the bubble collapse time (104 ns) is about 44% longer than the bubble growth time (72 ns), leading to an asymmetric time-shape. This asymmetry is a consequence of the large pressure under which the bubble is formed, leading to a very fast initial expansion. However, this asymmetry is not important enough to explain completely the asymmetric time-shape observed experimentally, where the bubble collapse time (≈300 ns) is about 275% longer than the bubble growth time (≈80ns). This much larger asymmetry is associated to the presence of bubbles of different sizes and lifetimes within the laser focal volume, arising from the Gaussian fluence distribution of the pump laser. The signal observed for times longer than 175 ns in figure 4.2b is thus associated to the presence of slightly larger

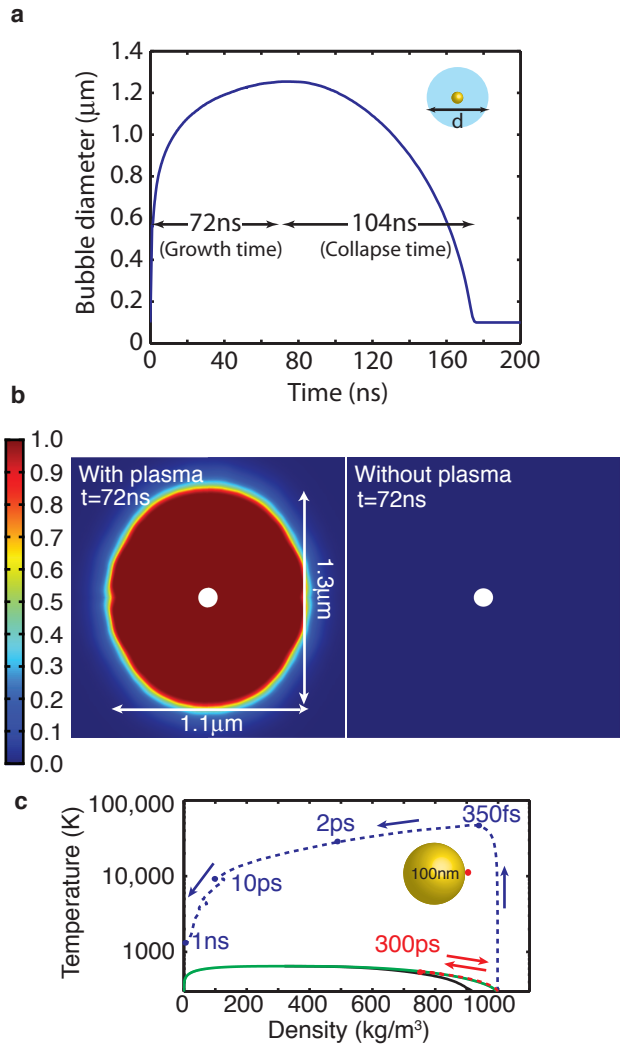

Figure 4.5 Generation of a vapour nanobubble around a 100 nm nanoparticle after a 200 mJ/cm^2, 45 fs, 800 nm laser irradiation. **a**. Time evolution of the average diameter of the vapour bubble created around the NP after the irradiation. **b**. The left panel shows the vapour bubble around the NP, 72 ns after the irradiation. The bubble is at its maximal extension. Dryness fraction is represented on the figure. The bubble boundary is fixed at a 10% dryness fraction. The right panel presents the bubble obtained when the contribution from the plasma is neglected. **c**. Phase space trajectory of water situated near the pole of the NP during the first nanosecond following the irradiation. Green line is the binodal curve, black line is the kinetic spinodal, red line is the trajectory when no plasma is present and blue curve is the trajectory including the plasma contribution. The trajectory when no plasma is present is along the binodal curve and reaches its maximal temperature 300 ps after the laser pulse.

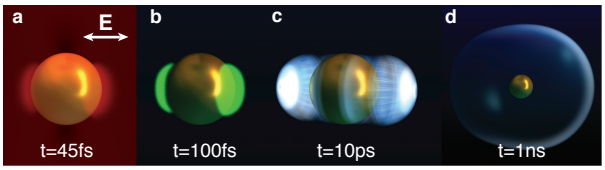

Figure 4.6 Schematics showing the dominant phenomena leading to the formation of a vapour bubble around an off-resonance plasmonic NP irradiated by an ultrafast infrared laser. **a**. Near-field is amplified during the pulse. **b**. Amplified near-field ionizes the surrounding water, creating a nanoplasma near the poles of the particle. **c**. Plasma fast relaxation and plasma-ions collisions heats the water isochorically, generates great stress-confinement and then releases a strong pressure wave in the surrounding medium. **d**. A nanoscale bubble is formed around the particle. The figure sketches the bubble 1 ns after the laser irradiation.

bubbles in the sample, which contribution becomes dominant as the average bubbles collapse and decrease their contribution to the signal.[193]

4.8 Conclusion

In conclusion, irradiating an off-resonance NP with a femtosecond laser initiates a series of phenomena that, under some conditions, leads to the formation of a cavitation bubble. Theoretical and experimental work presented in this paper allow identifying a dominant chain of event leading to cavitation that is presented in figure 4.6. The proposed model predicts that, following the irradiation of an off-resonance gold NP, the plasmonic enhancement of the near-field produces a nanoplasma around the nanostructure. Energy transfer from this plasma is then responsible for the release of a pressure wave and the generation of a cavitation bubble around the particle. It has been shown that heat transfer from the lattice alone would not yield such a cavitation bubble at that fluence, whereas its existence is experimentally confirmed, with a deduced diameter (813 nm) and growth time (80 ns) for a laser fluence of 200 mJ/cm^2, in good agreement with the calculation from the model (1.2 μm and 72 ns). This result strongly supports the plasma mediated plasmonic enhanced ultrafast laser nanocavitation brought forward in this work. It also clearly demonstrates the possibility to create vapour nanobubbles in a liquid environment using the NPs scattered near-field instead of relying on NPs extreme heating. As nanobubbles has been pointed out as very important for laser induced cellular damage, in particular for cell membrane optoporation, a deeper understanding of the basic mechanisms leading to cavitation provides the tools required to further develop and optimize new technology involving plasmonic enhanced ultrafast laser interaction with cells.

CHAPITRE 5

Plasma-Mediated Nanocavitation and Photothermal Effects in Ultrafast Laser Irradiation of Gold Nanorods in Water

Ce chapitre retranscrit un article soumis à Journal of Physical Chemistry C en 2012 [1]. Il présente les différents mécanismes d'interaction entre une impulsion laser femtoseconde et un nanobâton résonant en fonction de la fluence d'irradiation. Il démontre l'existence de deux régimes d'interaction. À basse fluence, l'énergie est majoritairement absorbée par le nanobâton menant à une rapide augmentation de sa température et à l'excitation de modes vibrationnels caractéristiques. À haute fluence, de façon similaire au cas des particules hors-résonance présenté au chapitre précédent, un plasma est formé directement dans le champ proche amplifié autour du nanobâton et sa relaxation mène à la formation d'une bulle de cavitation. Les résultats démontrent cependant que la formation de la bulle s'accompagne d'un endommagement significatif de la structure. Les résultats finalement révèlent une importante modification des propriétés optiques du nanobâton due à la présence de plasma dans son environnement. Un document complémentaire qui apporte des précisions sur les oscillations mécaniques observées expérimentalement et détaille la méthode permettant d'obtenir le diamètre maximal de la bulle à partir des études spectroscopiques est présenté en annexe B.

5.1 Authors

Etienne Boulais, Rémi Lachaine & Michel Meunier

Laser Processing Laboratory,
Department of Engineering Physics, École Polytechnique de Montréal,
CP6079, Succ. Centre-ville, Montréal, QC, Canada, H3C 3A7.

5.2 Abstract

We present a theoretical and experimental study that reveals the physical mechanism underlying the response of an in-resonance gold nanorod (AuNR) in water to a near infrared

1. E. Boulais, R. Lachaine et M. Meunier. Plasma-Mediated Nanocavitation and Photothermal Effects in Ultrafast Laser Irradiation of Gold Nanorods in Water. *J. Phys. Chem. C*, Manuscript ID : jp-2012-12475h, 2012

ultrafast laser pulse. Results reveal the presence of two different regimes of interaction, depending on the irradiation fluence. For fluences below 3 mJ/cm^2, AuNRs are in the so-called absorption regime and are shown to strongly absorb energy, leading to a fast temperature increase revealed by the onset of characteristic mechanical vibration of the structure. In-situ measurement demonstrates a permanent deformation of the AuNRs occurring for fluences over 100 μJ/cm^2. In the absorption regime, we show the formation of a nanoscale plasma around the structure, dominated by a photothermal emission from the AuNR, and the generation of a pressure wave. However, no cavitation occurs under the deformation threshold fluence (100 μJ/cm^2). For fluences over 3 mJ/cm^2, in the near-field regime, the energy transfer is dominated by the enhanced near-field around the particle that directly ionizes and heats a nanoplasma in the surrounding water. We theoretically and experimentally show that bubbles with diameters ($\approx$[200-600] nm can be generated in this near-field regime for fluences around [100-400] mJ/cm^2. Important shielding of the laser-nanostructure interaction by the surrounding plasma is shown to decrease considerably the near-field enhancement, the energy absorption and the diameter of the generated bubbles.

5.3 Introduction

Gold nanoparticles (AuNPs) interacting with laser beam have been extensively used in the past few years in biological medium as nanoheaters [20–24, 26, 27, 32–34], imaging contrast agents [21, 22, 58, 329–331], biosensors[18], drug delivery vectors [332, 333] and vapor bubble generators [70, 180, 191] for photothermal imaging [194, 195, 334, 335], photothermolysis [194, 267, 275, 276] or gene therapy applications [57, 294, 295]. The principal characteristic that makes gold NPs so interesting is the possibility to induce a so-called plasmonic resonance in the metal when interacting with an electromagnetic field at a particular wavelength, depending on the size, environment and structure of the NPs. This phenomenon, first described by the celebrated Mie theory [67], consists in the excitation of a collective oscillation of the conducting electrons in the nanostructure, resulting in unusually strong absorption and scattering properties when compared to other non-plasmonic micro and nano absorbers [92]. For spherical gold NPs in water, this resonance occurs for an incident irradiation wavelength near 540 nm, with a weak dependance on the particle dimensions.

For biological applications, it is usually advantageous to work in the optical window of biological material (600 nm-1100 nm) [82] to avoid issues concerning collateral damage to tissues during treatment or to enhance the effective depth. Since gold NPs resonance lies outside this window, gold nanorods (AuNRs) [19, 25, 89–92] and core-shell [28–30, 92] have been proposed as alternative structures having resonance in the near-infrared portion of the

electromagnetic spectrum. Optical properties of AuNRs have been extensively studied [89, 92] and the presence of the second plasmon resonance peak in the near infrared region has been associated to an electron oscillation along the long axis of the NR. The wavelength at which this resonance occurs has been in addition shown to be highly dependent on the length over diameter ratio, making these nanostructures particularly interesting for applications.

Ultrashort pulse laser irradiation of AuNRs, depending on the fluence, are used for in-vitro and in-vivo imaging [90, 91, 98, 336, 337], hyperthermal therapy [59] and targeted thermolysis [90, 91], the later being intimately associated with the formation of vapor bubbles in the cellular environment [57, 276, 294].

In this work, we investigate the response of in-resonance AuNRs in water after being irradiated with near-infrared (NIR) ultrashort pulses as a function of the irradiation fluence. Experimentally supported theoretical results reveals the presence of two distinct regimes of interaction. We will show that for fluences lower than 3 mJ/cm^2, the energy absorbed in the AuNRs dominates the energy absorbed in the near-field. The action of the AuNRs on its environment is then limited to thermal effect and to the generation of a nanoscale plasma around the structure due mainly to photothermal emission. We call this regime the absorption regime. In-situ spectroscopic measurement allows identifying a damage fluence threshold beyond which the plasmonic properties of the AuNRs are degraded, defining a fluence process window suitable for applications. At higher fluences, results reveal that the near-field enhanced laser irradiation creates and excites a nanoscale plasma directly in the water around the structure. We call this regime the near-field regime. At sufficient fluences, this plasma is shown to trigger a series of events leading to the formation of ∼200-600 nm vapor bubbles in the surrounding medium. Shielding of the laser-plasmon interaction by this plasma will also be shown to alter considerably the AuNRs' response to the ultrafast laser irradiation.

5.4 Experimental and Theoretical Methods

5.4.1 Modelling the ultrafast laser interaction with AuNRs

We developed a complete model that includes the different phenomena that occur following the irradiation by an ultrafast laser of a resonant AuNR in water. Those phenomena are presented in figure 5.1. Models previously proposed in the literature [172, 235] usually neglect plasma formation in the surrounding medium. However, this plasma, which is generated through a combination of direct photoionization by the enhanced near-field and temperature-assisted photothermal emission from the surface of the nanostructure, turns out to have important effects, especially at high fluences. In particular, the presence of the

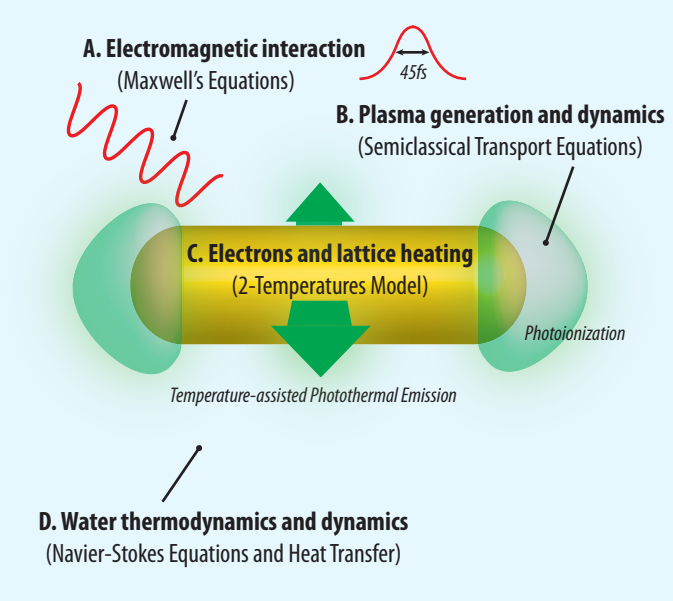

Figure 5.1 Schematic picture of the laser interaction model describing various phenomena occurring in a AuNR and in the surrounding water following laser irradiation. The letters A, B, C, and D indicate the four tightly coupled sub-models. Sources of plasma are shown in italic.

plasma in the AuNR's environment modifies the local permittivity, and has consequently an important impact on the optical properties of the AuNR and the enhanced near-field. The field distribution around the AuNR is calculated from the Helmholtz equation, considering the bulk gold optical properties and the locally modified water permittivity. From the field distribution, the electronic and lattice temperatures are calculated using a two-temperature hyperbolic model based on the semiclassical Boltzmann transport equation [309]. The density and energy time-dependent distributions of the plasma generated in the enhanced near-field are calculated using transport equations. A Navier-Stokes equation system added to a heat transfer equation and supported with an adequate equation of states is used to calculate the thermodynamic state of the water at all time. A combination of the IAPWS95 [170] and SESAME [322] equations of state ensures a sufficient validity range.

The phase change of the water is handled using the phase diagram defined by the equation of state. Under the saturation curve, liquid water is in a metastable state until it reaches the kinetic spinodal that represents the limit of mechanical stability where phase explosion occurs [72, 177]. Beyond that limit, water pressure returns to the saturation pressure and all other parameters return to their phase equilibrium value as water undergoes a phase transformation to a homogeneous liquid-vapor mixture at equilibrium. Surface tension is applied

at the interface of the bubble, fixed at a vapor dryness fraction of 10%. This method has the inconvenient to induce the formation of a smooth water/vapor transition instead of a sharp interface. It has however been proven to adequately capture the pressure and density evolution in water [235]. A finite-element scheme is used to solve the system of tightly coupled differential equations. Extensive discussion on the modelling, including precise equations and details on the used parameters, is presented elsewhere [70]. The mathematical model was solved using a finite-element method, using the Comsol software (www.comsol.com).

5.4.2 Deformation threshold fluence (DTF) measurement

The deformation of AuNRs has been induced using a Ti :Sapphire, 6 mJ/pulse, 45 fs, 800 nm laser (Spitifre from Spectra-Physics) with a 1 kHz repetition rate. A $1\times1\text{cm}^2$ four faces polished cuvette containing 2 mL of AuNRs with a concentration of 45 μg/mL in a water suspension has been irradiated for 12 hours with different fluences. The Gaussian beam spot diameter (measured at $1/e^2$) was 0.9 cm. The maximum fluence at the center of this Gaussian spot (twice the average fluence) has been considered. Extinction spectrum has been recorded every minute perpendicularly to the femtosecond laser beam using a StellarNet EPP2000 spectrometer from SpectraWiz.

5.4.3 Pump-probe measurements of AuNRs vibration

The 1 KHz, 45 fs, 800 nm laser beam has been separated in two beams (pump and probe) using a beamsplitter for ultrashort pulses. Pump beam maximal fluence was set to 100 $\mu\text{J/cm}^2$ at the center of the 0.9 cm (at $1/e^2$) diameter Gaussian beam. Probe beam fluence was 0.2 $\mu\text{J/cm}^2$ with a 0.1cm diameter. The much lower probe fluence ensures the pump beam dominance on excitation. Both beams were quasi-collinearly aligned (1.3° between beams) and probe beam was centered to the pump beam at the front end of the cuvette containing the AuNRs solution. Both polarizations were horizontal. Probe delay was set using two mirrors installed on an IMS600PP linear stage from Newport with a 1.25 μm resolution. The setup time resolution was limited to 500 fs due to the angle between the probe and pump beams. Beams were separated geometrically using this angle. Probe beam has been detected using a DET100 photodiode connected to a SR510 lock-in amplifier from Stanford Research Systems.

5.4.4 Cavitation bubble detection

A He :Ne, continuous wave, 5 mW, 633 nm probe beam has been collinearly aligned with the femtosecond beam. Both beams were focused into the AuNRs sample. The femtosecond pump laser repetition rate is set at 4 Hz for this experiment and a typical acquisition last

under 100 s. The low pump laser repetition rate is equivalent of using multiple single-shot experiments. Note that the cw probe irradiation was insufficient to induce significant heating in the sample. The waists of both beam (fs pump and cw probe) were set to (6±1 μm). The probe beam scattered field was filtered out using a spatial filter (15 μm diameter pinhole). Extinction cross-section change was thus detected. This detection was made using a Si 1-GHz photodiode with a 0.6 ns rise time connected to a 500 MHz Agilent oscilloscope.

5.5 Results and Discussion

5.5.1 Optical properties of gold nanorods

In this work, we focus on the interaction between a 45 fs, 800 nm ultrafast laser with a 10×41 nm^2 AuNRs colloidal suspension. Figure 5.2a shows the calculated absorption, scattering and extinction spectrum for such a sample. The optical properties are calculated from the field distribution simulated using the finite-element scheme discussed above. To account for the random orientation distribution of the sample, the calculation is performed for several polarizations and propagation vectors orientations relative to the AuNR's longitudinal axis. The result presented in Figure 5.2a is obtained by averaging the individual contribution from each orientation. Note the two plasmon peaks, a large one near 800 nm corresponding to the excitation of the longitudinal plasmon band (LP) and a smaller one near 510 nm associated to the transverse plasmon band (TP). The irradiation wavelength (800 nm) thus lies directly on the LP of the AuNRs. As can be seen from figure 5.2a, energy at this wavelength is mainly absorbed by the AuNRs, although a small amount is scattered in the medium. Figure 5.2b shows the enhanced near-field around the AuNR when the light polarization is aligned with the rod's longitudinal axis. Strong field enhancement ($|E|/|E_0| \approx 77$) is visible near the tips of the rod, while noticeable field absorption exists in the central part. It is important to notice that the optical properties and field distribution around the AuNR are highly orientation-dependent. Figure 5.2c shows the field distribution around a AuNR still at the resonance wavelength corresponding to the LP excitation (800 nm), but with a light polarization now perpendicular to the longitudinal axis. Results show that this polarization inhibits the excitation of plasmon in the LP band. The laser energy is thus only weakly absorbed, although some scattering remains, leading to a small enhancement in the near-field ($|E|/|E_0| \approx 2.9$). Since the contribution from AuNRs aligned with the incident polarization is clearly dominant, theoretical results presented in this work will only consider those AuNRs. However, we must keep in mind that the experimental results have been obtained from randomly distributed colloidal samples that include the contribution of misaligned AuNR as well.

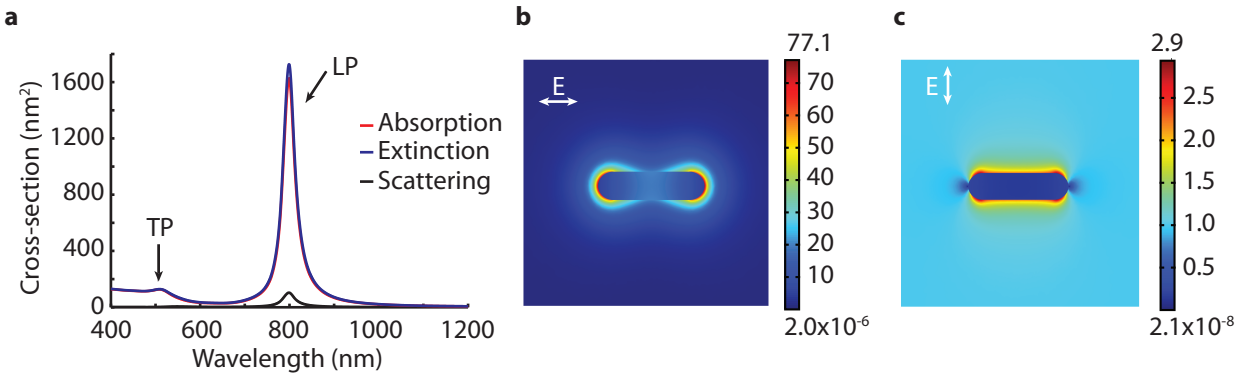

Figure 5.2 Optical properties of 10×41 nm^2 AuNRs. **a**. Calculated absorption, scattering and extinction cross-sections for randomly distributed AuNRs in water as a function of the incident wavelength. Peaks associated with the longitudinal plasmon band (LP) and the transverse plasmon band (TP) are indicated on the figure. **b**. Cross-section of the electric field enhancement distribution in and around a AuNR, showing both field absorption in the particle and near-field enhancement near the tips, when irradiated with a 800 nm linearly polarized along the rod's longitudinal axis . **c**. Cross-section of the electric field enhancement distribution in and around a AuNR, showing almost no field absorption in the particle and weak near-field enhancement, when irradiated with a 800 nm linearly polarized perpendicular to a rod's longitudinal axis .

5.5.2 The existence of two regimes of irradiation

The last section concerned only the linear optical properties of the AuNR that are insufficient to describe completely the physics of the interaction with an ultrafast laser. Indeed, while at low fluences the absorption cross-sections calculated from the linear theory are fairly accurate, the energy absorbed directly in the water by non-linear interaction in the near-field at higher fluences justifies the need for a complete non-linear theory.

Using the model presented in the Theoretical Methods and detailed elsewhere [70], we calculated the total energy deposited in the system by a 45 fs, 800 nm ultrafast laser pulse linearly polarized along the AuNR's longitudinal axis as a function of laser fluence. Figure 5.3 shows separately the energy absorbed in the AuNR (blue line) and in the plasma around the AuNR (green line) as a function of laser fluence. Note that the absorbed energy is presented as a cross-section. A transition from a linear to a non-linear regime as the laser fluence is increased is clearly visible from the figure.

The blue line in Figure 5.3 represents the absorption cross-section of the AuNR itself (σ_{abs}^{AuNR}), which in the limit of low fluences, is precisely the linear absorption cross-section. Note that the apparent discrepancy with the results shown in 5.2a comes from the fact that those results included random contribution from misaligned AuNRs, whereas results presented in Figure 5.3 only considers aligned AuNRs.

In Figure 5.3, the green line is the non-linear absorption cross-section arising from the contribution of the plasma (σ_{abs}^{plasma}) created in the near-field around the AuNR. As the fluence is increased, contribution from σ_{abs}^{plasma} becomes more and more important, while σ_{abs}^{AuNR} decreases due to what we will show to be shielding from the plasma. For fluences $F > F_{th}$ =3 mJ/cm^2, contribution from the plasma exceeds the absorption in the AuNR. This value is in agreement with a recent study from Bisker et al. that calculated a fluence around 2 mJ/cm^2 as the threshold for optical breakdown in the water surrounding a 14×56nm^2 AuNR irradiated with a 45 fs, 808 nm laser pulse [256].

F_{th} represents the limit between two distinct regimes of irradiation. For fluences $F < F_{th}$ =3 mJ/cm^2, the laser interaction is dominated by the energy absorption within the AuNR itself. This regime is thus called "the absorption regime". For fluences over F_{th}, the laser interaction is dominated by the energy absorbed by the plasma in the near-field. This regime is hence called "the near-field regime". The next sections are devoted to the exploration of the basic mechanisms of the ultrafast laser irradiation of AuNRs in both regimes.

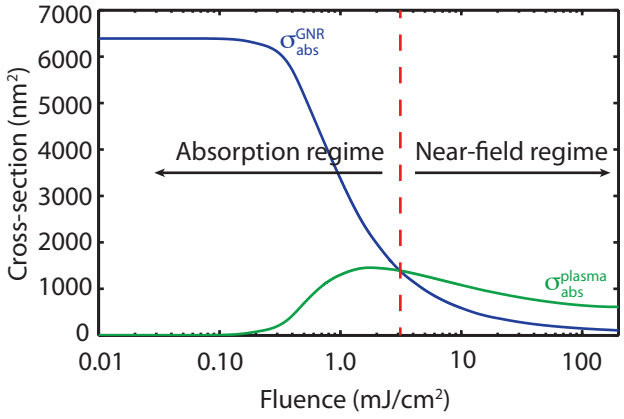

Figure 5.3 Cross-section of the energy absorbed in the AuNR (blue line) and the energy absorbed in the surrounding plasma (green line) for a $10\times41\text{nm}^2$ AuNR aligned with the polarization of a 800 nm, 45 fs laser pulse. The frontier between the absorption regime and the near-field regime is also indicated on the figure (dashed red line).

5.5.3 The absorption regime

Deformation of the AuNRs

As mentioned in the last section, the absorption regime is characterized by an energy absorption occurring in majority in the AuNR itself, the enhanced near-field being too weak to induce important non-linear energy absorption in water. According to figure 5.3, absorption in the near-field overcomes energy absorption in the particle for fluences larger than F_{th} =3 mJ/cm^2, giving a superior limit to the absorption regime. However, energy absorption in the AuNRs leads to a temperature increase in the lattice that may lead to deformations that can alter their plasmonic properties. We define the deformation threshold fluence (DTF) as the fluence from which the AuNRs' optical properties, monitored in real-time with a spectrometer (see figure 5.4a), are significantly degraded after a 12 h irradiation at 1 kHz. This long irradiation time ensure reaching homogeneity in the sample. As seen from figure 5.4b, a blue shift of the extinction peak is visible when the laser fluence reaches ≈100 μJ/cm^2. This blue shift arises most probably from the gradual transformation of the resonant AuNRs into small off-resonance spherical NPs [261, 338], which extinction cross-section is much smaller than for the AuNRs at 800 nm. The peak blue shift thus allows to measure a DTF around 100 μJ/cm^2. Note that the exact value of the DTF remains quite arbitrary and is function of the tolerance requirement regarding a specific application. For the vast majority of applications involving low fluence irradiation, it is very desirable that the AuNRs remain intact after the laser irradiation. In what follow, we will thus only consider fluences that lie around or below

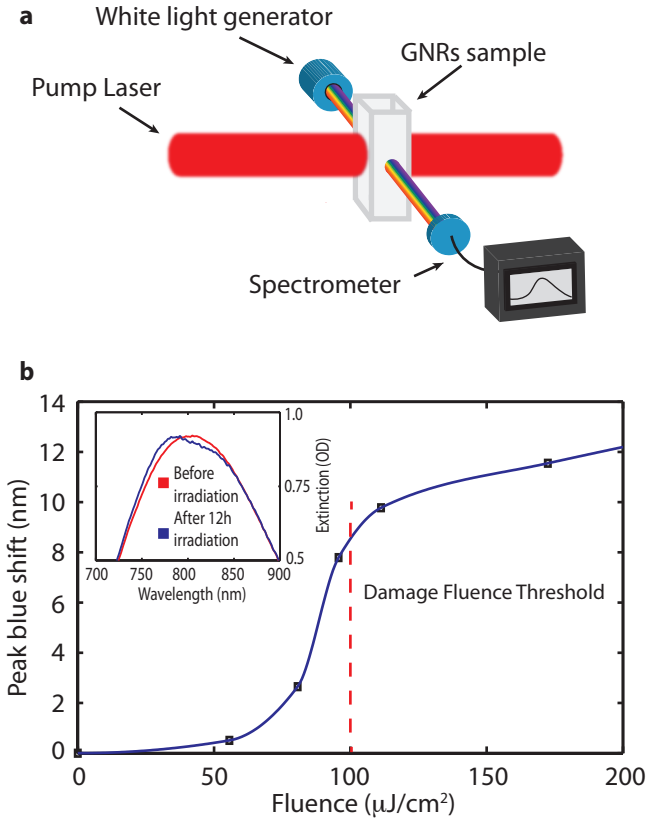

Figure 5.4 Deformation threshold fluence (DTF) for $10\times41\text{nm}^2$ AuNRs. **a**. Optical setup used to measure the DTF. A 45 fs, 1KHz, 800 nm laser irradiates a AuNRs sample during 12 h. The AuNRs optical spectrum is monitored in real-time during the irradiation. **b**. Blue shift of the position of the extinction peak of the AuNRs sample as a function of the pump laser fluence. Comparison of the shape of the peak before and after irradiation at a fluence of 500 $\mu\text{J/cm}^2$ is shown in inset.

the DTF (100 μJ/cm^2) and explore in greater depth the laser-nanostructure interaction in what one could call the "sub-deformation threshold absorption regime" that is suitable for most applications.

AuNR heating

The absorption regime at fluences below the deformation threshold is characterized by a limited impact on both the AuNRs and their surrounding medium, though some effects are still present. In this regime, the laser electromagnetic field is mainly absorbed by the nanostructure, as shown by the clear predominance of the absorption cross-section over the scattering cross-section at 800 nm (see figure 5.2a). Electrons transfer their energy to the lattice in a few ps ($\tau_{e-ph} \approx$1 ps) [141], rapidly heating the nanostructure. This fast temperature increase creates a stress state in the AuNR that results into rapid structural oscillations that are readily observable using a pump-probe optical setup (figure 5.5a) that exploits the variation of the extinction cross-section with the modification of the AuNRs' aspect ratio. In this experiment, a femtosecond laser pulse is split in two pulses. The first pulse is called the pump and is directed to the sample to excite the AuNRs. The second pulse is much lower in intensity and is called the probe pulse. This pulse first passes through an adjustable delay line before being directed to the sample, so that it arrives with a certain tunable time delay relative to the pump pulse. The transmission of the probe pulse is then measured, providing information on the state of the AuNR at the specific time corresponding to the time delay. Varying this delay, one can obtain a complete time-dependent characterization of the laser interaction.

Figure 5.5b shows the oscillation in the transmission of the probe beam as a function of the delay with the pump pulse. The measured period (63 ps) is in good agreement with the 64 ps period predicted by the thin rod theory [233]. The damping of the oscillation results from the combination of viscous stress between the rod and its environment, called homogeneous damping, and an inhomogeneous damping due to the rods' size distribution within the sample [230]. Based on TEM imaging of the sample and a simple model linking the rod's size distribution to a specific oscillation period and damping (see figure 1 in the Supporting Information), the red curve in figure 5.5b presents the simulated variation in the extinction due to the oscillations. The very good agreement indicates that the signal indeed originates from the AuNRs' structural oscillations.

Figure 5.6 shows the simulation results for the temperature reached at the centre of the AuNR as a function of the incident fluence. Figure 5.6a also indicates the theoretical melting temperature for 10×41 nm^2 AuNRs (1254 K), about 10% lower than the bulk melting point because of the reduced dimensionality [314] (See Supporting Info). Results show that

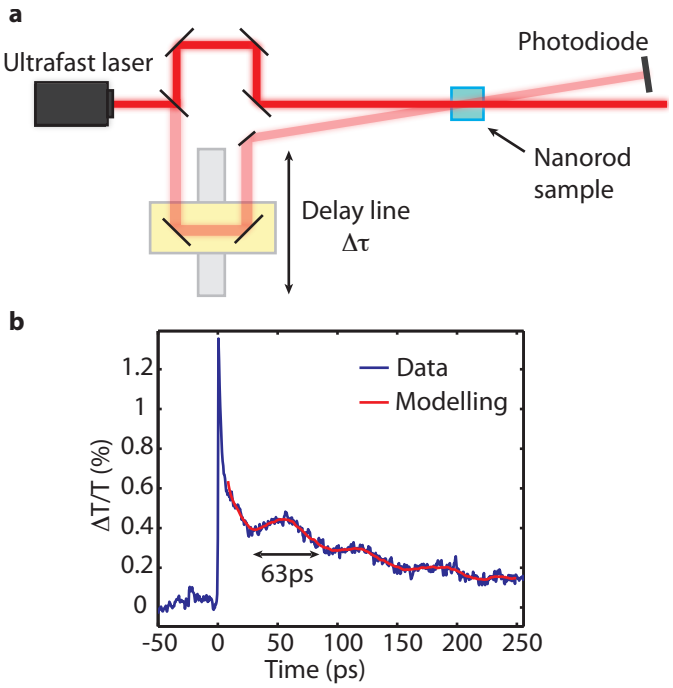

Figure 5.5 NR oscillations following a 100 μJ/cm^2, 45 fs irradiation. **a**. Pump-probe optical setup used to probe the oscillation. The ultrafast laser beam is splitted in two. The pump beam is directed at the sample while the much lower intensity probe beam passes first through a delay line. Probe intensity is recorded using a photodiode. **b**. Experimental (blue line) and simulated (red line) variation in the sample extinction as a function of time. The time origin is fixed at the pump irradiation time.

this temperature is reached for a fluence slightly over 120 μJ/cm^2, in good agreement with the experimental DTF of 100 μJ/cm^2. A deformation threshold somewhat below the melting threshold, as reported by Link et al.[261], seems indeed reasonable as high surface energy may lead to important restructuration before complete melting occurs. Link et al. experimentally determined that $\sim$60 fJ were required to melt 11$\times$41nm^2 AuNR completely and observed shape transformation after the absorption of $\sim$12 fJ [339] . This is consistent with our result as $\sim$6 fJ per pulse is deposited in the AuNR at 1 KHz at the DTF. Figure 5.6 also presents the temperature reached in the water at the boundary with the AuNR. This result will be discussed in the section "Pressure wave generation and bubble formation".

Plasma formation

In addition to heat generation in the AuNR, irradiation also triggers the generation of an electronic nanoscale plasma around the structure. This nanoplasma comes from the direct photoionization and collision ionization in the near-field, as well as from a photothermal emission at the metal/water interface [70]. Figure 5.7a shows the plasma generated around the structure 100 fs after a 100 μJ/cm^2 irradiation. Maximal plasma density occurs in the central region of the AuNR. This is a consequence of the photothermal emission process being dominant over the photoionization process at low fluences. This reflects the huge energy absorption cross-section compared to the energy scattering cross-section at 800 nm. Maximal plasma density thus occurs near the place where the energy is absorbed the most, heating up electrons in the AuNR and favoring thermal emission into the surrounding water.

Electronic plasma is known to contribute to damaging cells through chemical interactions [72]. Plasma density as low as 1.5$\times$10^{14} cm^{-3} has been reported to induce cell damage, and density of 2$\times$10^{16} cm^{-3}, to be able to dissect intracellular organites. AuNRs irradiated in the absorption regime may thus be used as generators of nanoplasma that can be used to locally interact with cellular components in the context of nanosurgery. As shown in figure 5.7b, maximal density reached in the vicinity of the AuNR gets over those reference plasma densities for irradiation fluences greater than 1 μJ/cm^2. Once created, plasma diffuses and can affect a certain volume around the structure. Figure 5.7c shows the radius of the zone affected by the above mentioned reference plasma densities as a function of the laser fluence. As seen from this figure, this volume can be finely tuned by changing the laser fluence, leading to the possibility of highly localized processes.

Though the presence of this plasma is desirable for certain applications, it can rather become a problem for others. For instance, the use of AuNRs as imaging contrast agents or biodetectors requires a minimal impact of the laser irradiation on the surrounding cell environment. However, as seen from figure 5.7c, the radius of the affected zone can get quite

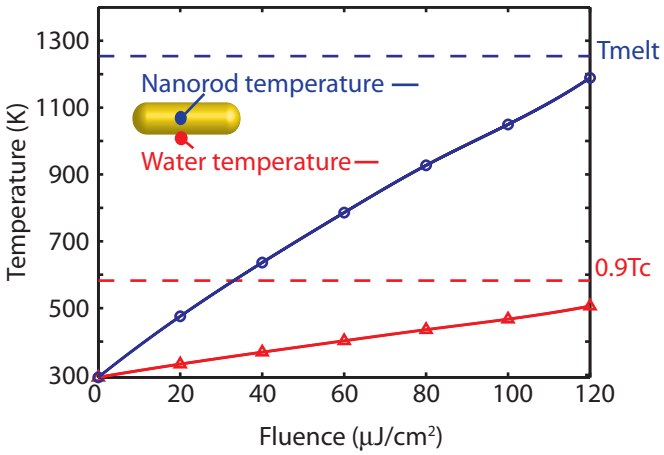

Figure 5.6 Simulated maximal temperature reached inside the AuNR (blue line) and in the surrounding water (red line) as a function of fluence following a 45 fs, 800 nm single pulse irradiation. The AuNR melting temperature (dotted blue line) and the $0.9T_c$ limit for water (dotted red line) are indicated on the figure.

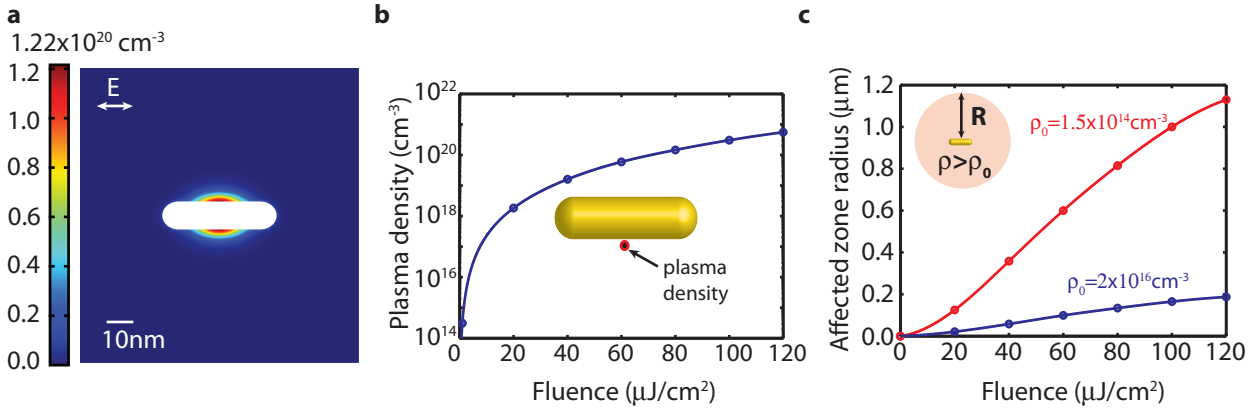

Figure 5.7 Plasmonic enhanced generation of nanoplasma. **a**. Cross-section of the nanoplasma distribution around the AuNR 100 fs after the maximum of a 45 fs, 800 nm, 100 μJ/cm^2 laser pulse. **b**. Maximal plasma density reached in the water as a function of the incident laser fluence. **c**. Maximal radius of the zone affected by a plasma with a density of 2×10^{16}cm^{-3} (blue line) and 1.5×10^{14}cm^{-3} (red line).

significant depending on the fluence. For instance, at 100 μJ/cm^2 a density of 2×10^{16}cm^{-3} is reached up to 165 nm from the AuNR, and a density of 1.5×10^{14}cm^{-3}, as far as 1.0 μm. The possibility of chemical damage brought by the photothermal emission should thus be taken into consideration and limit the range of suitable fluences when planning to use AuNRs in such applications.

Pressure wave generation and bubble formation

A combination of heat transfer from the plasma relaxation and from the AuNR lattice through a conduction process causes a fast temperature increase in the water medium in ∼50 ps. At those fluences, the heat transfer from the conduction process is largely dominant over the plasma-mediated heat transfer. Stress confinement is created, releasing a pressure wave upon its relaxation. Figure 5.8a shows the pressure around the AuNR, 10 ps after a 100 μJ/cm^2 irradiation. The maximal pressure (≈8 MPa) is located near the central part of the AuNR. As shown in figure 5.8b, the maximal pressure observed in the water range from ∼2-14 MPa for irradiation fluences between 10 μJ/cm^2 and 120 μJ/cm^2.
The onset of cavitation is often evaluated as the fluence required to heat the surrounding water above the $0.9T_c$ =582 K limit [159, 172, 234], indicated by a red line on figure 5.6. From this crude approximation, the theoretical cavitation onset should be slightly over 120 μJ/cm^2 as temperature at this fluence only reaches $\sim 0.88T_c$. The complete hydrodynamic model confirms this prediction and does not show the formation of a vapor bubble around the AuNR at 120 μJ/cm^2. This result is consistent with the one obtained by Ekici et al. [172] who theoretically determined a somewhat higher 450 μJ/cm^2 cavitation fluence threshold for 14×48 nm^2 NRs irradiated with a 250 fs, 760 nm pulse. Their model however did not consider any plasma generation. Our results thus demonstrate that, though 10×41nm^2 AuNRs are in-resonance with the irradiation and thus highly enhance the near-field, it is not possible to generate cavitation bubbles around them without damaging, deforming or even destroying them. This represents a major drawback of the use of AuNRs for the generation of vapor bubbles since it prohibits any multipulses operation. In addition, destruction of the AuNRs could lead to the creation of small particles that can be harmful to the cellular environment [57].

5.5.4 The near-field regime

For fluences larger than 3 mJ/cm^2, figure 5.3 shows that the laser intensity in the near-field become important enough to trigger a non-linear absorption directly in the surrounding

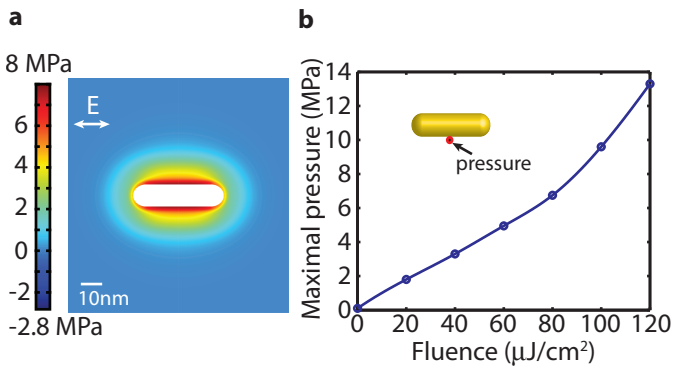

Figure 5.8 Pressure wave release in water. **a**. Cross-section of the pressure distribution around a AuNR 10 ps after a 100 μJ/cm^2, 45 fs, 800 nm laser impulsion. **b**. Maximal pressure reached around the nanostructure as a function of the incident laser fluence for a 45 fs, 800 nm laser impulsion.

water that overcomes the absorption in the nanostructure. The energy absorption process is then controlled by the enhanced electric field in the near-field of the nanostructure, hence justifying the name "near-field regime". Irradiation of AuNRs in that regime is principally motivated by the possibility to create nanoscale vapor bubbles around the structures with diameters in the (≈200-600 nm) range.

Experimental detection and characterization of the vapor bubbles

Those bubbles cannot be readily measured and characterized using direct microscopy technique, but can be detected using an in-situ optical detection setup described in figure 5.9a.

This setup exploits the variation in the extinction cross-section of the irradiated sample due to the presence of the vapor bubble around the AuNRs to evaluate their dimensions. A first laser, the ultrafast pump laser (45 fs, 4 Hz, 800 nm, 100 s acquisition time), is focused in a sample (1 cm wide cuvette) containing the AuNR suspension. At such large fluences, rods are expected to be heavily damaged by the ultrafast laser pulse. The slow 4 Hz repetition rate however allows an adequate mixing of the AuNR suspension between each pulse, ensuring that only undamaged AuNRs interact with each pump laser pulse. A second laser, the probe laser (CW, 633 nm, 5 mW), is collinear with the pump laser and its transmission through the sample is measured with a photodiode. It is possible to deduce the mean bubble diameter using Mie theory. More details on the technique is available elsewhere [70, 197].

Figure 5.9b shows a typical signal obtained at 200 mJ/cm^2. The increase in intensity near 0 ns is attributed to non-linear effects due to the high intensity ultrafast laser, including

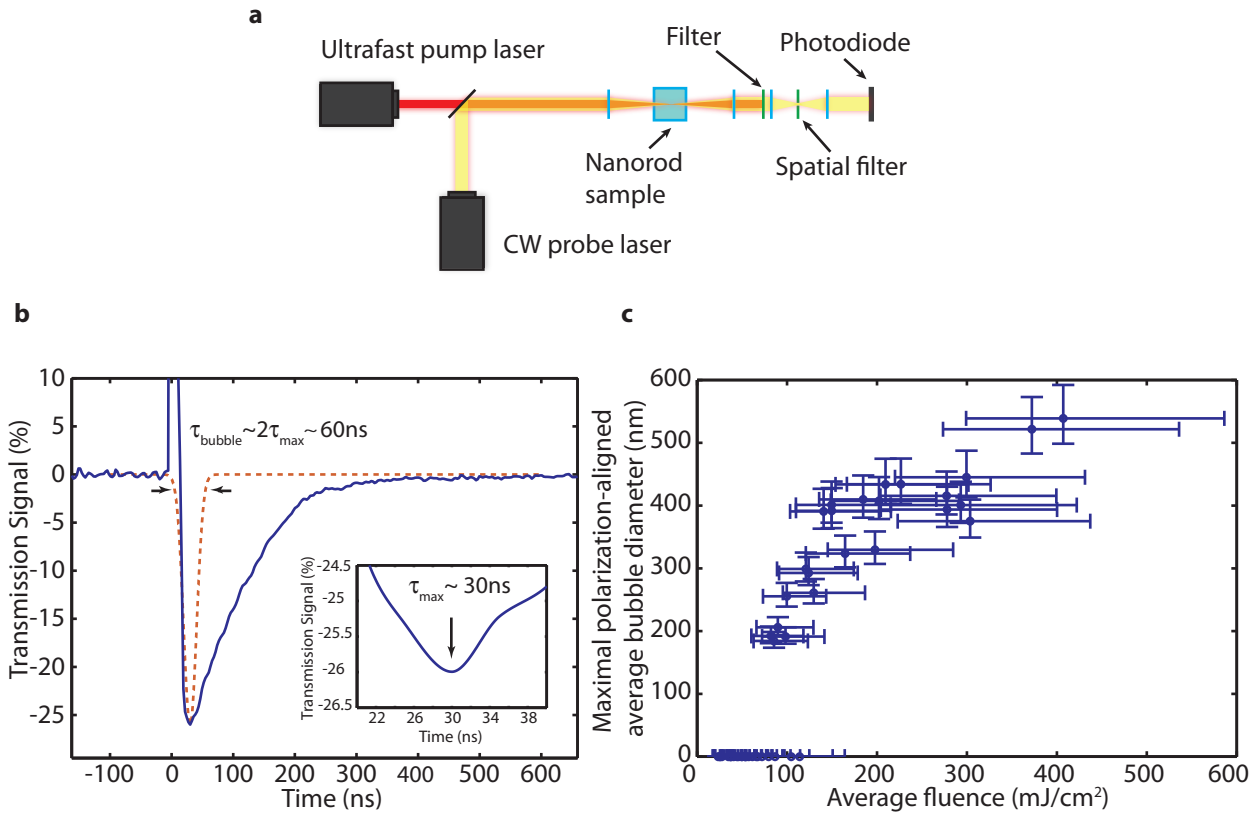

Figure 5.9 Characterization of plasmonic enhanced generated bubbles . **a**. In-situ detection system for the detection and characterization of the bubbles. The ultrafast 800 nm pump laser is focussed into the sample containing the AuNRs to generate the bubbles, and is then filtered out. The CW 633 nm probe laser is coaligned with the pump beam and pass through a spatial filter (pinhole) before being measured by a photodiode. Scattered field is blocked by a spatial filter, so that the variation in power detected in the photodiode can be associated to a change in the extinction cross-section. **b**. Experimental variation in the transmission signal of the probe beam following a 200 mJ/cm^2, 45 fs irradiation. A zoom near the minimum (≈30 ns) is shown in inset. The red curve sketches the contribution associated with the polarization-aligned average bubble. The approximate lifetime of the polarization-aligned average bubbles is indicated on the figure **c**. Deduced average bubble diameter as function of laser fluence.

self-phase modulation and plasma emission. We can see from this figure a very rapid growth time for the bubble (≈30 ns), followed by a relatively slow recovery (≈300 ns). This slow recovery time is associated to the presence of many bubbles of different sizes, and thus different lifetimes, in the focal volume and to the presence of dephasing oscillating bubbles that contribute to the total signal [70, 193]. This situation may originate from the fluence distribution within the focal volume, but also from the laser interaction with agglomerated AuNRs and gold nanospheres that are inevitably present in the sample. Some scattering may also come from thermal lensing due to the temperature increase in the focal volume.

Figure 5.9c shows the mean bubble average diameter produced around AuNRs aligned with the polarization as a function of fluence. The method used to obtain this result from the modification of the transmission of the probe laser is described in details in the the Supporting Info. In summary, it consists in writing the experimentally measured absorption coefficient as a function of the extinction cross-section of individual bubbles, knowing the concentration of the AuNRs and the dimension of the focal volume. It is then possible to deduce the diameter of the bubble from electromagnetic theory that gives the extinction cross-section of the bubble as a function of its diameter. Corrections accounting for the contribution of misaligned AuNRs are calculated from the fact that the energy deposited in the water (E_d) is roughly proportional to $cos\beta$, where β is the angle between the polarization vector and the AuNR's longitudinal axis, and from the dependence of the bubble's diameter (d_{bubble}) on the deposited energy (E_d), estimated as $d_{bubble} \sim E_d^{0.45}$ by Siems et al. [193]. The interested reader is referred to the Supporting Information for more information.

For a fluence of 200 mJ/cm^2, the average bubble produced in the focal volume by AuNRs aligned with the polarization is measured to be ≈(430±50) nm. Note that this represents an average bubble diameter. A Gaussian pulse with a given fluence (which is in fact an *average* fluence) is indeed composed of a spatial distribution of local fluences in the focal volume. This should thus create a distribution of bubble dimensions in the focal volume. We however consider that the *average* bubble calculated using our method is a good approximation for the size of the bubble produced by aligned AuNRs irradiated at a *local* fluence corresponding to the average fluence of the pulse.

Another common method used to evaluate bubble dimensions is the Rayleigh-Plesset equation that relates the lifetime of the bubble to its diameter [179].

$$\tau_{bubble} \approx 0.092 d_{bubble} \tag{5.1}$$

This formula may be inaccurate for nanoscale bubbles, but still gives a correct approximation of the maximal bubble diameter in those cases. [157, 191]. The application of this method with ensemble measurement is however complicated by the asymmetric time-shape.

Vapor bubbles are usually characterized by growth and collapse times that are fairly symmetric [157, 180, 191]. In the case of an ensemble measurement, this symmetric signal is however superposed with a long-lifetime asymmetric tail that can originate from several phenomena that we already discussed. As this tail is not related to the lifetime of the average bubble, it would not be justified to use the full lifetime of the signal (∼300 ns from figure 5.9a) in the Rayleigh-Plesset formula to calculate the average bubble diameter. Assuming that the maximal observed dip in the transmission signal shown in figure 5.9b is due in majority to the polarization-aligned average bubbles within the sample, we evaluate the growth time of the average polarization-aligned bubble τ_{growth} ≈30 ns for a fluence of 200 mJ/cm^2. According to the known symmetric growth and collapse phase of vapor bubbles, this growth time should approximately correspond to an average bubble lifetime τ_{bubble} ≈60 ns (see dashed red line in figure 5.9b). Using the Rayleigh-Plesset formula, this corresponds to an average diameter ≈650 nm . The error on that value is rather large as the asymmetric tail might influence the position of the minimum in figure 5.9b, making the evaluation of the bubble lifetime very approximate. The order of magnitude of the diameter however corresponds with the ≈430 nm diameter found with the optical scattering method.

Summarizing this experimental section, the optical probing technique presented demonstrates the plasmonic-enhanced generation of vapor bubbles around AuNRs for fluences over ∼75 mJ/cm^2. This optical technique allows evaluating the dimensions of the bubble. However, large errors are introduced by the use of an ensemble measurement. At 200 mJ/cm^2, the diameter of the average polarization-aligned vapor bubbles is ≈380 nm-480 nm. Although this result is approximate, the precision obtained is sufficient for the purpose of this paper that focuses on the cavitation mechanisms rather than on precisely evaluating the diameters of the produced bubble.

Plasma mediated nanocavitation

In order to get a better understanding of the physical mechanism leading to bubble formation after an irradiation of the AuNRs in the near-field regime, we simulated the interaction of a 10×41 nm^2 AuNR aligned with the polarization of a 200 mJ/cm^2 laser pulse. The simulation has been conducted using the complete model presented in the Theoretical Methods and detailed elsewhere [70].

Figure 5.10a and b show the plasma around the nanostructure 100 fs after the irradiation. Results show that, unlike in the absorption regime, plasma is principally formed near the tips of the AuNR. Indeed, enhanced near-field is now important enough to allow the formation of a plasma directly in water by photoionization and impact ionization.

Heat transferred from this plasma increases rapidly the water temperature, creating stress

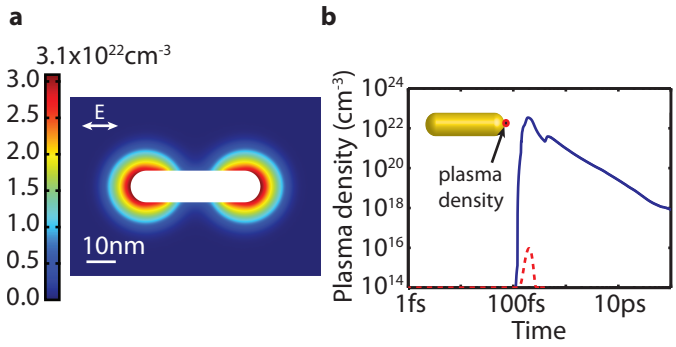

Figure 5.10 Plasma generated around a AuNR after a 200 mJ/cm^2, 45 fs, 800 nm irradiation. **a**. Cross-section of the spatial distribution of the plasma density 10 fs after the pulse maximum. **b**. Plasma density reached at the tip of the AuNR as a function of time (blue line). Time-shape of the 45 fs laser irradiation, centered at 200 fs, is indicated on the figure (dotted red line).

confinement that relaxes, emitting a strong pressure wave that originates from the tips of the AuNRs, where the plasma density is the highest (see figure 5.11a). This contrasts with the result obtained in the absorption regime where the maximal pressure was rather near the center of the AuNR, due to the localization of the photothermal emission and energy absorption in this range of fluence (see figure 5.8a). As shown in figure 5.11b, the magnitude of the pressure wave is around 180 GPa, almost 10^4 times higher than those emitted in the absorption regime, below the DTF.

Following the emission of the pressure wave, a vapor bubble is formed around the structure. Figure 5.11c shows the time evolution of the diameter of this bubble. Simulation shows the formation of a ≈490 nm diameter bubble, a 20 ns growth time and a 45 ns total lifetime. The bubble at its maximal extension is shown in 5.11d. This result is consistent with the experimental results (∼380-480 nm diameter, ∼30 ns growth time and ∼60 ns total lifetime) that were obtained for the average bubbles generated by a 200 mJ/cm^2, 45 fs laser pulse around polarization aligned AuNRs. The very fast initial growth of the bubble seen in Figure 5.11c is a consequence of the large pressure under which the bubble is created, due to the ultrafast nature of the laser irradiation. Very fast quasi-isochoric heat transfer from the heated plasma to the water molecules indeed heats the water to a high temperature and pressure state. The very high pressure in the initial stage of the bubble growth leads to a very fast expansion in the first nanoseconds after the bubble nucleation, as shown on figure 5.11c. This leads to an asymmetry in the time evolution of the bubble that is however much weaker than the one observed in the experimental signal (see Figure 5.9b). This larger asymmetry rather arises from phenomena due to the ensemble measurement and was discussed in section 5.5.4.

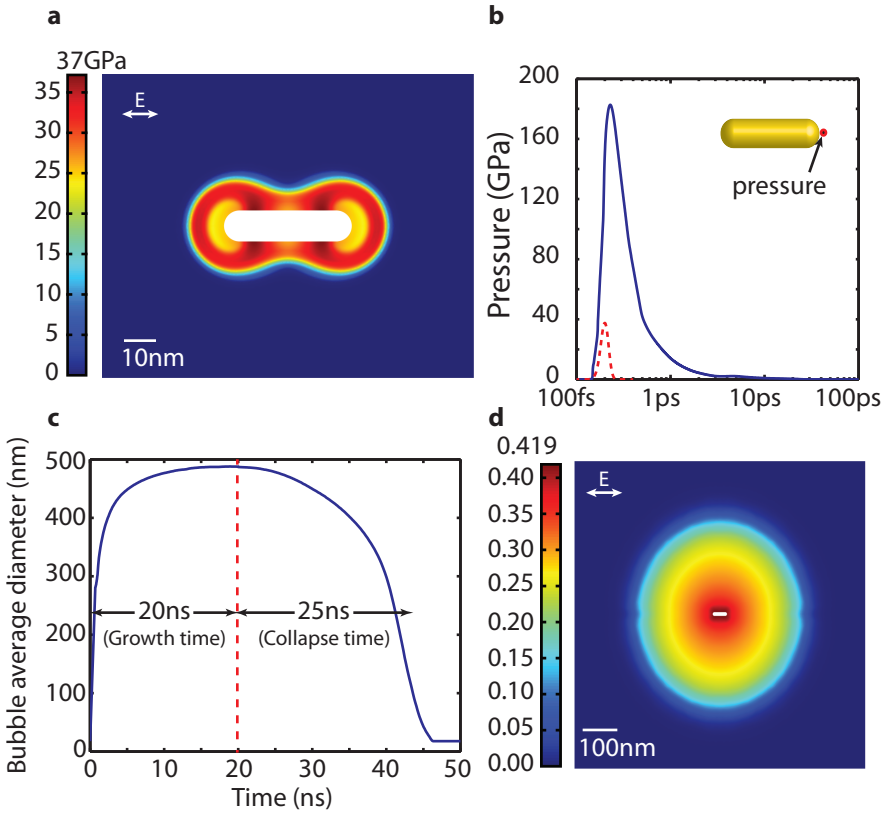

Figure 5.11 Pressure wave release in water and vapor bubble formation at high fluence. **a**. Cross-section of the pressure distribution around a AuNR, 500 fs after a 200 mJ/cm^2, 45 fs, 800 nm laser pulse. **b**. Pressure at the water/metal interface near the tip of the AuNR as a function of time. The 45fs laser pulse time profile, centred at 200 fs, is indicated (red dotted line). **c**. Time evolution of the average diameter of the vapor bubble created around the AuNR after irradiation. **d**. Vapor bubble at its maximal extension around the AuNR, 20 ns after irradiation. Vapor dryness fraction is shown.

Plasma shielding of the plasmon resonance

The domination of the plasma in the cavitation mechanism is quite surprising considering the linear optical properties of the AuNRs presented earlier (see figure 5.2a) showing a net domination of the energy absorbed in the AuNR. However, this calculation only considered linear optical properties of the AuNR-water system, and is therefore no longer valid for high laser intensity. Hence, despite the fact that the linear absorption cross-section of the AuNR is over 10 times higher than the scattering cross-section at the irradiation wavelength (see figure 5.2a), because of the non-linear absorption in water and the high near-field enhancement, interaction of the AuNR with its environment is controlled by the near-field that generates and heats a plasma directly in the water. Simulation results show that the energy absorbed in this plasma is indeed around 5.7 times superior than the one absorbed directly in the AuNR at 200 mJ/cm^2 (see figure 5.3). This situation is very similar to the one presented in a recent study from Boulais et al. [70] that demonstrates the domination of the nanoplasma formed around a gold nanosphere on the cavitation mechanism following an off-resonance 800 nm ultrafast irradiation. However, unlike the off-resonance interaction, the irradiation in the present case heavily damages the AuNRs. The use of AuNRs as generators of vapor bubbles is thus limited to single-pulse applications for which the possible degradation of the AuNRs does not constitute an important issue.

The similarity with the off-resonance case can be easily understood by noting that, because of the excitation of a plasma around the nanostructure, the local permittivity is altered during the laser irradiation. The AuNR thus loses progressively its resonant characteristics during the time of the laser pulse and a majority of the energy absorption is moved from the AuNR itself to the plasma in the surrounding water. Figure 5.12a shows that transition during a 200 mJ/cm^2 laser-nanostructure interaction. Results show that at the beginning of the interaction, when no important plasma density is present, the absorption cross-section of the AuNR (σ_{abs}^{AuNR}) is equivalent to the linear absorption cross-section (σ_{abs}^{lin}), and that the absorption cross-section of the surrounding plasma (σ_{abs}^{plasma}) is null. With time, the enhanced near-field interacts non-linearly with the water and creates a plasma around the AuNR. This plasma absorbs energy from the electromagnetic field and modifies the local permittivity, so that σ_{abs}^{AuNR} drops well below σ_{abs}^{lin} and that σ_{abs}^{plasma} becomes dominant. The modification of the local permittivity indeed alters the resonance condition so that a 800 nm irradiation is no longer resonant with a 10×41nm^2 AuNR, explaining the important decrease of σ_{abs}^{AuNR} seen in figure 5.12a. We call this phenomenon "plasma shielding of the plasmon resonance". This alteration in the resonance condition also affects the near-field enhancement. As seen from figure 5.12b, the modified permittivity degrades notably the electric field enhancement factor, which maximum goes from 77 (see figure 5.4b) to around 2.6. This reduction explains

the strong decrease of σ_{abs}^{plasma} observed in figure 5.12a between 150 fs and 200 fs.

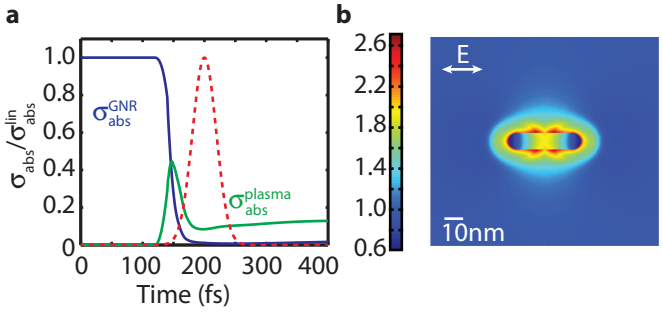

Figure 5.12 Plasma shielding of the plasmon resonance. **a**. Variation of the absorption cross-section of the AuNR (blue line) and of the surrounding plasma (green line) relative to the linear absorption cross-section as a function of time. **b**. Cross-section of the electric field enhancement factor at the time corresponding to the pulse maximum.

5.6 Conclusion

In summary, we demonstrated that the interaction of an ultrafast laser impulsion with an in-resonance AuNRs is highly dependent on the fluence of the incident radiation. Calculations revealed the presence of two distinct regimes of irradiation that depend on the laser fluence. For F<3 mJ/cm^2, the AuNRs are in the absorption regime and the laser energy is mainly absorbed in the AuNR itself. Results show that below the deformation threshold fluence, (F<100 μJ/cm^2), the AuNR's structural integrity is not compromised and the field enhancement due to the plasmonic interaction leads to low heating of the AuNR, small amplitude pressure wave emission, and low-density plasma generation in the surrounding medium. This plasma is mainly produced by a photothermal emission from the AuNR's surface due to field absorbed directly in the AuNR. It moreover brings the possibility to use AuNRs as nanoplasma generators that can induce highly localized chemical damage to cell components in the context of nanosurgery. We however showed that no bubbles were generated around the AuNRs for irradiations with fluences below the deformation threshold.

For F>3 mJ/cm^2, the AuNRs are in the near-field regime and the laser energy is absorbed directly in the water surrounding the AuNR through a photoionization process that occurs due to the enhanced near-field. We demonstrated and measured the formation of bubbles with average diameters ≈[200-600] nm around the AuNRs following a [100-400] mJ/cm^2 single pulse irradiation. However, irradiation at those fluences has been shown to destroy the AuNRs, raising potential toxicity concerns and compromising the efficiency of multipulse processes or scanning procedures. We presented a complete modelling of the nanocavitation

mechanisms. In addition to showing good agreement with the measured bubbles, simulation results allowed to demonstrate the formation of a nanoplasma initiated by the enhanced near-field at the tips of the AuNR, directly in the water. This plasma is created by the enhanced near-field around the AuNR and not by the absorbed field, in opposition to what is the case in the absorption regime. We showed that this plasma shields the laser-plasmon interaction, alters the resonance condition, and transforms the role of the AuNR in term of energy transfer. Simulation results demonstrated the strong influence of that plasma on the field distribution around the plasmonic nanostructure. It has been shown to induce a strong decrease in both the field enhancement around the AuNR and the energy absorbed in the AuNR, explaining the observed similarity to off-resonance interaction.

5.7 Acknowledgement

The authors would like to thank the Natural Science and Engineering Research Council (NSERC) and Le Fonds Québécois de la Recherche sur la Nature et les Technologies (FQRNT) for financial support. RQCHP is acknowledged for computing ressources. Assistance by Yves Drolet and fruitful discussions with Guillaume Poulin, are also acknowledged.

CHAPITRE 6

Discussion générale : Importance du plasma pour la nanocavitation et analyse du potentiel des nanostructures

Les résultats présentés aux chapitres 4 et 5 démontrent l'importance du plasma dans le processus de nanocavitation par laser ultrarapide amplifié par nanostructures plasmoniques. En particulier, ils présentent des mesures expérimentales de diamètre des bulles produites qui concordent bien avec les résultats théoriques obtenus par simulation en utilisant le modèle présenté en détail au chapitre 3.

Les résultats démontrent en outre que l'existence d'un processus de photoionisation en champ proche est nécessaire pour expliquer la présence des bulles observées expérimentalement. Une absorption d'énergie limitée à la particule, suivie d'un transfert à son environnement par un processus de conduction n'est en effet pas en mesure d'expliquer la génération de bulles qui sont expérimentalement observées dans le milieu aux fluences impliquées. L'ajout au modèle des processus de photoionisation, d'ionisation par collision et de dynamique de plasma permet de prédire la génération de ces bulles, avec un diamètre théorique et un temps caractéristique de croissance correspondant aux valeurs mesurées expérimentalement.

Ce processus de cavitation est inédit dans la littérature et a des conséquences importantes pour la nanochirurgie cellulaire, en particulier pour les procédés de transfection cellulaire. En effet, comme nous allons le voir dans la première partie de ce chapitre, le mécanisme de cavitation induite par le plasma procure certains avantages sur les processus utilisant directement le chauffage des NPs. Suite à cette discussion, après un bref rappel des principaux résultats concernant les différences entre les processus de cavitation induite par une irradiation en-résonance et hors-résonance, le chapitre présente une méthode d'analyse efficace afin d'évaluer le potentiel de nanostructures et de paramètres laser spécifiques pour la génération de bulles de vapeur dans l'eau. La méthode présentée est simple, efficace, et permet une analyse graphique des résultats. À l'aide de cette méthode, nous comparons entre eux des AuNPs (hors-résonance) ainsi que des AuNRs d'aspect constant 4.1 (en-résonance) de tailles différentes et nous évaluons leur potentiel d'utilisation en nanochirurgie cellulaire. Cette méthode permet de généraliser les résultats obtenus au chapitre 5 à l'ensemble des AuNRs en-résonance et confirme que ceux-ci ne sont pas adaptés aux procédés de nanochirurgie cellulaire dont le mode de fonctionnement requièrent la production de bulles.

6.1 Conséquences pour l'optoperforation de membranes cellulaires et la transfection cellulaire

La possibilité de créer des bulles autour de particules d'or hors-résonance à l'aide d'un laser ultrarapide avec une longueur d'onde située dans l'infrarouge est extrêmement intéressante pour les applications dans le cadre de nanochirurgie cellulaire par laser, spécialement dans le cadre de procédés de transfection cellulaire. Tel que vu au chapitre 2, ce type de procédé utilise les bulles de cavitation créées autour des nanostructures plasmoniques irradiées afin de perforer et perméabiliser la membrane cellulaire à certaines molécules (ADN, ARN, molécules de médicament) pour permettre leur incorporation à la cellule.

Premièrement, l'utilisation d'un laser dans l'infrarouge réduit l'incidence de dommages collatéraux aux structures cellulaires environnantes. En effet, les tissus biologiques ne sont que très peu absorbants aux longueurs d'onde situées dans l'intervalle ≈600 nm-1300 nm, aussi appelé fenêtre optique [82]. Un laser infrarouge est donc absorbé très faiblement par les structures biologiques à l'extérieur du champ proche des particules, ce qui restreint la zone affectée et permet d'atteindre des tissus plus profonds lors des traitements.

Ensuite, ce procédé permet l'emploi de nanostructures simples pour réaliser les traitements. En effet, puisque le procédé s'effectue hors-résonance, celui-ci ne requiert l'utilisation que de nanoparticules d'or sphériques (AuNPs), possiblement fonctionnalisées avec des molécules permettant un ciblage spécifique vers les cellules à traiter. Les méthodes de fabrications de ces nanostructures sont plutôt bien connues, et il est possible d'obtenir des suspensions colloïdales de AuNPs stables présentant une faible dispersion en terme de diamètres. La production de nanostructures en-résonance dans l'infrarouges (nanobâtons (AuNRs), structures coeur-couronne, nano-coquilles) est passablement plus complexe et donne des échantillons moins monodisperses, moins stables, en plus d'impliquer parfois l'emploi de surfactants toxiques, citons par exemple le Cetyl trimethylammonium bromide (CTAB) dans le cas des AuNRs.

Finalement, puisque l'énergie est déposée en majorité dans le plasma autour de la NP plutôt que dans la NP elle-même, une importante cavitation peut être induite dans le milieu sans induire de dommages substantiels aux NPs. Cela revêt une importance cruciale pour les applications biologiques, puisque la présence de petites particules d'or (<5 nm) qui pourraient être formées suite à la fragmentation de la NP est fréquemment associée à une cytotoxicité importante [57, 326, 340].

La figure 6.1 montre la température simulée atteinte en fonction du temps à l'intérieur d'une AuNP de 100 nm de diamètre suite à une irradiation de 45 fs, 200 mJ/cm^2. Bien que ce résultat montre que la NP atteint une température proche de sa température de fusion (1320 K, légèrement inférieure à la température de fusion de l'or massif en raison de ses dimensions

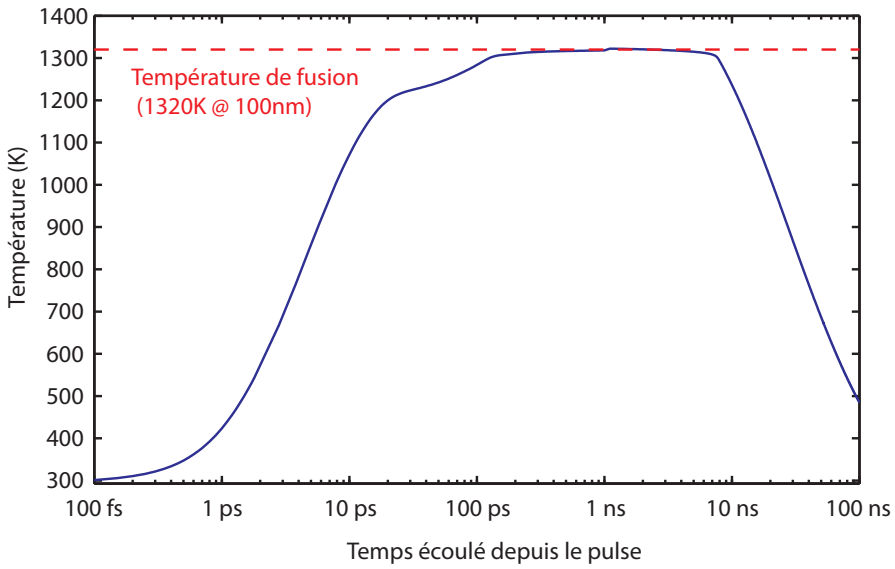

Figure 6.1 Température au centre d'une AuNP de 100 nm de diamètre en fonction du temps suite à une irradiation de fluence de 200 mJ/cm^2, d'une durée de 45 fs à une longueur d'onde de 800 nm.

réduites), des mesures spectroscopiques démontrent que la particule n'est pas brisée suite au traitement, et ce pour des fluences incidentes pouvant atteindre jusqu'à 400 mJ/cm^2.
Ce résultat est reproduit à la figure 6.2. Celui-ci est obtenu en irradiant la solution à une fluence donnée sur une période de 12 h tout en faisant l'acquisition du spectre d'extinction des particules en continu. La modification du diamètre des particules se reflète par une modification notable du spectre d'extinction. En particulier, une réduction du diamètre des particules entraîne un décalage vers le bleu du spectre. La figure 6.2 révèle qu'un tel décalage n'est visible que pour des fluences incidentes supérieures à 400 mJ/cm^2. En conséquence, on en conclut que les particules ne sont pas fragmentées lors d'une irradiation utilisant des fluences 0-200 mJ/cm^2 qui sont employées pour les expériences de transfection cellulaire. Cela améliore la sécurité du traitement en plus de permettre le développement de procédés impliquant de multiples impulsions laser.

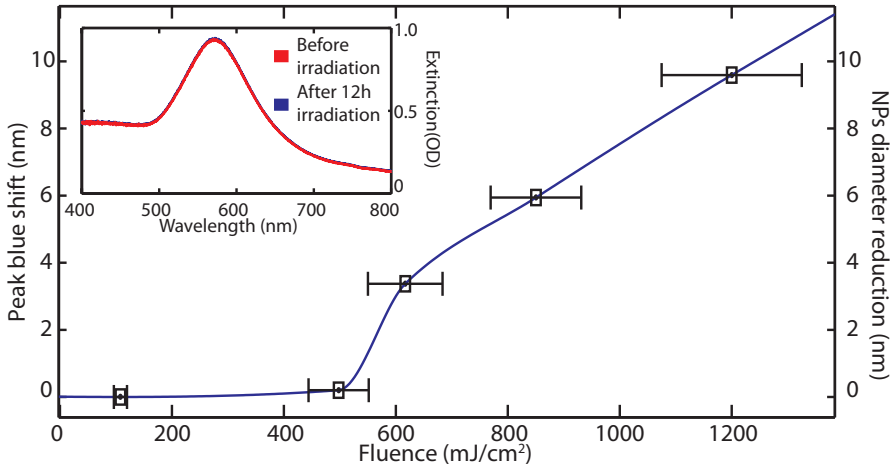

Figure 6.2 Modification de la position du maximum du spectre d'extinction après 12 h d'irradiation d'une suspension de AuNPs de 100 nm à l'aide d'impulsions d'une durée de 45 fs à une longueur d'onde de 800 nm et à une fréquence de 1 KHz, en fonction de la fluence incidente. Les barres d'erreurs pour l'ordonnée représentent 2× l'écart-type ($\approx \pm$ 0.3 nm, non-visible sur le graphique). L'échelle de gauche montre le déplacement du maximum vers le bleu, tandis que l'échelle de droite montre la modification du diamètre associée au déplacement, calculée à partir de la théorie de Mie. L'encadré compare le spectre de la suspension avant (bleu) et après (rouge) une irradiation de 12 h à une fluence de 100 mJ/cm^2. Tiré de [57].

6.2 Plasma et particules en-résonance

Suite à la démonstration de l'importance du plasma pour les processus de cavitation, on peut se demander s'il ne serait pas avantageux d'utiliser plutôt des structures en-résonance, tels que les nanorods (NRs), afin d'induire le processus de cavitation. En effet, ces structures présentent des amplifications de champ très importantes ($\approx$77 pour les AuNRs de 10×41 nm^2 étudiées au chapitre 5, voir figure 5.2c). De telles intensités de champ électrique laissent présager une absorption non-linéaire, une photoionisation et une génération de plasma beaucoup plus importantes dans le champ proche de ces nanostructures comparativement aux NPs utilisées au chapitre 4. En effet, l'amplification du champ électrique autour des AuNPs de 100 nm hors-résonance n'est que de l'ordre de $\approx$4.5.

Cette analyse simpliste néglige cependant l'impact de la présence du plasma dans l'environnement de la nanostructure sur ses propriétés optiques. Le chapitre 5 démontre en effet l'impact important de la modification de la permittivité locale due au plasma sur la distribution du champ électrique autour de NRs. Ainsi, bien que ceux-ci soient en-résonance à basses fluences, ils deviennent plutôt hors-résonance suite à la création du plasma, réduisant

substantiellement l'amplification du champ proche et l'absorption d'énergie (voir figure 5.12). Au final l'énergie totale absorbée dans le système eau-NR en-résonance suite à l'irradiation est de ≈1.4 pJ, soit près de 10× inférieure à l'énergie totale absorbée dans le système eau-NP hors-résonance (≈12 pJ) à une fluence équivalente (200 mJ/cm^2). Noter que dans les deux cas, l'énergie est en grande majorité (90% pour les AuNPs, et 80% pour les AuNRs) absorbée dans le plasma autour de la nanostructure. Cependant, contrairement aux AuNPs, le 20% absorbé par les AuNRs est plus que nécessaire pour les endommager, le seuil en fluence requis n'étant que de ≈ 100μJ/cm^2 (voir figure 5.4b).

6.3 Énergie et cavitation

La bulle de cavitation générée autour d'une nanostructure plasmonique en milieu aqueux est une conséquence directe du dépôt d'énergie dans le système eau-nanostructure par le laser. D'une façon grossière, le volume de la bulle devrait varier linéairement avec l'énergie déposée (Ed), de sorte que le diamètre de la bulle générée devrait varier selon $D = (\gamma E_d)^{1/3}$, γ étant une constante de proportionnalité. Une analyse expérimentale de la formation de bulles effectuée par Siems et al. montre plutôt que $D = (\gamma E_d)^{0.45}$ [193].
À partir de nos résultats de simulation, il est possible d'utiliser cette relation afin de développer une méthode simple d'évaluation de la taille des bulles engendrées par l'irradiation d'une nanostructure spécifique à l'aide de paramètres laser donnés. En effet, les résultats présentés au chapitre 4 montrent la formation d'une bulle de diamètre ≈1.2 μm suite à l'absorption de 12 pJ d'énergie, à la fois dans le plasma et la NP. Ce résultat correspond à un paramètre γ =0.0069 J^{-1}. Donc :

$$D_{max} \approx (0.0069 E_d)^{0.45} \tag{6.1}$$

où D_{max} est en m. En appliquant cette relation à l'énergie déposée suite à l'irradiation d'un AuNR de 10×41 nm^2 avec une impulsion laser de 200 mJ/cm^2 polarisée selon son axe longitudinal (1.4 pJ), on obtient un diamètre de D_{max} =493 nm. Ce résultat se compare très bien à celui obtenu suite à la simulation complète de la cavitation présentée au chapitre 5 (≈490 nm, voir figure 5.11c). Donc, les résultats semblent indiquer que l'équation 6.1 est valide pour déterminer le diamètre des bulles produites à partir du seul calcul de l'énergie déposée dans le système. Par contre, afin de déterminer les limites de l'applicabilité de l'équation 6.1, il serait indiqué de réaliser d'autres simulations à partir du modèle complet pour différents paramètres laser et structuraux et de comparer leur résultat à l'équation 6.1. Cela n'a cependant pas été effectué dans le cadre de cette thèse.
Le fait qu'il soit possible de déterminer le diamètre des bulles produites suite à l'irradiation

d'une nanostructure dans l'eau à partir du seul calcul de l'énergie déposée dans le système constitue un résultat majeur et particulièrement intéressant dans le cadre d'études de simulation. En effet, pour des impulsions laser ultrabrèves, cela implique que seule la simulation de l'interaction laser (c'est-à-dire quelques centaines de femtosecondes) est nécessaire pour déterminer le diamètre maximal approximativement atteint par la bulle plusieurs nanosecondes après l'impulsion. De plus, comme le temps d'interaction laser (et donc le temps de dépôt de l'énergie) est beaucoup plus court que le temps de couplage électron-phonon, seuls l'interaction électromagnétique, la dynamique du plasma et le chauffage des électrons de la AuNP doivent être considérés. En effet, le chauffage du réseau de la AuNP ainsi que l'hydrodynamique n'a aucun impact sur l'absorption d'énergie dans le système pour des impulsions ultrabrèves. En conséquence, à la figure 3.3, seules les équations (3.2-3.4) et (3.7-3.8) doivent être résolues. Cela simplifie considérablement le problème et réduit les ressources computationnelles requises à sa résolution. Ainsi, alors que le modèle complet requiert plusieurs jours, voire plusieurs semaines à résoudre, ce modèle simplifié ne demande que quelques heures de calcul. Il est donc beaucoup plus pratique pour effectuer des tests rapides afin d'évaluer le potentiel de structures ou de paramètres d'impulsion particuliers. La prochaine section présente un exemple d'analyse comparant le potentiel de AuNPs et de AuNRs de tailles variées pour la nanochirurgie cellulaire.

6.4 Influence de la taille et de la forme des nanostructures sur leurs performances

Nous avons appliqué le modèle simplifié à l'analyse du potentiel de performance de AuNPs et de AuNRs de diverses tailles soumis à une impulsion laser de 100 mJ/cm^2, 800 nm, 45 fs. Cette fluence a été choisie à partir de récents travaux qui ont montré que des fluences locales de l'ordre de 100 mJ/cm^2 offrent de meilleurs résultats que des fluences locales de l'orde de 200 mJ/cm^2 pour l'optoporation de cellules à l'aide de AuNPs (résultats non-publiés). Dans le cadre de la nanochirurgie par laser, nous dégageons deux paramètres de performance importants

1. La taille des bulles créées, reliée à l'énergie totale déposée dans le système, tel que vu à la section précédente.
2. La densité d'énergie absorbée à l'intérieur de la nanostructure, reliée à son élévation en température et à sa possible fragmentation.

En résumé, la nanostructure idéale, pour une énergie laser donnée, induira l'absorption d'une grande quantité d'énergie dans le milieu (E_d, en J), provoquant ainsi le phénomène de cavitation qui est à la base des dommages cellulaires importants utilisés en nanochirurgie.

Par contre, la densité d'énergie absorbée dans la nanostructure (ρ_E, en Jm^{-3}) doit rester aussi faible que possible afin d'éviter que celle-ci ne soit fragmentée lors de l'interaction laser, ce qui pourrait provoquer des problèmes de cytotoxicité en plus de proscrire l'utilisation de procédés utilisant de multiples impulsions.
Nous appelons le couple (E_d, ρ_E) le facteur de mérite. Nous avons calculé ce facteur de mérite pour des AuNPs de diamètres allant de 60 nm-250 nm (hors-résonance pour une irradiation à une longueur d'onde λ =800 nm) et pour des AuNRs d'aspect 4.1 de différentes tailles allant de 10×41 nm^2 à 80×328 nm^2 (en-résonance à λ =800 nm). Les résultats sont présentés à la figure 6.3. La ligne verte à la figure 6.3 représente la densité d'énergie approximative provoquant l'atteinte de la température de fusion à l'intérieur de la nanostructure. Celle-ci est calculée de manière simplifiée comme étant :

$$\rho_E^{fusion} \approx \left(T^{fusion} - T^{ambiant}\right) C_L^{approx} \tag{6.2}$$

où T^{fusion} est la température de fusion de l'or massif (1337 K), $T^{ambiant}$, la température ambiante (293 K), et C_L^{approx} ≈2.5×10^6 $\mathrm{Jkg}^{-1}\mathrm{K}^{-1}$ est la capacité thermique de l'or. Bien entendu le calcul de ρ_E n'est qu'une approximation, puisqu'il néglige complètement le transfert thermique avec l'environnement, la modification de la température de fusion avec la dimension des particules, ainsi que la dépendance en température de la capacité thermique. Néanmoins, cette approximation de ρ_E reste raisonnable dans le cas d'une interaction laser ultrabrève.
Les résultats pour les AuNPs, présentés à la figure 6.3, montre que les AuNPs qui induisent la plus forte déposition d'énergie aux paramètres laser considérés sont les AuNPs de diamètre 175 nm. Celles-ci permettent de déposer ≈6× plus d'énergie que les particules de 100 nm de diamètre (13.5 pJ comparativement à 2.3 pJ), et produisent des bulles d'un diamètre environ ≈2× plus important (≈ 1.4 μm comparativement à 620 nm). En fait, on constate que des particules de 175 nm irradiée à 100 $\mathrm{mJ/cm}^2$ déposent environ la même énergie dans le système que des particules de 100 nm irradiées à 200 $\mathrm{mJ/cm}^2$ (≈12 pJ d'après les résultats présentés au chapitre 4.
Au niveau de la densité d'énergie absorbée par les AuNPs, on constate que pour toutes les tailles étudiées [60 nm-250 nm], celle-ci demeure en deçà de la limite permettant d'atteindre une température près de la température de fusion. Cela s'explique par le fait que les particules sont hors-résonance avec la longueur d'onde incidente (800 nm) et n'absorbent que très peu l'énergie du laser. Tel qu'expliqué à la section 6.1, cela constitue un avantage majeur de la nanochirurgie par laser ultrarapide amplifié utilisant des particules hors-résonance.
Concernant les AuNRs, l'inspection de la figure 6.3 révèle que l'énergie maximale est déposée par des AuNRs de 40nm×164 nm^2, mais que celle-ci reste en deçà de l'énergie déposée par une AuNP de 175 nm. Cela est probablement dû au rayon de courbure réduit des NRs qui

crée un champ proche plus confiné, et qui par conséquent donne accès à un nombre réduit de molécules d'eau pouvant être ionisées. Aussi, on remarque que ces NRs présentent une densité d'énergie absorbées de l'ordre de 10× supérieure au seuil approximatif de fusion. Cela s'explique par le fait que les NRs sont en résonance avec la longueur d'onde incidente et absorbent fortement l'irradiation laser. Les NRs sont donc sans aucun doute déformés, voire détruits par l'irradiation laser. Tel que mentionné au chapitre 5, cela représente un inconvénient majeur et diminue drastiquement l'intérêt d'utiliser des NRs en-résonance dans le cadre de la nanochirurgie cellulaire. Cependant, alors que les conclusions du chapitre 5 se limitaient aux seuls NRs de dimension $10\times41\text{nm}^2$, le résultat présenté à la figure 6.3 généralise cette conclusion à l'ensemble des AuNRs d'aspect 4.1 en résonance à λ =800 nm.

En vue des résultats, il serait par conséquent indiqué d'utiliser des AuNPs un peu plus grosses (≈175 nm) que celles utilisées dans le cadre de l'étude réalisée par Baumgart et al. (≈100 nm) afin de réaliser la transfection cellulaire. Ces particules semblent en effet exciter un plasma beaucoup plus efficacement dans le milieu tout en présentant une densité d'énergie absorbée au niveau de la particule qui est similaire. L'utilisation de AuNRs en-résonance n'est pas indiqué, et ce, quelque soit leur taille.

On constate que cette méthode d'analyse est très utile afin de visualiser rapidement et facilement le potentiel d'une structure particulière pour produire des bulles en milieu aqueux sans être déformée. Plus une structure est représentée par un point s'approchant du coin supérieur gauche, plus son potentiel est élevé. L'application de cette méthode à d'autres types de structures (coeur-couronnes, coquilles, nano-étoiles,...) ou a l'analyse du potentiel de profils temporels d'irradiation particuliers (doubles impulsions, impulsions façonnées temporellement, impulsions façonnées spectralement) est directe. Une étude systématique dépasse cependant le cadre de cette thèse et sera le sujet de travaux futurs.

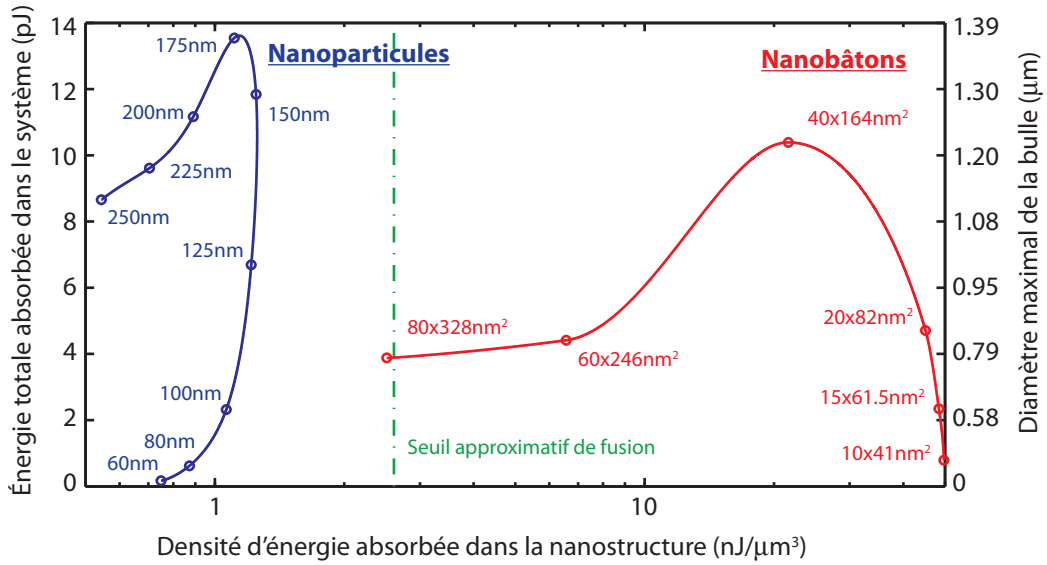

Figure 6.3 Facteur de mérite de AuNPs de différents diamètres (cercles bleus) et de AuNRs (cercles rouges) d'aspect 4.1 de différentes tailles lorsque soumis à une irradiation de 100 mJ/cm^2, 45 fs, à une longueur d'onde de 800 nm. La ligne pointillée verte présente le seuil de densité d'énergie (approximatif) qui amène la nanostructure près de la température de fusion. Les lignes pleines bleues et rouges sont des interpolations.

CHAPITRE 7

CONCLUSION ET RECOMMANDATIONS

Les travaux réalisés dans le cadre de cette thèse portaient sur l'étude des mécanismes fondamentaux et des phénomènes physiques induits par l'irradiation d'une nanostructure plasmonique en milieu cellulaire avec une impulsion laser femtoseconde. Ceux-ci cherchaient à mieux comprendre et éventuellement à optimiser les procédés de nanochirurgie cellulaire. Les objectifs, énoncés à l'introduction visaient spécifiquement à :

1. Développer un modèle mathématique capable de simuler adéquatement le dépôt d'énergie, l'élévation de température, l'émission d'ondes de pression et le phénomène de cavitation résultant de l'interaction d'une impulsion laser ultrabrève avec une nanostructure plasmonique en milieu biologique.
2. Utiliser ce modèle afin de dégager les éléments dominants de l'interaction laser et la chaîne principale des événements menant à la cavitation dans le milieu.
3. Développer un cadre d'évaluation du potentiel de nanostructures plasmoniques particulières pour application en nanochirurgie cellulaire.

Cette thèse a répondu avec succès à l'ensemble de ces objectifs. En effet, on y a présenté le développement d'une modélisation mathématique complète de l'interaction laser-nanostructure dans un environnement aqueux dont le comportement émule adéquatement le milieu cellulaire. Ce modèle, basé sur une description de type milieu-continu du système eau-nanostructure, simule le dépôt d'énergie par le laser ainsi que l'élévation de température, la génération de plasma, l'émission d'ondes de pression et la formation des bulles de vapeur qui en découlent. Une description adéquate de l'ensemble de ces phénomènes est nécessaire dans l'optique où chacun peut représenter une source significative de dommage aux structures cellulaires environnantes. Un tel modèle était inexistant dans la littérature et son introduction a permis l'étude détaillée des procédés de nanochirurgie cellulaire.
Ce modèle a permis d'analyser l'interaction d'une impulsion laser femtoseconde infrarouge ($45fs$, $800nm$, $200mJ/cm^2$) avec une nanoparticule d'or de $100nm$ hors-résonance plasmonique et avec un nanobâton d'or de $10 \times 41nm^2$ en-résonance plasmonique. Les résultats montrent la génération de bulles de cavitation autour des nanostructures pour des fluences de l'ordre de $100mJ/cm^2$. Des expériences de spectroscopie confirment les prédictions du modèle concernant la taille maximale ainsi que le temps caractéristique de croissance des bulles créées suite à une irradiation de $200mJ/cm^2$ pour les deux systèmes. Ce résultat valide le

modèle proposé et répond à l'objectif 1.

Pour une irradiation de fluence $200 mJ/cm^2$, les résultats révèlent la formation d'un plasma dans le champ proche des nanostructures. Les simulations montrent un transfert énergétique rapide de ce plasma vers les molécules d'eau générant de fortes ondes de pression qui sont émises dans le milieu. Elles démontrent de plus l'importance capitale de ce plasma pour le mécanisme de cavitation. En effet, autant pour la nanoparticule que pour le nanobâton, la majorité de l'énergie du laser est déposée dans le plasma généré dans le champ proche de la particule, directement dans le milieu, et n'est pas absorbée directement par la nanostructure. Dans le cas de la nanoparticule de $100 nm$, les résultats démontrent que la présence de plasma est même nécessaire pour expliquer la présence de toute cavitation, l'énergie absorbée dans la nanoparticule n'étant pas suffisante pour entraîner un changement de phase dans l'eau environnante.

Dans le cas du système hors-résonance, l'énergie absorbée par la nanoparticule est assez faible pour que celle-ci ne soit pas endommagée lors de l'interaction. Ce phénomène, confirmé par des expériences de spectroscopie, confère un avantage considérable aux procédés de nanochirurgie par laser utilisant des nanoparticules hors-résonance. En effet, la fragmentation des nanoparticules peut entraîner la formation de très petites particules qui sont toxiques pour les cellules. Le fait que les nanoparticules ne soient pas endommagées réduit donc ce risque et améliore la sécurité du procédé.

Par contre, dans le cas du système en-résonance, l'énergie absorbée dans le nanobâton est suffisante pour l'endommager significativement aux fluences requises pour entraîner la cavitation dans le milieu. Ce résultat est démontré par des expériences spectroscopiques. Aux fluences sous le seuil de dommage ($100 \mu J/cm^2$), seul un chauffage du milieu et la génération d'un plasma de faible densité par émission photothermique sont observés, et n'entraînent pas la formation de bulles. Cela réduit considérablement l'intérêt des nanobâtons d'or pour la nanochirurgie cellulaire, ou du moins pour les applications de nanochirurgie cellulaire où la présence de bulles de cavitation est nécessaire. Ce résultat marque aussi une différence notable avec les procédés utilisant des lasers continus et des impulsions lasers de l'ordre de la nanoseconde, où l'interaction avec une structure en-résonance est souhaitable et souvent nécessaire au succès du traitement.

L'étude complète de ces deux cas de figure a permis de constater l'importance prépondérante du plasma dans le mécanisme de formation des bulles de vapeur et de dégager la chaîne d'événements dominants menant à la cavitation dans le milieu, ce qui correspond à l'objectif 2.

Finalement, une analyse énergétique révèle que la taille de la bulle est principalement contrôlée par l'énergie déposée dans le plasma lors de l'interaction laser. Ainsi, on peut évaluer

la taille des bulles finales à partir de la simulation des quelques centaines de femtosecondes que dure l'interaction laser. Ce modèle simplifié réduit considérablement les temps de calculs nécessaires et s'avère utile pour évaluer rapidement les performances d'une structure particulière soumise à une irradiation spécifique.

À partir de ce modèle, nous avons développé un cadre d'évaluation du potentiel de nanostructures plasmoniques pour leur application en nanochirurgie cellulaire, ce qui correspond à l'objectif 3. Nous avons par la suite appliqué cette méthode à l'étude de nanoparticules d'or hors-résonance de différents diamètres et de nanobâtons d'or en-résonance de différentes tailles soumis à une impulsion femtoseconde. Ce cadre, basé sur un facteur de mérite reposant sur la minimisation de la densité d'énergie absorbée dans la nanostructure afin d'éviter sa fragmentation, et la maximisation de l'énergie déposée dans le milieu pour favoriser la création de bulle, permet de faire ressortir les nanoparticules d'or de $175nm$ comme le meilleur candidat pour les applications de nanochirurgie cellulaire où la présence de bulles est requise. Il confirme de plus le peu d'intérêt que présente l'utilisation de nanobâtons en-résonance pour ce type procédé.

Bien que le modèle présenté dans le cadre de cette thèse rencontre les objectifs fixés, un ensemble de recommandations peuvent être formulées afin d'améliorer la qualité de ses prédictions. En effet, bien que le modèle reproduise approximativement le diamètre des bulles observées dans les deux cas de figure présentés, l'incertitude des mesures expérimentales ne permet pas de le valider avec précision. Le modèle permet ainsi de dégager les tendances générales des phénomènes physiques impliqués, mais sa capacité à prédire avec exactitude le diamètre des bulles formées demeure inconnue. Aussi, plusieurs autres paramètres calculés par le modèle (pression, densité de plasma, énergie du plasma, température) ne sont pas directement confrontés à des expériences. Il serait important de développer de nouvelles approches de mesure pour permettre de valider, et possiblement améliorer, le modèle proposé. Entre autre, une détection directe de la présence du plasma dans l'eau serait souhaitable afin de démontrer hors de tout doute le mécanisme proposé dans la thèse.

Il serait aussi nécessaire d'évaluer l'influence de la présence de la membrane cellulaire sur les processus d'interaction laser et de cavitation. Pour ce faire, il serait intéressant de confronter les prédictions du modèle avec des expériences menées directement en milieu cellulaire. Des mesures spectroscopiques de la taille des bulles générées directement à proximité de membranes cellulaires seraient requises. La pertinence d'inclure l'effet de la présence de la membrane cellulaire dans le modèle d'interaction pourrait être évaluée à partir de ce résultat. De plus une étude de l'efficacité de transfection cellulaire en fonction de la taille des nanoparticules serait souhaitable afin de valider les résultats obtenus à l'aide du facteur de mérite introduit dans cette thèse et d'évaluer son utilité réelle à évaluer le potentiel de nanostruc-

tures pour des applications spécifiques.

En conclusion, l'ensemble des travaux présentés dans cette thèse répond avec succès aux objectifs du travail énoncés au début de la thèse. D'un point de vue théorique, ces travaux ont permis de développer une compréhension profonde des mécanismes d'interaction entre une impulsion laser ultrabrève et une nanostructure en milieu aqueux. Ils offrent la première preuve convaincante que le plasma généré dans le champ proche, et non le chauffage de la particule, peut mener à la cavitation dans le milieu sous certaines conditions d'irradiation. Cette idée nouvelle pourrait influencer de manière significative le développement de nouvelles technologies relatives à la génération de bulles de vapeur en milieu liquide qui ne se limitent pas à la nanochirurgie cellulaire.

D'un point de vue pratique, la méthode développée dans la thèse est très générale et est applicable à une panoplie de nanostructures plasmoniques et paramètres d'irradiation différents. Elle offre de très larges possibilités d'exploration et s'avérera sans aucun doute très utile pour la recherche des structures et paramètres laser adéquats en regard du développement d'applications spécifiques en nanochirurgie par laser.

Cette thèse est un bon exemple de synergie entre la recherche fondamentale et la recherche appliquée. Ce type d'approche aura sans aucun doute un rôle important à jouer dans le développement des technologies en nanochirurgie cellulaire et contribuera peut-être à repousser les limites de l'incursion humaine dans son exploration du vivant et de l'infiniment petit.

RÉFÉRENCES

[1] J. A. Schuller, E. S. Barnard, W. Cai, Y. C. Jun, J. S. White, and M. L. Brongersma, "Plasmonics for extreme light concentration and manipulation," *Nature materials*, vol. 9, no. 3, pp. 193–204, 2010.

[2] W. L. Barnes, A. Dereux, and T. W. Ebbesen, "Surface plasmon subwavelength optics," *Nature*, vol. 424, no. 6950, pp. 824–830, 2003.

[3] M. I. Stockman, "Nanoplasmonics : past, present, and glimpse into future," *Optics Express*, vol. 19, no. 22, pp. 22 029–22 106, 2011.

[4] H. A. Atwater and A. Polman, "Plasmonics for improved photovoltaic devices," *Nature materials*, vol. 9, no. 3, pp. 205–213, 2010.

[5] G. Konstantatos and E. H. Sargent, "Nanostructured materials for photon detection," *Nature Nanotechnology*, vol. 5, no. 6, pp. 391–400, 2010.

[6] P. Zijlstra, J. W. M. Chon, and M. Gu, "Five-dimensional optical recording mediated by surface plasmons in gold nanorods," *Nature*, vol. 459, no. 7245, pp. 410–413, 2009.

[7] J. W. M. Chon, C. Bullen, P. Zijlstra, and M. Gu, "Spectral encoding on Gold Nanorods Doped in a Silica Sol–Gel Matrix and Its Application to High-Density Optical Data Storage," *Advanced Functional Materials*, vol. 17, no. 6, pp. 875–880, 2007.

[8] L. Novotny, R. X. Bian, and X. S. Xie, "Theory of nanometric optical tweezers," *Physical Review Letters*, vol. 79, no. 4, pp. 645–648, 1997.

[9] E. Betzig, A. Lewis, A. Harootunian, M. Isaacson, and E. Kratschmer, "Near field scanning optical microscopy (NSOM) : development and biophysical applications," *Biophysical Journal*, vol. 49, no. 1, pp. 269–279, 1986.

[10] S. J. Tan, M. J. Campolongo, D. Luo, and W. Cheng, "Building plasmonic nanostructures with DNA," *Nature Nanotechnology*, vol. 6, no. 5, pp. 268–276, 2011.

[11] Y. Chen and W. Cheng, "DNA-based plasmonic nanoarchitectures : from structural design to emerging applications," *Wiley Interdisciplinary Reviews : Nanomedicine and Nanobiotechnology*, pp. 1–18, 2012.

[12] A. Kuzyk, R. Schreiber, Z. Fan, G. Pardatscher, E. M. Roller, A. Högele, F. C. Simmel, A. O. Govorov, and T. Liedl, "DNA-based self-assembly of chiral plasmonic nanostructures with tailored optical response," *Nature*, vol. 483, no. 7389, pp. 311–314, 2012.

[13] D. J. Bergman and M. I. Stockman, "Surface plasmon amplification by stimulated emission of radiation : quantum generation of coherent surface plasmons in nanosystems," *Physical Review Letters*, vol. 90, no. 2, p. 27402, 2003.

[14] M. I. Stockman, "Spasers explained," *Nature Photonics*, vol. 2, no. 6, pp. 327–329, 2008.

[15] R. F. Oulton, V. J. Sorger, T. Zentgraf, R. M. Ma, C. Gladden, L. Dai, G. Bartal, and X. Zhang, "Plasmon lasers at deep subwavelength scale," *Nature*, vol. 461, no. 7264, pp. 629–632, 2009.

[16] M. A. Noginov, G. Zhu, A. M. Belgrave, R. Bakker, V. M. Shalaev, E. E. Narimanov, S. Stout, E. Herz, T. Suteewong, and U. Wiesner, "Demonstration of a spaser-based nanolaser," *Nature*, vol. 460, no. 7259, pp. 1110–1112, 2009.

[17] N. I. Zheludev, S. L. Prosvirnin, N. Papasimakis, and V. A. Fedotov, "Lasing spaser," *Nature Photonics*, vol. 2, no. 6, pp. 351–354, 2008.

[18] J. N. Anker, W. P. Hall, O. Lyandres, N. C. Shah, J. Zhao, and R. P. Van Duyne, "Biosensing with plasmonic nanosensors," *Nature materials*, vol. 7, no. 6, pp. 442–453, 2008.

[19] P. Zijlstra, P. M. R. Paulo, and M. Orrit, "Optical detection of single non-absorbing molecules using the surface plasmon resonance of a gold nanorod," *Nature Nanotechnology*, vol. 7, no. 6, pp. 379–382, 2012.

[20] S. Jain, D. G. Hirst, and J. M. O'Sullivan, "Gold nanoparticles as novel agents for cancer therapy," *British Journal of Radiology*, vol. 85, no. 1010, pp. 101–113, 2012.

[21] R. A. Sperling, P. R. Gil, F. Zhang, M. Zanella, and W. J. Parak, "Biological applications of gold nanoparticles," *Chemical Society Reviews*, vol. 37, no. 9, pp. 1896–1908, 2008.

[22] P. K. Jain, I. H. El-Sayed, and M. A. El-Sayed, "Au nanoparticles target cancer," *Nano Today*, vol. 2, no. 1, pp. 18–29, 2007.

[23] P. Cherukuri, E. S. Glazer, and S. A. Curley, "Targeted hyperthermia using metal nanoparticles," *Advanced Drug Delivery Reviews*, vol. 62, no. 3, pp. 339–345, 2010.

[24] E. B. Dickerson, E. C. Dreaden, X. Huang, I. H. El-Sayed, H. Chu, S. Pushpanketh, J. F. McDonald, and M. A. El-Sayed, "Gold nanorod assisted near-infrared plasmonic photothermal therapy (PPTT) of squamous cell carcinoma in mice," *Cancer Letters*, vol. 269, no. 1, pp. 57–66, 2008.

[25] X. Huang, I. H. El-Sayed, W. Qian, and M. A. El-Sayed, "Cancer cell imaging and photothermal therapy in the near-infrared region by using gold nanorods," *Journal of the American Chemical Society*, vol. 128, no. 6, pp. 2115–2120, 2006.

[26] I. H. El-Sayed, X. Huang, and M. A. El-Sayed, "Selective laser photo-thermal therapy of epithelial carcinoma using anti-EGFR antibody conjugated gold nanoparticles," *Cancer Letters*, vol. 239, no. 1, pp. 129–135, 2006.

[27] X. Huang, P. K. Jain, I. H. El-Sayed, and M. A. El-Sayed, "Plasmonic photothermal therapy (PPTT) using gold nanoparticles," *Lasers in Medical Science*, vol. 23, no. 3, pp. 217–228, 2008.

[28] L. R. Hirsch, R. J. Stafford, J. A. Bankson, S. R. Sershen, B. Rivera, R. E. Price, J. D. Hazle, N. J. Halas, and J. L. West, "Nanoshell-mediated near-infrared thermal therapy of tumors under magnetic resonance guidance," *Proceedings of the National Academy of Sciences of the United States of America*, vol. 100, no. 23, pp. 13 549–13 554, 2003.

[29] C. Loo, A. Lowery, N. Halas, J. West, and R. Drezek, "Immunotargeted Nanoshells for Integrated Cancer Imaging and Therapy ," *Nano Letters*, vol. 5, no. 4, pp. 709–711, 2005.

[30] S. Lal, S. E. Clare, and N. J. Halas, "Nanoshell-enabled photothermal cancer therapy : impending clinical impact," *Accounts of Chemical Research*, vol. 41, no. 12, pp. 1842–1851, 2008.

[31] D. P. O'Neal, L. R. Hirsch, N. J. Halas, J. D. Payne, and J. L. West, "Photo-thermal tumor ablation in mice using near infrared-absorbing nanoparticles," *Cancer Letters*, vol. 209, no. 2, pp. 171–176, 2004.

[32] A. O. Govorov and H. H. Richardson, "Generating heat with metal nanoparticles," *Nano Today*, vol. 2, no. 1, pp. 30–38, 2007.

[33] A. O. Govorov, W. Zhang, T. Skeini, H. Richardson, J. Lee, and N. A. Kotov, "Gold nanoparticle ensembles as heaters and actuators : melting and collective plasmon resonances," *Nanoscale Research Letters*, vol. 1, no. 1, pp. 84–90, 2006.

[34] H. H. Richardson, M. T. Carlson, P. J. Tandler, P. Hernandez, and A. O. Govorov, "Experimental and theoretical studies of light-to-heat conversion and collective heating effects in metal nanoparticle solutions," *Nano Letters*, vol. 9, no. 3, p. 1139, 2009.

[35] J. You, R. Zhang, G. Zhang, M. Zhong, Y. Liu, C. S. Van Pelt, D. Liang, W. Wei, A. K. Sood, and C. Li, "Photothermal-chemotherapy with doxorubicin-loaded hollow gold nanospheres : A platform for near-infrared light-trigged drug release," *Journal of Controlled Release*, vol. 158, pp. 319–328, 2011.

[36] S. M. Lee, H. Park, and K. H. Yoo, "Synergistic cancer therapeutic effects of locally delivered drug and heat using multifunctional nanoparticles," *Advanced Materials*, vol. 22, no. 36, pp. 4049–4053, 2010.

[37] J. Yang, J. Lee, J. Kang, S. J. Oh, H. J. Ko, J. H. Son, K. Lee, J. S. Suh, Y. M. Huh, and S. Haam, "Smart Drug-Loaded Polymer Gold Nanoshells for Systemic and Localized Therapy of Human Epithelial Cancer," *Advanced Materials*, vol. 21, no. 43, pp. 4339–4342, 2009.

[38] K. Park, S. Lee, E. Kang, K. Kim, K. Choi, and I. C. Kwon, "New generation of multifunctional nanoparticles for cancer imaging and therapy," *Advanced Functional Materials*, vol. 19, no. 10, pp. 1553–1566, 2009.

[39] H. Liu, D. Chen, L. Li, T. Liu, L. Tan, X. Wu, and F. Tang, "Multifunctional gold nanoshells on silica nanorattles : a platform for the combination of photothermal therapy and chemotherapy with low systemic toxicity," *Angewandte Chemie*, vol. 123, no. 4, pp. 921–925, 2011.

[40] S. Preuss, A. Demchuk, and M. Stuke, "Sub-picosecond UV laser ablation of metals," *Applied Physics A : Materials Science & Processing*, vol. 61, no. 1, pp. 33–37, 1995.

[41] S. Nolte, C. Momma, H. Jacobs, A. Tünnermann, B. N. Chichkov, B. Wellegehausen, and H. Welling, "Ablation of metals by ultrashort laser pulses," *JOSA B*, vol. 14, no. 10, pp. 2716–2722, 1997.

[42] J. Bonse, S. Baudach, J. Kruger, W. Kautek, and M. Lenzner, "Femtosecond laser ablation of silicon–modification thresholds and morphology," *Applied Physics A : Materials Science & Processing*, vol. 74, no. 1, pp. 19–25, 2002.

[43] R. R. Gattass and E. Mazur, "Femtosecond laser micromachining in transparent materials," *Nature Photonics*, vol. 2, pp. 219–225, 2008.

[44] C. B. Schaffer, A. Brodeur, and E. Mazur, "Laser-induced breakdown and damage in bulk transparent materials induced by tightly focused femtosecond laser pulses," *Measurement Science and Technology*, vol. 12, no. 11, p. 1784, 2001.

[45] A. Vogel and V. Venugopalan, "Mechanisms of pulsed laser ablation of biological tissues," *Chemical Reviews*, vol. 103, no. 2, pp. 577–644, 2003.

[46] B. N. Chichkov, C. Momma, S. Nolte, F. Von Alvensleben, and A. Tünnermann, "Femtosecond, picosecond and nanosecond laser ablation of solids," *Applied Physics A : Materials Science & Processing*, vol. 63, no. 2, pp. 109–115, 1996.

[47] L. Jiang and H. Tsai, "Femtosecond laser ablation : challenges and opportunities," in *Proceeding of NSF Workshop on Research Needs in Thermal, Aspects of Material Removal, Stillwater, OK*, 2003, pp. 163–177.

[48] C. B. Schaffer, A. Brodeur, J. F. García, and E. Mazur, "Micromachining bulk glass by use of femtosecond laser pulses with nanojoule energy," *Optics Letters*, vol. 26, no. 2, pp. 93–95, 2001.

[49] T. Juhasz, F. H. Loesel, R. M. Kurtz, C. Horvath, J. F. Bille, and G. Mourou, "Corneal refractive surgery with femtosecond lasers," *IEEE Journal of Selected Topics in Quantum Electronics*, vol. 5, no. 4, pp. 902–910, 1999.

[50] H. K. Soong and J. B. Malta, "Femtosecond lasers in ophthalmology," *American journal of ophthalmology*, vol. 147, no. 2, pp. 189–197. e2, 2009.

[51] K. König, I. Riemann, and W. Fritzsche, "Nanodissection of human chromosomes with near-infrared femtosecond laser pulses," *Optics Letters*, vol. 26, no. 11, pp. 819–821, 2001.

[52] A. Heisterkamp, I. Z. Maxwell, E. Mazur, J. M. Underwood, J. A. Nickerson, S. Kumar, and D. E. Ingber, "Pulse energy dependence of subcellular dissection by femtosecond laser pulses." *Optics Express*, vol. 13, no. 10, pp. 3690–3696, May 2005.

[53] N. Shen, D. Datta, C. B. Schaffer, P. LeDuc, D. E. Ingber, and E. Mazur, "Ablation of cytoskeletal filaments and mitochondria in live cells using a femtosecond laser nanoscissor," *Mech. Chem. Biosyst*, vol. 2, no. 1, pp. 17–25, 2005.

[54] U. K. Tirlapur and K. König, "Targeted transfection by femtosecond laser," *Nature*, vol. 418, no. 6895, pp. 290–291, 2002.

[55] J. Baumgart, W. Bintig, A. Ngezahayo, S. Willenbrock, H. Murua Escobar, W. Ertmer, H. Lubatschowski, and A. Heisterkamp, "Quantified femtosecond laser based optoperforation of living GFSHR-17 and MTH53 a cells," *Optics Express*, vol. 16, no. 5, pp. 3021–3031, 2008.

[56] J. D. Byrne, T. Betancourt, and L. Brannon-Peppas, "Active targeting schemes for nanoparticle systems in cancer therapeutics," *Advanced Drug Delivery Reviews*, vol. 60, no. 15, pp. 1615–1626, 2008.

[57] J. Baumgart, L. Humbert, É. Boulais, R. Lachaine, J. J. Lebrun, and M. Meunier, "Off-resonance plasmonic enhanced femtosecond laser optoporation and transfection of cancer cells," *Biomaterials*, vol. 33, pp. 2345–2350, 2011.

[58] X. Huang, W. Qian, I. H. El-Sayed, and M. A. El-Sayed, "The potential use of the enhanced nonlinear properties of gold nanospheres in photothermal cancer therapy ," *Lasers in Surgery and Medicine*, vol. 39, no. 9, pp. 747–753, 2007.

[59] J. L. Li, D. Day, and M. Gu, "Ultra-Low Energy Threshold for Cancer Photothermal Therapy Using Transferrin-Conjugated Gold Nanorods," *Advanced Materials*, vol. 20, no. 20, pp. 3866–3871, 2008.

[60] A. Csaki, F. Garwe, A. Steinbrück, G. Maubach, G. Festag, A. Weise, I. Riemann, K. König, and W. Fritzsche, "A parallel approach for subwavelength molecular surgery using gene-specific positioned metal nanoparticles as laser light antennas," *Nano Letters*, vol. 7, no. 2, pp. 247–253, 2007.

[61] W. J. Galush, S. A. Shelby, M. J. Mulvihill, A. Tao, P. Yang, and J. T. Groves, "A nanocube plasmonic sensor for molecular binding on membrane surfaces," *Nano Letters*, vol. 9, no. 5, pp. 2077–2082, 2009.

[62] A. V. Kabashin, P. Evans, S. Pastkovsky, W. Hendren, G. A. Wurtz, R. Atkinson, R. Pollard, V. A. Podolskiy, and A. V. Zayats, "Plasmonic nanorod metamaterials for biosensing," *Nature materials*, vol. 8, no. 11, pp. 867–871, 2009.

[63] C. Wu, A. B. Khanikaev, R. Adato, N. Arju, A. A. Yanik, H. Altug, and G. Shvets, "Fano-resonant asymmetric metamaterials for ultrasensitive spectroscopy and identification of molecular monolayers," *Nature materials*, vol. 11, pp. 69–75, 2011.

[64] B. Luk'Yanchuk, N. I. Zheludev, S. A. Maier, N. J. Halas, P. Nordlander, H. Giessen, and C. T. Chong, "The Fano resonance in plasmonic nanostructures and metamaterials," *Nature materials*, vol. 9, no. 9, pp. 707–715, 2010.

[65] S. Nie and S. R. Emory, "Probing single molecules and single nanoparticles by surface-enhanced raman scattering ," *Science*, vol. 275, no. 5303, pp. 1102–1106, 1997.

[66] X. Qian, X.-H. Peng, D. O. Ansari, Q. Yin-Goen, G. Z. Chen, D. M. Shin, L. Yang, A. N. Young, M. D. Wang, and S. Nie, "In vivo tumor targeting and spectroscopic detection with surface-enhanced Raman nanoparticle tags ," *Nature Biotechnology*, vol. 26, pp. 83–90, 2008.

[67] G. Mie, "Beitrage zur Optik truber Medien, speziell kolloidaler Metallosungen," *Ann. Phys*, vol. 4, pp. 1–69, 1908.

[68] S. A. Maier and H. A. Atwater, "Plasmonics : Localization and guiding of electromagnetic energy in metal/dielectric structures," *Journal of Applied Physics*, vol. 98, no. 1, p. 011101, 2005.

[69] H. Goldstein, C. Poole, and J. Safko, "Oscillations," in *Classical Mechanics*, A. Wesley, Ed., San Francisco, 2002, pp. 259–265.

[70] É. Boulais, R. Lachaine, and M. Meunier, "Plasma mediated off-resonance plasmonic enhanced ultrafast laser induced nanocavitation," *Nano Letters*, vol. 12, pp. 4763–4769, 2012.

[71] A. Yurtsever and A. H. Zewail, "Direct Visualization of Near-Fields in Nanoplasmonics and Nanophotonics," *Nano Letters*, vol. 12, no. 6, pp. 3334–3338, 2012.

[72] A. Vogel, J. Noack, G. Hüttman, and G. Paltauf, "Mechanisms of femtosecond laser nanosurgery of cells and tissues," *Applied Physics B : Lasers and Optics*, vol. 81, no. 8, pp. 1015–1047, 2005.

[73] P. B. Johnson and R. W. Christy, "Optical constants of the noble metals," *Physical Review B (Condensed Matter and Materials Physics)*, vol. 6, no. 12, pp. 4370–4379, 1972.

[74] J. A. Scholl, A. L. Koh, and J. A. Dionne, "Quantum plasmon resonances of individual metallic nanoparticles," *Nature*, vol. 483, no. 7390, pp. 421–427, 2012.

[75] S. Link and M. A. El-Sayed, "Spectral properties and relaxation dynamics of surface plasmon electronic oscillations in gold and silver nanodots and nanorods," *The Journal of Physical Chemistry B*, vol. 103, no. 40, pp. 8410–8426, 1999.

[76] E. S. Kooij and B. Poelsema, "Shape and size effects in the optical properties of metallic nanorods," *Physical Chemistry Chemical Physics*, vol. 8, no. 28, pp. 3349–3357, 2006.

[77] R. D. Averitt, S. L. Westcott, and N. J. Halas, "Linear optical properties of gold nanoshells," *JOSA B*, vol. 16, no. 10, pp. 1824–1832, 1999.

[78] R. D. Averitt, D. Sarkar, and N. J. Halas, "Plasmon Resonance Shifts of Au-Coated Au_ 2 S Nanoshells : Insight into Multicomponent Nanoparticle Growth," *Physical Review Letters*, vol. 78, no. 22, pp. 4217–4220, 1997.

[79] R. D. Averitt, S. L. Westcott, and N. J. Halas, "Ultrafast electron dynamics in gold nanoshells," *Physical Review B (Condensed Matter and Materials Physics)*, vol. 58, no. 16, pp. 10 203–10 206, 1998.

[80] C. L. Nehl, N. K. Grady, G. P. Goodrich, F. Tam, N. J. Halas, and J. H. Hafner, "Scattering spectra of single gold nanoshells," *Nano Letters*, vol. 4, no. 12, pp. 2355–2359, 2004.

[81] R. Bardhan, W. Chen, C. Perez Torres, M. Bartels, R. M. Huschka, L. L. Zhao, E. Morosan, R. G. Pautler, A. Joshi, and N. J. Halas, "Nanoshells with targeted simultaneous enhancement of magnetic and optical imaging and photothermal therapeutic response," *Advanced Functional Materials*, vol. 19, no. 24, pp. 3901–3909, 2009.

[82] R. Weissleder, "A clearer vision for in vivo imaging. Progress continues in the development of smaller, more penetrable probes for biological imaging," *Nature Biotechnology*, vol. 19, no. 4, pp. 316–317, 2001.

[83] C. Loo, L. Hirsch, M. H. Lee, E. Chang, J. West, N. Halas, and R. Drezek, "Gold nanoshell bioconjugates for molecular imaging in living cells," *Optics Letters*, vol. 30, no. 9, pp. 1012–1014, 2005.

[84] A. M. Gobin, D. P. O'Neal, D. M. Watkins, N. J. Halas, R. A. Drezek, and J. L. West, "Near infrared laser-tissue welding using nanoshells as an exogenous absorber," *Lasers in Surgery and Medicine*, vol. 37, no. 2, pp. 123–129, 2005.

[85] J. R. Cole, N. A. Mirin, M. W. Knight, G. P. Goodrich, and N. J. Halas, "Photothermal efficiencies of nanoshells and nanorods for clinical therapeutic applications," *The Journal of Physical Chemistry C*, vol. 113, no. 28, pp. 12 090–12 094, 2009.

[86] R. Bardhan, S. Lal, A. Joshi, and N. J. Halas, "Theranostic nanoshells : from probe design to imaging and treatment of cancer," *Accounts of Chemical Research*, vol. 44, no. 10, pp. 936–946, 2011.

[87] M.-R. Choi, K. J. Stanton-Maxey, J. K. Stanley, C. S. Levin, R. Bardhan, D. Akin, S. Badve, J. Sturgis, J. P. Robinson, R. Bashir, N. J. Halas, and S. E. Clare, "A cellular Trojan Horse for delivery of therapeutic nanoparticles into tumors," *Nano Letters*, vol. 7, no. 12, pp. 3759–3765, 2007.

[88] O. B. Toon and T. P. Ackerman, "Algorithms for the calculation of scattering by stratified spheres," *Applied Optics*, vol. 20, no. 20, pp. 3657–3660, 1981.

[89] Y. Y. Yu, S. S. Chang, C. L. Lee, and C. R. C. Wang, "Gold nanorods : electrochemical synthesis and optical properties," *The Journal of Physical Chemistry B*, vol. 101, no. 34, pp. 6661–6664, 1997.

[90] C. L. Chen, L. R. Kuo, C. L. Chang, Y. K. Hwu, C. K. Huang, S. Y. Lee, K. Chen, S. J. Lin, J. D. Huang, and Y. Y. Chen, "In situ real-time investigation of cancer cell photothermolysis mediated by excited gold nanorod surface plasmons," *Biomaterials*, vol. 31, no. 14, pp. 4104–4112, 2010.

[91] L. Tong, Y. Zhao, T. B. Huff, M. N. Hansen, A. Wei, and J. X. Cheng, "Gold nanorods mediate tumor cell death by compromising membrane integrity," *Advanced Materials*, vol. 19, no. 20, pp. 3136–3141, 2007.

[92] P. K. Jain, K. S. Lee, I. H. El-Sayed, and M. A. El-Sayed, "Calculated absorption and scattering properties of gold nanoparticles of different size, shape, and composition : applications in biological imaging and biomedicine," *The Journal of Physical Chemistry B*, vol. 110, no. 14, pp. 7238–7248, 2006.

[93] M. A. Yurkin and A. G. Hoekstra, "The discrete dipole approximation : an overview and recent developments," *Journal of Quantitative Spectroscopy and Radiative Transfer*, vol. 106, no. 1–3, pp. 558–589, 2007.

[94] K. Yee, "Numerical solution of initial boundary value problems involving Maxwell's equations in isotropic media," *Antennas and Propagation, IEEE Transactions on*, vol. 14, no. 3, pp. 302–307, 1966.

[95] J. L. Volakis, A. Chatterjee, and L. C. Kempel, "Review of the finite-element method for three-dimensional electromagnetic scattering," *JOSA A*, vol. 11, no. 4, pp. 1422–1433, 1994.

[96] S. Asano and G. Yamamoto, "Light scattering by a spheroidal particle ," *Applied Optics*, vol. 14, pp. 29–49, 1975.

[97] S. Link, M. B. Mohamed, and M. A. El-Sayed, "Simulation of the optical absorption spectra of gold nanorods as a function of their aspect ratio and the effect of the medium dielectric constant," *The Journal of Physical Chemistry B*, vol. 103, no. 16, pp. 3073–3077, 1999.

[98] L. Tong, Q. Wei, A. Wei, and J. X. Cheng, "Gold Nanorods as Contrast Agents for Biological Imaging : Optical Properties, Surface Conjugation and Photothermal Effects," *Photochemistry and photobiology*, vol. 85, no. 1, pp. 21–32, 2009.

[99] M. B. Mohamed, V. Volkov, S. Link, and M. A. El-Sayed, "The lightning'gold nanorods : fluorescence enhancement of over a million compared to the gold metal," *Chemical Physics Letters*, vol. 317, no. 6, pp. 517–523, 2000.

[100] K. Imura, T. Nagahara, and H. Okamoto, "Near-field two-photon-induced photoluminescence from single gold nanorods and imaging of plasmon modes," *The Journal of Physical Chemistry B*, vol. 109, no. 27, pp. 13 214–13 220, 2005.

[101] C. Sönnichsen and A. P. Alivisatos, "Gold nanorods as novel nonbleaching plasmon-based orientation sensors for polarized single-particle microscopy," *Nano Letters*, vol. 5, no. 2, pp. 301–304, 2005.

[102] J. Chen, F. Saeki, J. Benjamin, H. Cang, M. J. Cobb, Z. Y. Li, L. Au, H. Zhang, M. B. Kimmey, and X. Li, "Gold nanocages : bioconjugation and their potential use as optical imaging contrast agents," *Nano Letters*, vol. 5, no. 3, pp. 473–477, 2005.

[103] J. Chen, D. Wang, J. Xi, L. Au, A. Siekkinen, A. Warsen, Z. Y. Li, H. Zhang, Y. Xia, and X. Li, "Immuno gold nanocages with tailored optical properties for targeted photothermal destruction of cancer cells," *Nano Letters*, vol. 7, no. 5, pp. 1318–1322, 2007.

[104] S. E. Skrabalak, J. Chen, Y. Sun, X. Lu, L. Au, C. M. Cobley, and Y. Xia, "Gold nanocages : synthesis, properties, and applications," *Accounts of Chemical Research*, vol. 41, no. 12, pp. 1587–1595, 2008.

[105] J. Chen, B. Wiley, Z. Y. Li, D. Campbell, F. Saeki, H. Cang, L. Au, J. Lee, X. Li, and Y. Xia, "Gold nanocages : engineering their structure for biomedical applications," *Advanced Materials*, vol. 17, no. 18, pp. 2255–2261, 2005.

[106] M. S. Yavuz, Y. Cheng, J. Chen, C. M. Cobley, Q. Zhang, M. Rycenga, J. Xie, C. KIM, K. H. Song, and A. G. Schwartz, "Gold nanocages covered by smart polymers for controlled release with near-infrared light," *Nature materials*, vol. 8, no. 12, pp. 935–939, 2009.

[107] T. S. Ahmadi, Z. L. Wang, T. C. Green, A. Henglein, and M. A. El-Sayed, "Shape-controlled synthesis of colloidal platinum nanoparticles," *Science*, vol. 272, no. 5270, pp. 1924–1925, 1996.

[108] Y. Sun and Y. Xia, "Shape-controlled synthesis of gold and silver nanoparticles," *Science*, vol. 298, no. 5601, pp. 2176–2179, 2002.

[109] F. Kim, S. Connor, H. Song, T. Kuykendall, and P. Yang, "Platonic gold nanocrystals," *Angewandte Chemie*, vol. 116, no. 28, pp. 3759–3763, 2004.

[110] R. Jin, Y. W. Cao, C. A. Mirkin, K. L. Kelly, G. C. Schatz, and J. G. Zheng, "Photoinduced conversion of silver nanospheres to nanoprisms," *Science*, vol. 294, no. 5548, pp. 1901–1903, 2001.

[111] R. Jin, Y. C. Cao, E. Hao, G. S. Métraux, G. C. Schatz, and C. A. Mirkin, "Controlling anisotropic nanoparticle growth through plasmon excitation," *Nature*, vol. 425, no. 6957, pp. 487–490, 2003.

[112] S. Shiv Shankar, A. Rai, B. Ankamwar, A. Singh, A. Ahmad, and M. Sastry, "Biological synthesis of triangular gold nanoprisms ," *Nature materials*, no. 3, pp. 482–488, 2004.

[113] C. L. Nehl, H. Liao, and J. H. Hafner, "Optical properties of star-shaped gold nanoparticles," *Nano Letters*, vol. 6, no. 4, pp. 683–688, 2006.

[114] F. Hao, C. L. Nehl, J. H. Hafner, and P. Nordlander, "Plasmon resonances of a gold nanostar," *Nano Letters*, vol. 7, no. 3, pp. 729–732, 2007.

[115] H. Yuan, C. G. Khoury, C. M. Wilson, G. A. Grant, A. J. Bennett, and T. Vo-Dinh, "In vivo particle tracking and photothermal ablation using plasmon-resonant gold nanostars," *Nanomedicine : Nanotechnology, Biology, and Medicine*, vol. 8, pp. 1355–1363, 2012.

[116] R. Rodríguez-Oliveros and J. A. Sánchez-Gil, "Gold nanostars as thermoplasmonic nanoparticles for optical heating," *Optics Express*, vol. 20, no. 1, pp. 621–626, 2012.

[117] H. Wang, D. W. Brandl, F. Le, P. Nordlander, and N. J. Halas, "Nanorice : a hybrid plasmonic nanostructure," *Nano Letters*, vol. 6, no. 4, pp. 827–832, 2006.

[118] J. Benjamin, Y. Chen, J. M. McLellan, Y. Xiong, Z. Y. Li, D. Ginger, and Y. Xia, "Synthesis and optical properties of silver nanobars and nanorice," *Nano Letters*, vol. 7, no. 4, pp. 1032–1036, 2007.

[119] H. Wei, A. Reyes-Coronado, P. Nordlander, J. Aizpurua, and H. Xu, "Multipolar plasmon resonances in individual Ag nanorice," *ACS Nano*, vol. 4, no. 5, pp. 2649–2654, 2010.

[120] N. Hooshmand, P. K. Jain, and M. A. El-Sayed, "Plasmonic spheroidal metal nanoshells showing larger tunability and stronger near fields than their spherical counterparts : an effect of enhanced plasmon coupling," *The Journal of Physical Chemistry Letters*, vol. 2, no. 5, pp. 374–378, 2011.

[121] E. M. Larsson, J. Alegret, M. Käll, and D. S. Sutherland, "Sensing characteristics of NIR localized surface plasmon resonances in gold nanorings for application as ultrasensitive biosensors," *Nano Letters*, vol. 7, no. 5, pp. 1256–1263, 2007.

[122] F. Hao, E. M. Larsson, T. A. Ali, D. S. Sutherland, and P. Nordlander, "Shedding light on dark plasmons in gold nanorings," *Chemical Physics Letters*, vol. 458, no. 4, pp. 262–266, 2008.

[123] J. Aizpurua, P. Hanarp, D. S. Sutherland, M. Käll, G. W. Bryant, and F. J. García de Abajo, "Optical properties of gold nanorings," *Physical Review Letters*, vol. 90, no. 5, p. 57401, 2003.

[124] R. Bukasov and J. S. Shumaker-Parry, "Highly tunable infrared extinction properties of gold nanocrescents," *Nano Letters*, vol. 7, no. 5, pp. 1113–1118, 2007.

[125] Y. Lu, G. L. Liu, J. Kim, Y. X. Mejia, and Lee, L.P., "Nanophotonic crescent moon structures with sharp edge for ultrasensitive biomolecular detection by local electromagnetic field enhancement effect," *Nano Letters*, vol. 5, no. 1, pp. 119–124, 2005.

[126] A. Plech, V. Kotaidis, M. Lorenc, and J. Boneberg, "Femtosecond laser near-field ablation from gold nanoparticles," *Nature Physics*, vol. 2, no. 1, pp. 44–47, 2005.

[127] S. Link and M. A. El-Sayed, "Shape and size dependence of radiative, non-radiative and photothermal properties of gold nanocrystals," *International Reviews in Physical Chemistry*, vol. 19, no. 3, pp. 409–453, 2000.

[128] T. S. Ahmadi, S. L. Logunov, and M. A. El-Sayed, "Picosecond dynamics of colloidal gold nanoparticles," *The Journal of Physical Chemistry*, vol. 100, no. 20, pp. 8053–8056, 1996.

[129] C. K. Sun, F. Vallee, L. H. Acioli, E. P. Ippen, and J. G. Fujimoto, "Femtosecond-tunable measurement of electron thermalization in gold," *Physical Review B (Condensed Matter and Materials Physics)*, vol. 50, no. 20, p. 15337, 1994.

[130] C. Sönnichsen, T. Franzl, T. Wilk, G. von Plessen, J. Feldmann, O. Wilson, and P. Mulvaney, "Drastic reduction of plasmon damping in gold nanorods," *Physical Review Letters*, vol. 88, no. 7, p. 77402, 2002.

[131] F. Hubenthal, C. Hendrich, and F. Träger, "Damping of the localized surface plasmon polariton resonance of gold nanoparticles," *Applied Physics B : Lasers and Optics*, vol. 100, no. 1, pp. 225–230, 2010.

[132] J. Bosbach, C. Hendrich, F. Stietz, T. Vartanyan, and F. Träger, "Ultrafast dephasing of surface plasmon excitation in silver nanoparticles : Influence of particle size, shape, and chemical surrounding," *Physical Review Letters*, vol. 89, no. 25, p. 257404, 2002.

[133] F. Hubenthal, "Ultrafast dephasing time of localized surface plasmon polariton resonance and the involved damping mechanisms in colloidal gold nanoparticles ," *Progress in surface science*, vol. 82, no. 4, pp. 378–387, 2007.

[134] U. Kreibig, "Interface-induced dephasing of Mie plasmon polaritons," *Applied Physics B : Lasers and Optics*, vol. 93, no. 1, pp. 79–89, 2008.

[135] E. Zaremba and B. Persson, "Dynamic polarizability of small metal particles," *Physical Review B (Condensed Matter and Materials Physics)*, vol. 35, no. 2, p. 596, 1987.

[136] N. I. Grigorchuk, "Resonance Plasmon Linewidth Oscillations in Spheroidal Metallic Nanoparticle Embedded in a Dielectric Matrix," *Journal of Applied Physics*, vol. 112, no. 6, p. 064306, 2012.

[137] C. A. Ullrich, P. G. Reinhard, and E. Suraud, "Electron emission from strongly excited metal clusters," *Physical Review A*, vol. 57, no. 3, p. 1938, 1998.

[138] R. A. Molina, D. Weinmann, and R. A. Jalabert, "Oscillatory Size-Dependence of the Surface Plasmon Linewidth in Metallic Nanoparticles," *Physical Review B*, vol. 65, p. 155427, 2002.

[139] J. Y. Bigot, J. Y. Merle, O. Cregut, and A. Daunois, "Electron dynamics in copper metallic nanoparticles probed with femtosecond optical pulses," *Physical Review Letters*, vol. 75, no. 25, pp. 4702–4705, 1995.

[140] S. Link, C. Burda, Z. L. Wang, and M. A. El-Sayed, "Electron dynamics in gold and gold–silver alloy nanoparticles : The influence of a nonequilibrium electron distribution and the size dependence of the electron–phonon relaxation," *The Journal of Chemical Physics*, vol. 111, pp. 1255–1264, 1999.

[141] A. M. Dowgiallo and K. L. Knappenberger, "Ultrafast electron–phonon coupling in hollow gold nanospheres," *Physical Chemistry Chemical Physics*, vol. 13, no. 48, pp. 21 585–21 592, 2011.

[142] R. W. Schoenlein, W. Z. Lin, J. G. Fujimoto, and G. L. Eesley, "Femtosecond studies of nonequilibrium electronic processes in metals," *Physical Review Letters*, vol. 58, no. 16, pp. 1680–1683, 1987.

[143] A. Arbouet, C. Voisin, D. Christofilos, P. Langot, N. D. Fatti, F. Vallee, J. Lerme, G. Celep, E. Cottancin, and M. Gaudry, "Electron-phonon scattering in metal clusters," *Physical Review Letters*, vol. 90, no. 17, p. 177401, 2003.

[144] N. N. Nedyalkov, P. A. Atanasov, and M. Obara, "Near-field properties of a gold nanoparticle array on different substrates excited by a femtosecond laser," *Nanotechnology*, vol. 18, no. 30, p. 305703, 2007.

[145] P. A. Atanasov, N. N. Nedyalkov, T. Sakai, and M. Obara, "Localization of the electromagnetic field in the vicinity of gold nanoparticles : Surface modification of different substrates," *Applied Surface Science*, vol. 254, no. 4, pp. 794–798, 2007.

[146] D. Eversole, B. Luk'Yanchuk, and A. Ben-Yakar, "Plasmonic laser nanoablation of silicon by the scattering of femtosecond pulses near gold nanospheres," *Applied Physics A : Materials Science & Processing*, vol. 89, no. 2, pp. 283–291, 2007.

[147] T. Miyanishi, T. Sakai, N. N. Nedyalkov, and M. Obara, "Femtosecond-laser nanofabrication onto silicon surface with near-field localization generated by plasmon polaritons in gold nanoparticles with oblique irradiation," *Applied Physics A : Materials Science & Processing*, vol. 96, no. 4, pp. 843–850, 2009.

[148] N. Nedyalkov, T. Sakai, T. Miyanishi, and M. Obara, "Near field properties in the vicinity of gold nanoparticles placed on various substrates for precise nanostructuring," *Journal of Physics D : Applied Physics*, vol. 39, no. 23, p. 5037, 2006.

[149] N. N. Nedyalkov, S. Imamova, P. A. Atanasov, Y. Tanaka, and M. Obara, "Interaction between ultrashort laser pulses and gold nanoparticles : nanoheater and nanolens effect," *Journal of Nanoparticle Research*, vol. 13, no. 5, pp. 2181–2193, 2011.

[150] S. M. Huang, M. H. Hong, B. S. Lukyanchuk, and T. C. Chong, "Direct and subdiffraction-limit laser nanofabrication in silicon," *Applied Physics Letters*, vol. 82, no. 26, pp. 4809–4811, 2003.

[151] G. Obara, Y. Tanaka, T. Miyanishi, and M. Obara, "Uniform plasmonic near-field nanopatterning by backward irradiation of femtosecond laser," *Applied Physics A : Materials Science & Processing*, vol. 102, no. 3, pp. 551–557, 2011.

[152] J. Boneberg, J. König-Birk, H. J. Münzer, P. Leiderer, K. L. Shuford, and G. C. Schatz, "Optical near-fields of triangular nanostructures," *Applied Physics A : Materials Science & Processing*, vol. 89, no. 2, pp. 299–303, 2007.

[153] P. Leiderer, C. Bartels, J. König-Birk, M. Mosbacher, and J. Boneberg, "Imaging optical near-fields of nanostructures," *Applied Physics Letters*, vol. 85, no. 22, pp. 5370–5372, 2004.

[154] R. K. Harrison and A. Ben-Yakar, "Role of near-field enhancement in plasmonic laser nanoablation using gold nanorods on a silicon substrate," *Optics Express*, vol. 18, no. 21, pp. 22 556–22 571, 2010.

[155] A. Robitaille, E. Boulais, and M. Meunier, "Mechanisms of plasmon-enhanced femtosecond laser nanoablation of silicon," *Optics Express*, p. Submitted, 2012.

[156] A. Plech, P. Leiderer, and J. Boneberg, "Femtosecond laser near field ablation," *Laser & Photonics Reviews*, vol. 3, no. 5, pp. 435–451, 2009.

[157] A. Vogel, N. Linz, S. Freidank, and G. Paltauf, "Femtosecond-laser-induced nanocavitation in water : implications for optical breakdown threshold and cell surgery," *Physical Review Letters*, vol. 100, no. 3, p. 38102, 2008.

[158] V. K. Pustovalov, A. S. Smetannikov, and V. P. Zharov, "Photothermal and accompanied phenomena of selective nanophotothermolysis with gold nanoparticles and laser pulses," *Laser Physics Letters*, vol. 5, no. 11, pp. 775–792, 2008.

[159] V. Kotaidis, C. Dahmen, G. von Plessen, F. Springer, and A. Plech, "Excitation of nanoscale vapor bubbles at the surface of gold nanoparticles in water," *The Journal of Chemical Physics*, vol. 124, p. 184702, 2006.

[160] P. Lorazo, L. J. Lewis, and M. Meunier, "Thermodynamic pathways to melting, ablation, and solidification in absorbing solids under pulsed laser irradiation," *Physical Review B (Condensed Matter and Materials Physics)*, vol. 73, no. 13, p. 134108, 2006.

[161] D. Perez, L. J. Lewis, P. Lorazo, and M. Meunier, "Ablation of molecular solids under nanosecond laser pulses : The role of inertial confinement," *Applied Physics Letters*, vol. 89, no. 14, pp. 141 907–141 907–3, 2006.

[162] A. Miotello and R. Kelly, "Critical assessment of thermal models for laser sputtering at high fluences," *Applied Physics Letters*, vol. 67, no. 24, pp. 3535–3537, 1995.

[163] A. Miotello and R. Kelly, "Laser-induced phase explosion : new physical problems when a condensed phase approaches the thermodynamic critical temperature," *Applied Physics A : Materials Science & Processing*, vol. 69, no. 7, pp. 67–73, 1999.

[164] N. M. Bulgakova and A. V. Bulgakov, "Pulsed laser ablation of solids : transition from normal vaporization to phase explosion," *Applied Physics A : Materials Science & Processing*, vol. 73, no. 2, pp. 199–208, 2001.

[165] B. R. Novak, E. J. Maginn, and M. J. McCready, "Comparison of heterogeneous and homogeneous bubble nucleation using molecular simulations," *Physical Review B (Condensed Matter and Materials Physics)*, vol. 75, no. 8, p. 085413, 2007.

[166] V. P. Carey and A. P. Wemhoff, "Thermodynamic analysis of near-wall effects on phase stability and homogeneous nucleation during rapid surface heating," *International Journal of Heat and Mass Transfer*, vol. 48, no. 25, pp. 5431–5445, 2005.

[167] J. L. Katz and M. Blander, "Condensation and boiling : Corrections to homogeneous nucleation theory for nonideal gases," *Journal of Colloid and Interface Science*, vol. 42, no. 3, pp. 496–502, 1973.

[168] X. Xu and D. A. Willis, "Non-equilibrium phase change in metal induced by nanosecond pulsed laser irradiation," *Transactions-American Society of Mechanical Engineers Journal of Heat Transfer*, vol. 124, no. 2, pp. 293–298, 2002.

[169] M. M. Martynyuk, "Phase explosion of a metastable fluid," *Combustion, Explosion, and Shock Waves*, vol. 13, no. 2, pp. 178–191, 1977.

[170] Wagner and A. W Pruss, "The IAPWS formulation 1995 for the thermodynamic properties of ordinary water substance for general and scientific use," *J. Phys. Chem. Ref. Data*, vol. 31, no. 2, pp. 387–535, 2002.

[171] B. J. Garrison, T. E. Itina, and L. V. Zhigilei, "Limit of overheating and the threshold behavior in laser ablation," *Physical Review E*, vol. 68, no. 4, p. 041501, 2003.

[172] O. Ekici, R. K. Harrison, N. J. Durr, D. S. Eversole, M. Lee, and A. Ben-Yakar, "Thermal analysis of gold nanorods heated with femtosecond laser pulses," *Journal of Physics D : Applied Physics*, vol. 41, no. 18, p. 185501, 2008.

[173] D. Perez and L. J. Lewis, "Molecular-dynamics study of ablation of solids under femtosecond laser pulses ," *Physical Review B (Condensed Matter and Materials Physics)*, vol. 67, no. 18, p. 184102, 2003.

[174] D. W. Oxtoby and R. Evans, "Nonclassical nucleation theory for the gas–liquid transition," *The Journal of Chemical Physics*, vol. 89, p. 7521, 1988.

[175] V. Talanquer and D. W. Oxtoby, "Dynamical density functional theory of gas–liquid nucleation," *The Journal of Chemical Physics*, vol. 100, no. 7, pp. 5190–5200, 1994.

[176] J. W. Cahn and J. E. Hilliard, "Free Energy of a Nonuniform System. III. Nucleation in a Two-Component Incompressible Fluid," *The Journal of Chemical Physics*, vol. 31, p. 688, 1959.

[177] S. B. Kiselev and J. F. Ely, "Curvature effect on the physical boundary of metastable states in liquids," *Physica A : Statistical Mechanics and its Applications*, vol. 299, no. 3, pp. 357–370, 2001.

[178] S. B. Kiselev, "Kinetic boundary of metastable states in superheated and stretched liquids," *Physica A : Statistical Mechanics and its Applications*, vol. 269, no. 2, pp. 252–268, 1999.

[179] J. Neumann and R. Brinkmann, "Self-limited growth of laser-induced vapor bubbles around single microabsorbers," *Applied Physics Letters*, vol. 93, no. 3, pp. 033 901–033 901–3, 2008.

[180] E. Lukianova-Hleb, Y. Hu, L. Latterini, L. Tarpani, S. Lee, R. A. Drezek, J. H. Hafner, and D. O. Lapotko, "Plasmonic nanobubbles as transient vapor nanobubbles generated around plasmonic nanoparticles," *ACS Nano*, vol. 4, no. 4, pp. 2109–2123, 2010.

[181] L. Rayleigh, "On the pressure developed in a liquid during the collapse of a spherical cavity," *Philos. Mag. Series 6*, vol. 34, no. 200, pp. 94–98, 1917.

[182] J. Neumann and R. Brinkmann, "Microbubble dynamics around laser heated microparticles," in *Proceeding of the SPIE*, vol. 5142, 2002, p. 82.

[183] S. R. Aglyamov, A. B. Karpiouk, F. Bourgeois, A. Ben-Yakar, and S. Y. Emelianov, "Ultrasound measurements of cavitation bubble radius for femtosecond laser-induced breakdown in water," *Optics Letters*, vol. 33, no. 12, pp. 1357–1359, 2008.

[184] D. Lapotko, "Plasmonic nanobubbles as tunable cellular probes for cancer theranostics," *Cancers*, vol. 3, no. 1, pp. 802–840, 2011.

[185] C. E. Brennen, *Cavitation and bubble dynamics*, ser. Oxford engineering science series. New York, NY : Oxford Univ. Press, 1995.

[186] I. Akhatov, O. Lindau, A. Topolnikov, R. Mettin, N. Vakhitova, and W. Lauterborn, "Collapse and rebound of a laser-induced cavitation bubble," *Physics of Fluids*, vol. 13, no. 10, pp. 2805–2819, 2001.

[187] C. D. Ohl, O. Lindau, and W. Lauterborn, "Luminescence from spherically and aspherically collapsing laser induced bubbles," *Physical Review Letters*, vol. 80, no. 2, pp. 393–396, 1998.

[188] L. D. Landau and E. M. Lifshitz, *Fluid Mechanics*, 2nd ed., ser. Course of Theoretical Physics. Butterworth-Heinemann, 2010, vol. 6.

[189] E. P. Furlani, I. H. Karampelas, and Q. Xie, "Analysis of pulsed laser plasmon-assisted photothermal heating and bubble generation at the nanoscale," *Lab on a Chip*, vol. 12, pp. 3707–3719, 2012.

[190] M. S. Plesset and A. Prosperetti, "Bubble dynamics and cavitation," *Annual Review of Fluid Mechanics*, vol. 9, no. 1, pp. 145–185, 1977.

[191] V. Kotaidis and A. Plech, "Cavitation dynamics on the nanoscale," *Applied Physics Letters*, vol. 87, no. 21, pp. 213 102–213 102–3, 2005.

[192] E. A. Brujan, "Numerical investigation on the dynamics of cavitation nanobubbles," *Microfluidics and nanofluidics*, vol. 11, no. 5, pp. 511–517, 2011.

[193] A. Siems, S. Weber, J. Boneberg, and A. Plech, "Thermodynamics of nanosecond nanobubble formation at laser-excited metal nanoparticles," *New Journal of Physics*, vol. 13, no. 4, p. 043018, 2011.

[194] E. Y. Lukianova-Hleb, E. Y. Hanna, J. H. Hafner, and D. O. Lapotko, "Tunable plasmonic nanobubbles for cell theranostics," *Nanotechnology*, vol. 21, no. 8, p. 085102, 2010.

[195] V. P. Zharov and D. O. Lapotko, "Photothermal imaging of nanoparticles and cells," *IEEE Journal of Selected Topics in Quantum Electronics*, vol. 11, no. 4, pp. 733–751, 2005.

[196] D. Lapotko, "Optical excitation and detection of vapor bubbles around plasmonic nanoparticles," *Optics Express*, vol. 17, no. 4, pp. 2538–2556, 2009.

[197] R. Lachaine, É. Boulais, E. Bourbeau, and M. Meunier, "Effect of pulse duration on plasmonic enhanced ultrafast laser-induced bubble generation in water," *Applied Physics A : Materials Science & Processing*, pp. 1–4, 2012.

[198] A. Plech, V. Kotaidis, S. Gresillon, C. Dahmen, and G. von Plessen, "Laser-induced heating and melting of gold nanoparticles studied by time-resolved x-ray scattering," *Physical Review B (Condensed Matter and Materials Physics)*, vol. 70, no. 19, p. 195423, 2004.

[199] C. B. Schaffer, N. Nishimura, E. N. Glezer, A. M. T. Kim, and E. Mazur, "Dynamics of femtosecond laser-induced breakdown in water from femtoseconds to microseconds," *Optics Express*, vol. 10, no. 3, pp. 196–203, 2002.

[200] M. J. Zohdy, C. Tse, J. Y. Ye, and M. O'Donnell, "Optical and acoustic detection of laser-generated microbubbles in single cells," *Ultrasonics, Ferroelectrics and Frequency Control, IEEE Transactions on*, vol. 53, no. 1, pp. 117–125, 2006.

[201] E. Y. Lukianova-Hleb and D. O. Lapotko, "Influence of transient environmental photothermal effects on optical scattering by gold nanoparticles," *Nano Letters*, vol. 9, no. 5, p. 2160, 2009.

[202] A. Takami, H. Kurita, and S. Koda, "Laser-induced size reduction of noble metal particles," *The Journal of Physical Chemistry B*, vol. 103, no. 8, pp. 1226–1232, 1999.

[203] S. Link, C. Burda, B. Nikoobakht, and M. A. El-Sayed, "Laser-induced shape changes of colloidal gold nanorods using femtosecond and nanosecond laser pulses," *The Journal of Physical Chemistry B*, vol. 104, no. 26, pp. 6152–6163, 2000.

[204] S. Link, C. Burda, M. B. Mohamed, B. Nikoobakht, and M. A. El-Sayed, "Laser photothermal melting and fragmentation of gold nanorods : energy and laser pulse-width dependence," *The Journal of Physical Chemistry A*, vol. 103, no. 9, pp. 1165–1170, 1999.

[205] C. M. Aguirre, C. E. Moran, J. F. Young, and N. J. Halas, "Laser-induced reshaping of metallodielectric nanoshells under femtosecond and nanosecond plasmon resonant

illumination," *The Journal of Physical Chemistry B*, vol. 108, no. 22, pp. 7040–7045, 2004.

[206] S. L. Lai, J. Y. Guo, V. Petrova, G. Ramanath, and L. H. Allen, "Size-dependent melting properties of small tin particles : nanocalorimetric measurements," *Physical Review Letters*, vol. 77, no. 1, pp. 99–102, 1996.

[207] K. Dick, T. Dhanasekaran, Z. Zhang, and D. Meisel, "Size-dependent melting of silica-encapsulated gold nanoparticles," *Journal of the American Chemical Society*, vol. 124, no. 10, pp. 2312–2317, 2002.

[208] P. Zijlstra, J. W. M. Chon, and M. Gu, "White light scattering spectroscopy and electron microscopy of laser induced melting in single gold nanorods," *Physical Chemistry Chemical Physics*, vol. 11, no. 28, pp. 5915–5921, 2009.

[209] A. N. Goldstein, C. M. Echer, and A. P. Alivisatos, "Melting in semiconductor nanocrystals." *Science*, vol. 256, no. 5062, p. 1425, 1992.

[210] H. Petrova, J. P. Juste, I. Pastoriza-Santos, G. V. Hartland, L. M. Liz-Marzán, and P. Mulvaney, "On the temperature stability of gold nanorods : comparison between thermal and ultrafast laser-induced heating," *Physical Chemistry Chemical Physics*, vol. 8, no. 7, pp. 814–821, 2005.

[211] A. Plech, R. Cerna, V. Kotaidis, F. Hudert, A. Bartels, and T. Dekorsy, "A Surface Phase Transition of Supported Gold Nanoparticles," *Nano Letters*, vol. 7, no. 4, pp. 1026–1031, Apr. 2007.

[212] S. Inasawa, M. Sugiyama, and Y. Yamaguchi, "Laser-induced shape transformation of gold nanoparticles below the melting point : The effect of surface melting," *The Journal of Physical Chemistry B*, vol. 109, no. 8, pp. 3104–3111, 2005.

[213] F. Ercolessi, W. Andreoni, and E. Tosatti, "Melting of small gold particles : Mechanism and size effects," *Physical Review Letters*, vol. 66, no. 7, pp. 911–914, 1991.

[214] R. R. Letfullin, C. Joenathan, T. F. George, and V. P. Zharov, "Laser-induced explosion of gold nanoparticles : potential role for nanophotothermolysis of cancer," *Nanomedicine*, vol. 1, no. 4, pp. 473–480, 2006.

[215] S. Hashimoto, D. Werner, and T. Uwada, "Studies on the interaction of pulsed lasers with plasmonic gold nanoparticles toward light manipulation, heat management, and nanofabrication," *Journal of Photochemistry and Photobiology C : Photochemistry Reviews*, vol. 13, pp. 28–54, 2012.

[216] K. Yamada, Y. Tokumoto, T. Nagata, and F. Mafuné, "Mechanism of laser-induced size-reduction of gold nanoparticles as studied by nanosecond transient absorption spectroscopy," *The Journal of Physical Chemistry B*, vol. 110, no. 24, pp. 11 751–11 756, 2006.

[217] T. Q. Qiu and C. L. Tien, "Heat transfer mechanisms during short-pulse laser heating of metals ," *J. Heat Transfer*, vol. 115, no. 4, pp. 835–841, 1993.

[218] J. K. Chen and J. E. Beraun, "Numerical study of ultrashort laser pulse interactions with metal films," *Numerical Heat Transfer, Part A : Applications*, vol. 40, no. 1, pp. 1–20, 2001.

[219] P. Grua, J. P. Morreeuw, H. Bercegol, G. Jonusauskas, and F. Vallee, "Electron kinetics and emission for metal nanoparticles exposed to intense laser pulses," *Physical Review B (Condensed Matter and Materials Physics)*, vol. 68, no. 3, pp. 35 424–35 421, 2003.

[220] W. Y. Wang, D. M. Riffe, Y. S. Lee, and M. C. Downer, "Time-resolved electron temperature measurement in a highly-excited gold target using femtosecond thermionic emission," *Physical Review B (Condensed Matter and Materials Physics)*, vol. 50, no. 11, p. 8016, 1994.

[221] J. H. Hodak, I. Martini, and G. V. Hartland, "Spectroscopy and dynamics of nanometer-sized noble metal particles," *The Journal of Physical Chemistry B*, vol. 102, no. 36, pp. 6958–6967, 1998.

[222] J. H. Hodak, A. Henglein, and G. V. Hartland, "Electron-phonon coupling dynamics in very small (between 2 and 8 nm diameter) Au nanoparticles," *The Journal of Chemical Physics*, vol. 112, p. 5942, 2000.

[223] G. V. Hartland, "Measurements of the material properties of metal nanoparticles by time-resolved spectroscopy," *Physical Chemistry Chemical Physics*, vol. 6, no. 23, pp. 5263–5274, 2004.

[224] S. I. Anisimov, B. L. Kapeliovich, and T. L. Perel'man, "Electron emission from metal surfaces exposed to ultrashort laser pulses," *Sov. Phys.-JETP*, vol. 39, no. 2, pp. 375–377, 1974.

[225] F. Vallée, "Energy exchange at short time scales : Electron–phonon interactionsin metals and metallic nanostructures," in *Microscale and Nanoscale Heat Transfer*, ser. Topics in Applied Physics, S. Volz, Ed. Springer Berlin Heidelberg, 2007, vol. 107, pp. 309–332.

[226] R. R. Letfullin, T. F. George, G. C. Duree, and B. M. Bollinger, "Ultrashort laser pulse heating of nanoparticles : comparison of theoretical approaches," *Advances in Optical Technologies*, p. 251718, 2008.

[227] R. H. M. Groeneveld, R. Sprik, and A. Lagendijk, "Effect of a nonthermal electron distribution on the electron-phonon energy relaxation process in noble metals," *Physical Review B (Condensed Matter and Materials Physics)*, vol. 45, no. 9, p. 5079, 1992.

[228] Z. Ge, D. G. Cahill, and P. V. Braun, "AuPd metal nanoparticles as probes of nanoscale thermal transport in aqueous solution," *The Journal of Physical Chemistry B*, vol. 108, no. 49, pp. 18 870–18 875, 2004.

[229] O. M. Wilson, X. Hu, D. G. Cahill, and P. V. Braun, "Colloidal metal particles as probes of nanoscale thermal transport in fluids," *Physical Review B (Condensed Matter and Materials Physics)*, vol. 66, no. 22, p. 224301, 2002.

[230] M. Pelton, J. E. Sader, J. Burgin, M. Liu, P. Guyot-Sionnest, and D. Gosztola, "Damping of acoustic vibrations in gold nanoparticles," *Nature Nanotechnology*, vol. 4, no. 8, pp. 492–495, 2009.

[231] J. H. Hodak, A. Henglein, and G. V. Hartland, "Size dependent properties of Au particles : Coherent excitation and dephasing of acoustic vibrational modes," *The Journal of Chemical Physics*, vol. 111, p. 8613, 1999.

[232] M. Hu, X. Wang, G. V. Hartland, P. Mulvaney, J. P. Juste, and J. E. Sader, "Vibrational response of nanorods to ultrafast laser induced heating : Theoretical and experimental analysis," *Journal of the American Chemical Society*, vol. 125, no. 48, pp. 14 925–14 933, 2003.

[233] M. Hu, P. Hillyard, G. V. Hartland, T. Kosel, J. Pérez-Juste, and P. Mulvaney, "Determination of the elastic constants of gold nanorods produced by seed mediated growth," *Nano Letters*, vol. 4, no. 12, pp. 2493–2497, 2004.

[234] M. Hu, H. Petrova, and G. V. Hartland, "Investigation of the Properties of Gold Nanoparticles in Aqueous Solution at Extremely High Lattice Temperatures ," *Chemical Physics Letters*, vol. 391, no. 4, pp. 220–225, 2004.

[235] A. N. Volkov, C. Sevilla, and L. V. Zhigilei, "Numerical modeling of short pulse laser interaction with Au nanoparticle surrounded by water," *Applied Surface Science*, vol. 253, no. 15, pp. 6394–6399, 2007.

[236] V. Kotaidis, C. Dahmen, G. von Plessen, F. Springer, and A. Plech, "Excitation of nanoscale vapor bubbles at the surface of gold nanoparticles in water," *The Journal of Chemical Physics*, vol. 124, p. 184702, 2006.

[237] J. Noack and A. Vogel, "Laser-induced plasma formation in water at nanosecond to femtosecond time scales : calculation of thresholds, absorption coefficients, and energy density," *Quantum Electronics, IEEE Journal of*, vol. 35, no. 8, pp. 1156–1167, 1999.

[238] C. A. Sacchi, "Laser-induced electric breakdown in water," *JOSA B*, vol. 8, no. 2, pp. 337–345, 1991.

[239] D. Grand, A. Bernas, and E. Amouyal, "Photoionization of aqueous indole : Conduction band edge and energy gap in liquid water ," *Chemical Physics*, vol. 44, no. 1, pp. 73–79, 1979.

[240] J. W. Boyle, J. A. Ghormley, C. J. Hochanadel, and J. F. Riley, "Production of hydrated electrons by flash photolysis of liquid water with light in the first continuum," *The Journal of Physical Chemistry*, vol. 73, no. 9, pp. 2886–2890, 1969.

[241] F. Williams, S. P. Varma, and S. Hillenius, "Liquid water as a lone-pair amorphous semiconductor," *The Journal of Chemical Physics*, vol. 64, p. 1549, 1976.

[242] D. N. Nikogosyan, A. A. Oraevsky, and V. I. Rupasov, "Two-photon ionization and dissociation of liquid water by powerful laser UV radiation ," *Chemical Physics*, vol. 77, no. 1, pp. 131–143, 1983.

[243] J. V. Coe, A. D. Earhart, M. H. Cohen, G. J. Hoffman, H. W. Sarkas, and K. H. Bowen, "Using cluster studies to approach the electronic structure of bulk water : Reassessing the vacuum level, conduction band edge, and band gap of water," *The Journal of Chemical Physics*, vol. 107, no. 16, p. 6023, 1997.

[244] do Couto, P.C., S. G. Estacio, and B. J. C. Cabral, "The Kohn-Sham density of states and band gap of water : From small clusters to liquid water," *The Journal of Chemical Physics*, vol. 123, p. 054510, 2005.

[245] L. V. Keldysh, "Ionization in the field of a strong electromagnetic wave," *Zh. Eksperim. i Teor. Fiz.*, vol. 47, pp. 1945–1957, 1964.

[246] P. K. Kennedy, "A first-order model for computation of laser-induced breakdown thresholds in ocular and aqueous media. I. Theory," *Quantum Electronics, IEEE Journal of*, vol. 31, no. 12, pp. 2241–2249, 1995.

[247] V. E. Gruzdev, "Photoionization rate in wide band-gap crystals," *Physical Review B (Condensed Matter and Materials Physics)*, vol. 75, no. 20, p. 205106, 2007.

[248] A. C. Tien, S. Backus, H. Kapteyn, M. Murnane, and G. Mourou, "Short-pulse laser damage in transparent materials as a function of pulse duration," *Physical Review Letters*, vol. 82, no. 19, pp. 3883–3886, 1999.

[249] M. Lenzner, J. Kruger, S. Sartania, Z. Cheng, C. Spielmann, and others, "Femtosecond Optical Breakdown in Dielectrics," *Physical Review Letters*, vol. 80, no. 18, pp. 4076–4079, 1998.

[250] B. C. Stuart, M. D. Feit, S. Herman, A. M. Rubenchik, B. W. Shore, and M. D. Perry, "Nanosecond-to-femtosecond laser-induced breakdown in dielectrics," *Physical Review B (Condensed Matter and Materials Physics)*, vol. 53, no. 4, p. 1749, 1996.

[251] H. Date, K. L. Sutherland, H. Hasegawa, and M. Shimozuma, "Ionization and excitation collision processes of electrons in liquid water," *Nuclear Inst. and Methods in Physics Research, B*, vol. 265, no. 2, pp. 515–520, 2007.

[252] N. E. Andreev, M. E. Veĭsman, V. P. Efremov, and V. E. Fortov, "The generation of a dense hot plasma by intense subpicosecond laser pulses," *High Temperature*, vol. 41, no. 5, pp. 594–608, 2003.

[253] L. Hallo, A. Bourgeade, V. T. Tikhonchuk, C. Mezel, and J. Breil, "Model and numerical simulations of the propagation and absorption of a short laser pulse in a transparent dielectric material : Blast-wave launch and cavity formation," *Physical Review B (Condensed Matter and Materials Physics)*, vol. 76, no. 2, p. 024101, 2007.

[254] Y. M. Zolotovitskii, L. I. Korshunov, and V. A. Benderskii, "Electron work function from metals in a liquid dielectric," *Russian Chemical Bulletin*, vol. 21, no. 4, pp. 760–763, 1972.

[255] N. M. Bulgakova, R. Stoian, A. Rosenfeld, I. V. Hertel, and E. Campbell, "Electronic transport and consequences for material removal in ultrafast pulsed laser ablation of materials," *Physical Review B (Condensed Matter and Materials Physics)*, vol. 69, no. 5, p. 054102, 2004.

[256] G. Bisker and D. Yelin, "Noble-metal nanoparticles and short pulses for nanomanipulations : theoretical analysis," *JOSA B*, vol. 29, no. 6, pp. 1383–1393, 2012.

[257] O. Warshavski, L. Minai, G. Bisker, and D. Yelin, "Effect of Single Femtosecond Pulses on Gold Nanoparticles," *The Journal of Physical Chemistry C*, vol. 115, no. 10, pp. 3910–3917, Mar. 2011.

[258] C. Cheng and X. Xu, "Mechanisms of decomposition of metal during femtosecond laser ablation," *Physical Review B (Condensed Matter and Materials Physics)*, vol. 72, no. 16, p. 165415, 2005.

[259] D. Perez and L. J. Lewis, "Ablation of solids under femtosecond laser pulses," *Physical Review Letters*, vol. 89, no. 25, p. 255504, 2002.

[260] F. Vidal, T. W. Johnston, S. Laville, O. Barthélemy, M. Chaker, B. Le Drogoff, J. Margot, and M. Sabsabi, "Critical-point phase separation in laser ablation of conductors," *Physical Review Letters*, vol. 86, no. 12, pp. 2573–2576, 2001.

[261] S. Link, Z. L. Wang, and M. A. El-Sayed, "How Does a Gold Nanorod Melt ?" *The Journal of Physical Chemistry B*, vol. 104, no. 33, pp. 7867–7870, 2000.

[262] S. Link, C. Burda, B. Nikoobakht, and M. A. El-Sayed, "How long does it take to melt a gold nanorod ? : A femtosecond pump–probe absorption spectroscopic study," *Chemical Physics Letters*, vol. 315, no. 1, pp. 12–18, 1999.

[263] D. Werner, A. Furube, T. Okamoto, and S. Hashimoto, "Femtosecond Laser-Induced Size Reduction of Aqueous Gold Nanoparticles : In Situ and Pump,àí Probe Spectroscopy Investigations Revealing Coulomb Explosion," *The Journal of Physical Chemistry C*, vol. 115, no. 17, pp. 8503–8512, 2011.

[264] C. Novo and P. Mulvaney, "Charge-induced Rayleigh instabilities in small gold rods," *Nano Letters*, vol. 7, no. 2, pp. 520–524, 2007.

[265] J. R. Lepock, H. E. Frey, and K. P. Ritchie, "Protein denaturation in intact hepatocytes and isolated cellular organelles during heat shock," *The Journal of cell biology*, vol. 122, no. 6, pp. 1267–1276, 1993.

[266] D. Peer, J. M. Karp, S. Hong, O. C. Farokhzad, R. Margalit, and R. Langer, "Nanocarriers as an emerging platform for cancer therapy," *Nature Nanotechnology*, vol. 2, no. 12, pp. 751–760, 2007.

[267] D. S. Wagner, N. A. Delk, E. Y. Lukianova-Hleb, J. H. Hafner, M. C. Farach-Carson, and D. O. Lapotko, "The in vivo performance of plasmonic nanobubbles as cell theranostic agents in zebrafish hosting prostate cancer xenografts," *Biomaterials*, vol. 31, no. 29, pp. 7567–7574, 2010.

[268] S. N. Goldberg, "Radiofrequency tumor ablation : principles and techniques," *European Journal of Ultrasound*, vol. 13, no. 2, pp. 129–147, 2001.

[269] G. S. Gazelle, S. N. Goldberg, L. Solbiati, and T. Livraghi, "Tumor Ablation with Radio-frequency Energy1," *Radiology*, vol. 217, no. 3, pp. 633–646, 2000.

[270] M. G. Lubner, C. L. Brace, J. L. Hinshaw, and F. T. Lee, "MicrowaveTumor Ablation : Mechanism of Action, Clinical Results, and Devices," *Journal of Vascular and Interventional Radiology*, vol. 21, no. 8, pp. S192–S203, 2010.

[271] J. E. Kennedy, "High-intensity focused ultrasound in the treatment of solid tumours," *Nature Reviews Cancer*, vol. 5, pp. 321–327, 2005.

[272] M. Nikfarjam and C. Christophi, "Interstitial laser thermotherapy for liver tumours," *British journal of surgery*, vol. 90, no. 9, pp. 1033–1047, 2003.

[273] R. A. Sultan, "Tumour ablation by laser in general surgery," *Lasers in Medical Science*, vol. 5, no. 2, pp. 185–193, 1990.

[274] V. P. Zharov, K. E. Mercer, E. N. Galitovskaya, and M. S. Smeltzer, "Photothermal nanotherapeutics and nanodiagnostics for selective killing of bacteria targeted with gold nanoparticles," *Biophysical Journal*, vol. 90, no. 2, pp. 619–627, 2006.

[275] V. P. Zharov, E. N. Galitovskaya, C. Johnson, and T. Kelly, "Synergistic enhancement of selective nanophotothermolysis with gold nanoclusters : potential for cancer therapy," *Lasers in Surgery and Medicine*, vol. 37, no. 3, pp. 219–226, 2005.

[276] C. M. Pitsillides, E. K. Joe, X. Wei, R. Anderson, and C. P. Lin, "Selective cell targeting with light-absorbing microparticles and nanoparticles,," *Biophysical Journal*, vol. 84, no. 6, pp. 4023–4032, 2003.

[277] N. N. Nedyalkov, P. A. Atanasov, R. A. Toshkova, E. G. Gardeva, L. S. Yossifova, and M. T. Alexandrov, "Laser heating of gold nanoparticles : Photothermal cancer cell therapy," in *Proceeding of the SPIE*, vol. 8427, 2012, p. 84272P.

[278] J. L. Li, L. Wang, X. Y. Liu, Z. P. Zhang, H. C. Guo, W. M. Liu, and S. H. Tang, "In vitro cancer cell imaging and therapy using transferrin-conjugated gold nanoparticles," *Cancer Letters*, vol. 274, no. 2, pp. 319–326, 2009.

[279] V. P. Zharov, V. Galitovsky, and M. Viegas, "Photothermal detection of local thermal effects during selective nanophotothermolysis," *Applied Physics Letters*, vol. 83, no. 24, pp. 4897–4899, 2003.

[280] G. Baffou and H. Rigneault, "Femtosecond-pulsed optical heating of gold nanoparticles," *Physical Review B (Condensed Matter and Materials Physics)*, vol. 84, no. 3, p. 035415, 2011.

[281] X. Huang, B. Kang, W. Qian, M. A. Mackey, Chen, P. C., A. K. Oyelere, I. H. El-Sayed, and M. A. El-Sayed, "Comparative study of photothermolysis of cancer cells with nuclear-targeted or cytoplasm-targeted gold nanospheres : Continuous wave or pulsed lasers," *Journal of Biomedical Optics*, vol. 15, no. 5, p. 058002, 2010.

[282] B. Boudaïffa, P. Cloutier, D. Hunting, M. A. Huels, and L. Sanche, "Resonant formation of DNA strand breaks by low-energy (3 to 20 eV) electrons," *Science*, vol. 287, no. 5458, pp. 1658–1660, 2000.

[283] L. Sanche, "Low energy electron-driven damage in biomolecules," *The European Physical Journal D-Atomic, Molecular, Optical and Plasma Physics*, vol. 35, no. 2, pp. 367–390, 2005.

[284] L. Sanche, "Mechanisms of Low Energy Electron Damage to Condensed Biomolecules and DNA ," *Radiation Protection Dosimetry*, vol. 99, no. 1-4, pp. 57–62, 2002.

[285] G. Huttmann, B. Radt, J. Serbin, B. I. Lange, and R. Birngruber, "High precision cell surgery with nanoparticles," *Medical Laser Application*, vol. 17, no. 1, pp. 9–14, 2002.

[286] M. Tsukakoshi, S. Kurata, Y. Nomiya, Y. Ikawa, and T. Kasuya, "A novel method of DNA transfection by laser microbeam cell surgery," *Applied Physics B : Lasers and Optics*, vol. 35, no. 3, pp. 135–140, 1984.

[287] V. Kohli, J. P. Acker, and A. Y. Elezzabi, "Reversible permeabilization using high-intensity femtosecond laser pulses : Applications to biopreservation," *Biotechnology and bioengineering*, vol. 92, no. 7, pp. 889–899, 2005.

[288] D. J. Stevenson, F. J. Gunn Moore, P. Campbell, and K. Dholakia, "Single cell optical transfection," *Journal of The Royal Society Interface*, vol. 7, no. 47, pp. 863–871, 2010.

[289] E. Zeira, A. Manevitch, Z. Manevitch, E. Kedar, M. Gropp, N. Daudi, R. Barsuk, M. Harati, H. Yotvat, and P. J. Troilo, "Femtosecond laser : a new intradermal DNA delivery method for efficient, long-term gene expression and genetic immunization," *The FASEB Journal*, vol. 21, no. 13, pp. 3522–3533, 2007.

[290] C. P. Yao, Z. X. Zhang, R. Rahmanzadeh, and G. Huettmann, "Laser-based gene transfection and gene therapy," *NanoBioscience, IEEE Transactions on*, vol. 7, no. 2, pp. 111–119, 2008.

[291] X. Tsampoula, K. Taguchi, T. Cizmar, V. Garces-Chavez, N. Ma, S. Mohanty, K. Mohanty, F. Gunn-Moore, and K. Dholakia, "Fibre based cellular transfection," *Optics Express*, vol. 16, no. 21, pp. 17 007–17 013, 2008.

[292] A. Uchugonova, K. König, R. Bueckle, A. Isemann, and G. Tempea, "Targeted transfection of stem cells with sub-20 femtosecond laser pulses," *Optics Express*, vol. 16, no. 13, pp. 9357–9364, 2008.

[293] C. T. A. Brown, D. J. Stevenson, X. Tsampoula, C. McDougall, A. A. Lagatsky, W. Sibbett, F. J. Gunn Moore, and K. Dholakia, "Enhanced operation of femtosecond lasers and applications in cell transfection," *Journal of biophotonics*, vol. 1, no. 3, pp. 183–199, 2008.

[294] C. Yao, R. Rahmanzadeh, E. Endl, Z. Zhang, J. Gerdes, and G. Huttmann, "Elevation of plasma membrane permeability by laser irradiation of selectively bound nanoparticles," *Journal of Biomedical Optics*, vol. 10, no. 6, pp. 064 012–064 012–8, 2005.

[295] E. Y. Lukianova-Hleb, A. P. Samaniego, J. Wen, L. S. Metelitsa, C. C. Chang, and D. O. Lapotko, "Selective gene transfection of individual cells in vitro with plasmonic nanobubbles," *Journal of Controlled Release*, vol. 152, no. 2, pp. 286–293, 2011.

[296] A. Ben-Yakar, D. Eversole, and O. Ekici, "Spherical and Anisotropic Gold Nanomaterials in Plasmonic Laser Phototherapy of Cancer," in *Non-Magnetic Metallic Nanomaterials for Life Sciences of the 10 volume series on Nanomaterials for Life Sciences*, C. Kumar, Ed. John Wiley & Sons : Weinheim, 2008, pp. 493–539.

[297] M. Schomaker, J. Baumgart, A. Ngezahayo, J. Bullerdiek, I. Nolte, H. Escobar, H. Lubatschowski, and A. Heisterkamp, "Fs-laser cell perforation using gold nanoparticles of different shapes," in *Proceeding of the SPIE*, vol. 7589, 2010, p. 75890C.

[298] M. Schomaker, J. Baumgart, D. Motekaitis, D. Heinemann, J. Krawinkel, M. Pangalos, W. Bintig, É. Boulais, R. Lachaine, and B. S. L. Lalonde, "Mechanisms of gold

nanoparticle mediated ultrashort laser cell membrane perforation," in *Proceeding of the SPIE*, vol. 7925, 2011, p. 79250F.

[299] L. J. E. Anderson, E. Hansen, E. Y. Lukianova-Hleb, J. H. Hafner, and D. O. Lapotko, "Optically guided controlled release from liposomes with tunable plasmonic nanobubbles," *Journal of Controlled Release*, vol. 144, no. 2, pp. 151–158, 2010.

[300] E. Y. Lukianova-Hleb, A. Belyanin, S. Kashinath, X. Wu, and D. O. Lapotko, "Plasmonic nanobubble-enhanced endosomal escape processes for selective and guided intracellular delivery of chemotherapy to drug-resistant cancer cells," *Biomaterials*, vol. 33, pp. 1821–1826, 2012.

[301] A. Wijaya, S. B. Schaffer, I. G. Pallares, and K. Hamad-Schifferli, "Selective release of multiple DNA oligonucleotides from gold nanorods," *ACS Nano*, vol. 3, no. 1, pp. 80–86, 2008.

[302] F. Thibaudau, "Ultrafast Photothermal Release of DNA from Gold Nanoparticles," *The Journal of Physical Chemistry Letters*, vol. 3, no. 7, pp. 902–907, 2012.

[303] P. K. Jain, W. Qian, and M. A. El-Sayed, "Ultrafast cooling of photoexcited electrons in gold nanoparticle-thiolated DNA conjugates involves the dissociation of the gold-thiol bond," *Journal of the American Chemical Society*, vol. 128, no. 7, pp. 2426–2433, 2006.

[304] G. B. Braun, A. Pallaoro, G. Wu, D. Missirlis, J. A. Zasadzinski, M. Tirrell, and N. O. Reich, "Laser-Activated Gene Silencing via Gold Nanoshell,àí siRNA Conjugates," *ACS Nano*, vol. 3, no. 7, pp. 2007–2015, 2009.

[305] F. M. Kahnert, "Numerical methods in electromagnetic scattering theory," *J. Quant. Spectrosc. Radiat. Transf.*, vol. 79-80, no. 13, pp. 775–824, 2003.

[306] Y. Dou, L. V. Zhigilei, N. Winograd, and B. J. Garrison, "Explosive boiling of water films adjacent to heated surfaces : A microscopic description," *The Journal of Physical Chemistry A*, vol. 105, no. 12, pp. 2748–2755, 2001.

[307] *The database used was the one from the Naval Research Laboratory, Center for Computational Materials Science, previously available at cst-www.nrl.navy.mil/database.html. Consulted in May 2009. It seems however that this database is no longer available.*

[308] N. W. Ashcroft and N. D. Mermin, *Solid State Physics*. Harcourt College Publishers, 1976.

[309] J. K. Chen, D. Y. Tzou, and J. E. Beraun, "A semiclassical two-temperature model for ultrafast laser heating," *International Journal of Heat and Mass Transfer*, vol. 49, no. 1-2, pp. 307–316, Jan. 2006.

[310] P. Zijlstra, A. L. Tchebotareva, J. W. M. Chon, M. Gu, and M. Orrit, "Acoustic Oscillations and Elastic Moduli of Single Gold Nanorods," *Nano Letters*, vol. 8, no. 10, pp. 3493–3497, Oct. 2008.

[311] J. H. Bechtel, W. Lee Smith, and N. Bloembergen, "Two-photon photoemission from metals induced by picosecond laser pulses," *Physical Review B (Condensed Matter and Materials Physics)*, vol. 15, no. 10, pp. 4557–4563, 1977.

[312] J. P. Girardeau-Montaut and C. Girardeau-Montaut, "Theory of ultrashort nonlinear multiphoton photoelectric emission from metals," *Physical Review B (Condensed Matter and Materials Physics)*, vol. 51, no. 19, p. 13560, 1995.

[313] E. M. Logothetis and P. L. Hartman, "Laser-Induced Electron Emission from Solids : Many-Photon Photoelectric Effects and Thermionic Emission," *Phys. Rev.*, vol. 187, no. 2, pp. 460–474, 1969.

[314] W. H. Qi and M. P. Wang, "Size and shape dependent melting temperature of metallic nanoparticles," *Materials Chemistry and Physics*, vol. 88, no. 2, pp. 280–284, 2004.

[315] D. Xie, W. Qi, and M. Wang, " Size and shape dependent melting-thermodynamic properties of metallic nanoparticles," *Chin Shu Hsueh Pao*, vol. 40, pp. 1041–1044, 2004.

[316] Y. T. Lee and R. M. More, "An electron conductivity model for dense plasmas," *Physics of Fluids*, vol. 27, p. 1273, 1984.

[317] P. M. Bellan, *Fundamentals of Plasma Physics*. Cambridge University Press, 2008.

[318] C. L. Arnold, A. Heisterkamp, W. Ertmer, and H. Lubatschowski, "Computational model for nonlinear plasma formation in high NA micromachining of transparent materials and biological cells," *Optics Express*, vol. 15, no. 16, pp. 10 303–10 317, 2007.

[319] M. Veysman, B. Cros, N. E. Andreev, and G. Maynard, "Theory and simulation of short intense laser pulse propagation in capillary tubes with wall ablation," *Physics of Plasmas*, vol. 13, no. 5, pp. 53 114–53 111, 2006.

[320] A. Cavalleri, K. Sokolowski-Tinten, J. Bialkowski, M. Schreiner, and D. Von der Linde, "Femtosecond melting and ablation of semiconductors studied with time of flight mass spectroscopy," *Journal of Applied Physics*, vol. 85, no. 6, pp. 3301–3309, 1999.

[321] K. Sokolowski-Tinten, J. Bialkowski, A. Cavalleri, D. Von der Linde, A. Oparin, J. Meyer-ter Vehn, and S. I. Anisimov, "Transient states of matter during short pulse laser ablation," *Physical Review Letters*, vol. 81, no. 1, pp. 224–227, 1998.

[322] SESAME, "The water table used here was SESAME table 7150," *The Los Alamos National Laboratory Equation-of-State Database, edited by Sp. P. Lyon and J. D. Johnson, Los Alamos National Laboratory, Report No. ucrl-7118 and ucrl-52190.*, 1979.

[323] K. E. Jensen, C. H. Whiting, and G. M. Hulbert, "A generalized-alpha method for integrating the filtered Navier-Stokes equations with a stabilized finite element method," *Computer Methods in Applied Mechanics and Engineering*, vol. 190, no. 3–4, pp. 305–319, 2000.

[324] J. Chung and G. M. Hulbert, "A time integration algorithm for structural dynamics with improved numerical dissipation : The generalized-alpha method," *Journal of Applied Mechanics*, vol. 60, pp. 371–375, 1993.

[325] D. Lapotko, "Plasmonic nanoparticle-generated photothermal bubbles and their biomedical applications," *Nanomedicine*, vol. 4, no. 7, pp. 813–845, 2009.

[326] N. M. Schaeublin, L. K. Braydich-Stolle, A. M. Schrand, J. M. Miller, J. Hutchison, J. J. Schlager, and S. M. Hussain, "Surface charge of gold nanoparticles mediates mechanism of toxicity," *Nanoscale*, vol. 3, no. 2, pp. 410–420, 2011.

[327] A. Plech, P. Leiderer, and J. Boneberg, "Femtosecond laser near field ablation," *Laser & Photonics Reviews*, vol. 3, no. 5, pp. 435–451, 2009.

[328] J. Sinzig and M. Quinten, "Scattering and absorption by spherical multilayer particles," *Applied Physics A : Materials Science & Processing*, vol. 58, no. 2, pp. 157–162, 1994.

[329] K. Sokolov, M. Follen, J. Aaron, I. Pavlova, A. Malpica, R. Lotan, and R. Richards-Kortum, "Real-time vital optical imaging of precancer using anti-epidermal growth factor receptor antibodies conjugated to gold nanoparticles," *Cancer Research*, vol. 63, no. 9, pp. 1999–2004, 2003.

[330] S. Kumar, N. Harrison, R. Richards-Kortum, and K. Sokolov, "Plasmonic nanosensors for imaging intracellular biomarkers in live cells," *Nano Letters*, vol. 7, no. 5, pp. 1338–1343, 2007.

[331] D. Yelin, D. Oron, S. Thiberge, E. Moses, and Y. Silberberg, "Multiphoton plasmon-resonance microscopy," *Optics Express*, vol. 11, no. 12, pp. 1385–1391, 2003.

[332] P. Ghosh, G. Han, M. De, C. K. Kim, and V. M. Rotello, "Gold nanoparticles in delivery applications," *Advanced Drug Delivery Reviews*, vol. 60, no. 11, pp. 1307–1315, 2008.

[333] A. S. Angelatos, B. Radt, and F. Caruso, "Light-Responsive Polyelectrolyte/Gold Nanoparticle Microcapsules," *The Journal of Physical Chemistry B*, vol. 109, no. 7, pp. 3071–3076, 2005.

[334] D. Lapotko, T. Romanovskaya, and V. Zharov, "Photothermal images of live cells in presence of drug," *Journal of Biomedical Optics*, vol. 7, p. 425, 2002.

[335] E. Y. Hleb, Y. Hu, R. A. Drezek, J. H. Hafner, and D. Lapotko, "Photothermal bubbles as optical scattering probes for imaging living cells," *Nanomedicine*, vol. 3, no. 6, pp. 797–812, 2008.

[336] H. Wang, T. B. Huff, D. A. Zweifel, W. He, P. S. Low, A. Wei, and J. X. Cheng, "In vitro and in vivo two-photon luminescence imaging of single gold nanorods," *Proceedings of the National Academy of Sciences of the United States of America*, vol. 102, no. 44, pp. 15 752–15 756, 2005.

[337] N. J. Durr, T. Larson, D. K. Smith, B. A. Korgel, K. Sokolov, and A. Ben-Yakar, "Two-photon luminescence imaging of cancer cells using molecularly targeted gold nanorods," *Nano Letters*, vol. 7, no. 4, pp. 941–945, 2007.

[338] E. Y. Hleb and D. O. Lapotko, "Photothermal properties of gold nanoparticles under exposure to high optical energies," *Nanotechnology*, vol. 19, no. 35, p. 355702, 2008.

[339] S. Link and M. A. El-Sayed, "Spectroscopic determination of the melting energy of a gold nanorod," *The Journal of Chemical Physics*, vol. 114, p. 2362, 2001.

[340] S. G. Skuridin, V. A. Dubinskaya, V. M. Rudoy, O. V. Dement'eva, S. T. Zakhidov, T. L. Marshak, V. A. Kuz'min, V. I. Popenko, and Y. M. Evdokimov, "Effect of gold nanoparticles on DNA package in model systems," *Doklady Biochemistry and Biophysics*, vol. 432, no. 1, pp. 141–143, 2010.

ANNEXE A

Plasma-Mediated off-Resonance Plasmonic Enhanced Ultrafast Laser-Induced Nanocavitation : Supplementary Information

Cette annexe présente le Supplementary Information de l'article retranscrit au chapitre 4 [1]. Il détaille le modèle utilisé et présente un graphique montrant le comportement oscillatoire des bulles créées autour des nanoparticules à haute fluence.

1. E. Boulais, R. Lachaine et M. Meunier, Plasma mediated off-resonance plasmonic enhanced ultrafast laser induced nanocavitation. *Nano Lett.* **12**(9), 4763-4669, 2012.

Plasma-Mediated off-Resonance Plasmonic Enhanced Ultrafast Laser-Induced Nanocavitation : Supplementary Information

Etienne Boulais, Rémi Lachaine, and Michel Meunier*

Laser Processing and Plasmonics Laboratory, Engineering Physics Department, École Polytechnique de Montréal, Montréal, Québec, H3C 3A7, Canada

E-mail: michel.meunier@polymtl.ca

Precisions on the model

This section details the complete mathematical model used to describe the interaction between an ultrafast laser irradiation and an off-resonance plasmonic nanoparticle in water. The whole model, which includes 10 coupled differential equations (equations (1) to (10)), is summarized in figure 1. Simulations have been performed using Comsol, a commercial finite-element software distributed by Comsol inc. (www.comsol.com) on high performance parallel-computing facility provided by the RQCHP. Full 3D simulation is used for the electromagnetic interaction sub-model as the other sub-models are solved under axial symmetry.

Electromagnetic interaction

Electromagnetic interaction between the laser irradiation and the nanostructure-water system is calculated using Maxwell's equation. A very fast transient, typically in the order of the femtosec-

*To whom correspondence should be addressed

ond, allows to use the harmonic approximation where the field is assumed to be sinusoidal at all time. Trivial algebraic manipulations along with the assumption of no uncompensated charges and slow variation of the material properties compared to the electric field oscillation allow to rewrite Maxwell's equations as an Helmohltz equation for the electric field (equation (1)). The conductivity is linked to the permittivity through the well known relation $\sigma = \omega\varepsilon_0\varepsilon''$, with ω, the laser radial pulsation and ε'', the imaginary part of the relative permittivity. Note that this expression also implies that the energy loss by the field to photoionize the material is negligible when compared to the energy loss to plasma heating. Calculations show that this condition is verified in our case. Gold optical properties are assumed constant throughout the process and are taken from.[1] Water optical properties are taken from.[2] Plasma generation inside the water medium however affects the optical properties, its impact being modelled as a Drude permittivity.[3]

$$\varepsilon = \varepsilon_\infty - \frac{ne^2}{\varepsilon_0 m(\omega^2 + j\omega\gamma_c)} \tag{11}$$

where ε_∞ is the water relative permittivity, m is the electron mass and γ_c is the electron scattering time. Proper discussion on the evaluation of γ_c is given later.

Two-temperature model

Thermodynamic evolution of the gold nanostructure is modelled using an hyperbolic two-temperature model based on the Boltzmann transport equation[4] (equation (2) to equation (4)) . Parameters and material properties used in the two-temperature model are summarized in Table 1. The gold nanostructure couples with its environment in two ways. Energy is transferred from the gold lattice to the water molecules through a conduction process. However, only a finite rate of heat can be transferred to the water because of the finite interface conductance. For water/gold interface, the rate of heat transferred is given in Table 1.

Energy is also transferred from the electrons through thermo-assisted photoemission into the water. In the range of fluence considered, this emission is described by the Fowler-DuBridge

theory.[5] This ejection process must be distinguished from Fowler-Nordheim emission, where the electric field is intense enough to allow tunnelling through the barrier, that occurs for electric field much higher than what is used in this paper. Emitted current from gold is written

$$\mathbf{J} = \mathbf{J_0} + c_{Au} \frac{(k_b T_e)^2}{4(3\hbar\omega - W)^2} F\left(\frac{3\hbar\omega - W}{k_b T_e}\right) I^3 \mathbf{n} \tag{12}$$

where $\mathbf{J}_0$ is the usual thermionic emission expression, c_{Au} is the three-photons ionization cross-section, ω is the laser radial frequency, k_b is the Boltzmann constant, W is the extraction potential, I is the laser intensity and $F(x)$ is the so-called Fowler function.

Note that the increase in the extraction potential due to the degeneracy of the electron plasma has been taken into account. However, no corrections concerning the polarization of the particle have been applied. Polarization should indeed limit the emitted current from the particle.[6] The idealized calculated emitted current is thus only a limit current, the real current being lower. As shown in the main paper, carriers generated by this idealized thermal emission are negligible when compared to other sources, so that the real current will also be negligible.

Plasma in water

Equations describing plasma dynamics in water correspond to equation (6) and equation (7). Constants and plasma properties used in the plasma dynamics model are summarized in Table 2. Note that equation for ν_{ei} in Table 2 simplifies to the classical result from Fokker-Planck theory in the limit where electron plasma is non degenerate.[7]

Water dynamic

Equations describing water dynamics correspond to equation (8) to equation (10). Those three partial differential equations are completed by an appropriate equation of state. Both IAPWS95[8] and SESAME[9] equations of state are used in their own pressure and temperature validity range. Thermal conductivity, viscosity and surface tensions expression are also supplied by the IAPWS

database.

Table 1: Gold properties

Parameter	Symbol	Value	Ref.
Gold density	ρ_g	=19300 kgm^{-3}	10
Electronic density of state	$g(\varepsilon)$	Theoretical density of state	11
Electronic heat capacity	C_e	standard calculation from $g(\varepsilon)$	12
Lattice heat capacity	C_l	$=\rho_g(109.579+0.128T_l-3.4\times10^{-4}T_l^2+5.24\times10^{-7}T_l^3-3.93\times10^{-10}T_l^4+1.17\times10^{-13}T_l^5)Jm^{-3}K^{-1}$	10
Electron collision time	τ_e^g	$=(1.2\times10^7T_e^2+1.23\times10^{11}T_l)^{-1}s$	13
Ion collision time	τ_l^g	=0.8 ps	4
Sound velocity	v_l	$\approx$ 2000 m/s	14,15
Lattice thermal conductivity	K_l	$=\frac{1}{3}v_l^2\tau_l^gC_l$	16
Ambiant electron-phonon coupling	G_0	=2.5$\times10^{16}$ Wm^{-3}K^{-1}	17
T-dependant electron-phonon coupling	G	$=\frac{G_0}{g(\varepsilon_f)}\int g^2(\varepsilon)\left(-\frac{\partial f}{\partial\varepsilon}\right)d\varepsilon$	17,18
Phonon mismatch factor	q_0	=105$\times10^6$ Wm^{-2}K^{-1}	10
Three-photons ionization cross-section	c_{Au}	$=1\times10^{-7}\ \frac{Acm^4}{MW^3}$	19
Gold/water extraction potential	W	=3.72 eV	20
Heat transfer at the water/gold interface	$\mathbf{q_l}\vert_\Gamma$	$=q_0(T_l-T_m)$	10
Electromagnetic rate of work	S_{EM}	$=\frac{1}{2}Re[\mathbf{J}^*\cdot\mathbf{E}]=\frac{1}{2}\omega\varepsilon''\vert\mathbf{E}\vert^2$	21

Precisions on the optical setup for bubble diameter measurement

The pump laser is a $6mJ, 45fs$ (Spitfire Spectra Physics) laser which wavelength is centred at $800nm$ with a $1kHz$ repetition rate. The probe laser is a continuous wave 5 mW He:Ne at 633nm. Pump and probe laser are both focussed on a $5.5\mu m$ radius area, as deduced from a combination of knife-edge and direct CCD measurement. The sample contains 1.2×10^9 particles/mL of $100nm$ diameter gold nanospheres from the company Spi supplies (www.2spi.com). Variation of the extinction coefficient of the sample is measured with a Thorlabs 1601-Fs-AC 1GHz Si photoreceiver which photocurrent is read by a 500MHz Agilent oscilloscope.

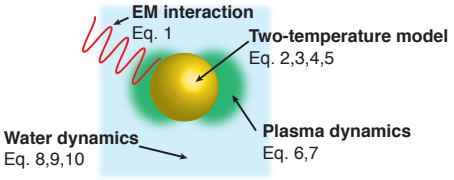

Equations	Variables
Electromagnetic interaction	
(1) $\nabla^2\mathbf{E}+k_0^2\varepsilon_r\mathbf{E}=0$	$\mathbf{E}$: Electric Field k_0 : Wave number ε_r : Complex relative permittivity
Two-temperature model	
(2) $C_e\frac{\partial T_e}{\partial t}+\nabla\cdot\mathbf{q}_e-G(T_e-T_l)+S_{EM}$	G : Electron-phonon coupling S_{EM} : Electromagnetic rate of work T_e : Electronic temperature T_l : Lattice temperature $\mathbf{q}_e$: Electronic heat current density $\mathbf{q}_l$: Lattice heat current density C_e : Electronic heat capacity C_l : Lattice heat capacity τ^{Au}_e : Electron scattering time τ^{Au}_l : Phonon scattering time κ_e : Electronic thermal conductivity κ_l : Lattice thermal conductivity
(3) $\tau_e^{Au}\frac{\partial\mathbf{q}_e}{\partial t}+\mathbf{q}_e=-\kappa_e\nabla T_e$	
(4) $C_l\frac{\partial T_l}{\partial t}+\nabla\cdot\mathbf{q}_l=G(T_e-T_l)$	
(5) $\tau_l^{Au}\frac{\partial\mathbf{q}_l}{\partial t}+\mathbf{q}_l=-\kappa_l\nabla T_l$	
Plasma dynamics	
(6) $\frac{\partial u}{\partial t}+\nabla\cdot\mathbf{J}^q=S_{EM}-Q_{ei}-Q_{rad}$ $-\tilde{\Delta}S_{coll}-S_{rec}(u/n_e)$	u : Plasma kinetic energy n_e : Plasma density $\mathbf{J}^n$: Electron current density $\mathbf{J}^q$: Thermal current density Q_{ei} : Electron-ion energetic coupling Q_{rad} : Energetic loss by radiation S_{photo} : Photoionization rate S_{coll} : Collision ionization rate S_{rec} : Collision ionization rate $\tilde{\Delta}$: Ionization potential
(7) $\frac{\partial n_e}{\partial t}+\nabla\cdot\mathbf{J}^n=S_{photo}+S_{coll}-S_{rec}$	
Water dynamics	
(8) $\frac{\partial\rho}{\partial t}+\nabla\cdot(\rho\mathbf{v})=0$	ρ : Water density $\mathbf{v}$: Water velocity T_m : Water temperature S : Water entropy κ : Water thermal conductivity η : Viscosity coefficient σ_s : Surface tension κ_s : Bubble curvature δ_s : Dirac delta with a support on the bubble interface $\mathbf{n}$: Unit vector normal to the bubble surface
(9) $\rho T_m\left(\frac{\partial S}{\partial t}+\mathbf{v}\cdot\nabla S\right)=\nabla\cdot(\kappa\nabla T_m)$ $+\frac{1}{2}\eta\left(\frac{\partial v_i}{\partial x_k}+\frac{\partial v_k}{\partial x_i}-\frac{2}{3}\delta_{ik}\frac{\partial v_l}{\partial x_l}\right)^2$ $+Q_{ei}+S_{rec}(u/n_e)$	
(10) $\rho\left(\frac{\partial v_i}{\partial t}+v_k\frac{\partial v_i}{\partial x_k}\right)=-\frac{\partial p}{\partial x_i}+\sigma_s\kappa_s\delta_s\mathbf{n}$ $+\frac{\partial}{\partial x_k}\left[\eta\left(\frac{\partial v_i}{\partial x_k}+\frac{\partial v_k}{\partial x_i}-\frac{2}{3}\delta_{ik}\frac{\partial v_l}{\partial x_l}\right)\right]$	

Figure 1: General picture of the nanocavitation model

Table 2: Plasma dynamics

Parameter	Symbol	Value	Ref.
Collision cross-section	σ_a	$= 2\times10^{-19}$ m^2	22
Free electron mass	m_e	$=9.109\times10^{-31}$ kg	–
Collision ionization cross-section	σ_0	$=8.97\times10^{-22}$ m^2	23
Electron velocity	v_e	Calculated from $g(\varepsilon)$	12
Electron chemical potential	μ	Caclulated from $g(\varepsilon)$	12
Ionization potential	Δ	=6.5 eV	24
Effective extraction potential	$\tilde{\Delta}$	Expression from Keldysh theory	24
Plasmon frequency	ω_p	$=\sqrt{\frac{n_e e^2}{m_e\varepsilon_0}}$	25
Valence electron density	n_0	$=6.68\times10^{22}$ cm^{-3}	24
Initial neutral molecule density	n_{a0}	$=3.34\times10^{22}$ cm^{-3}	–
Neutral molecule density	n_a	$=(n_{a0}-0.5n_e)$	–
Plasma recombination time	τ_e^w	$=2\times10^{-9}$ cm^{3}s^{-1}	24
Normalized kinetic energy	β	$= u/\tilde{\Delta}$	27
Collision ionization frequency	ν_{ci}	$= n_{a0}(1-n_e/n_0)\sigma_0 v_e[(7.5\beta-1)\sqrt{\beta\pi}e^{-1/\beta}(3.5\beta^2-3\beta+1)erfc(1/\sqrt{\beta})]$	27
Photoionization rate	S_{photo}	Expression from Keldysh theory	24,28
Recombination rate	S_{rec}	$= \tau_e^w n_e^2$	24
Electromagnetic rate of work	S_{EM}	$= \frac{1}{2}Re[\mathbf{J}^*\cdot\mathbf{E}] = \frac{1}{2}Re[\sigma^*]\,\lvert\mathbf{E}\rvert^2$	21
Collision ionization rate	S_{coll}	$= \nu_{ci} n_e$	27
Plasma collision frequency with ionized species	ν_{ei}	$= min\left(\frac{\omega_p}{\sqrt{6}}, \frac{Ze^4 n_e\Lambda}{3\varepsilon_0^2 m_e^{1/2}(2\pi T_e)^{3/2}\left(1+e^{-\mu/k_bT_e}\right)F_{1/2}}\right)$	26,29
Fermi integral of order j	F_j	$= \frac{1}{\Gamma(j+1)}\int_0^\infty \frac{t^j dt}{1+e^{t-\mu/k_bT_e}}$	26
Coulomb Logarithm	Λ	$= \frac{1}{2}ln\left(1+\left(\frac{b_{max}}{b_{min}}\right)^2\right)$	26
Maximal impact factor	b_{max}	$= \left(\frac{n_e^2}{\varepsilon_0 k_b\sqrt{T_e^2+T_F^2}} + \frac{n_e^2}{\varepsilon_0 k_b T_m}\right)^{-1/2}$	26
Minimal impact factor	b_{min}	$= max\left(\frac{Ze^2}{4\pi\varepsilon_0 m_e v_e^2}, \frac{h}{2m_e v_e}\right)$	26
Plasma collision frequency with neutral species	ν_{en}	$= n_a\sigma_a v_e$	27
Electron-ion energetic coupling	Q_{ei}	$= 3\frac{m_e}{m_i}n_e(\nu_{ei}+\nu_{en})k_b(T_e-T_m)$	30
Energetic loss by plasma radiation	Q_{rad}	$= \frac{1}{4\pi\varepsilon_0}\frac{4e^2(k_bT_e)^2}{\sqrt{3}\hbar mc^3}n_e(\nu_{ei}+\nu_{en})$	30
Electron current	$\mathbf{J}^n$	$= (-1/e)(\mathbf{L}^{11}(\nabla\mu/e)+\mathbf{L}^{12}(-\nabla T_e))$	31
Heat current	$\mathbf{J}^q$	$= (-1/e)(\mathbf{L}^{21}(\nabla\mu/e)+\mathbf{L}^{22}(-\nabla T_e))$	31
Onsager coefficients	$\mathbf{L}^{ij}$	Expression from semiclassical theory of conduction	31

Evidence of oscillatory bubble behaviour

Figure 2 shows the experimental variation of the transmitted power from a He:Ne CW probe following a 45 fs, 800 nm irradiation of a sample containing 1.2×10^9 particles/mL of 100 nm diameter gold nanopsheres at 450 mJ/cm^2. The presence of oscillation is usually linked to successive growth and collapse phases of vapour bubbles,[32–37] clearly indicating that the signal is due to vapour bubbles.

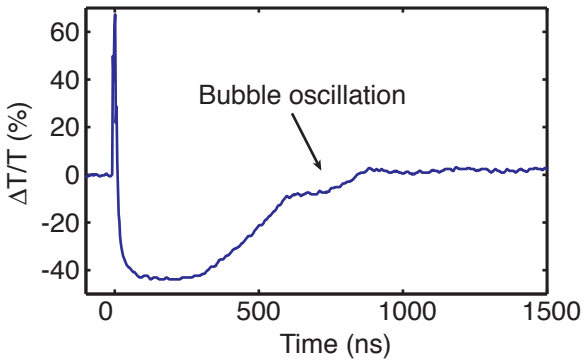

Figure 2: Experimental variation of the transmitted power from a He:Ne CW probe following a 45 fs, 800 nm irradiation of a sample containing 1.2×10^9 particles/mL of 100 nm diameter gold nanopsheres at 450 mJ/cm^2. Oscillatory behaviour is indicated on the figure.

References

(1) Johnson, P.; Christy, R. *Phys. Rev. B* **1972**, *6*, 4370–4379.

(2) The International Association for the Properties of Water,; Steam, *Erlangen, Germany* **1997**,

(3) Yu, P.; Cardona, M. *Fundamentals of Semiconductors*, 3rd ed.; Springer: Berlin, 2005; Chapter 6.

(4) Chen, J.; Beraun, J. *Num. Heat Transfer, part A* **2001**, *40*, 1–20.

(5) Bulgakova, N.; Stoian, R.; Rosenfeld, A.; Hertel, I.; Campbell, E. *Phys. Rev. B* **2004**, *69*, 054102.

(6) Riffe, D.; Wang, X.; Downer, M.; Fisher, D.; Tajima, T.; Erskine, J.; More, R. *J. Opt. Soc. Am. B* **1993**, *10*, 1424–1435.

(7) Bellan, P. *Fundamentals of plasma physics*; Cambridge University Press: Cambridge, 2006; Chapter 13.

(8) Wagner,; W. Pruss, A. *J. Phys. Chem. Ref. Data* **2002**, *31*, 387–535.

(9) *SESAME: The Los Alamos National Laboratory Equation-of-State Database, edited by S. P. Lyon and J. D. Johnson, Los Alamos National Laboratory, Report No. ucrl-7118 and ucrl-52190, 1979.* | *The water table used here was SESAME table 7150*

(10) Ekici, O.; Harrison, R.; Durr, N.; Eversole, D.; Lee, M.; Ben-Yakar, A. *J. Phys. D : Appl. Phys.* **2008**, *41*, 185501.

(11) *The database used was the one from the Naval Research Laboratory, Center for Computational Materials Science, previously available at cst-www.nrl.navy.mil/database.html. Consulted in May 2009. It seems however that this database is no longer available*

(12) Ashcroft, N.; Mermin, N. *Solid state physics*; Harcourt College Publishers: Fort Worth, 1976; Chapter 2.

(13) Chen, J.; Tzou, D.; Beraun, J. *Int. Journal of Heat and Mass Transfer* **2006**, *49*, 307–316.

(14) Zijlstra, P.; Tchebotareva, A.; Chon,; M., J. W.; Gu, M.; Orrit, M. *Nanoletters* **2008**, *8*, 3493–3497.

(15) Petrova, H.; Perez-Juste, J.; Zhang, Z.; Zhang, J.; Kosel, T.; Hartland, G. *J. Mater. Chem.* **2008**, *16*, 3957–3963.

(16) Ashcroft, N.; Mermin, N. *Solid state physics*; Harcourt College Publishers: Fort Worth, 1976; Chapter 1.

(17) Grua, P.; Morreeuw, J.; Bercegol, H.; Jonusauskas, G.; Vallee, F. *Phys. Rev. B.* **2003**, *68*, 35424.

(18) Wang, X.; Riffe, D.; Lee, Y.-S.; Downer, M. C. *Phys. Rev. B.* **1994**, *50*, 8016–8019.

(19) Logothetis, E.; Hartman, P. *Phys. Rev.* **1969**, *187*, 460–474.

(20) Zolotovitskii, Y.; Korshunov, L.; Benderskii, V. *Russian Chemical Bulletin.* **1972**, *21*, 760–763.

(21) Jackson, J. *Classical electrodynamics*, 3rd ed.; Wiley: New-York, 1998; Chapter 6.

(22) Date, H.; Sutherland, K.; Hasegawa, H.; Shimozuma, M. *Nuclear Instruments and Methods in Physics Research B* **2007**, *265*, 515–520.

(23) Arnold, C.; Heisterkamp, A.; Ertmer, W.; Lubatschowski, H. *Proc. of SPIE* **2008**, *6881*, 688104.

(24) Vogel, A.; Noack, G.; Hüttmann, G.; Paltauf, G. *Appl. Phys. B* **2005**, *81*, 1015–1047.

(25) Bellan, P. *Fundamentals of plasma physics*; Cambridge University Press: Cambridge, 2006; Chapter 4.

(26) Lee, Y.; More, R. *Physics of Fluids* **1984**, *27*, 1273–1286.

(27) Hallo, L.; Bourgeade, A.; Tikhonchuk, V.; Mezel, C.; Breil, J. *Phys. Rev. B* **2007**, *76*, 101–113.

(28) Keldysh, L. *Zhurnal Eksperimental'noi i Teoreticheskoi Fiziki* **1965**, *47*, 1945–1957.

(29) Andreev, N.; Veisman, M.; Efremov, V.; Fortov, V. *High Temp.* **2003**, *41*, 594–608.

(30) Veysman, M.; Cros, B.; Andreev, N.; Maynard, G. *Physics of Plasma* **2006**, *13*, 53114.

(31) Ashcroft, N.; Mermin, N. *Solid state physics*; Harcourt College Publishers: Fort Worth, 1976; Chapter 13.

(32) Lukianova-Hleb, E.; Hu, Y.; Latterini, L.; Tarpani, L.; Lee, S.; Drezek, R.; Hafner, J.; Lapotko, D. *ACS Nano* **2010**, *4*, 2109–2123.

(33) Vogel, A.; Linz, N.; Freidank, S.; Paltauf, G. *Phys. Rev. Lett.* **2008**, *100*, 038102.

(34) Rayleigh, L. *Philos. Mag. Series 6* **1917**, *34*, 94–98.

(35) Neumann, J.; Brinkmann, R. *Proc. SPIE* **2003**, *5142*, 82.

(36) Brinkmann, R.; Neumann, J. *Appl. Phys. Lett.* **2008**, *93*, 033901.

(37) Aglyamov, S.; Karpiouk, A.; Bourgeois, F.; Ben-Yakar, A.; Emelianov, S. *Opt. Lett.* **2008**, *33*, 1357–1359.

ANNEXE B

Plasma-Mediated Nanocavitation and Photothermal Effects in Ultrafast Laser Irradiation of Gold Nanorods in Water : Supporting Information

Cette annexe présente le Supplementary Information de l'article retranscrit au chapitre 5 [1]. Il apporte des précisions sur les oscillations mécaniques observées expérimentalement et explique la méthode permettant d'obtenir le diamètre maximal de la bulle à partir des études spectroscopiques présentées dans le manuscrit principal.

1. E. Boulais, R. Lachaine et M. Meunier. Plasma-Mediated Nanocavitation and Photothermal Effects in Ultrafast Laser Irradiation of Gold Nanorods in Water. *J. Phys. Chem. C*, Manuscript ID : jp-2012-12475h, 2012

Plasma-Mediated Nanocavitation and Photothermal Effects in Ultrafast Laser Irradiation of Gold Nanorods in Water : Supporting Information

Etienne Boulais, Rémi Lachaine, and Michel Meunier*

Laser Processing and Plasmonics Laboratory, Engineering Physics Department, École Polytechnique de Montréal, Montréal, Québec, H3C 3A7, Canada

E-mail: michel.meunier@polymtl.ca

Structural Oscillations

The structural oscillation of nanostructures following a laser irradiation can be modelled with the following equation[1]

$$\Delta\Omega(t) = A_0 e^{-\frac{t}{T_1}} e^{-\frac{t^2}{T_2^{*2}}} sin\left(\frac{2\pi t}{T_0} + \phi\right) + A_1 e^{-t/\tau_{cool}} \quad (1)$$

where $\Delta\Omega$ is the absorption time variation, T_1 is the homogeneous damping due to friction, T_2^* is the inhomogeneous damping due to the dephasing effect coming from the size distribution within the sample, T_0 is the oscillation period and τ_{cool} is the heat transfer from the nanostructure to its environment.

T_1 is fixed at $261ps$, as in the paper from Pelton et al.[1] We used TEM imaging to determine the size distribution within the nanorod sample. Results are presented in figure 1. An average length of $L_0 = 46.9nm$ has been found, with a standard deviation $\sigma_L = 3.4nm$.

*To whom correspondence should be addressed

The oscillation period T_0 can be calculated from the thin rod theory.[2]

$$T_0 = \frac{2L_0}{\sqrt{E/\rho}} = 63.6ps \tag{2}$$

The inhomogeneous damping can be calculated from this value and the standard deviation

$$T_2^* = \frac{T_0^2\sqrt{E/\rho}}{2\sqrt{2}\pi\sigma_L} = 198ps \tag{3}$$

A_0, A_1, ϕ and τ_{cool} are used as fit parameters. Regression gives : $A_0 = 0.06$, $A_1 = 0.55$, $\phi = 1.8$ and $\tau_{cool} = 174ps$.The result is in good agreement with the experimental observation, as shown in figure 4b of the paper.

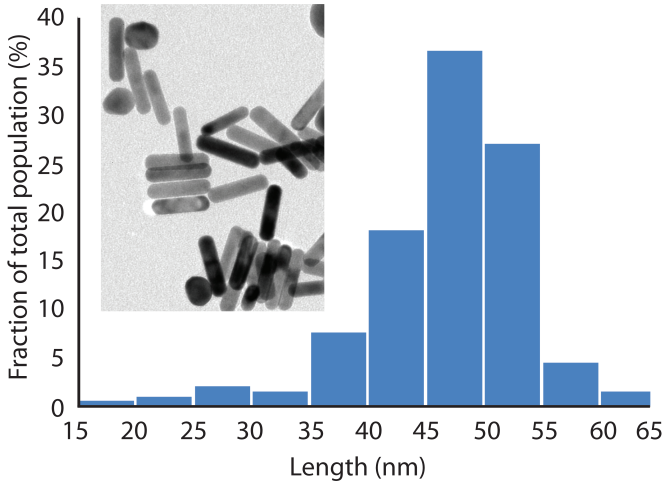

Figure 1: Length distribution in the gold nanorods colloidal suspension from TEM imaging. TEM imaging of the gold nanorod suspension is shown in inset.

Melting temperature of a gold nanorod

For a nanostructure, the melting temperature is dependant on the dimension of the particle. We define the geometric parameter α[3]

$$\alpha = \frac{\sigma_s}{4\pi \left(\frac{3V}{4\pi}\right)^{2/3}} \tag{4}$$

where σ_s is the particle's surface, and V is its volume. The corrected melting temperature can than be written

$$T_f = T_f^0 \left(1 - 6\alpha \frac{d_0}{D_{eff}}\right) \tag{5}$$

where T_f^0 is the bulk melting temperature(1338K for gold[4]), d_0 is the atomic radius ($144pm$ for gold[5]) and D_{eff} is the effective diameter of the particle, defined as

$$D_{eff} = 2\left(\frac{3V}{4\pi}\right)^{1/3} \tag{6}$$

For a $10nm \times 41nm$ gold nanorod, $D_{eff} = 17.8nm$, $\alpha = 1.29$ and $T_f = 1254K$.

Calculation of the average bubble diameter from light scattering experiment

In the section entitled *Experimental detection and characterization of the vapor bubbles* in the main manuscript, the analysis of the light-scattering signal shown in figure 9b must take into consideration the random orientation of the AuNRs relative to the laser polarization. In particular, we are interested in finding the diameter of the bubbles produced by AuNRs aligned with the polarization.

We first performed simulation of the energy deposited in the particle-water system, using the model presented in the section *Theoretical Methods* in the main manuscript and detailed in,[6] as a function of the angle between the laser polarization and the AuNR's longitudinal axis. The result is presented in figure 2 and shows that the deposited energy E_d scales as

$$E_d = E_d^{max} cos(\beta) \tag{7}$$

where β is the angle between the polarization vector of the electric field and the AuNR's longitudinal axis. According to Siems et al.,[7] the diameter of the vapor bubble scales with energy as:

$$d_{bubble} = A E_d^{0.45} \tag{8}$$

In a spherical coordinate system, at a given fluence and for a given polarization orientation (θ, ϕ) incident on a AuNR with its longitudinal axis along the x axis, the bubble diameter can be expressed as:

$$d_{bubble} = d_{bubble}^{max} \left[|sin(\theta)cos(\phi)| \right]^{0.45} (10) \tag{9}$$

with d_{bubble}^{max}, the diameter of the bubbles generated with a polarization parallel to the AuNR's longitudinal axis. Hence, the experimentally deduced absorption coefficient α_{exp} can be written as:

$$\alpha_{exp} = \frac{N \int \sigma(d_{bubble}(\theta, \phi)) sin(\theta) d\theta d\phi}{\int sin(\theta) d\theta d\phi} \frac{(\xi w_{pump})^2}{w_{probe}^2} \tag{10}$$

so that

$$T = e^{-\alpha_{exp}(\xi L)} \tag{11}$$

where T is the transmissivity of the probe beam, N is the nanorod concentration, L is the Rayleigh length and $\sigma(d_{bubble}(\theta, \phi))$ is the extinction cross-section associated to a vapor bubble of diameter d_{bubble} around a AuNR. ξ is a corrective factor accounting for the reduction of the effective focal volume due to the non-linear effects in water, and has been evaluated as $\xi = \sqrt{5}/5$ by Vogel et al.[8] for a $800nm$ laser. Note that the pump and probe waists (w_{pump} and w_{probe}) are equal and measure $(6 \pm 1)\mu m$. Knowing the function $\sigma(d_{bubble}(\theta, \phi))$ from Mie theory and from the expression for $d_{bubble}(\theta, \phi)$ given in equation 9, we may inverse equation 10 to get the bubble diameter d_{bubble}^{max} associated to the AuNRs that are aligned with the polarization. For a fluence of $200 mJ/cm^2$, results show a diameter $d_{bubble}^{max} \sim 430nm$. Note that the Mie theory can be used for bubbles larger

than $\sim 100nm$ as the presence of the nanostructure then influences very weakly the total extinction cross-section that is dominated by the vapor bubble.[9]

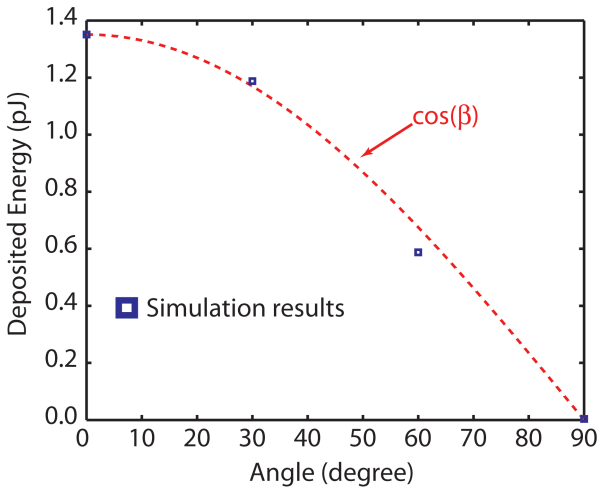

Figure 2: Simulation of the energy deposited in the water-AuNR system as a function of the angle between the laser polarization vector and the AuNR's great axis for a $45fs$, $800nm$, $200mJ/cm^2$ pulse.

References

(1) Pelton, M.; Sader, J. E.; Burgin, J.; Liu, M.; Guyot-Sionnest, P.; Gosztola, D. Damping of acoustic vibrations in gold nanoparticles. *Nature Nanotechnology* **2009**, *4*, 492–495.

(2) Hu, M.; Hillyard, P.; Hartland, G. V.; Kosel, T.; Pérez-Juste, J.; Mulvaney, P. Determination of the elastic constants of gold nanorods produced by seed mediated growth. *Nano Letters* **2004**, *4*, 2493–2497.

(3) Qi, W. H.; Wang, M. P. Size and shape dependent melting temperature of metallic nanoparticles. *Materials Chemistry and Physics* **2004**, *88*, 280–284.

(4) Plech, A.; Kotaidis, V.; Grésillon, S.; Dahmen, C.; von Plessen, G. Laser-induced heating and melting of gold nanoparticles studied by time-resolved x-ray scattering. *Physical Review B* **2004**, *70*, 195423.

(5) Pauling, S. Atomic radii and interatomic distances in metals. *J. Am. Chem. Soc.* **1947**, *69*, 542–553.

(6) Boulais, É.; Lachaine, R.; Meunier, M. Plasma mediated off-resonance plasmonic enhanced ultrafast laser induced nanocavitation. *Nano Letters* **2012**, *12*, 4763–4769.

(7) Siems, A.; Weber, S.; Boneberg, J.; Plech, A. Thermodynamics of nanosecond nanobubble formation at laser-excited metal nanoparticles. *New Journal of Physics* **2011**, *13*, 043018.

(8) Vogel, A.; Noack, J.; Hüttman, G.; Paltauf, G. Mechanisms of femtosecond laser nanosurgery of cells and tissues. *Applied Physics B: Lasers and Optics* **2005**, *81*, 1015–1047.

(9) Lachaine, R.; Boulais, É.; Bourbeau, E.; Meunier, M. Effect of pulse duration on plasmonic enhanced ultrafast laser-induced bubble generation in water. *Applied Physics A: Materials Science & Processing* **2012**, 1–4.

ANNEXE C

Liste des publications

Liste des publications de Etienne Boulais

A. Journaux avec arbitrage

1. **Boulais, E.**, Lachaine, R., Hatef, A. & Meunier, M. Plasmonics for pulsed-laser cell nanosurgery : fundamentals and applications, *Submitted to J. of Photochem. and Photobiol. C: Photochemistry Reviews*, (2012).

2. St-Louis Lalonde, B., **Boulais, E.**, Lebrun, J.J. & Meunier, M. Visible and Near infrared resonance plasmonic enhanced nanosecond laser optoporation of cancer cells. *Biomedical Optics Express*, *In press*, (2012).

3. Hatef,. A., Seyed, M.S., Deschênes, S., **Boulais, E.** & Meunier, M. Coherently-enabled environmental control of optics and energy transfer pathways of hybrid quantum dot-metallic nanoparticles systems. *Optics Express*, *In press*, (2012).

4. **Boulais, E.**, Lachaine, R. & Meunier, M. Plasma-Mediated Nanocavitation and Photothermal Effects in Ultrafast Laser Irradiation of Gold Nanorods in Water, *Submitted to J. Phys. Chem. C*, (2012)

5. Robitaille, A., **Boulais, E.** & Meunier, M. Mechanisms of plasmon-enhanced femtosecond laser nanoablation of silicon, *Submitted to Optics Express,* (2012).

6. Hatef, A., Seyed, M.S., **Boulais, E.** & Meunier M. Quantum dot-metallic nanorod sensors via exciton-plasmon interaction, *Nanotechnol.* **24**, 015502, (2013).

7. **Boulais, E.**, Lachaine, R. & Meunier, M. Plasma mediated off-resonance plasmonic enhanced ultrafast laser induced nanocavitation, *Nano Lett.* **12**(9),4763-4769, (2012).

8. Lachaine, R. **Boulais, E.**, Bourbeau, E. & Meunier, M. Effect of pulse duration on plasmonic enhanced ultrafast laser-induced bubble generation in water, *Appl. Phys. A*, Online First, (2012).

9. Baumgart, J., Humbert, L., **Boulais, E.**, Lachaine, R., Lebrun, J.-J. & Meunier, M. Off-resonance plasmonic enhanced femtosecond laser optoporation and transfection of cancer cells. *Biomaterials* **33**(7), 2345-2350 (2012).

10. **Boulais E**, Robitaille A, Desjeans-Gauthier P. & Meunier, M. Role of near-field enhancement in plasmonic laser nanoablation using gold nanorods on a silion substrate: comment. *Opt. Express* **19**, 6177-6178 (2011) .

11. Singh, R., Audet, Y., Gagnon, Y., Savaria, Y., **Boulais, E.** & Meunier, M. A laser-trimmed rail-to-rail precision CMOS operational amplifier. *IEEE Transactions on circuits and systems* **58**(2), 75-59 (2011).

12. **Boulais, E.**, Fantoni, J., Chateauneuf, A., Savaria, Y. & Meunier, M. Laser-induced resistance fine tuning of integrated polysilicon thin-film resistors. *IEEE Transactions on Electron Devices* **58**(2), 572-575 (2011).

13. Lachaine, R., **Boulais, E.** & Meunier, M. Optical in-situ probing method for laser antifuse linking. *Semiconductor Science and Technology* **25**(6), 065015 (2010).

14. **Boulais, E.**, Degorces, J.-Y., Binet, V., Savaria, Y. & Meunier, M. Thermodynamics and transport model of charge injection in silicon irradiated by a pulsed focused laser. *IEEE Transaction on Electron Devices* **55**(10), 2728-2735 (2008).

B. Proceedings

1. **Boulais, E.**, Lachain, R. & Meunier, M. Basic mechanisms of the femtosecond laser interaction with a plasmonic nanostructure in water. *Proceedings of the SPIE 7925*, 79250G (2011).

2. Schomaker, M., Baumgart, J., Motekaitis, D., Heinemann, D., Krawinkel, J., Pangalos, M., Bintig, W., **Boulais, E.**, Lachaine, R., St-Louis Lalonde, B., Ngezahavo, A., Meunier, M. & Heisterkamp, A. Mechanisms of gold nanoparticle mediated ultrashort laser cell membrane perforation. *Proceedings of the SPIE* 7925, 79250F (2011).

C. Divulgations d'invention

1. **Boulais, E.**, Meunier, M., & Savaria, Y., Method and apparatus for iterative laser tuning of polysilicon film. Disclosure to École Polytechnique, DIV-357, (2008)

2. Meunier, M., Lachaine, R. et **Boulais, E.** Plasmon-enhanced spectral and temporal shaped (PE- STEPS) laser process. Disclosure to École Polytechnique, DIV-539, (2012).

D. Conférences invitées

1. **Boulais, E.**, Baumgart, J., Lachaine, R., Desjeans-Gauthier, P. & Meunier, M. Plasmonic enhanced femtosecond laser nanoprocessing : Fundamentals and biomedical applications. *PICALO,* Wuhan, China*,* (2010).

E. Autres conférences

1. **Boulais, E**., Lachaine, R., Robitaille, A. and Meunier, M. Fundamentals and applications of in and off-resonance plasmonic enhanced ultrafast laser nanoprocessing. *LPM* (2012).

2. Robitaille, A., **Boulais, E.** & Meunier, M. Basic physical mechanisms of near-field enhanced femtosecond laser ablation. *Conference on laser ablation COLA* (2011).

3. **Boulais, E.**, Lachaine, R. & Meunier, M. Modeling plasmonic enhanced laser induced nanocavitation in water. *Laser precision microfabrication LPM* (2011).

4. **Boulais, E.**, Baumgart, J., Lachaine, R., Desjeans-Gauthier, P. & Meunier, M. Plasmonic enhanced femtosecond laser nanoprocessing and cell nanosurgery, SPIE *Photonics West* (2010).

5. **Boulais, E.**, Lachaine, R., Poulin, G. & Meunier, M. Ultrafast laser interaction with plasmonic nanostructures in water. *SPIE Photonics West* (2010).

6. Meunier M., **Boulais, E.** & Desjeans-Gauthier, P. Gold nanorod enhanced femtosecond laser nanoprocesssing. *Conference on laser ablation COLA* (2009).

7. Meunier M., **Boulais, E.** & Desjeans-Gauthier, P. Gold nanorod enhanced femtosecond laser nanoprocesssing. *Laser precision microfabrication LPM* (2009).

8. **Boulais, E.** & Meunier, M. Modeling ultrafast laser induced heating of nanoplasmonic structures on biological tissues. *Laser precision microfabrication* (2008).

9. **Boulais, E.**, Wild, G., Degorces, J.-Y., Savaria, Y. & Meunier, M. Modeling laser-induced charge injection effects on surrounding sensitive silicon microelectronics devices. *SPIE Photonics North* (2006).

10. Wild, G., **Boulais, E.**, Savaria, Y. & Meunier, M. Characterization of laser-induced photoexcitation effects on a surrounding CMOS ring oscillator. *Canadian semiconductor technology conference* (2005).